Quantum sensing in diamond and silicon carbide: mapping spins and taming charges

van de Stolpe, G.L.

DOI
10.4233/uuid:d6f957b2-5eda-4068-b474-5de8d4dc319d

Publication date
2024

Document Version
Final published version

Citation (APA)
van de Stolpe, G. L. (2024). *Quantum sensing in diamond and silicon carbide: mapping spins and taming charges*. [Dissertation (TU Delft), Delft University of Technology]. https://doi.org/10.4233/uuid:d6f957b2-5eda-4068-b474-5de8d4dc319d

QUANTUM SENSING IN DIAMOND AND SILICON CARBIDE: MAPPING SPINS AND TAMING CHARGES

Dissertation

for the purpose of obtaining the degree of doctor
at Delft University of Technology,
by the authority of the Rector Magnificus, Prof. dr. ir. T.H.J.J. van der Hagen,
Chair of the Board for Doctorates,
to be defended publicly on
November 6th 2024 at 10:00 o'clock

by

Guido Luuk VAN DE STOLPE

Master of Science in Physics,
Leiden University, The Netherlands,
born in 's-Hertogenbosch, The Netherlands.

This dissertation has been approved by the promotor:
Prof. dr. ir. R. Hanson

Composition of the doctoral committee:

Rector Magnificus	Chairperson
Prof. dr. ir. R. Hanson	Delft University of Technology, promotor
Dr. ir. T. H. Taminiau	Delft University of Technology, copromotor
Independent members:	
Prof. dr. A. F. Otte	Delft University of Technology
Prof. dr. F. E. Schreck	University of Amsterdam
Dr. T. van der Sar	Delft University of Technology
Dr. F. Kaiser	Delft University of Technology
Reserve member:	
Prof. dr. S. Gröblacher	Delft University of Technology

Cover design: Guido van de Stolpe

Printed by: Gildeprint

ISBN 978-94-6384-666-0

An electronic version of this dissertation is available at
http://repository.tudelft.nl/.

CONTENTS

SUMMARY

Solid-state defects in diamond and silicon carbide have emerged as a promising platform for exploring various quantum technologies, such as distributed quantum computing, quantum simulations of many-body physics, and nano-scale nuclear magnetic resonance. The noise environment surrounding such defects, consisting of magnetic and electrical impurities, directly impacts the spin and optical coherence, posing a key challenge for advancing quantum technologies. Systematic study of these spins and charges is crucial for mitigating their noise contribution. In some cases, establishing control over the environment can even convert it into a resource, to be used for storing, or processing (quantum) information. In this thesis, we develop experimental and analytical tools that enable a more detailed study of the defect spin and charge environment, and can be exploited to manipulate its microscopic configuration.

First, we investigate the charge environment surrounding single V2 centers in commercially available silicon carbide, whose dynamics causes significant spectral diffusion of the optical transitions (Chapter 3). After carefully characterising the diffusion and ionisation rates, we realise probabilistic tuning of the optical transitions and manage to preserve the emission frequency for extended periods of time. The observation of optical coherence in such mass-fabricated material might provide opportunities for scaling up quantum technologies.

Second, we study the ^{13}C nuclear spin environment surrounding single nitrogen-vacancy centers in diamond. Such nuclear spins can be used to store and process quantum information, and provide a test bed for exploring magnetic resonance imaging techniques at the nano-scale. We develop a general framework for spin detection and control based on decoherence-protected radio-frequency quantum gates (Chapter 4). Our insights provide pathways for improving both the sensitivity of detection schemes and the fidelity of quantum gates. Finally, we map out a network consisting of 50 ^{13}C nuclear spins, characterising both the electron-nuclear interactions, as well as the nuclear-nuclear couplings with high spectral resolution (Chapter 5). Importantly, our methods can also be used for selective spin readout, a crucial step towards using the network as quantum simulator of many-body physics (Chapter 6).

This thesis provides new methods to characterise and control the environment of solid-state defects and might inspire applications in the field of magnetic and electrical sensing at the nano-scale. Furthermore, the degree of control demonstrated here, may enable advances towards quantum simulation and distributed quantum computing on this platform.

SAMENVATTING

Vastestofdefecten in diamant en siliciumcarbide zijn een veelbelovend platform voor de ontwikkeling van diverse kwantumtechnologieën, zoals gedistribueerde kwantumcomputers, kwantumsimulaties van veellichamenfysica en nanoschaal kernspinresonantie. De ruisomgeving rond zulke defecten, bestaande uit magnetische en elektrische imperfecties, heeft een sterke invloed op de spin- en optische coherentie van het defect, en vormt daardoor een belangrijke uitdaging voor de ontwikkeling van kwantumtechnologieën. Systematisch onderzoek naar deze spins en ladingen is cruciaal om hun ruisbijdrage te verminderen. In sommige gevallen kan de omgeving, door er controle over te ontwikkelen, zelfs worden ingezet als een hulpbron, die kan worden gebruikt voor het opslaan of verwerken van (kwantum)informatie. In dit proefschrift ontwikkelen we experimenteel en analytisch gereedschap waarmee we de defectspin- en ladingomgeving in meer detail kunnen bestuderen, en die kunnen worden gebruikt om de microscopische configuratie ervan te manipuleren.

Eerst onderzoeken we de elektrische omgeving rondom individuele V2-centra in commercieel verkrijgbaar siliciumcarbide, waar we significante spectrale diffusie van de optische transities observeren (Hoofdstuk 3). Na zorgvuldige karakterisatie van de diffusie- en ionisatietijdschalen, vinden we een manier om de optische transities probabilistisch te variëren en slagen we erin de emissiefrequentie gedurende langere perioden constant te houden. Het feit dat V2-centra optisch coherent zijn in zulk massaal gefabriceerd materiaal kan kansen bieden voor het opschalen van kwantumtechnologieën.

Vervolgens bestuderen we de ^{13}C-kernspinomgeving rond enkele NV centra in diamant. Dergelijke kernspins kunnen worden gebruikt om kwantuminformatie op te slaan en te verwerken, en bieden een testplatform voor het verkennen van technieken voor nanoschaal MRI. We ontwikkelen een algemeen *framework* voor spin-detectie en controle op basis van decoherentie-beschermde radiofrequentie kwantumoperaties (Hoofdstuk 4). Onze inzichten kunnen gebruikt worden om zowel de gevoeligheid van detectietechnieken als de nauwkeurigheid van kwantumoperaties te verbeteren. Ten slotte brengen we een netwerk van 50 ^{13}C-kernspins in kaart, waarbij we zowel de elektron-kerninteracties als de kern-kernkoppelingen met hoge spectrale resolutie karakteriseren (Hoofdstuk 5). Deze methoden kunnen ook worden gebruikt om de spintoestand selectief uit te lezen, een cruciale stap om het netwerk als kwantumsimulator van veellichamenfysica te gaan gebruiken (Hoofdstuk 6).

Dit proefschrift beschrijft nieuwe methoden om de omgeving van vastestofdefecten te karakteriseren en te controleren, en kan relevant zijn voor de ontwikkeling van toepassingen op het gebied van magnetische en elektrische nanoschaal meetmethodes. Bovendien kan de mate van controle die hier gedemonstreerd is bijdragen aan de vooruitgang van kwantumsimulaties en gedistribueerde kwantumcomputers op dit platform.

1

INTRODUCTION

1.1. THE QUANTUM SCIENCE AND TECHNOLOGY FEEDBACK LOOP

Traditionally, science and technology have different objectives: the former uses events to deduce theories, while the latter uses theories to induce events. In practice however, the two are often closely related, especially in the field of quantum mechanics; explaining the photo-electric effect enables to the production of efficient photovoltaic cells, while the theory of nuclear magnetic resonance provides the basis for MRI machines. In the past decades, four new branches of quantum technology have emerged: quantum sensing[1], simulation[2], computing[3] and communication[4]. For these four, symbiosis between science and technology remains especially relevant, as they operate at the edge of our scientific knowledge. New scientific insights are often needed to accelerate technological development, while at the same time state-of-the-art technologies are needed to explore previously inaccessible regimes of physics. In this spirit, the work in this thesis is not focused on developing a single technology or answering a specific scientific question, but rather aims to contribute at the intersection of various technologies and different scientific disciplines within physics. To understand how the research in this thesis relates to future technological applications and to current scientific questions, I introduce the quantum science and technology *feedback loop* sketched in Fig. 1.1.

The *feedback loop* illustrates my view of the approach to quantum research. By first exploring, and then developing control over quantum systems, we can establish their use in quantum technologies. The developed methods can then be used either to further study the quantum system itself, increasing our knowledge and advancing certain fundamental fields of science, or can be commercialised to be used outside academia. The former creates a self-reinforcing growth of knowledge and technical skills, while the latter provides a dot on the horizon to work towards and may only become practical at a later stage of development. Notably, progress towards such a moonshot goal is often small and indirect, and judging the merit of research just on this basis might make advances look insignificant. However, taking into account the *feedback loop* and our increasing understanding of the system, research also has a more tangible, direct impact.

With that caveat in mind, I will first list the three moonshot goals this thesis aims to contribute to, which provide a general direction and motivation for the performed research. Then, I will introduce the quantum system we work with: solid-state defects in diamond and silicon carbide, and will introduce the different research projects covered in chapters 3,

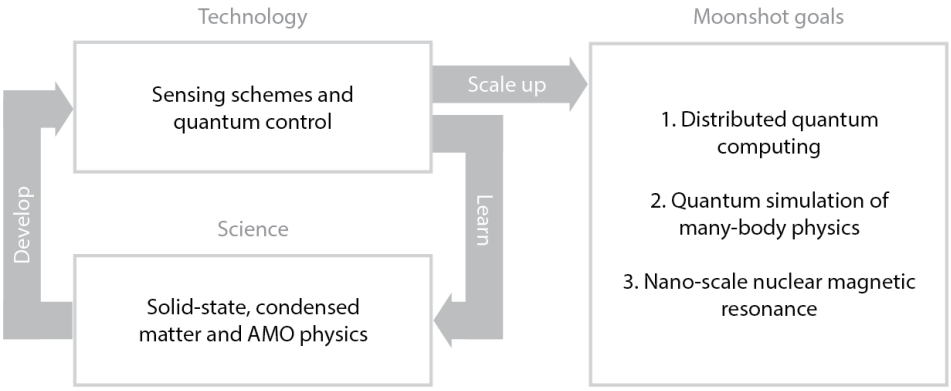

Figure 1.1: **The quantum science and technology feedback loop.** The research in this thesis depends on (and contributes to) a symbiosis between quantum science and technology. Our approach is to manipulate a quantum system by developing sensing and control techniques. Such technological advances allow us to learn more about the system, thereby advancing fundamental science, which in turn can be used for further technological development, creating a feedback loop. This self-reinforcing loop has as ultimate goal to eventually scale-up technologies that have the potential for practical use outside our specific research field (denoted as 'moonshot goals').

4 and 5. In chapter 6, I will explain in more detail how these results relate to the moonshot goals, and how they contribute directly to scientific understanding (via the *feedback loop*).

1. **Distributed quantum computation (DQC).** Quantum computing aims to use isolated quantum systems, such as single atoms or electrons, for information processing. The ability to create large, coherent superpositions of quantum states, naturally offers parallelism that can be exploited for computations. For a specific set of problems, superpolynomial computational speedup is expected, compared to the performance of classical computers[3,5]. However, to achieve practical quantum advantage, millions of well-connected quantum bits (qubits) are likely needed, posing a significant scalability problem[6]. One promising approach is to use a modular architecture, consisting of independent 'nodes', connected by optical interconnects[7–9]. Each node consists of a small register of spins that serve as processing qubits, whose spin state can be entangled with a photonic state, which is used to exchange quantum information between nodes. One of the main outstanding challenges is to engineer nodes that consist of (a number of) high-quality processing qubits that also provide a coherent optical interface for generating spin-photon entanglement[10].

2. **Quantum simulation of many-body physics (QS).** Closely related to quantum computation, quantum simulation aims to use large, controlled quantum systems to mimic the dynamics, or energy spectrum, of a specific physical system of interest. This 'analog', non-universal form of quantum computing typically puts less stringent requirements on the fidelity of operations, compared to 'digital', universal quantum computing[2], making it a promising application in the near-term intermediate scale quantum (NISQ) era[2,6]. Scaling up the system size, and complexity of simulated dy-

namics is key for attaining quantum advantage over simulations with classical computers.

3. **Nano-scale nuclear magnetic resonance (nano-NMR).** Nuclear magnetic resonance spectroscopy aims to reconstruct the spatial configuration of nuclear spins in a molecule (or material) by measuring magnetic interactions [11]. Scaling this technique down to the nanometer length scale is of specific interest, as it might allow for the imaging of single molecules like viruses and proteins, possibly while recording their dynamics in an *in vitro* setting [12]. Impressive advances have been made by exploiting nanometer-size quantum sensors, leading to the detection of few-nm^{-3} detection volumes [13,14]. However, various outstanding challenges remain [12,15]. These include preparing the sample of interest close to the (quantum) sensor while preserving its characteristics [16,17], stabilising the sensor in such a challenging environment [16,18–20] and designing effective polarisation and detection protocols that can reconstruct the spatial structure at the single-molecule level [21–24].

1.2. OPTICALLY ACTIVE SOLID-STATE DEFECTS

Solid-state defects, such as the nitrogen-vacancy (NV) center in diamond [25] or the silicon-vacancy (V_{Si}) in silicon carbide [26,27], are a promising platform for all four branches of quantum technology, providing a coherent spin-photon interface at elevated temperatures (up to 20 K for the V_{Si} [27]) and spin coherence up to room temperature [28–30], while being relatively easy to operate due to their embedding in a host crystal. Some recent advances include: the demonstration of a three node quantum network [31,32], the fault-tolerant operation of a logical qubit [33], quantum simulations of many-body physics [34–36] and a wide range of sensing and metrology demonstrations, ranging from scanning magnetometry [37,38] to electrometry and nuclear-magnetic-resonance spectroscopy at the nano scale [21,39,40].

In this thesis, we study the spin and charge environment of solid-state defects in diamond and silicon carbide (see Fig. 1.2). For many of the aforementioned applications, a good understanding of the spin and charge environment is key. On the one hand, the environment acts as a noise source to the defect. Fluctuating spins and charges create magnetic and electric fields that limit the defect's spin and optical coherence, respectively. On the other hand, in some cases, it is possible to establish (quantum) control over this spin and charge environment, converting a noise source into a resource. For example, we show that nuclear spins in the diamond crystal (the main source of spin decoherence) can in fact be controlled as quantum bits, with potential for performing quantum simulations (chapter 5), while the defect's charge environment (the main source of optical decoherence) can be used for tuning the optical emission frequency (chapter 3).

The structure of this thesis is organised in a topical way, spanning first the charge, and then the spin environment.

In **chapter 2**, I briefly explain the key concepts necessary to understand the operation of the solid-state defects used in this work.

In **chapter 3**, we study the optical coherence of negatively charged V_{Si} centers in commercially available bulk silicon carbide (SiC). We implement a charge-resonance check to herald the charge environment of the defect in specific configurations. Next, we study the dynamics of the charge environment by monitoring changes in the defect's optical transi-

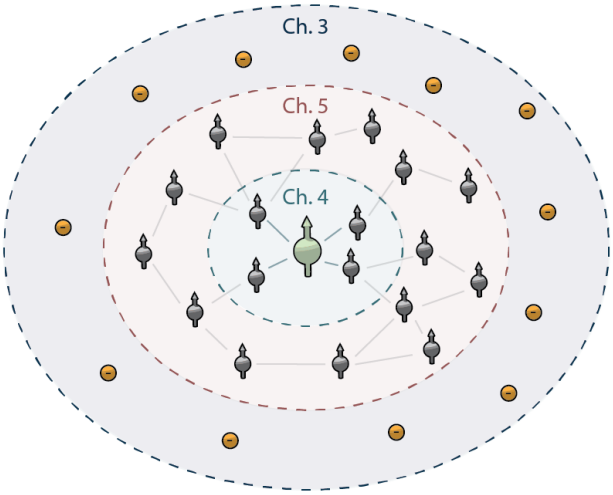

Figure 1.2: **System overview.** Schematic illustrating the spin and charge environment of a solid-state defect (mint green central spin). Chapter 3 (dark blue band) investigates the fluctuating charge environment (yellow dots) by studying changes in the defect's optical transition frequency. Chapter 4 (green ellipse) examines the DDRF sequence[41], which exploits the electron-nuclear hyperfine interaction (green lines) for sensing and selective quantum control of nuclear spins (dark grey). Chapter 5 discusses new methods to map out a (randomly-oriented) network of nuclear spins surrounding the defect, yielding both the nuclear-nuclear interactions (grey lines) as well as the hyperfine interactions with high spectral resolution.

tion frequency and map out its dependence on laser excitation. We develop a spectroscopy method that probes the degree of optical coherence on a timescale faster than the spectral diffusion dynamics. This allows for the observation of near-lifetime-limited optical coherence, even for defects in fabricated nano-structures. Finally, we employ probabilistic control over the charge environment to tune the defect emission frequency over a gigahertz range, which is relevant to generating entanglement between different nodes in the context of distributed quantum computing[31,42].

In **chapter 4**, we dive into the (hyperfine-coupled) nuclear spin environment of the NV center. We re-examine a recently developed class of decoherence-protected electron-nuclear gates known as DDRF gates[41]. By relaxing various approximations made in previous work, we can analytically describe behaviour that was limiting gate fidelities and sensitivity of the sequence. Armed with this knowledge, we study a more general version of the DDRF gate, which allows for more systematic mitigation of crosstalk and enables an expected order-of-magnitude increase in sensitivity for the detection of nuclear spins.

In **chapter 5**, we investigate the nuclear-spin environment of the NV center in more detail. We develop sensing sequences that can map out the structure of a 50-spin network, even when characteristic spin frequencies overlap spectrally. The presented high-resolution hyperfine spectroscopy method can be used to validate density-functional calculations[43]. Furthermore, establishing individual initialisation, control and readout of a large part of the network opens the door for studying nuclear hyperpolarisation dynamics[44,45] (relevant to nano-NMR), and for quantum simulations of many-body physics[35].

In **chapter 6**, I summarise the main results of this thesis and illustrate how they relate

to each other, and to the moonshot goals, in the context of the *feedback loop* in figure 1.1. Finally, I provide an outlook for the challenges and opportunities that lay ahead.

1

REFERENCES

[1] C. L. Degen, F. Reinhard and P. Cappellaro, *Quantum sensing,* Rev. Mod. Phys. **89**, 035002 (2017).

[2] I. M. Georgescu, S. Ashhab and F. Nori, *Quantum simulation,* Rev. Mod. Phys. **86**, 153 (2014).

[3] A. Steane, *Quantum computing,* Rep. Prog. Phys. **61**, 117 (1998).

[4] N. Gisin, G. Ribordy, W. Tittel and H. Zbinden, *Quantum cryptography,* Rev. Mod. Phys. **74**, 145 (2002).

[5] S. Jordan, *Quantum algorithm zoo,* https://quantumalgorithmzoo.org/ .

[6] M. E. Beverland *et al.*, *Assessing requirements to scale to practical quantum advantage,* (2022), arXiv:2211.07629 [quant-ph] .

[7] N. H. Nickerson, J. F. Fitzsimons and S. C. Benjamin, *Freely Scalable Quantum Technologies Using Cells of 5-to-50 Qubits with Very Lossy and Noisy Photonic Links,* Phys. Rev. X **4**, 041041 (2014).

[8] S. Simmons, *Scalable Fault-Tolerant Quantum Technologies with Silicon Color Centers,* PRX Quantum **5**, 010102 (2024).

[9] S. De Bone, P. Möller, C. E. Bradley, T. H. Taminiau and D. Elkouss, *Thresholds for the distributed surface code in the presence of memory decoherence,* AVS Quantum Sci. **6**, 033801 (2024).

[10] M. Ruf, N. H. Wan, H. Choi, D. Englund and R. Hanson, *Quantum networks based on color centers in diamond,* J. Appl. Phys. **130**, 070901 (2021).

[11] A. S. Borisov, P. Hazendonk and P. G. Hayes, *Solid-State Nuclear Magnetic Resonance Spectroscopy: A Review of Modern Techniques and Applications for Inorganic Polymers,* J Inorg Organomet Polym , 30 (2010).

[12] R. Budakian *et al.*, *Roadmap on nanoscale magnetic resonance imaging,* Nanotechnology **35**, 412001 (2024).

[13] H. J. Mamin *et al.*, *Nanoscale Nuclear Magnetic Resonance with a Nitrogen-Vacancy Spin Sensor,* Science **339**, 557 (2013).

[14] T. Staudacher *et al.*, *Nuclear Magnetic Resonance Spectroscopy on a (5-Nanometer)* ^{3} *Sample Volume,* Science **339**, 561 (2013).

[15] A. Ajoy, U. Bissbort, M. D. Lukin, R. L. Walsworth and P. Cappellaro, *Atomic-Scale Nuclear Spin Imaging Using Quantum-Assisted Sensors in Diamond,* Phys. Rev. X **5**, 011001 (2015).

[16] E. Janitz *et al.*, *Diamond surface engineering for molecular sensing with nitrogen—vacancy centers,* J. Mater. Chem. C **10**, 13533 (2022).

[17] J. M. Abendroth *et al.*, *Single-Nitrogen–Vacancy NMR of Amine-Functionalized Diamond Surfaces,* Nano Lett. **22**, 7294 (2022).

[18] D. Bluvstein, Z. Zhang, C. A. McLellan, N. R. Williams and A. C. B. Jayich, *Extending the Quantum Coherence of a Near-Surface Qubit by Coherently Driving the Paramagnetic Surface Environment,* Phys. Rev. Lett. **123**, 146804 (2019).

[19] M. Kim *et al.*, *Decoherence of Near-Surface Nitrogen-Vacancy Centers Due to Electric Field Noise,* Phys. Rev. Lett. **115**, 087602 (2015).

[20] V. Petráková *et al.*, *Luminescence properties of engineered nitrogen vacancy centers in a close surface proximity,* physica status solidi (a) **208**, 2051 (2011).

[21] M. H. Abobeih *et al.*, *Atomic-scale imaging of a 27-nuclear-spin cluster using a quantum sensor,* Nature **576**, 411 (2019).

[22] V. S. Perunicic, C. D. Hill, L. T. Hall and L. Hollenberg, *A quantum spin-probe molecular microscope,* Nat Commun **7**, 12667 (2016).

[23] V. S. Perunicic, M. Usman, C. D. Hill and L. C. L. Hollenberg, *A silicon qubit platform for in situ single molecule structure determination,* (2021), arXiv:2112.03623 [quant-ph] .

[24] N. Aslam *et al.*, *Nanoscale nuclear magnetic resonance with chemical resolution,* Science **357**, 67 (2017).

[25] M. W. Doherty *et al.*, *The nitrogen-vacancy colour centre in diamond,* Physics Reports **528**, 1 (2013).

[26] D. M. Lukin, M. A. Guidry and J. Vučković, *Integrated Quantum Photonics with Silicon Carbide: Challenges and Prospects,* PRX Quantum **1**, 020102 (2020).

[27] P. Udvarhelyi *et al.*, *Vibronic States and Their Effect on the Temperature and Strain Dependence of Silicon-Vacancy Qubits in $4H$-$\mathrm{Si}\mathrm{C}$,* Phys. Rev. Applied **13**, 054017 (2020).

[28] M. Widmann *et al.*, *Coherent control of single spins in silicon carbide at room temperature,* Nat. Mater. **14**, 164 (2015).

[29] R. Hanson, O. Gywat and D. D. Awschalom, *Room-temperature manipulation and decoherence of a single spin in diamond,* Phys. Rev. B **74**, 161203 (2006).

[30] G. Wolfowicz *et al.*, *Quantum guidelines for solid-state spin defects,* Nat Rev Mater **6**, 906 (2021).

[31] M. Pompili *et al.*, *Realization of a multinode quantum network of remote solid-state qubits,* Science **372**, 259 (2021).

[32] S. L. N. Hermans *et al.*, *Qubit teleportation between non-neighbouring nodes in a quantum network,* Nature **605**, 663 (2022).

[33] M. H. Abobeih *et al.*, *Fault-tolerant operation of a logical qubit in a diamond quantum processor,* Nature **606**, 884 (2022).

[34] E. J. Davis *et al.*, *Probing many-body dynamics in a two-dimensional dipolar spin ensemble,* Nat. Phys. **19**, 836 (2023).

[35] J. Randall *et al.*, *Many-body–localized discrete time crystal with a programmable spin-based quantum simulator,* Science **374**, 1474 (2021).

[36] J. Geng, V. Vorobyov, D. Dasari and J. Wrachtrup, *Ancilla assisted Discrete Time Crystals in Non-interacting Spin Systems,* arXiv:2107.11748 [cond-mat, physics:quant-ph] (2021), arXiv:2107.11748 [cond-mat, physics:quant-ph] .

[37] M. Garsi *et al.*, *Three-dimensional imaging of integrated-circuit activity using quantum defects in diamond,* Phys. Rev. Applied **21**, 014055 (2024).

[38] P. J. Scheidegger, S. Diesch, M. L. Palm and C. L. Degen, *Scanning nitrogen-vacancy magnetometry down to 350 mK,* Appl. Phys. Lett. **120**, 224001 (2022).

[39] W. Ji *et al.*, *Correlated sensing with a solid-state quantum multisensor system for atomic-scale structural analysis,* Nat. Photon. (2024), 10.1038/s41566-023-01352-4.

[40] F. Shi *et al.*, *Single-protein spin resonance spectroscopy under ambient conditions,* Science **347**, 1135 (2015).

[41] C. E. Bradley *et al.*, *A Ten-Qubit Solid-State Spin Register with Quantum Memory up to One Minute,* Phys. Rev. X **9**, 031045 (2019).

[42] P. C. Humphreys *et al.*, *Deterministic delivery of remote entanglement on a quantum network,* Nature **558**, 268 (2018).

[43] I. Takács and V. Ivády, *Accurate hyperfine tensors for solid state quantum applications: Case of the NV center in diamond,* Commun Phys **7**, 178 (2024).

[44] O. T. Whaites *et al.*, *Hyperpolarization of nuclear spins: Polarization blockade,* Phys. Rev. Research **5**, 043291 (2023).

[45] O. T. Whaites and T. S. Monteiro, *Hyperpolarisation Dynamics: Asymptotic Polarisation,* (2024), arXiv:2404.07578 [physics, physics:quant-ph] .

2

METHODS

In this chapter, I introduce the general level structure of the solid-state defects studied in this thesis and explain how we manipulate the optical and spin degrees of freedom in a prototypical experiment. Then, I will briefly touch upon the design of nuclear magnetic resonance experiments at the nano-scale, which is central to the results presented in chapter 4 and 5. Finally, I will discuss the experimental setups and samples used to perform the experiments.

2.1. A SPIN-PHOTON INTERFACE

There exists a large variety of solid-state defects across various host materials [1]. Their spin-, optical, and charge characteristics deviate significantly, which has ignited a scientific quest for defects boasting favourable properties for specific applications [2]. The two defects studied in this thesis are the NV center in diamond and the quasi-cubic-lattice-site V_{Si} center in silicon carbide, commonly known as the V2 center [3]. Both feature good spin coherence up to room temperature [1,4], life-time limited optical coherence at 4K [5,6] and relatively stable charge states in bulk crystals [7,8], making them attractive candidates for both quantum sensing and (distributed) quantum information processing applications [3,9]. An excellent general review on solid-state defects for quantum technologies is given by Wolfowicz [1], while Ruf [9] and Lukin [3] specifically focus on diamond and silicon carbide defects, respectively. Moreover, details on the crystal and level structure of the NV and the V2 center can be found in Doherty [10] and Liu [11], respectively.

Here, we limit ourselves to discussing the general level structure (see Fig. 2.1a), which resembles that of an atom in free space [2]. The defect has a number of ground-state spin levels (3 for the spin-1 NV center, and 4 for the spin-3/2 V2 center) and corresponding excited-state levels, which are separated by an optical energy splitting (order hundreds of THz). We can define a qubit subspace spanning two ground-state spin levels (denoted $|0\rangle$ and $|1\rangle$), for which the spin-orbit coupling lifts the degeneracy of the ground-to-excited state splittings ($|0\rangle \rightarrow |e_0\rangle \neq |1\rangle \rightarrow |e_1\rangle$ in Fig. 2.1). In that case, the defect transition frequency is dependent on its spin state (i.e. the qubit state), creating a spin-photon interface.

Evidently, we can use two lasers resonant with the $|0\rangle \rightarrow |e_0\rangle$ and $|1\rangle \rightarrow |e_1\rangle$ transitions (solid red arrows in Fig 2.1a), combined with microwave (MW) radiation resonant with the $|0\rangle \rightarrow |1\rangle$ transition (solid grey arrows in Fig 2.1a) to manipulate the system and access the complete state-space. However, the relaxation timescale of the excited states is more than 12 orders of magnitude shorter than that of the ground states (few nanoseconds versus > 1 h [12]), typically resulting in a rapid decay to the ground states. Generally, two different decay pathways are possible (ignoring phonon-assisted processes for simplicity). Either the spin-state is preserved and a photon is emitted (e.g. $|e_0\rangle \rightarrow |0\rangle$, solid wavy arrows in Fig 2.1a), or the spin-state is flipped by decaying through an intersystem crossing (ISC) [1,13] and no photon is emitted (e.g. $|e_0\rangle \rightarrow |1\rangle$, dashed wavy arrows in Fig 2.1a).

Importantly, these processes can be exploited to both initialise and read out the spin state of the defect. For example, by shining laser light resonant with the $|0\rangle \rightarrow |e_0\rangle$ transition for a sufficient amount of time, the $|0\rangle$ state will be depopulated, initialising the system in the $|1\rangle$ state [13] (second panel of Fig. 2.1b). Alternatively, by exciting e.g. the $|1\rangle \rightarrow |e_1\rangle$ transition and collecting the emitted photons, one can probe (i.e. readout) whether the defect is in the $|1\rangle$ state, potentially in a single shot [13,14] (fourth panel of Fig. 2.1b).

Having established these key operations on the system, we can now construct the typical quantum experiment as performed in this thesis (in particular in chapters 4 and 5). Figure 2.1b illustrates the four key steps. First, we perform a charge-resonance check (CR-check), which validates that the defect is in the correct charge state and that the optical transitions are on resonance with the lasers. The lasers are turned on simultaneously, in which case only significant photon emission is expected if the defect is on resonance and in the right charge state. Further details can be found in Bernien [15] and in chapter 3, where we employ

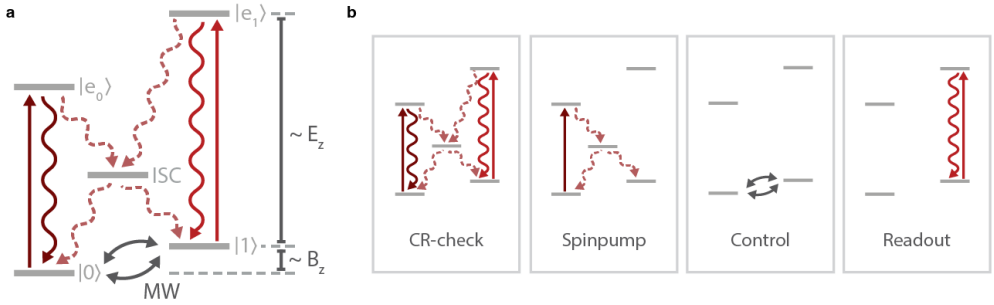

Figure 2.1: **Defect level structure and operation**. **a)** Simplified level scheme corresponding to the defects studied in this thesis. A qubit subspace is defined by two spin ground states ($|0\rangle$ and $|1\rangle$), that have distinct (optical) ground-to-excited state splittings ($|0\rangle \rightarrow |e_0\rangle \neq |1\rangle \rightarrow |e_1\rangle$). The ground states can be selectively excited by resonant laser illumination (red solid arrows), upon which the defect quickly decays back to the ground state, either by emitting a photon (solid wavy arrow), or by decaying via an intersystem crossing (dashed wavy arrow). Microwave (MW) radiation can be applied to manipulate the ground-state spin. The optical transition frequency is sensitive to electric fields (E_z), while the ground-state spin transition can be used to sense magnetic fields (B_z). **b)** The four key components that make up most experiments in this thesis. Two resonant lasers are turned on to check that the defect is in the right charge state and on its optical transitions are on resonance. Next, an optical spinpump initialises the defect in one of the spin states. Then, MW fields are applied to let the spin interact with its environment in a controlled manner. Finally, the spin state is read out by exciting one of the optical transitions and detecting the emitted photons.

such a CR-check to study the defect's spectral dynamics. Next, the defect is initialised in one of the spin states by optical pumping (spinpump). Then, we apply MW (and possibly RF) radiation to manipulate the spin state, and allow the defect to interact with the magnetic environment, altering its spin state (control). Finally, we read out the spin state by exciting one of the optical transitions and detecting the emitted photons (readout, for details see Robledo[13]).

2.2. NUCLEAR-MAGNETIC RESONANCE AT THE NANO-SCALE

To appreciate how the system in Fig. 2.1 can be used as a quantum sensor of the local spin and charge environment, we note that both the $|0\rangle \rightarrow |1\rangle$, and the ground-to-excited-state transition frequencies are dependent on external physical variables, such as strain, temperature and the local electric and magnetic field[10], allowing one to probe these quantities. Sensing schemes typically rely on the accurate measurement of one or more transition frequencies, which provide information about the (microscopic) environment. Alternatively, one could measure induced changes in the relaxation rates (i.e. T_1-times[14]), but such schemes are not considered in this work. An excellent review on the topic of quantum sensing is given by Degen[14]. Here, we briefly review some key points relevant to the nuclear-magnetic-resonance (NMR) schemes developed in this thesis (particularly those introduced in chapter 5).

NMR studies the evolution of nuclear spins under a perturbing interaction with radio-frequency (RF) fields, with the goal of accurately determining system characteristics such as the nuclear transition frequencies, decoherence and relaxation timescales and other dy-

namics, which contain valuable information on the microscopic spin environment[16].

NMR sequences at the nano-scale generally consist of three components: a preparation stage, an evolution stage and a detection stage. During the preparation stage, nuclear spins of interest are typically polarised, although some schemes rely solely on the presence of a statistical polarisation[17,18]. In traditional NMR, a strong (multiple Tesla) magnetic field is applied to enhance the nuclear-spin polarisation (on the order of 10^{-5})[19]. However, much higher degrees of polarisation can be achieved by transferring optically induced polarisation from the defect electron spin to nearby nuclei, commonly known as dynamic nuclear polarisation (DNP)[19,20]. Alternatively, in controlled settings, single nuclear spins may be polarised selectively using SWAP-like sequences[21]. The preparation stage typically concludes with a partial excitation (e.g. a $\pi/2$-pulse), that creates a coherent superposition of spin states[16].

Next, the nuclear spins evolve (i.e. acquire phase), during which they may be manipulated with additional RF fields. These RF pulses are meant to encode a specific quantity of interest (for example the coupling strength to another nuclear species) into the phase evolution.

Finally, the nuclear-spin phase is detected with the defect electron spin, by letting the electron and nuclear spin interact for specific amount of time, in which the electron spin state changes dependent on the (final) nuclear spin state. The nuclear I_x expectation value, which contains the phase information, may be rotated prior to this interaction period, depending on the precise form of the electron-nuclear interaction ($\sim S_z I_x$ for the commonly used dynamical decoupling sequences, with S_z the electron spin-z operator[21,22]).

FREQUENCY-SPACE PICTURE

In order to design suitable NMR sequences for extracting quantities of interest, it is useful to consider their form in frequency space. Many of the sequences presented in chapter 5 rely on the selective excitation of nuclear spins in a particular bandwidth, for example to decouple those from spins at other frequencies. Furthermore, during the readout phase (Fig. 2.2a), it is typically beneficial to only pick up signal from spins at a specific frequency band.

First, we consider the spectral profile of an RF pulse applied to the nuclear spins during an NMR sequence. Naively, one would expect that the frequency selectivity of such a pulse is inversely proportional to the pulse length, as the two are related via the Fourier theorem. However, due to the sinusoidal response of the spins to the RF field, this is in general not true outside the 'so-called' linear regime[23].

The transition probability for a spin starting in the $|0\rangle$ state, under application of a circularly polarised RF field (commonly known as the 'Rabi problem') is given by[24]:

$$P_{\mathrm{t,n}}(\delta, t) = \frac{B^2}{\delta^2 + B^2} \sin^2\left(\frac{1}{2}\sqrt{\delta^2 + B^2}\, t\right) \tag{2.1}$$

with $P_{\mathrm{t,n}}$ the nuclear transition probability, B the strength of the RF field (given by the product of the magnetic field amplitude and the nuclear gyromagnetic ratio), δ the detuning between the RF frequency and the spin transition, and t the length of the RF pulse. The transition probabilities according to Eq. 2.1 for a $\pi/2$-, π- and 3π-pulse are shown in Figure 2.2b, c and d, respectively (setting $t = \{\pi/(2B), \pi/B, 3\pi/B\}$). Although the width of the central peak decreases with the pulse length (as expected from Fourier theory), for longer

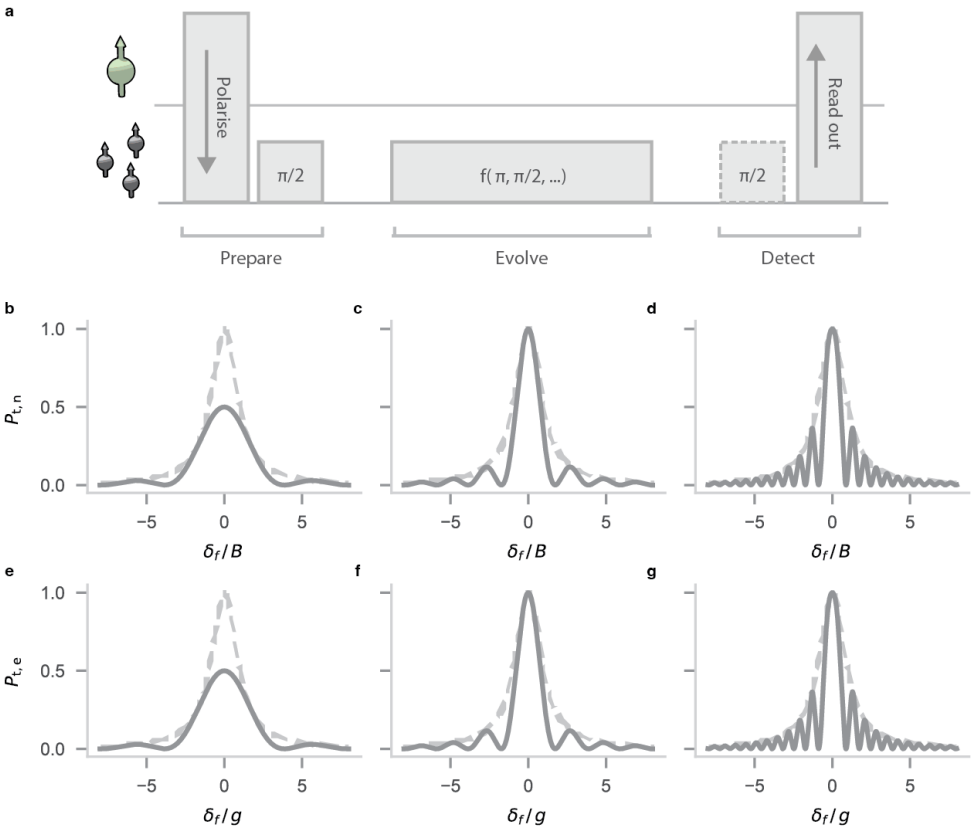

Figure 2.2: **Nano-scale nuclear magnetic resonance**. **a)** General structure of a sensing sequence, with the top line denoting the defect electron spin (mint green), and the bottom line denoting one or more nuclear spins. First, optically induced polarisation from the electron spin is transferred to the nuclear spins after which they are brought into a superposition (denoted $\pi/2$). Then, the nuclear spins evolve under the application of RF pulses (denoted $f(\pi, \pi/2, ...)$) to encode a quantity of interest into their quantum phase. Finally, the nuclear-spin phase is detected by the defect electron spin, possibly after a performing some nuclear basis rotations (denoted $\pi/2$). **b-d)** Spectral line shape of a $\pi/2$, π and $3\pi/2$ RF pulse, respectively, with the y-axis denoting the transition probability if the nuclear spin starts in the spin-up ($|0\rangle$) state (Eq. 2.1). Grey dashed line is a normalised Lorentzian function with a FWHM $2B$. **e-g)** Transition probability for the electron spin interacting with a nuclear spin under the dynamical decoupling sequence (xx-type[22]), for $g\,t = \pi/2$, $g\,t = \pi$ and $g\,t = 3\pi/2$, respectively (Eq. 2.2). Grey dashed line is a normalised Lorentzian function with FWHM $2g$.

pulses ($t \gtrsim \pi/2$) the side peaks become more prominent. In this regime, it is more insightful to report the FWHM maximum of the Lorentzian envelope (given by $B^2/(\delta^2 + B^2)$), which has a FWHM of $2B$. Note that Eq. 2.1 only considers the transition probability, and therefore does not provide insight about the phase shift imparted by the RF field. Such a phase shift, commonly known as the AC Stark shift[23], typically acts over a much larger spectral range than the perturbative components considered in Fig. 2.2. Whether these phase shifts can be neglected in practice, depends on the design of the specific NMR sequence.

Next, we consider the spectral profile of the detection sequence, specific to the (spin-1) NV center in diamond. Here, we treat the commonly-used Carr-Purcell-Meiboom-Gill (CPMG) dynamical decoupling (DD) sequence, but a similar argument can be made for the recently developed DDRF sequence[21], which produces similar dynamics (see chapter 4). The DD sequence consist of a series of N π-pules, spaced by an interpulse-length 2τ, applied to the defect electron spin[22]. The sequence decouples the electron spin from quasi-static noise sources, with the potential of extending its coherence by several orders of magnitude[12]. However, for an external field that oscillates resonantly with the spacing between π-pulses, the interaction with the electron spin is not cancelled out[14]. By changing the pulse-spacing 2τ of the sequence, the electron spin becomes sensitive to different frequency-components of the external field. From a sensing perspective, this allows for the detection of signals in a specific frequency band. In particular, the spectral profile of the CPMG sequence is given by a number of narrow resonances around center frequencies $f_k = (2k+1)/(4\tau)$, with k any integer[14]. A particularly intuitive explanation of this effect is given by the filter-function formalism described by Degen[14] (section VI, note that the authors define the interpulse spacing as τ instead of 2τ). It is important to note that this framework only strictly holds for sensing classical signals, i.e. when the system Hamiltonian is of the form: $H = A\cos(\omega t)\, S_z$, with A and ω the amplitude and frequency of the signal and S_z the electron-spin-z operator[25].

Indeed, in a nano-NMR setting, the target signal might consist of only one, or just a few, nuclear spins[26]. In this regime, the nuclear spin evolution can be perturbed significantly by the defect electron spin during the detection phase as a result of measurement back-action[22,27]. In the single-nuclear-spin case, the spectral profile (given by the electron-spin transition probability for in-phase $\pi/2$ pulses) can be calculated analytically[22]:

$$P_{\mathrm{t,e}} = \frac{g^2}{\delta^2 + g^2} \sin^2\left(\frac{1}{2}\sqrt{\delta^2 + g^2}\, t\right), \tag{2.2}$$

where $g = \frac{A_\perp}{(2k+1)\pi}$ is the effective interaction strength, with $A_\perp$ the perpendicular component of the hyperfine coupling[22]. Eq. 2.2 is obtained by substituting: $\delta_k \rightarrow \frac{\delta t}{N}$ and $m_x \rightarrow \frac{gt}{N}$ in Eq. 14 of the supplementary materials of Taminiau[22], where δ is again the detuning from the nuclear resonance conditions, which occur at: $\frac{2k+1}{4\tau} \approx \frac{1}{2\pi}(\omega_{\mathrm{L}} - \frac{A_\parallel}{2})$[22]. Eq. 2.2 is evaluated for $t = \{\pi/(2g), \pi/g, 3\pi/g\}$ in figure 2.2e-g, respectively. Note that it has the same form as Eq. 2.1, only with the substitution of B by g, resulting in an approximate sensing bandwidth given by the maximum of $\frac{1}{t}$ (weak measurement regime) and $\frac{g}{\pi}$ (strong measurement regime), here quoted in Hz. The resonance conditions, interaction strength and bandwidth of RF pulses and the CMPG detection sequence for the sensing of single nuclear spins are summarised in Table 2.1.

Table 2.1: Summary of the spectral profile of RF pulses and the dynamical-decoupling detection sequence for single nuclear spins. Here, $m_s = \{-1, 0, 1\}$ is the electron spin projection and $A_\parallel$ and $A_\perp$ are the parallel and perpendicular hyperfine components, respectively.

	RF pulse	Detection sequence (DD)
Resonance condition (rad s^{-1})	$\omega_{\mathrm{RF}} = \sqrt{(\omega_{\mathrm{L}} + m_{\mathrm{s}} A_\parallel)^2 + (m_{\mathrm{s}} A_\perp)^2}$	$\omega_k = 2\pi \frac{2k+1}{4\tau} \approx (\omega_{\mathrm{L}} - \frac{A_\parallel}{2})$
Interaction strength (rad s^{-1})	B	$g = \frac{A_\perp}{(2k+1)\pi}$
Bandwidth (rad s^{-1})	$\approx \max\left[\frac{2\pi}{t}, 2B\right]$	$\approx \max\left[\frac{2\pi}{t}, 2g\right]$

2.3. EXPERIMENTAL SETUP

The experiments presented in this thesis were performed on two different types of solid-state defects, namely the V2 center in silicon carbide (chapter 3) and the NV center in diamond (chapter 4 & 5), and on three different experimental setups. However, these setups are very similar in their design and functioning. A schematic of the silicon carbide (SiC) setup, specifically built for the work in this thesis, is given in Fig. 2.3. An extensive review of this particular setup is given by Loenen[28], while the NV center setups are detailed by Bradley[29].

Here, I highlight some key aspects. All experiments are performed at ≈ 4K a in closed-cycle cryostat (Montana), which allows for resonant addressing of the defect's optical transitions and enhances the spin T_1 relaxation time. We typically use two so-called 'resonant' lasers (916 nm in Fig. 2.3) and a higher-energy 'repump' laser (785 nm in Fig. 2.3), which can be used both for readout at elevated temperatures and for resetting the defect charge state. The resonant lasers are frequency-locked (with a wave-meter (WM)) and their power can be modulated quickly (order tens of nanoseconds) by acousto-optic-modulators (AOM). They are focused onto the sample by a movable, room temperature objective. Phonon-sideband (PSB) emission is collected by the same objective, and detected on a avalanche-photodiode (APD). Permanent neodymium magnets can be placed both inside the cryostat (mounting it on the sample holder), or on mobile stages outside the cryostat (used primarily for field stabilisation). Microwave (MW) or radiofrequency (RF) pulses are generated by an arbitrary-waveform generator and are supplied either via a stripline deposited on the sample, or via a bond-wire drawn across it. The ordering and coarse timing (1 µs resolution) of the experimental sequences is managed by an ADwin microcontroller, while more precise inter-pulse timings (~ 1 ns for the pulse sequences described in chapter 4 and 5) are handled by the AWG. Experiments are programmed in Python, using the open-source 'Quantum Measurement Infrastructure' (QMI) framework, developed centrally at QuTech, and adapted to the SiC setup.

2.4. SAMPLES

Both for the experiments on the NV center and on the V2 center, multiple samples are used. For the NV center experiments, we use (2 x 2 mm) diamond samples grown by chemical vapour deposition (Element 6 type IIa, cleaved along 111-direction) with a natural abun-

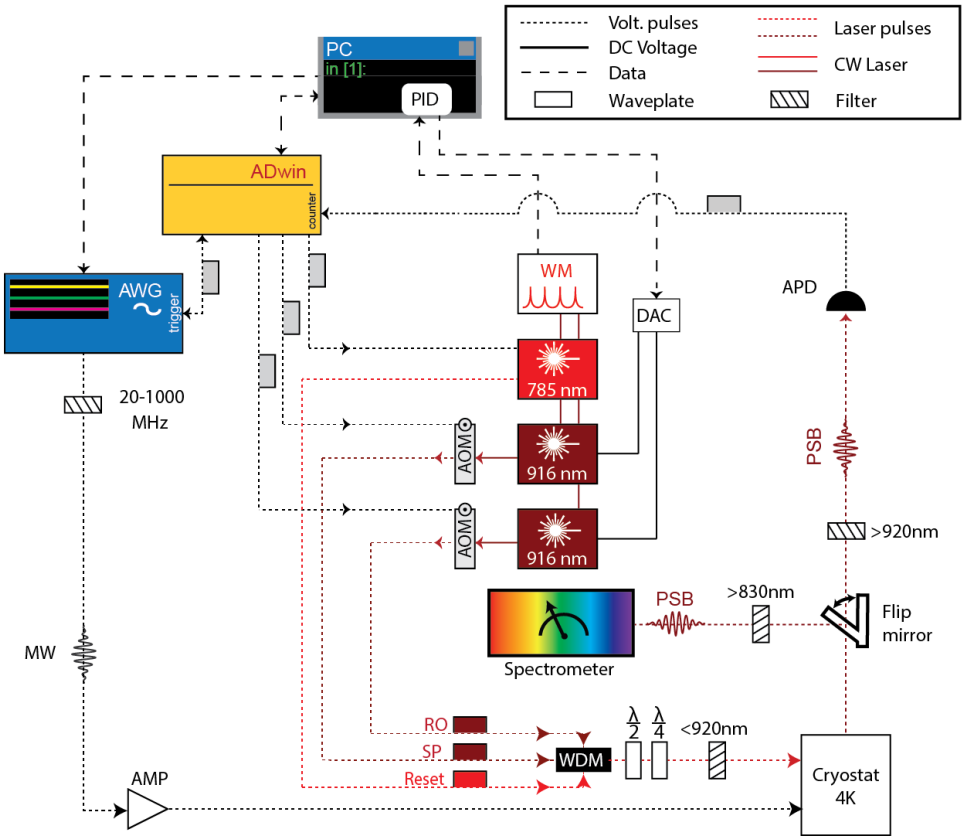

Figure 2.3: **Experimental setup for chapter 3**. See main text for the description of the key components. RO: readout, SP: spinpump, WDM: wavelength-division multiplexer, AMP: amplifier. This figure is adapted from Loenen[28], where also the model numbers of all components are listed.

dance of ^{13}C (1.1%) [12,30]. Naturally occurring single NV centers are selected on the absence of couplings stronger than ≈ 500 kHz. After initial characterisation, a solid-immersion lense (SIL) is milled around the selected centers by a focused ion beam, which can increase the collection efficiency to about 20% [13,31] (see Fig. 2.4a). Gold striplines are deposited close (< 1 µm) to the edge of the SIL for the application of MW and RF pulses, resulting in NV electron-spin Rabi frequencies up to tens of MHz [26,32]. An extensive review on the full fabrication process of these devices is given by Bradley [29].

The V2 experiments are performed on (8 x 8 mm) diced samples from a 100 mm diameter, high-purity semi-insulating (HPSI), on-axis, 4H-SiC bulk wafer, purchased from Wolfspeed (product code: W4TRF0R-0200). The samples are electron-irradiated (fluences of 10^{12} to 10^{14} cm^{-2}) and subsequently annealed (650 °C for 30 min) to create V2 defects. However, as we see little variation in the V2 center density (in spatial confocal scans), even when the irradiation dose is varied over two orders of magnitude, we suspect the V2 centers we study naturally occur in the HPSI material and the contribution from irradiation is negligible.

The HPSI wafers we use are c-plane, meaning the c-axis (4H stacking direction) is oriented perpendicular to the wafer surface, such that the optical dipole moment of V2 centers is oriented mostly perpendicular to the surface [5,33,34]. For such a configuration, the collection efficiency can be calculated analytically to be 0.26% (by integrating Eq. 8 in Lukosz [35] over the collection angle of an NA = 0.9 objective). This poor collection efficiency is due to the high refractive index of silicon carbide (n = 2.6) in combination with the unfavourable dipole orientation, leading to a large portion of the light being channeled back into the silicon carbide sample through total internal reflection. To solve this challenge, we use reactive-ion etching to create nanopillars (Fig 2.4b, see chapter 3 for details on the fabrication protocol), which can enhance the collection efficiency to ≈ 40 − 50%, for both parallel and perpendicular dipole orientations [28,36]. As we have no control over the position of the V2 center, we compute numerically the collection efficiency while varying the height of the defect inside the pillar (while keeping it centered on the symmetry axis), resulting in efficiencies ranging from 10 − 40% [28].

Even though nanopillars can enhance the collection efficiency by two orders of magnitude, which is sufficient for performing the experiments done in chapter 3, future work towards the demonstration of remote entanglement [37,38] will likely require more efficient devices. In particular, photonic crystal cavities (PCC, see Fig. 2.4c) can enhance the emission in the zero-phonon line via the Purcell effect (see Ruf [39] and Joannopoulos [40] for an overview), leading to a higher fraction of coherently emitted photons that can be used for quantum networking [38]. Figure 2.4c shows one of our most recently designed devices, where the free-hanging periodically modulated beam acts as a 'alligator'-type one-dimensional PCC. Such 'alligator'-type cavities enhance the transverse-magnetic optical modes, making them suitable for integration with V2 centers in c-plane SiC [28,40], unlike the more conventional 'ladder'-type cavities explored for example by Lukin [34]. At this point, further characterisation, and corresponding engineering improvements are needed for bringing these devices to a performance level where they can be used for the next generation of experiments on this platform.

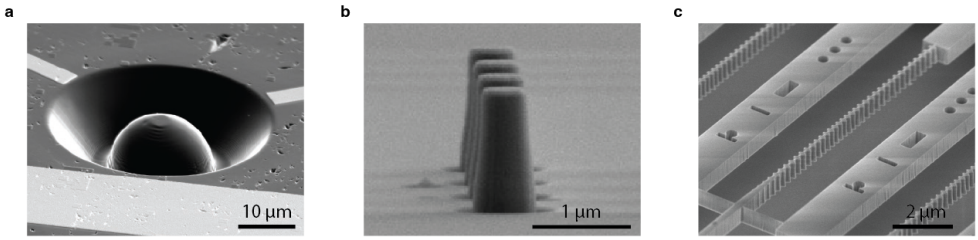

Figure 2.4: **Sample architecture**. **a)** Representative scanning electron image (SEM) of the diamond NV center samples used in this work. A Solid-immersion lens is fabricated around a selected NV center. Gold striplines are deposited for the application of MW and RF radiation (bottom). Image adapted from Robledo [13]. **b)** SEM image of one of the SiC samples, showing a row of nanopillars (≈ 500 nm diameter) created by reactive-ion etching, which are expected to increase the optical collection efficiency by two orders of magnitude. **c)** To further enhance the defect's spin-photon interface, we designed and fabricated free-hanging photonic-crystal cavities (periodically modulated beam in the center of the image) for the next generation of experiments.

REFERENCES

[1] G. Wolfowicz *et al.*, *Quantum guidelines for solid-state spin defects,* Nat Rev Mater **6**, 906 (2021).

[2] L. C. Bassett, A. Alkauskas, A. L. Exarhos and K.-M. C. Fu, *Quantum defects by design,* Nanophotonics **8**, 1867 (2019).

[3] D. M. Lukin, M. A. Guidry and J. Vučković, *Integrated Quantum Photonics with Silicon Carbide: Challenges and Prospects,* PRX Quantum **1**, 020102 (2020).

[4] M. Widmann *et al.*, *Coherent control of single spins in silicon carbide at room temperature,* Nat. Mater. **14**, 164 (2015).

[5] C. Babin *et al.*, *Fabrication and nanophotonic waveguide integration of silicon carbide colour centres with preserved spin-optical coherence,* Nat. Mater. **21**, 67 (2022).

[6] K.-M. C. Fu *et al.*, *Observation of the Dynamic Jahn-Teller Effect in the Excited States of Nitrogen-Vacancy Centers in Diamond,* Phys. Rev. Lett. **103**, 256404 (2009).

[7] N. T. Son and I. G. Ivanov, *Charge state control of the silicon vacancy and divacancy in silicon carbide,* J. Appl. Phys. **129**, 215702 (2021).

[8] D. A. Hopper, J. D. Lauigan, T.-Y. Huang and L. C. Bassett, *Real-Time Charge Initialization of Diamond Nitrogen-Vacancy Centers for Enhanced Spin Readout,* Phys. Rev. Applied **13**, 024016 (2020).

[9] M. Ruf, N. H. Wan, H. Choi, D. Englund and R. Hanson, *Quantum networks based on color centers in diamond,* J. Appl. Phys. **130**, 070901 (2021).

[10] M. W. Doherty *et al.*, *The nitrogen-vacancy colour centre in diamond,* Physics Reports **528**, 1 (2013).

[11] D. Liu *et al.*, *The silicon vacancy centers in SiC: Determination of intrinsic spin dynamics for integrated quantum photonics,* npj Quantum Inf **10**, 72 (2024).

[12] M. H. Abobeih *et al.*, *One-second coherence for a single electron spin coupled to a multi-qubit nuclear-spin environment,* Nat Commun **9**, 2552 (2018).

[13] L. Robledo *et al.*, *High-fidelity projective read-out of a solid-state spin quantum register,* Nature **477**, 574 (2011).

[14] C. L. Degen, F. Reinhard and P. Cappellaro, *Quantum sensing,* Rev. Mod. Phys. **89**, 035002 (2017).

[15] H. Bernien *et al.*, *Heralded entanglement between solid-state qubits separated by three metres,* Nature **497**, 86 (2013).

[16] A. S. Borisov, P. Hazendonk and P. G. Hayes, *Solid-State Nuclear Magnetic Resonance Spectroscopy: A Review of Modern Techniques and Applications for Inorganic Polymers,* J Inorg Organomet Polym , 30 (2010).

[17] T. Staudacher *et al.*, *Nuclear Magnetic Resonance Spectroscopy on a (5-Nanometer)* ^{3} *Sample Volume,* Science **339**, 561 (2013).

[18] H. J. Mamin *et al.*, *Nanoscale Nuclear Magnetic Resonance with a Nitrogen-Vacancy Spin Sensor,* Science **339**, 557 (2013).

[19] I. Schwartz *et al.*, *Robust optical polarization of nuclear spin baths using Hamiltonian engineering of nitrogen-vacancy center quantum dynamics,* Sci. Adv. **4**, eaat8978 (2018).

[20] P. London *et al.*, *Detecting and Polarizing Nuclear Spins with Double Resonance on a Single Electron Spin,* Phys. Rev. Lett. **111**, 067601 (2013).

[21] C. E. Bradley *et al.*, *A Ten-Qubit Solid-State Spin Register with Quantum Memory up to One Minute,* Phys. Rev. X **9**, 031045 (2019).

[22] T. H. Taminiau *et al.*, *Detection and Control of Individual Nuclear Spins Using a Weakly Coupled Electron Spin,* Phys. Rev. Lett. **109**, 137602 (2012).

[23] L. M. K. Vandersypen and I. L. Chuang, *NMR techniques for quantum control and computation,* Rev. Mod. Phys. **76**, 1037 (2005).

[24] F. Bloch and I. I. Rabi, *Atoms in Variable Magnetic Fields,* Rev. Mod. Phys. **17**, 237 (1945).

[25] J. M. Taylor *et al.*, *High-sensitivity diamond magnetometer with nanoscale resolution,* Nat. Phys. **4**, 810 (2008).

[26] M. H. Abobeih *et al.*, *Atomic-scale imaging of a 27-nuclear-spin cluster using a quantum sensor,* Nature **576**, 411 (2019).

[27] K. S. Cujia, J. M. Boss, K. Herb, J. Zopes and C. L. Degen, *Tracking the precession of single nuclear spins by weak measurements,* Nature **571**, 230 (2019).

[28] S. J. H. Loenen, *Spins in Diamond and Silicon Carbide for Quantum Networks*, Ph.D. thesis, TU Delft (2024).

[29] C. Bradley, *Order from Disorder: Control of Multi-Qubit Spin Registers in Diamond*, Ph.D. thesis, [object Object] (2021).

[30] S. Baier *et al.*, *Orbital and Spin Dynamics of Single Neutrally-Charged Nitrogen-Vacancy Centers in Diamond,* Phys. Rev. Lett. **125**, 193601 (2020).

[31] J. P. Hadden *et al.*, *Strongly enhanced photon collection from diamond defect centers under microfabricated integrated solid immersion lenses,* Appl. Phys. Lett. **97**, 241901 (2010).

[32] G. De Lange, Z. H. Wang, D. Ristè, V. V. Dobrovitski and R. Hanson, *Universal Dynamical Decoupling of a Single Solid-State Spin from a Spin Bath,* Science **330**, 60 (2010).

[33] R. Nagy *et al.*, *Quantum Properties of Dichroic Silicon Vacancies in Silicon Carbide,* Phys. Rev. Applied **9**, 034022 (2018).

[34] D. M. Lukin *et al.*, *4H-silicon-carbide-on-insulator for integrated quantum and nonlinear photonics,* Nat. Photon. **14**, 330 (2020).

[35] W. Lukosz and R. E. Kunz, *Light emission by magnetic and electric dipoles close to a plane dielectric interface II Radiation patterns of perpendicular oriented dipoles,* J. Opt. Soc. Am. **67**, 1615 (1977).

[36] B. J. M. Hausmann *et al.*, *Fabrication of diamond nanowires for quantum information processing applications,* Diamond and Related Materials **19**, 621 (2010).

[37] P. C. Humphreys *et al.*, *Deterministic delivery of remote entanglement on a quantum network,* Nature **558**, 268 (2018).

[38] M. Pompili *et al.*, *Realization of a multinode quantum network of remote solid-state qubits,* Science **372**, 259 (2021).

[39] M. Ruf, *Cavity-Enhanced Quantum Network Nodes in Diamond*, Ph.D. thesis, Delft University of Technology (2021).

[40] J. D. Joannopoulos, ed., *Photonic Crystals: Molding the Flow of Light*, 2nd ed. (Princeton University Press, Princeton, 2008).

3

CHECK-PROBE SPECTROSCOPY OF LIFETIME-LIMITED EMITTERS IN BULK-GROWN SILICON CARBIDE

G.L. van de Stolpe*, L.J. Feije*, S.J.H. Loenen*, A. Das, G.M. Timmer, T.W. de Jong, T.H. Taminiau

Solid-state single-photon emitters provide a versatile platform for exploring quantum technologies such as optically connected quantum networks. A key challenge is to ensure optical coherence and spectral stability of the emitters. Here, we introduce a high-bandwidth 'check-probe' scheme to quantitatively measure (laser-induced) spectral diffusion and ionisation rates, as well as homogeneous linewidths. We demonstrate these methods on single V2 *centers in commercially available bulk-grown 4H-silicon carbide. Despite observing significant spectral diffusion under laser illumination ($\gtrsim$ GHz s^{-1}), the optical transitions are narrow ($\sim$ 35 MHz), and remain stable in the dark ($\gtrsim$ 1 s). Through Landau-Zener-Stückelberg interferometry, we determine the optical coherence to be near-lifetime limited ($T_2 = 16.4(4)$ ns), hinting at the potential for using bulk-grown materials for developing quantum technologies. These results advance our understanding of spectral diffusion of quantum emitters in semiconductor materials, and may have applications for studying charge dynamics across other platforms.*

*These authors contributed equally to this work

3.1. INTRODUCTION

Optically active solid-state defects have enabled pioneering experiments in the field of distributed quantum computation [1–4] and quantum networks [5,6]. Proof-of-principle experiments have demonstrated primitives for quantum error correction [1–3] and the realisation of a three-node network [7,8]. Key to these applications is the ability to connect multiple emitters via their coherent spin-optical interface, with many applications requiring narrow, stable optical transitions [6,7].

Spectral diffusion of the transitions, caused by fluctuating charge impurities within the bulk material or at the surface, poses a major challenge, especially when emitters are integrated in nanostructures [9–12]. Moreover, laser pulses used to probe or manipulate the emitter can exacerbate such diffusion [10,13]. Experimental techniques that enable the quantitative study of spectral diffusion and its timescales provide insight into the environmental charge dynamics, potentially allow for targeted optimisation of material properties and fabrication processes, and enable pathways to mitigate diffusion through pre-selection [13,14]. However, commonly used methods may significantly disturb the system through continuous laser illumination, complicating the unambiguous determination of transition linewidths and diffusion rates under different laser illumination conditions [9,10,15–17].

Here, we introduce a comprehensive check-probe spectroscopy toolbox for characterising and mitigating spectral diffusion of single solid-state emitters. Our methods offer high-bandwidth, quantitatively extract diffusion and ionisation rates, and introduce minimal system disturbance from laser illumination, enabling accurate measurements even in heavily diffusive environments. Additionally, our work provides a framework for the quantitative analysis of heralded preparation of the charge environment, which has become an indispensable tool to mitigate spectral diffusion in quantum network and other experiments [3,7,8,13,14,18].

We apply these methods to study single k-site V_{Si} (V2) centers (a next-generation candidate for quantum networks [15,19,20]), embedded in nanopillars etched in commercially available bulk-grown 4H-silicon carbide (SiC) [21,22]. This system exhibits a high degree of spectral diffusion (> 1 GHz diffusion-averaged linewidth), typical for single quantum emitters in bulk-grown silicon or silicon carbide [23,24]. First, we determine spectral diffusion rates with and without laser illumination. Using this knowledge, we select configurations of the system with narrow spectral transitions, which can be tuned over the breadth of the inhomogeous linewidth and can be stored for over a second and accessed on-demand. Finally, through the observation of Landau-Zener-Stückelberg interference [25], we determine the optical coherence time to be: $T_2 = 16.4(4)$ ns, consistent with the lifetime limit for these defects [26].

Although high-purity epitaxial layers provide a starting point with less spectral diffusion [15,19,27] (Appendix A.8), our observation of lifetime-limited coherence in nanostructures in bulk-grown silicon carbide, hints towards the possibility of using such mass-fabricated material for quantum technology development and applications. Furthermore, the techniques developed here might facilitate the targeted optimisation of material and fabrication recipes, and can be readily transferred to other platforms [18,24,28–30].

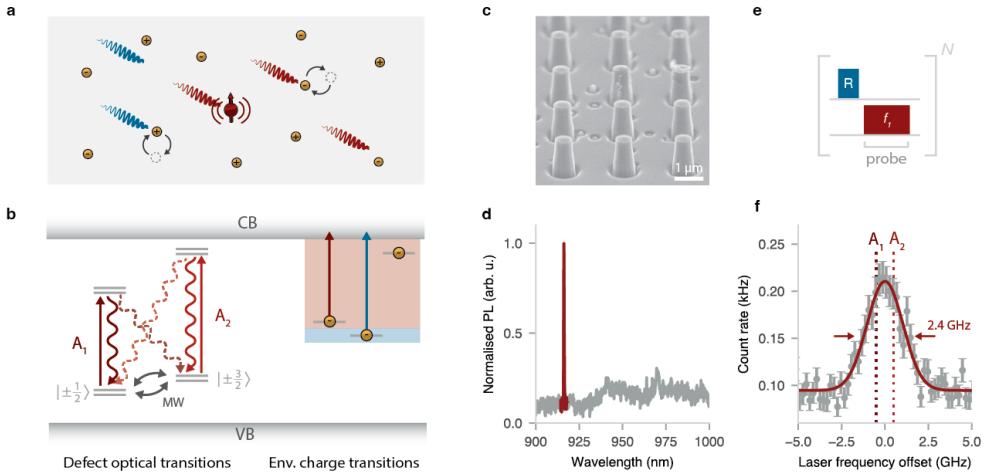

Figure 3.1: **Emitter optical properties and laser-induced charge dynamics. a)** Schematic of the system. A single V2 center in SiC is surrounded by charges (yellow circles) associated to intrinsic residual impurities[31]. Under laser illumination, these charges can be mobilised after excitation to (from) the conduction (valence) band, indicated by blue and red wiggly lines. **b)** Energy diagram, depicting the V2 center's optical transitions (left) and possible laser-induced charge dynamics of the (unknown) impurities in the environment (right). The spin-dependent A_1 and A_2 transitions can be excited with a tunable, near-infrared (NIR) laser (916 nm, red arrow), while a high-energy repump laser (785 nm, blue arrow) is used to scramble the charge state of the V2 center and its environment. The ground-state spin ($S = \frac{3}{2}$) can be manipulated with microwave (MW) radiation. **c)** Scanning-electron-microscopy image of a sample used in this work, which is diced from a 4 inch commercially available 4H-SiC bulk wafer. Nanopillars (~ 500 nm diameter) are fabricated to improve the photon collection efficiency. **d)** Representative low-temperature (4K) emission spectrum of a V2 center under repump-laser excitation, showing the characteristic zero-phonon line at 916 nm (red highlight). **e)** Experimental sequence of the diffusion-averaged photoluminescence-excitation spectroscopy (PLE). The frequency f_1 of the NIR laser (red) is scanned over the V2 zero-phonon line, while emission in the phonon sideband is collected. The repump laser (blue) scrambles the charge state of the emitter and its environment before every repetition (total N). **f)** Measured PLE spectrum. Averaging over many charge-environment configurations results in a single, broad peak (2.4(1) GHz FWHM) that encompasses the A_1 and A_2 transitions (separated by ~ 1 GHz). The laser frequency is offset from 327.10 THz.

3.2. SYSTEM: SINGLE V2 CENTERS IN NANO-STRUCTURED BULK-GROWN SILICON CARBIDE

We consider spectral diffusion caused by fluctuating charges in the environment of the emitter, for example associated to material impurities or surface defects that modify the optical transition frequency via the Stark shift[32–35]. Although these dynamics are largely frozen at cryogenic temperatures[17], charges can still be mobilised through laser illumination used for the optical addressing of the emitter[9,10,17,24] (Fig. 3.1a). In particular, charges can be excited to the conduction (or valence) band via a single-photon process if the energy difference from the occupied charge state is smaller than the associated energy of the laser frequency (Fig. 3.1b). Subsequent decay to a different spatial position causes fluctuations in the electric field at the location of the emitter[10,17].

This work considers single k-site V_{Si} (V2) centers in commercially available bulk-grown silicon carbide at 4K. In this material, diffusion is likely caused by charges associated with

residual defects and shallow dopants (concentrations $\sim 10^{15}\text{cm}^{-3}$) that are created during the growth process[31]. We apply two types of lasers: a 785 nm 'repump' laser for charge-state reinitialisation ($\sim$ 10 µW), and two frequency-tunable near-infrared ('NIR') lasers ($\sim$ 10 nW) for resonant excitation of the V2 center's spin-dependent A_1 and A_2 zero-phonon-line transitions (Fig. 3.1b and d)[19].

We fabricate nanopillars that enhance the optical collection efficiency (Methods), to mitigate the effects of the unfavourable dipole orientation in c-plane 4H-SiC (Fig. 3.1c). In about one in every 10 pillars, we observe a low-temperature spectrum with a characteristic zero-phonon line at 916 nm (Fig. 3.1d), hinting at the presence of single V2 centers confined to the nanopillars. The dimensions of the nanopillar, with a diameter of $\sim$ 500 nm and a height of $\sim$ 1.2 µm, mean that surface- and fabrication-related effects might contribute to the diffusion dynamics.

3.3. PHOTOLUMINESCENCE EXCITATION SPECTROSCOPY

First, we measure the V2 diffusion-averaged optical absorption linewidth via photoluminescence excitation spectroscopy (PLE). By repeatedly interleaving repump pulses ('R', 10 µs, 10 µW) with NIR pulses at a varying frequency f_1 (10 µs, 10 nW, Fig. 3.1e), we randomise the V2 charge environment before each repetition, effectively averaging over many spectral configurations. In a system without spectral diffusion, we would expect to observe two distinct narrow lines (FHWM of $\sim$ 26 MHz and $\sim$ 11 MHz), separated by $\Delta \approx 1$ GHz[19,26,36], corresponding to the separation of the A_1 and A_2 transitions. However, we observe a broad Gaussian peak (2.4(1) GHz, see Fig. 3.1f), hinting at a high degree of spectral diffusion, consistent with comparable experiments in similar bulk semiconductor materials[24,28].

In order to probe the individual A_1 and A_2 transitions, we employ a two-laser PLE scan[28]. Compared to the sequence in figure 3.1e, we now fix frequency f_1 close to the middle of the broad resonance (Fig. 3.1f) and add a second NIR laser at frequency f_2 (Fig. 3.2a). We observe a significant increase in the detected count rate when the frequency difference satisfies: $f_2 - f_1 \approx \Delta = 954(2)$ MHz, explained by a strong reduction in optical pumping (which otherwise quickly diminishes the signal[28]). Importantly, the relatively narrow resonance condition (FWHM of 89(9) MHz) observed in Fig. 3.2b suggests that the homogeneous linewidth is much narrower than the diffusion-averaged linewidth in Fig. 3.1f.

Next, we fix the laser frequency difference to Δ and record the counts per experimental repetition (Fig. 3.2c). We obtain a telegraph-like signal, consistent with a single V2 center that is spectrally diffusing. Such a signal allows for the implementation of a charge-resonance check[14,18], which probes whether the V2 center is in the desired negative charge state, and its two transitions are resonant with the NIR lasers. If the number of detected counts passes a threshold T (e.g. the grey dashed line in Fig. 3.2c), we conclude that the defect was on resonance in that specific experimental repetition, allowing for post-selection (or pre-selection) of the data. In the following, we will explore how such post-selection tactics can be exploited to gain insights in the spectral diffusion dynamics.

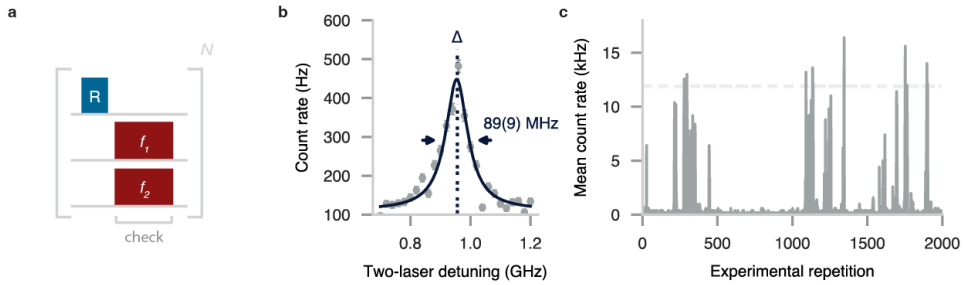

Figure 3.2: **Two-laser photoluminescence excitation spectroscopy. a)** Experimental sequence. A short (10 µs, 10 µW) high-energy (785 nm) repump laser pulse ('R') partially scrambles the charge state of both the environment and the V2 center. Emission is collected during the 'check' block, when two NIR lasers at frequencies f_1 and f_2 are turned on (approximately resonant with the broad peak in Fig. 3.1g). **b)** We observe an increase in count rate if the laser frequency difference is equal to $\Delta = 954(2)$ MHz, the spacing between the A_1 and A_2 transitions. A Lorentzian fit obtains a FWHM of 89(9) MHz. **c)** Detected mean count rate per experimental repetition, when the length of the 'check' block is set to 5 ms. In most repetitions, the defect is off-resonant with the lasers. When the A_1 and A_2 transitions coincide with laser frequencies f_1 and f_2, we observe significant emission ($\gg$ 1 kHz). Thresholding (dashed line) on the detected counts can be employed to prepare specific (i.e. 'on resonance') spectral configurations of the V2 center.

3.4. CHECK-PROBE SPECTROSCOPY: IONISATION AND SPECTRAL DIFFUSION DYNAMICS

Next, we develop a method to measure the ionisation and spectral diffusion dynamics of the V2 center. Currently, various experimental techniques exist, based either on tracking the transition frequency with subsequent PLE scans [10,15,16], or on autocorrelation-type measurements [9,37]. The former method struggles with measuring dynamics faster than the acquisition timescale of a single scan [15,38] (see also Fig. A.8). The latter, although fast, offers limited flexibility for probing diffusion under external perturbations [9].

Here, we take a different approach, based on a pulsed *check-probe* scheme as outlined in Fig. 3.3a. Following a charge-randomisation (repump) step, two 'check' blocks are executed (as in Fig.3.2a), separated by a perturbation of the system (grey block marked 'X'). Such a perturbation might consist of turning on (or off) specific lasers (e.g. NIR or repump) during the delay time t. This pulsed scheme features both high bandwidth (limited by the operating speed of the lasers), and allows one to isolate diffusion originating from the perturbation from other sources.

Importantly, one can either post-select on high counts (i.e. 'check') in the block before, or after the perturbation, effectively initialising the emitter on resonance at the start, or at the end of the experiment. By 'probing' the emitter brightness after (before) the perturbation, we effectively track its evolution forward (backward) in time, denoted as delay time $t > 0$ ($t < 0$) in Fig. 3.3a. This allows for the distinction between time-symmetric and non-time-symmetric perturbation processes (e.g. spectral diffusion or ionisation of the emitter, see Fig. 3.3b), as opposed to evaluating the purely symmetric autocorrelation function [9].

To quantitatively describe the signal, we derive an analytical expression that takes into account spectral diffusion and ionisation of the emitter. In this system, spectral diffusion

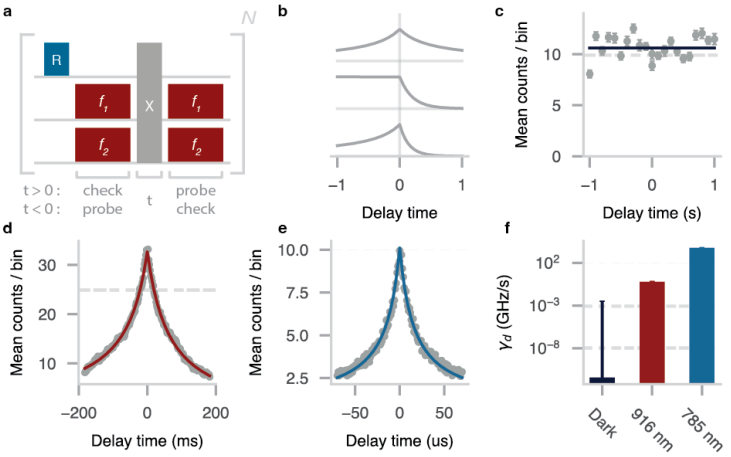

Figure 3.3: **Spectral diffusion dynamics. a)** Experimental sequence. A 'check' block (2 ms, 20 nW) is followed by a system perturbation (marked 'X'), which here consists either of turning off the lasers (c), turning on the NIR lasers (d), or turning on the repump laser (e). A second block (2 ms, 20 nW) probes whether the defect has diffused away, or has ionised (denoted 'probe'). Data is post-selected by imposing a minimum-counts threshold (T), heralding the emitter on resonance in the first (second) block and computing the mean number of counts in the second (first) block, which encodes the emitter brightness at future (past) delay times t. **b)** Schematic illustrating the expected signal (according to Eq. 3.1), when either ionisation or spectral diffusion is dominant (setting $\gamma_r \approx 0$). **c)** No significant spectral diffusion or ionisation is observed when the lasers are turned off. The solid line is a fit to the data using Eq. 3.1. Dashed grey line denotes the set threshold (in a 2 ms window). **d)** Experiment and fit under 20 nW of NIR laser power (916 nm). **e)** Experiment and fit under 1 µW of repump laser power. **f)** Extracted saturation-diffusion rates, obtained at laser powers of ~ 20 nW (NIR) and ~ 5 µW (repump). See Fig. A.3 for underlying data and error analysis.

is mainly caused by laser-induced reorientation of charges surrounding the defect, whose dynamics can be approximated by a bath of fluctuating electric dipoles[17]. To model this, we employ the spectral propagator formalism[38,39], which describes the evolution of the spectral probability density function in time, and whose form is given by a Lorentzian with linearly increasing linewidth $\gamma(t) = \gamma_d |t|$[39] (with γ_d the effective diffusion rate). Note that this description is valid only at short timescales ($\gamma_d |t| \ll 1$ GHz), as the spectral probability density should eventually converge to the diffusion-averaged distribution observed in Fig. 3.1f[39]. Furthermore, we take the spectral propagator to be time-symmetric, and model the ionisation (charge recapture) of the emitter as an exponential decay of fluorescence, governed by rate γ_i (γ_r).

The mean number of observed counts at delay time t can be described by (Appendix A.1):

$$C(t) = \begin{cases} C_0 \left(1 + \gamma_d \, t \, / \, \Gamma\right)^{-1} e^{-\gamma_i t}, & \text{if } t > 0. \\ C_0 \left(1 - \gamma_d \, t \, / \, \Gamma\right)^{-1} e^{\gamma_r t}, & \text{otherwise.} \end{cases} \tag{3.1}$$

with C_0 the mean number of observed counts at $t = 0$, Γ the emitter's (Lorentzian) homogeneous linewidth, and $\gamma_d, \gamma_i, \gamma_r > 0$. Note that Eq. 3.1 in general does not obey time-inversion symmetry (for $\gamma_i \neq \gamma_r$), and in specific cases allows for a clear distinction between ionisation

and diffusion processes (e.g. if $\gamma_r \approx 0$, see Fig. 3.3b). Next to that, the functional form of Eq. 3.1 captures information about the type of processes at play: emitter charge dynamics are described by an exponential decay while spectral diffusion has a power law dependence.

We experimentally implement the sequence for three distinct perturbations: (i) no laser illumination (Fig. 3.3c), (ii) illumination with the two NIR lasers (20 nW, Fig. 3.3d), and (iii) illumination with the repump laser (1 µW, Fig. 3.3e). We observe a wide range of dynamics, from the microsecond to second timescale, and observe excellent agreement between the data and the model (solid lines are fits to Eq. 3.1).

To quantitatively extract ionisation and diffusion rates under the perturbations, we set $\Gamma = 36$ MHz, (independently determined in Fig. 3.4e). We find that extracted rates are weakly dependent on the set threshold value, resulting from non-perfect initialisation on-resonance, but converge for higher T (Appendix A.2). Averaging over a range of threshold values, we find diffusion rates $\gamma_d = 0.00(2)\,\mathrm{GHz\,s^{-1}}, 0.60(2)\,\mathrm{GHz\,s^{-1}}, 2.4(2)\times10^3\,\mathrm{GHz\,s^{-1}}$, for perturbations (i), (ii) and (iii), respectively. In the dark, where almost no diffusion is apparent, the fit only converges if we set $\gamma_i, \gamma_r = 0$, which is a reasonable assumption at 4 K, given the deep-level nature of the V2 center [17,31].

Ionisation effects are only observed under the NIR-laser perturbation, due to the short diffusion timescale during the repump-laser perturbation (resulting in divergent fit results for γ_i and γ_r). From the data in Fig. 3.3d, we extract $\gamma_i = 1.0(2)$ Hz and $\gamma_r = 0.03(4)$ Hz. Correcting for reduced ionisation when the V2 center is off-resonance with the NIR lasers results in an ionisation rate $\gamma_i^0 = 3(1)$ Hz (see Appendix A.1).

We repeat the experiments for various laser powers, and observe a saturation-type behavior of the diffusion rates, both under NIR-lasers and repump laser excitation (Fig. A.3). The higher saturation-diffusion rate measured for the repump laser is likely due to the larger fraction of charge traps that can be ionised via a single-photon process (see Fig.3.1b and Fig. 3.3f). Different V2 centers in the material, show some variation in the (saturation) diffusion rates (Figs. A.8 and A.4. Note that the behaviour at powers beyond those accessed in these experiments will determine if spectral stability persists under repeated fast optical π-pulses, as commonly used for remote entanglement generation experiments [7,14,18].

3.5. CHECK-PROBE SPECTROSCOPY: LINEWIDTH

Having established the spectral diffusion timescales, we characterise the homogeneous linewidth with minimal laser-induced disturbance. We use an optical spectroscopy method based on the check-probe scheme (similar to Ref. [40]) that, in this system, only requires laser illumination on timescales short compared to the laser-induced diffusion timescales (contrary to commonly used 'scanning' PLE [10,13,15,16,19,41], Fig. A.8).

First, we execute an alternative implementation of the 'check' block (compared to Figs 3.2a and 3.3a), that consists of a single NIR-laser pulse at f_1, together with a MW pulse that mixes the spin states (Fig. 3.4a). By post-selecting on high counts, either the A_1 or A_2 transition is initialised on-resonance with f_1. A second laser is used to probe the defect emission at a frequency f_2 immediately thereafter (~ µs timescale, here limited by the microprocessor clock cycle). By studying the mean number of counts during the f_2 pulse, (an upper bound for) the homogeneous linewidth can be extracted (Fig. 3.4b).

We introduce a quantitative model for the signal that extracts the homogeneous

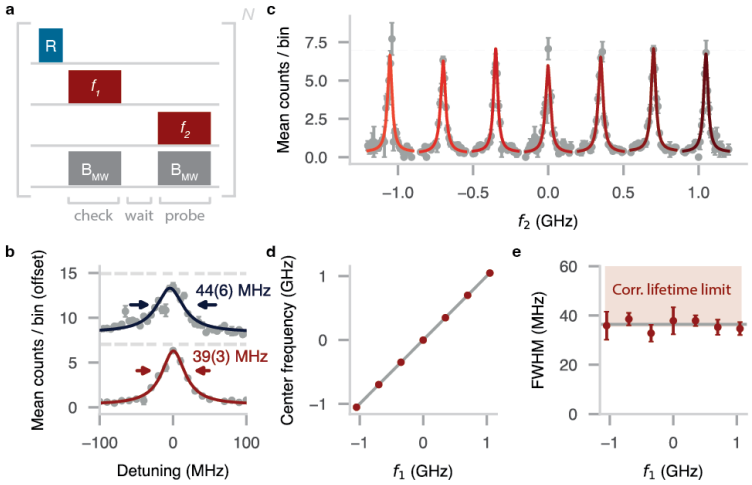

Figure 3.4: **Homogeneous linewidth and state preparation a)** Experimental sequence. A resonant laser at f_1 and a microwave (MW) pulse resonant with the ground-state spin transition act as a resonance check, initialising the optical transition near f_1. Next, a second laser probes the defect emission at f_2 (for 2 ms), yielding a measurement of the linewidth with minimal disturbance. **b)** Experimental data showing narrow optical transitions, with the bottom (top) data corresponding to a waiting time of 5 µs (40 ms) between the f_1 and f_2 laser pulses (offset for clarity). Data are fitted to a Lorentzian with a FWHM of 39(3) MHz (44(6) MHz). The counts threshold is set to $T = 7$ during the f_1 pulse. **c)** Data and fits as in (b)(bottom), scanning f_2 around f_1, when f_1 is set at different frequencies (various shades of red) within the broad diffusion-averaged line measured in Fig. 3.1g. **d)** Measured resonance center frequency as a function of the set f_1 frequency (solid grey line: $f = f_1$). The defect emission frequency can effectively be tuned over a GHz range. **e)** Corresponding linewidths extracted from (c), with inverse-variance weighted mean 36(1) MHz (solid grey line). The shaded region denotes the expected minimum linewidth (~ 36 MHz), given the lifetime limit of ~ 20 MHz, and correcting for power broadening (~ 26 MHz, Fig. 3.5j) and residual inhomogeneous broadening (~ 15 MHz, Eq. 3.2).

linewidth and considers the residual inhomogeneous broadening resulting from non-perfect initialisation on-resonance. To this end, we compute the spectral probability density immediately after the 'check' block, as a function of the number of detected photons $m \geq T$ using Bayesian inference (see Appendix A.4):

$$P(f \mid m \geq T) = \frac{1}{N_T}\left(1 - \Gamma_i\left[T, \lambda(f - f_1)\right]\right), \tag{3.2}$$

with f the emitter frequency, $\lambda(f)$ the pure (i.e. homogeneous) spectral response of the emitter, $\Gamma_i[a,z]$ the incomplete Gamma function and N_T a normalisation constant (Appendix A.4). The expression in Eq. 3.2 is strongly dependent on T, with higher threshold values leading to distributions that are sharply peaked around f_1. Note that this analysis assumes negligible laser-induced diffusion during the 'check' block, placing limits on the used laser power and the block's duration ($\ll 1/\gamma_d$).

The measured signal, i.e. the mean number of detected counts in the 'probe' block is then given by:

$$C(f) = P(f \mid m \geq T) * \lambda(f), \tag{3.3}$$

where $*$ denotes the linear convolution. Importantly, as both terms in Eq. 3.3 contain $\lambda(f)$, the pure spectral response can be recovered by varying T in post-processing (Appendix A.4). In particular, for the Lorentzian spectral response:

$$\lambda_{\mathrm{L}}(f) = C_0 \frac{(\frac{\Gamma}{2})^2}{f^2 + (\frac{\Gamma}{2})^2}, \tag{3.4}$$

with FWHM Γ and on-resonance brightness C_0, the signal converges to: $C(f) \to \lambda_{\mathrm{L}}(f - f_1)$ at high threshold values ($T \gg \max[\lambda(f)]$), simplifying the analysis (Appendix A.4).

We demonstrate the check-probe spectroscopy method on the same V2 center as used in Figs. 3.1f, 3.2 and 3.3 (Methods), and observe narrow Lorentzian resonances around the f_1 laser frequency (39(3) MHz at $T = 7$, see Fig. 3.4b). Correcting for residual broadening by fitting Eq. 3.3 to the data for $1 \leq T \leq 13$ (using Eqs. 3.2 and 3.4), we extract: $C_0 = 6.5(1)$ counts (3.22(7) kHz count rate) and $\Gamma = 33(1)$ MHz. This spectrum (as well as the those measured in Fig. 3.5) corresponds to an average over the A_1 and A_2 transitions, resulting in: $\Gamma \approx (\Gamma_{A_1} + \Gamma_{A_2})/2$ (< 5% deviation, assuming equal initialisation probability, see Appendix A.5). Note that this ambiguity between the transitions can be fully resolved by executing the 'check' block with two NIR lasers, as in Fig. 3.2. The discrepancy between the extracted mean linewidth and the mean lifetime limit (~ 20 MHz) is well-explained by power-broadening, with optical Rabi frequencies estimated to be ~ 26 MHz (next section, see Fig. 3.5j).

Next, to verify our previous inference that spectral diffusion is virtually absent without laser illumination (Fig. 3.3c), we insert a 40 ms waiting time between the f_1 and f_2 pulses (Fig. 3.4b, top), which does not increases the linewidth within the fit error ($T = 7$). Importantly, this allows for the preparation of the transition at a specific frequency, 'storing' it in the dark, so that the V2 center can be used to produce coherent photons at a later time. Furthermore, the broad nature of the diffusion-averaged linewidth depicted in Fig. 3.1f, enables probabilistic tuning of the emission frequency over more than a gigahertz[18]. We demonstrate this by varying the f_1 frequency, initialising the emitter at different spectral locations, and probing the transition with the NIR laser at frequency f_2 (Fig. 3.4c, d and e). Such tuning of the V2 emission frequency without the need for externally applied electric fields[32,33] might open up new opportunities for optically interfacing multiple centers.

3.6. CHECK-PROBE SPECTROSCOPY: LANDAU-ZENER-STÜCKELBERG INTERFERENCE

To further benchmark the check-probe spectroscopy method, we use it to resolve Landau-Zener-Stückelberg (LZS) interference fringes in the optical spectrum[25]. Such fringes demonstrate coherent control of the orbital states of the V2 defect using MW frequency electric fields, and enable the independent determination of the optical coherence and Rabi frequency[25], allowing for the separation of their contributions to the linewidths measured in Fig. 3.4.

LZS interference fringes can arise when a strong AC electric field shifts the optical transition across the laser frequency multiple times within the coherence time of the emitter[33,42]. Each time a crossing occurs, the emitter is excited with a small probability amplitude and as-

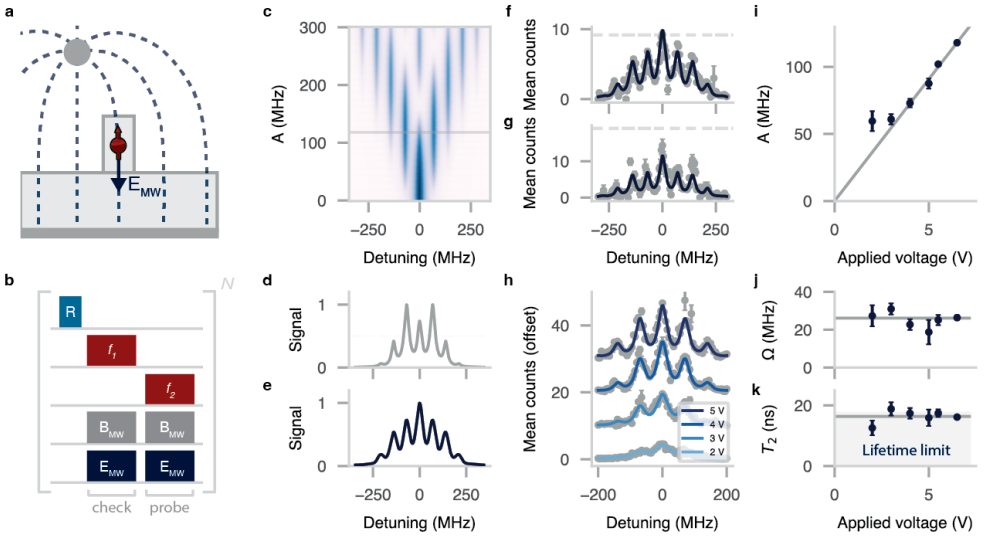

Figure 3.5: **Landau-Zener-Stückelberg (LZS) interference. a)** Schematic showing the electric-field generated by the MW drive, connecting the bond wire and ground plane (dark grey, not drawn to scale), which can generate significant stark shifts. **b)** Sequence, as in Fig. 3.4a, but now explicitly including the electric field (E_{MW}). **c)** Characteristic LZS interference pattern (theory) as function of the laser detuning, and the electric field strength A. At higher electric fields, side bands emerge at multiples of the driving frequency $\omega = 70\,\text{MHz}$. **d)** Line cut through (c) for $A = 118\,\text{MHz}$. The dashed line denotes an example threshold T. **e)** The experimental spectrum expected from the situation in (d). The signal differs from the original spectrum as it is weighted over the probability to pass the threshold for different detuning. **f)** Mean detected counts as a function of the two-laser detuning when the MW amplitude is set to 6.5 V, approximately equal to the value in (d). The threshold ($T = 10$) is set to about half the maximum amplitude, as in (d). The fit function (solid line) is obtained by fitting the dataset for a range of threshold values (see Fig. A.6). **g)** Same dataset as in (f), but with $T = 20$. The signal distortion due to the threshold is well-captured by the fit. **h)** Experimental data (grey) and fit (solid lines) as in (f), varying the applied voltage ($T = \{6, 10, 13, 15\}$). Data are offset by 10 counts for clarity. **i)** Extracted electric field strength A as a function of the applied voltage. Solid grey line is a linear guide to the eye. **j)** Extracted optical Rabi frequency Ω. Solid grey line denotes the inverse-variance weighted mean. **k)** Extracted optical coherence time T_2. Shaded region denotes the mean lifetime limit: $T_2 = 2T_1 \approx 17\,\text{ns}$ Solid grey line denotes the inverse-variance weighted mean of the data points.

sociated 'Stückelberg' phase. These amplitudes can interfere constructively or destructively, creating fringes in the spectrum (see Ref.[25] for an extensive review on the phenomenon).

In our setup, MW radiation is applied by running an AC current through an aluminum alloy wire spanned across the sample (Fig. 3.5a). The original purpose of the wire is to enable mixing of the ground-state spin in the 'check' and 'probe' blocks used in Fig. 3.4. However, this geometry also creates significant *electric* fields at microwave frequencies (Fig. 3.5a). Taking the defect ground and excited states as basis states ($|g\rangle = |0\rangle$ and $|e\rangle = |1\rangle$), the (optical) evolution of the system is described by the Hamiltonian (in the rotating frame of the emitter)[42]:

$$H = \frac{\Omega}{2}\sigma_x + \frac{\delta + A\cos(\omega t)}{2}\sigma_z, \tag{3.5}$$

where Ω is the optical Rabi frequency, δ is the detuning between the optical transition and the laser frequency, A is the stark-shift amplitude (which scales with the electric field ampli-

tude), ω is the MW driving frequency and σ_x, σ_z are the Pauli spin matrices. For the experimental parameters used here, the system is considered to be in the 'fast-passage' regime (defined as $A\omega \gg \Omega^2$ [25]), meaning the excitation probability amplitude during a single crossing is small (Methods). In this regime, the spectral response of the emitter can be described by[25]:

$$\lambda_{\mathrm{LZS}}(f) = C_0 \sum_k \frac{\Omega_k^2}{\frac{1}{T_1 T_2} + \frac{T_2}{T_1}\left(k\omega - f\right)^2 + \Omega_k^2}, \tag{3.6}$$

where C_0 is the on-resonance emitter brightness for $A = 0$, $\Omega_k = \Omega J_k\left(\frac{A}{\omega}\right)$, with J_k the Bessel function, and T_1, T_2 are the emitter's optical relaxation and (pure-dephasing) coherence times respectively. Figure 3.5c shows the optical spectrum as a function of A, obtained by evaluating Eq. 3.6 for our sample parameters. At higher electric field amplitudes (i.e. higher A), multiple characteristic interference fringes appear, spaced by the driving frequency ω (here 70 MHz), creating a complex optical spectrum.

Measuring such complex spectra with the check-probe optical spectroscopy method requires taking into account signal distortions arising from the form of the spectral probability density after the check block (Eq. 3.2). To see why this is the case, we consider an exemplary theoretical spectrum plotted in Fig. 3.5d (for $A = 118$ MHz), where the threshold T is set to about half the maximum signal amplitude (dashed line in Fig. 3.5d). Such a threshold is passed (with high probability) not only when the central peak is on resonance with f_1, but also when one of the nearest fringes is on resonance with the laser. Computing the resulting weighted signal (inserting Eq. 3.6 in Eq. 3.3) yields the distorted, experimentally expected spectrum shown in Fig. 3.5e.

To experimentally measure the LZS interference signal, we execute the sequence in Fig. 3.5b, now explicitly including the electric field components generated by the MW drive. These components were also implicitly present in previously discussed experiments (Fig. 3.4), but their effects could largely be neglected under the conditions: $\omega > A$ and $\omega > \Gamma \approx \sqrt{(\pi T_2)^{-2} + \Omega^2}$ [25]. We set the MW driving frequency ω to the ground-state zero field splitting (70 MHz), so that the magnetic field components efficiently mix the spin states [19,43], and set the (peak-to-peak) MW amplitude between the wire and the ground plane to 6.5 V. Figures 3.5f and g show the measured spectrum for a threshold of $T = 10$ and $T = 20$ respectively. The former corresponds roughly to the example threshold in Fig. 3.5d, and the observed signal matches well with the expected spectrum in Fig. 3.5e. Setting $T = 20$ alters the measured spectrum, highlighting the interplay between the threshold and corresponding distortion. The solid lines are generated by a single fit of the complete dataset using Eq. 3.3 for $1 < T < 21$ (post-processed, see Fig. A.6).

We repeat this procedure while varying the MW amplitude (Fig 3.5h) and extract A, Ω and the estimated pure-dephasing T_2 coherence time (Figs 3.5i,j and k), keeping ω and the optical relaxation time $T_1 = 8.7$ ns fixed (again using the mean of the A_1 and A_2 transitions [26]). For amplitude values above 2 V we observe a linear relation between the MW amplitude and A, as expected. For lower values, a significant deviation is observed, possibly because the system is no longer well-described by the fast-passage limit (i.e. $A\omega \sim \Omega^2$). Indeed, the optical Rabi frequency is estimated to be 26(1) MHz (weighted mean of Fig. 3.5j), on the order of $\sqrt{A\omega}$. Finally, we find a mean $T_2 = 16.4(4)$ ns, approximately equal to the

mean lifetime limit ($2\,T_1 \approx 17\,\mathrm{ns}$[26]).

3.7. DISCUSSION

In this work, we introduced a high-bandwidth check-probe scheme that allows for quantitative characterisation of spectral diffusion and ionisation processes under the influence of external perturbations. Our methods enable measurements of the homogeneous transition linewidth of single quantum emitters, under minimal system disturbance.

We applied these methods to study the optical coherence of the V2 center in commercially available bulk-grown silicon carbide. Despite high levels of spectral diffusion under laser illumination, we reveal near-lifetime-limited linewidths with slow dynamics, enabling the preparation of a frequency-tunable coherent optical transition[18,32,33]. Although higher purity materials are likely desired, such coherent optical transitions in bulk-grown SiC might enable nanophotonic device development, testing and characterisation (e.g. cavity coupling, Purcell enhancement) using widely available materials[44]. Future avenues for research in bulk-grown material include investigating the spin coherence properties and the spectral stability under higher-power laser pulses used for long-distance entanglement generation[7,8].

Finally, the presented methods are applicable to other platforms where spectral diffusion forms a natural challenge, such as rare-earth doped crystals[45], localised excitons[30] or semiconductor quantum dots[29], and might enable new insights in the charge environment dynamics of such systems.

3.8. METHODS

SAMPLE PARAMETERS

The sample was diced directly from a 4-inch High-Purity Semi-Insulating (HPSI) wafer obtained from the company Wolfspeed, model type W4TRF0R-0200. We note that the HPSI terminology originates from the silicon carbide electronics industry. In the quantum technology context considered here, this material has a significant amount of residual impurities (order $\sim 10^{15}\,\mathrm{cm}^{-3}$ according to Son et al.[31]) and is hence considered low purity with respect to a concentration of $\sim 10^{13}\,\mathrm{cm}^{-3}$ typical for epitaxially grown layers on the c-axis of silicon carbide[15,46]. On a different sample, diced from a wafer with the same model type, a Secondary-Ion Mass Spectroscopy (SIMS) measurement determined the concentration of nitrogen donors as $[\mathrm{N}] = 1.1 \times 10^{15}\,\mathrm{cm}^{-3}$. In addition to intrinsic silicon vacancies, we generate additional silicon vacancies through a 2 MeV electron irradiation with a fluence of $5 \times 10^{13}\,\mathrm{cm}^{-2}$. The sample was annealed at 600 °C for 30 min in an Argon atmosphere. To enhance the optical collection efficiency and mitigate the unfavourable V2 dipole orientation for confocal access along the SiC growth axis (c-axis), we fabricate nanopillars. We deposit 25 nm of Al_2O_3 and 75 nm of nickel on lithographically defined disks. A subsequent SF_6/O_2 ICP-RIE etches the pillars, see figure 3.1c. The nanopillars have a diameter of 450 nm at the top and 650 nm at the bottom and are 1.2 µm high. Considering the modest efficiency of our detector (≈ 25% at 950 nm), the V2 centers studied here appear to be significantly brighter than those in epitaxially grown layers[19,41,43,47], which is consistent with previous studies in commercially available material[22,48].

EXPERIMENTAL SETUP

All experiments are performed using a home-built confocal microscopy setup at 4K (Montana Instruments S100). The NIR lasers (Toptica DL Pro and the Spectra-Physics Velocity TLB-6718-P) are frequency-locked to a wavemeter (HF-Angstrom WS/U-10U) and their power is modulated by acousto-optic-modulators (G&H SF05958). A wavelength division multiplexer (OZ Optics) combines the 785 nm repump (Cobolt 06-MLD785) and NIR laser light, after which it is focused onto the sample by a movable, room temperature objective (Olympus MPLFLN 100x), which is kept at vacuum and is thermally isolated by a heat shield. A 90:10 beam splitter that directs the laser light into the objective, allows V2 center phonon-sideband emission to pass through, to be detected on an avalanche photodiode (COUNT-50N, filtered by a Semrock FF01-937/LP-25 long pass filter at a slight angle). Alternatively, emission can be directed to a spectrometer (Princeton Instruments IsoPlane 81), filtered by a 830 nm long pass filter (Semrock BLP01-830R-25). Microwave pulses are generated by an arbitrary-waveform generator (Zurich Instruments HDAWG8), amplified (Mini-circuits LZY-22+), and delivered with a bond-wire drawn across the sample. The coarse time scheduling (1 µs resolution) of the experiments is managed by a microcontroller (ADwin Pro II). For a schematic of the setup see Fig. A.9.

MAGNETIC FIELD

For the check-probe optical spectroscopy measurements in Fig. 3.4 (and Fig. A.8), we apply an external magnetic field of ≈ 1 mT along the defect symmetry axis (c-axis). All other exper-

iments are performed at approximately zero field. We apply the field by placing a permanent neodymium magnet outside the cryostat. We align it by performing the sequence depicted in Fig. 3.1e, with f_1 set at the center frequency of the broad resonance (Fig. 3.1f), and monitoring the average photoluminescence (f_1 pulse is set to 2 ms). A (slightly) misaligned field causes spin-mixing between the $m_s = \pm\frac{3}{2}$ and $m_s = \pm\frac{1}{2}$ subspace, which increases the detected signal. Minimising for the photoluminescence thus optimises the field alignment along the symmetry axis.

LZS FAST-PASSAGE REGIME

The fast-passage regime is defined by: $A\omega \gg \Omega^2$ [25], with $\omega = 70\,\text{MHz}$. From the measurements in Fig. 3.4, we can estimate: $\Omega < 40\,\text{MHz}$. Furthermore, we can get a rough estimate for A by approximating the electric field at the defect to be: $E \approx \frac{U}{d}(\epsilon+2)/3$, with U the applied voltage, $d \approx 500\,\mu\text{m}$ the distance between the wire and the ground plane and $\epsilon \approx 10$ the dielectric constant of silicon carbide (using the local field approximation [33]). There is some debate on the value of the Stark-shift coefficient [32,33]. Here, we take the value from Ref. [33]: $3.65\,\text{GHz m MV}^{-1}$ and estimate $A \approx 29\,\text{MHz}$ for an applied voltage of 1 V. Hence, $A\omega > \Omega^2$ for $U > 1\,\text{V}$, and the fast-passage requirement is satisfied for most measurements in Fig. 3.5. The excellent agreement between the data and our model (especially for higher values of U) and the corresponding extracted values for Ω and A, further justify using the fast-passage solution of the LZS Hamiltonian.

ERROR ANALYSIS

For all quoted experimental values, the value between brackets indicates one standard deviation or the standard error obtained from the fit (unless stated otherwise). The error bars on the mean counts are based on Poissonian shot noise. The uncertainty on fit parameters is rescaled to match the sample variance of the residuals after the fit.

REFERENCES

[1] G. Waldherr *et al.*, *Quantum error correction in a solid-state hybrid spin register,* Nature **506**, 204 (2014).

[2] J. Cramer *et al.*, *Repeated quantum error correction on a continuously encoded qubit by real-time feedback,* Nat Commun **7**, 11526 (2016).

[3] M. H. Abobeih *et al.*, *Fault-tolerant operation of a logical qubit in a diamond quantum processor,* Nature **606**, 884 (2022).

[4] S. De Bone, P. Möller, C. E. Bradley, T. H. Taminiau and D. Elkouss, *Thresholds for the distributed surface code in the presence of memory decoherence,* AVS Quantum Science **6**, 033801 (2024).

[5] M. Pompili *et al.*, *Experimental demonstration of entanglement delivery using a quantum network stack,* npj Quantum Inf **8**, 1 (2022).

[6] C. M. Knaut *et al.*, *Entanglement of nanophotonic quantum memory nodes in a telecom network,* Nature **629**, 573 (2024).

[7] M. Pompili *et al.*, *Realization of a multinode quantum network of remote solid-state qubits,* Science **372**, 259 (2021).

[8] S. L. N. Hermans *et al.*, *Qubit teleportation between non-neighbouring nodes in a quantum network,* Nature **605**, 663 (2022).

[9] J. Wolters, N. Sadzak, A. W. Schell, T. Schröder and O. Benson, *Measurement of the Ultrafast Spectral Diffusion of the Optical Transition of Nitrogen Vacancy Centers in Nano-Size Diamond Using Correlation Interferometry,* Phys. Rev. Lett. **110**, 027401 (2013).

[10] L. Orphal-Kobin *et al.*, *Optically Coherent Nitrogen-Vacancy Defect Centers in Diamond Nanostructures,* Phys. Rev. X **13**, 011042 (2023).

[11] A. Faraon, C. Santori, Z. Huang, V. M. Acosta and R. G. Beausoleil, *Coupling of Nitrogen-Vacancy Centers to Photonic Crystal Cavities in Monocrystalline Diamond,* Phys. Rev. Lett. **109**, 033604 (2012).

[12] M. Ruf *et al.*, *Optically Coherent Nitrogen-Vacancy Centers in Micrometer-Thin Etched Diamond Membranes,* Nano Lett. **19**, 3987 (2019).

[13] L. Robledo, H. Bernien, I. Van Weperen and R. Hanson, *Control and Coherence of the Optical Transition of Single Nitrogen Vacancy Centers in Diamond,* Phys. Rev. Lett. **105**, 177403 (2010).

[14] H. Bernien *et al.*, *Heralded entanglement between solid-state qubits separated by three metres,* Nature **497**, 86 (2013).

[15] J. Heiler *et al.*, *Spectral stability of V2 centres in sub-micron 4H-SiC membranes,* npj Quantum Mater. **9**, 34 (2024).

[16] M. K. Koch, V. Bharadwaj and A. Kubanek, *Limits for coherent optical control of quantum emitters in layered materials,* (2023), arXiv:2312.11090 [quant-ph] .

[17] D. R. Candido and M. E. Flatté, *Suppression of the Optical Linewidth and Spin Decoherence of a Quantum Spin Center in a p - n Diode,* PRX Quantum **2**, 040310 (2021).

[18] J. M. Brevoord *et al.*, *Heralded initialization of charge state and optical-transition frequency of diamond tin-vacancy centers,* Phys. Rev. Applied **21**, 054047 (2024).

[19] C. Babin *et al.*, *Fabrication and nanophotonic waveguide integration of silicon carbide colour centres with preserved spin-optical coherence,* Nat. Mater. **21**, 67 (2022).

[20] D. M. Lukin, M. A. Guidry and J. Vučković, *Integrated Quantum Photonics with Silicon Carbide: Challenges and Prospects,* PRX Quantum **1**, 020102 (2020).

[21] B. J. M. Hausmann *et al.*, *Fabrication of diamond nanowires for quantum information processing applications,* Diamond and Related Materials **19**, 621 (2010).

[22] M. Radulaski *et al.*, *Scalable Quantum Photonics with Single Color Centers in Silicon Carbide,* Nano Lett. **17**, 1782 (2017).

[23] E. R. MacQuarrie *et al.*, *Generating T centres in photonic silicon-on-insulator material by ion implantation,* New J. Phys. **23**, 103008 (2021).

[24] C. P. Anderson *et al.*, *Electrical and optical control of single spins integrated in scalable semiconductor devices,* Science **366**, 1225 (2019).

[25] S. Shevchenko, S. Ashhab and F. Nori, *Landau–Zener–Stückelberg interferometry,* Physics Reports **492**, 1 (2010).

[26] D. Liu *et al.*, *The silicon vacancy centers in SiC: Determination of intrinsic spin dynamics for integrated quantum photonics,* npj Quantum Inf **10**, 72 (2024).

[27] R.-Z. Fang *et al.*, *Experimental Generation of Spin-Photon Entanglement in Silicon Carbide,* Phys. Rev. Lett. **132**, 160801 (2024).

[28] D. B. Higginbottom *et al.*, *Optical observation of single spins in silicon,* Nature **607**, 266 (2022).

[29] R. G. Neuhauser, K. T. Shimizu, W. K. Woo, S. A. Empedocles and M. G. Bawendi, *Correlation between Fluorescence Intermittency and Spectral Diffusion in Single Semiconductor Quantum Dots,* Phys. Rev. Lett. **85**, 3301 (2000).

[30] O. Iff *et al.*, *Substrate engineering for high-quality emission of free and localized excitons from atomic monolayers in hybrid architectures,* Optica **4**, 669 (2017).

[31] N. T. Son and I. G. Ivanov, *Charge state control of the silicon vacancy and divacancy in silicon carbide,* Journal of Applied Physics **129**, 215702 (2021).

[32] M. Rühl, L. Bergmann, M. Krieger and H. B. Weber, *Stark Tuning of the Silicon Vacancy in Silicon Carbide,* Nano Lett. **20**, 658 (2020).

[33] D. M. Lukin *et al.*, *Spectrally reconfigurable quantum emitters enabled by optimized fast modulation,* npj Quantum Inf **6**, 1 (2020).

[34] G. Pieplow *et al.*, *Quantum Electrometer for Time-Resolved Material Science at the Atomic Lattice Scale,* (2024), arXiv:2401.14290 [cond-mat, physics:physics, physics:quant-ph] .

[35] W. Ji *et al.*, *Correlated sensing with a solid-state quantum multisensor system for atomic-scale structural analysis,* Nat. Photon. **18**, 230 (2024).

[36] P. Udvarhelyi *et al.*, *Vibronic States and Their Effect on the Temperature and Strain Dependence of Silicon-Vacancy Qubits in 4H-SiC,* Phys. Rev. Appl. **13**, 054017 (2020).

[37] L. Fleury, A. Zumbusch, M. Orrit, R. Brown and J. Bernard, *Spectral diffusion and individual two-level systems probed by fluorescence of single terrylene molecules in a polyethylene matrix,* Journal of Luminescence **56**, 15 (1993).

[38] T. Basché, ed., *Single-Molecule Optical Detection, Imaging and Spectroscopy* (VCH, Weinheim, 1997).

[39] G. Zumofen and J. Klafter, *Spectral random walk of a single molecule,* Chemical Physics Letters **219**, 303 (1994).

[40] S. L. N. Hermans *et al.*, *Entangling remote qubits using the single-photon protocol: An in-depth theoretical and experimental study,* New J. Phys. **25**, 013011 (2023).

[41] D. M. Lukin *et al.*, *Two-Emitter Multimode Cavity Quantum Electrodynamics in Thin-Film Silicon Carbide Photonics,* Phys. Rev. X **13**, 011005 (2023).

[42] K. C. Miao *et al.*, *Electrically driven optical interferometry with spins in silicon carbide,* Sci. Adv. **5**, eaay0527 (2019).

[43] H. B. Banks *et al.*, *Resonant Optical Spin Initialization and Readout of Single Silicon Vacancies in 4H-SiC,* Phys. Rev. Appl. **11**, 024013 (2019).

[44] D. M. Lukin *et al.*, *4H-silicon-carbide-on-insulator for integrated quantum and nonlinear photonics,* Nat. Photonics **14**, 330 (2020).

[45] C. Thiel, T. Böttger and R. Cone, *Rare-earth-doped materials for applications in quantum information storage and signal processing,* Journal of Luminescence **131**, 353 (2011).

[46] R. Nagy *et al.*, *High-fidelity spin and optical control of single silicon-vacancy centres in silicon carbide,* Nat Commun **10**, 1954 (2019).

[47] J. Körber *et al.*, *Fluorescence Enhancement of Single V2 Centers in a 4H-SiC Cavity Antenna,* Nano Lett. **24**, 9289 (2024).

[48] M. Widmann *et al.*, *Coherent control of single spins in silicon carbide at room temperature,* Nature Mater **14**, 164 (2015).

4

IMPROVED ELECTRON-NUCLEAR QUANTUM GATES FOR SPIN SENSING AND CONTROL

H. B. van Ommen*, G. L. van de Stolpe*, N. Demetriou, H. K. C. Beukers, J. Yun, T. R. J. Fortuin, M. Luliano, A. R.-P. Montblanch, R. Hanson, T.H. Taminiau

The ability to sense and control nuclear spins near solid-state defects might enable a range of quantum technologies. Dynamically Decoupled Radio-Frequency (DDRF) control offers a high degree of design flexibility and long electron-spin coherence times. However, previous studies considered simplified models and little is known about optimal gate design and fundamental limits. Here, we develop a generalised DDRF framework that has important implications for spin sensing and control. Our analytical model, which we corroborate by experiments on a single NV center in diamond, reveals the mechanisms that govern the selectivity of gates and their effective Rabi frequencies, and enables flexible detuned gate designs. We apply these insights to numerically show a 60x sensitivity enhancement for detecting weakly coupled spins and study the optimisation of quantum gates in multi-qubit registers. These results advance the understanding for a broad class of gates and provide a toolbox for application-specific design, enabling improved quantum control and sensing.

*These authors contributed equally to this work

4.1. INTRODUCTION

Sensing and controlling nuclear spins in the vicinity of optically active solid-state defects, such as the nitrogen vacancy (NV) center in diamond, has opened up various opportunities in the fields of quantum sensing and quantum information processing [1–4]. Sensing nuclear spins outside the host crystal might bring chemical structure determination to the single-molecule level [1,3,5,6]. More strongly coupled nuclear spins inside the host material can be used for quantum information processing, for which advances in the number of available qubits [7], in gate fidelities [8,9] and in the possibility to connect systems via an optical interface [2,10] have led to proof-of-principle demonstrations of increasing complexity [3,4,11].

Central to these developments has been the ability to sense and control nuclear spins using the defect's electron spin through the hyperfine interaction [12–17]. In particular, dynamical decoupling (DD) protocols have been used to detect nuclear magnetic resonance signals [18,19] and allow for selective, universal nuclear spin control [20]. Compared to traditional DD sensing, the recently developed DDRF sequence [14], which combines DD with radio-frequency (RF) pulses, unlocks additional sensing and control directions (Fig. 4.1a) and offers increased flexibility for gate optimisation [9]. These advantages have helped enable the sensing of large nuclear spin clusters [3,7], extend the number of nuclear spins available to defect centers for information processing [14,21,22], and realise high two-qubit gate fidelities ($> 99.9\%$) [9].

In this work, we introduce a generalised version of the DDRF framework, enhancing the sequence's performance for nuclear sensing and control, as well as revealing important limitations on sensitivity and selectivity. We derive analytical expressions that give a more complete description of the electron-nuclear dynamics compared to previous work [14] and verify their predictions experimentally using a single NV center and its surrounding ^{13}C nuclear spins. Based on these insights, we modify the DDRF sequence to optimize the effective electron-nuclear interaction strength and mitigate crosstalk of quantum gates. These results have applications in the field of nano-NMR [1,3,6] and provide a comprehensive toolbox for designing quantum gates in multi-qubit electron-nuclear spin systems [14,21].

4.2. DECOHERENCE-PROTECTED RADIO-FREQUENCY QUANTUM GATES

We first describe the DDRF gates. Compared to the original description [14], we present a generalized framework, explicitly including the off-resonant driving of nuclear-spin transitions. We will show that this refinement has important implications for the performance of quantum gates and sensing sequences implemented with DDRF control.

We consider an electronic spin interacting with a number of nuclear spins via a hyperfine interaction (see Fig. 4.1a). To retain generality for defects with different spin numbers [23–27], we assume two electron spin states are selected to use as a qubit and describe these as a pseudo spin-$\frac{1}{2}$ system spanned by $|0\rangle$ and $|1\rangle$.

The main challenge for electron-nuclear gates in such systems is that the electron interacts with all nuclear spins, as well as other noise sources, leading to decoherence and crosstalk [13,14,28]. Hence, a well-designed electron-nuclear two-qubit gate or sensing sequence aims to realize a conditional interaction with a selected (group of) target spin(s),

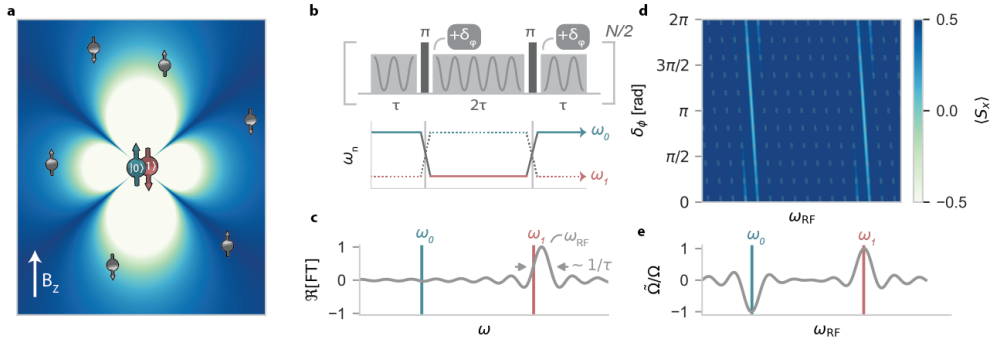

Figure 4.1: **The DDRF framework. a)** Schematic of the system considered here, comprising a single electron spin (red/blue colors denote the spin state), surrounded by a non-uniform distribution of nuclear spins (grey). The background brightness corresponds to the hyperfine ($A_\parallel$) frequency shift Δ induced by the electron spin. B_z is the external magnetic field. **b)** DDRF sequence, where RF driving (with phase updates δ_ϕ) of the nuclear spin (grey) is interleaved with decoupling pulses on the electron spin (black). The bottom row indicates the nuclear spin's precession frequency (ω_n), for initial electron-spin state $|0\rangle$ (solid line) or $|1\rangle$ state (dotted line). The total sequence time is $T = 2N\tau$. **c)** Schematic showing the Fourier transform (FT) of a single RF pulse applied at frequency $\omega_{RF} = \omega_1 + \Delta_1$. The bandwidth of the pulse is inversely proportional to the pulse length ($\propto 1/(2\tau)$). **d)** Simulated nuclear-spin spectroscopy, where the electron spin (starting in $\frac{|0\rangle+|1\rangle}{\sqrt{2}}$) is used to sense an unpolarised nuclear spin by applying the DDRF sequence of (b). Brighter colors indicate a drop in electron coherence ($\langle S_x \rangle$), observed when δ_ϕ matches Eq. 4.3 (grey dashed line). **e)** Effective nuclear-spin Rabi frequency $\tilde{\Omega}$ (Eq. 4.5) of the DDRF sequence, as a fraction of the bare Rabi frequency Ω, when following the phase increment δ_ϕ (Eq. 4.3, dashed line in d). A significant electron-nuclear interaction is possible over a range of RF frequencies ($\omega_{RF} \neq \omega_1$), albeit with a lower effective interaction strength $\tilde{\Omega}$.

while protecting electron coherence by decoupling all other interactions and noise sources.

The DDRF gate consists of a sequence of dynamical decoupling (DD) pulses on the electron spin, interleaved with RF pulses that drive the nuclear spin transitions, as illustrated in Fig. 4.1b. We consider sequences of the form $(\tau - \pi - 2\tau - \pi - \tau)^{N/2}$, with N the number of π-pulses and 2τ the interpulse delay. The DD sequence aims to decouple the electron spin from the surrounding spins and magnetic field fluctuations, extending the electron-spin coherence[15]. The interleaved RF pulses aim to manipulate selected nuclear spins and to re-couple them to the electron spin[14].

In the frame of the electron energy splitting, the Hamiltonian for the electron spin and a single nuclear spin is[14] (Appendix B.1):

$$H = \bar{\omega} I_z + \Delta \sigma_z I_z, \tag{4.1}$$

where $\bar{\omega} = (\omega_0 + \omega_1)/2$ is the mean nuclear-spin frequency, with ω_0 and ω_1 the nuclear spin precession frequencies for electron-spin states $|0\rangle$ or $|1\rangle$, respectively. $\Delta = \omega_0 - \omega_1$ is set by the strength of the electron-nuclear hyperfine interaction[12] (Appendix B.1). σ_z and I_z are the electronic and nuclear spin-$\frac{1}{2}$ operators, respectively. Note that we neglect the anisotropy of the hyperfine interaction (terms such as $A_\perp \sigma_z I_x$). While this interaction can create complex dynamics and can be used for qubit control[12,20], the effects can be minimized by applying strong magnetic fields ($\bar{\omega} \gg A_\perp$) and setting the interpulse delay τ to a multiple of the nuclear spin Larmor period $\tau_L = 2\pi/\omega_L$[14].

The RF pulses selectively drive nuclear spins, recoupling them to the electron-spin. In the interaction picture, the Hamiltonian during the RF pulses for a single nuclear spin is (in the rotating frame at the RF frequency ω_{RF}):

$$H_{\mathrm{RF}} = |0\rangle\langle 0| \otimes \Delta_0 I_z + |1\rangle\langle 1| \otimes \Delta_1 I_z + \mathbb{I} \otimes \Omega(\cos\phi I_x + \sin\phi I_y), \tag{4.2}$$

with $\Delta_0 = \omega_{\mathrm{RF}} - \omega_0$ and $\Delta_1 = \omega_{\mathrm{RF}} - \omega_1$ the detunings between the nuclear-spin transition frequencies and the RF frequency, ϕ the phase and Ω the Rabi frequency of the (bare) RF drive.

Because the frequencies Δ_0 and Δ_1 differ by Δ, an RF pulse will generally cause a different nuclear-spin evolution for the $|0\rangle$ and $|1\rangle$ electron states, enabling the construction of conditional two-qubit gates. Similarly, other spins with $\Delta_0', \Delta_1' \neq \Delta_0, \Delta_1$ undergo a different evolution, introducing an element of selectivity between different nuclear spins. Previous work[14] assumed that resonant RF driving ($\Delta_1 = 0$) combined with $\Delta_0 \gg \Omega$ resulted in negligible driving during the electron $|0\rangle$ state, thus neglecting that part of the driving term in H_{RF}. Below, we show that this term cannot generally be neglected due to the broad effective bandwidth of the short RF pulses (small τ) in the DDRF sequence.

To ensure that the DDRF sequence generates the desired gate, the phase of each RF pulse must be set so that the pulses result in a constructive build-up of rotations on the nuclear spin. This equates to following the phase evolution of the nuclear spin in the frame of the RF frequency. In the decoupling sequence, this is achieved by incrementing the phase of the next RF pulse by a phase-angle δ_ϕ every time a decoupling π-pulse is applied on the electron spin (Fig. 4.1b).

In one DDRF block ($N = 2$), the nuclear spin accumulates a total phase of $2\Delta_0\tau + 2\Delta_1\tau$ (up to a correction for the AC-Stark shift, see Appendix B.3). By adding a π phase shift with each decoupling pulse, the direction of the RF drive is inverted synchronous to the flipping of the electron spin state, creating a conditional electron-nuclear interaction. This gives rise to a resonance condition, satisfied by setting a single-pulse phase increment:

$$\delta_\phi = -(\Delta_0 + \Delta_1)\tau + \pi, \tag{4.3}$$

up to multiples of 2π. The dependence of the mean precession frequency during the gate, $(\Delta_0 + \Delta_1)/2$, on the electron-nuclear hyperfine interaction means that this resonance condition provides an additional mechanism for selectivity between different nuclear spins. Importantly, Eq. 4.3 constitutes a generalisation of the phase-increment resonance considered in previous work (restricted to $\Delta_1 = 0, \Delta_0 = \Delta$)[14].

To quantify the strength of the conditional interaction, we evaluate the unitary of the total DDRF sequence under the Hamiltonian in Eq. 4.2, setting the phase increment to Eq. 4.3. We assume that the rotation due to an individual RF pulse is small ($\Omega\tau \ll 1$), which is typical for DDRF gates, because the gate's total rotation angle is broken up into N pieces. In this limit, the evolution can be described by a conditional rotation V_{CROT} of the nuclear spin (Appendix B.10):

$$V_{\mathrm{CROT}} = |0\rangle\langle 0| \otimes R_x(N\tilde{\Omega}\tau) + |1\rangle\langle 1| \otimes R_x(-N\tilde{\Omega}\tau), \tag{4.4}$$

with an *effective* Rabi frequency given by:

$$\tilde{\Omega} = \Omega\left(\mathrm{sinc}(\Delta_1\tau) - \mathrm{sinc}(\Delta_0\tau)\right), \tag{4.5}$$

where $R_x(\theta) = e^{-i\theta I_x}$, with the x axis set by the phase of the first RF pulse and the sinc function is defined as: $\mathrm{sinc}(x) = \sin(x)/x$. Note that previous work neglected off-resonant driving, setting $\Delta_0\tau \gg 1$ and $\Delta_1 = 0$, so that Eq. 4.5 reduces to $\tilde{\Omega} = \Omega$ [14].

Setting $\tilde{\Omega}N\tau = \pi/2$ in Eq. 4.4 results in a fully entangling gate, equivalent to a CNOT up to single qubit rotations. Furthermore, Eq. 4.5 shows that such a gate can be constructed in the neighborhood of the ω_0 and ω_1 frequencies, over a bandwidth given by $\sim 1/\tau$ (see Figs. 4.1 c-e). Note that this can be understood as the result of evaluating the Fourier transform of an individual RF pulse (applied at ω_{rf}) at the nuclear-spin transitions ω_0 and ω_1, and that the bandwidth is much larger than would be expected from power broadening due to Ω.

In the next sections, we first experimentally verify Eqs. 4.3 and 4.5 by performing DDRF spectroscopy on a single NV center in diamond (Section 4.3). Then, we investigate the weak-coupling regime ($\Delta\tau \lesssim \pi$), for which Eq. 4.5 poses an inherent trade-off between effective interaction strength and electron decoherence (Section 4.4). Finally, we apply these findings to two applications: sensing a single nuclear spin (Section 4.5) and qubit control in a realistic nuclear spin quantum register (Sections 4.6 and 4.7).

4.3. GENERALISED DDRF SPECTROSCOPY

Even though all results in this work can be generalised to other electron-nuclear spin systems, in the following we will consider in particular the $m_s = \{0, -1\}$ electron-spin subspace of the NV center in diamond ($S = 1$) and its surrounding ^{13}C nuclear spins. The main difference with other electron spin systems is how Δ_0 and Δ_1 depend on the hyperfine coupling. See Beukers et al. [29] for experiments and simulation on an electron spin-1/2 system (the tin-vacancy center in diamond), for which the dependence of $\Delta_0 + \Delta_1$ vanishes up to second order corrections due to the perpendicular hyperfine component $A_\perp$ [20,30,31].

All experimental results are obtained from a single NV center in a natural abundance (1.1%) ^{13}C diamond sample at cryogenic temperatures (4 K), with a B_z = 189.1 mT magnetic field along the NV symmetry axis (Appendix 4.9). At this field, the nuclear quantisation axes are approximately parallel to the z-axis, and $A_\perp$ only contributes as a frequency shift (Appendix B.1).

To verify equations 4.3 and 4.5 experimentally, we perform nuclear spin spectroscopy using DDRF, by varying both the RF frequency and single-pulse phase increment δ_ϕ (Fig. 4.2a, similar to Fig. 4.1d). First the electron spin is initialized in a superposition. A drop in measured electron coherence after application of the DDRF gate indicates interaction between the electron spin and one or more nuclear spins.

We observe a number of traces that all follow the predicted resonance condition (Eq. 4.3). The spectrum shows isolated traces indicating interactions with single nuclear spins, and a broad band-like feature corresponding to a bath of weakly coupled spins. The measured data is well-recreated by a numerical simulation modelling 15 individual spins (see Table B.1), together with a statistically distributed spin bath of many weakly coupled spins (Fig 4.2b, see Appendix B.2 for simulation details).

Next, we show that the phase-increment condition (Eq. 4.3), together with the single-pulse bandwidth, enables the construction of electron-nuclear gates even if the RF driving frequency is far off resonance ($\Delta_1 \gg \Omega$). We perform such detuned gates on a single nuclear spin and compare them to an on-resonant gate applied to the same spin (Fig. 4.2c-e).

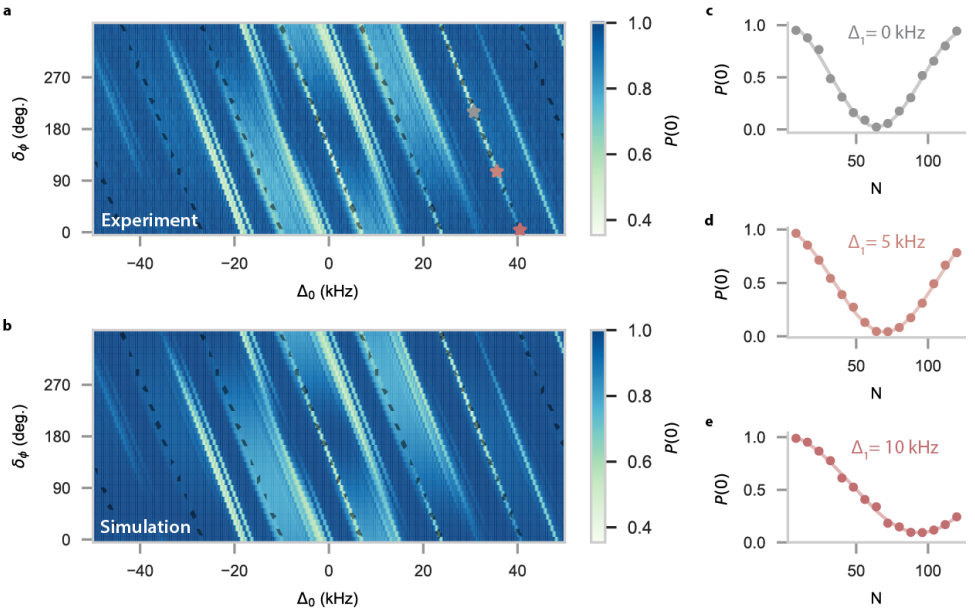

Figure 4.2: **Generalised DDRF spectroscopy. a)** Experimental data showing DDRF spectroscopy on the nuclear spin environment of an NV center, sweeping the RF frequency $\Delta_0 = \omega_{RF} - \omega_0$ and the phase update δ_ϕ (τ = 29.632us, $N = 24$, $\Omega = 356$ Hz). Single nuclear spins show up as descending diagonal lines following their frequency-phase resonance (Eq. 4.3), while the bath of weakly-coupled spins shows up as a band. The black dashed line indicates the resonance condition of a single spin (C_0, $\Delta = -30.7$kHz). Colored stars correspond to the parameters used for the data in (c). $P(0)$ corresponds to the remaining electron spin coherence (Appendix 4.9). **b)** Numerical calculation of the DDRF spectroscopy signal using the hyperfine couplings of 15 individual nuclear spins, and a statistical distribution for weakly coupled (bath) spins with $|\Delta| < 6$ kHz (Appendix B.2). **c-e)** Experimental demonstration of two-qubit gates with a detuned RF field ($N = 32, \Omega = 313$ Hz, $\Delta_1 = 5$, 10 kHz, $\tau = 24.654\mu$s), showing lower effective Rabi frequencies compared to resonant driving (grey data, $\Delta_1 = 0$ kHz).

All gates achieve near-unity contrast (up to some decay due to experimental noise), though the detuned version yields a reduced gate speed as predicted by Eq. 4.5. We further confirm the entangling nature of detuned gates by evaluating the process matrix obtained from numerical simulations (see Appendix B.3).

The discussion in this section shows that nuclear-spin resonance conditions are set by both the RF frequency and the single-pulse phase increment. Furthermore, quantum gates can be constructed even with significantly detuned driving frequencies by properly updating the pulse phases. This insight expands the parameter space from which gates and sensing sequences can be constructed, yielding additional possibilities for optimisation.

4.4. WEAK-COUPLING REGIME ($\Delta\tau \lesssim \pi$)

When the bandwidth related to the RF pulses ($\sim 1/\tau$) is larger than, or on the same order as the hyperfine splitting Δ, it is no longer valid to assume driving of only one of the nuclear spin transitions ω_1 and ω_0 (Fig. 4.3a, Eq. 4.2). In this readily encountered regime, rota-

tions for the electron $|0\rangle$ state can cancel (or add to) the rotations for the electron $|1\rangle$ state, reducing (or enhancing) the effective rotation.

We first consider the conditional gate (Eq. 4.4), for which the π phase shift in δ_ϕ inverts the RF rotation axis between subsequent pulses. In the limit of small $\Delta\tau$, $\tilde{\Omega}$ is strongly attenuated (Eq. 4.5), proportional to $(\Delta\tau)^{-2}$ for on-resonance addressing ($\Delta_1 = 0$), and proportional to $(\Delta\tau)^{-1}$ for the optimal driving condition discussed in the next section (see Fig. 4.4b). Additionally, the extrema of $\tilde{\Omega}$ shift away from the ω_1, ω_0 transitions (Fig. 4.3b and Eq. 4.9). This explains why the spectroscopy signals of weakly coupled spins ($\Delta \ll 1/\tau$) are suppressed and appear at detuned frequencies (broad features in Fig. 4.2a).

This analysis reveals an inherent trade-off present in DDRF gates. While a short interpulse delay τ improves the electron spin's coherence[15], it also reduces the effective Rabi frequency, thereby increasing the total gate duration $T = \pi/\tilde{\Omega}$ required for a $\pm\pi/2$ gate, or requiring an increase in Ω.

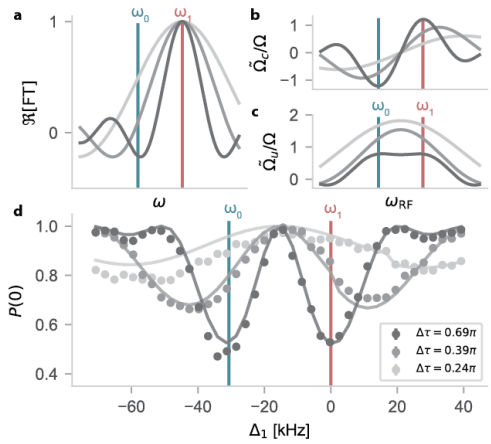

Figure 4.3: **Weak-coupling regime.** **a)** Schematic showing the Fourier transform of a single RF pulse (as in Fig. 4.1c) applied at $\omega_{RF} = \omega_1$, for $\Delta\tau \lesssim \pi$. As τ decreases, the pulse bandwidth increases, leading to the addressing of both the ω_1 and ω_0 transitions. **b)** The effective Rabi frequency $\tilde{\Omega}_c$ for a conditional gate (as a function of ω_{RF}) is enhanced or suppressed when both transitions are addressed (Eq. 4.5). **c)** Same as in (b), but for an unconditional gate (Eq. 4.7). **d)** Experimental spectroscopy data as in Fig. 4.2a confirming the effective Rabi frequency for conditional gates for various $\Delta\tau$ (fixing the gate time $2N\tau \approx 1.4$ ms, $\Omega = 313$ Hz). Here, δ_ϕ is set to track the phase increment resonance condition of a single nuclear spin ($C_0, \Delta = -30.7$ kHz, black dashed line in Fig. 4.2a). Shorter τ leads to a contrast reduction and a shift of the optimal RF frequency. The analytical prediction (solid grey lines), using no free parameters, is calculated using $P(0) = 1/2\,(1 + \cos 2\tilde{\Omega} N\tau)$, with $\tilde{\Omega}$ taken from (b). We attribute the model-data discrepancy to the specifics of the RF pulse envelope shape and variable RF transmission, which have not been taken into account (Appendix 4.9)

We experimentally validate Eq. 4.5 by driving nuclear spin C_0 at different RF frequencies, while updating the RF phases according to Eq. 4.3 (Fig. 4.3d). This amounts to tracking the nuclear resonance condition apparent in Fig. 4.2a. Such a measurement directly yields the spectral signature of the reduced Rabi frequency, which is in good agreement with Eq. 4.5.

We repeat this measurement for different RF pulse durations τ, keeping the RF amplitude ($\Omega = 313$ Hz at ω_1) and the total DDRF driving time (≈ 1.4 ms) fixed using N. For shorter τ a decrease in signal contrast and a shift of the optimal RF frequency can be observed, as

predicted by Eq. 4.5.

The DDRF gate can also be used to perform an unconditional rotation of the nuclear spin, by leaving out the π phase shift from δ_ϕ (Eq. 4.3)[14]. The DDRF gate unitary then becomes

$$V_{\mathrm{ROT}} = \mathbb{I} \otimes R_x(N\Omega_u\tau)\,, \tag{4.6}$$

with effective (unconditional) Rabi frequency:

$$\tilde{\Omega}_u = \Omega\left(\mathrm{sinc}(\Delta_1\,\tau) + \mathrm{sinc}(\Delta_0\,\tau)\right)\,. \tag{4.7}$$

In contrast to the conditional case, $\tilde{\Omega}_u$ is enhanced at small $\Delta\tau$ (Fig. 4.3c), as without the extra π phase shift the RF rotations build up constructively. In the limit $\Delta \ll 1/(2\tau)$ the effective Rabi frequency Ω_u approaches 2Ω, identical to constant RF driving of a nuclear-spin transition while keeping the electron spin in an eigenstate[4].

We identify three approaches for mitigating the reduced Rabi frequency for conditional gates. First, for a fixed gate length $2N\tau$, the number of decoupling pulses N can be traded for RF pulse length ($\approx 2\tau$), shrinking the pulse bandwidth to avoid driving both transitions. This comes at the cost of decreasing effectiveness of the electron decoupling, as longer interpulse delays protect less effectively against low-frequency noise[15]. Second, given a certain pulse length, the RF frequency can be detuned to maximise Eq. 4.5. Third, one could increase the physical RF amplitude to compensate for the reduction in Rabi frequency, although this poses experimental challenges, and our model validity is constrained to $\Omega\tau \ll 1$. The next sections explore these approaches in more detail, in the context of nuclear-spin sensing and multi-qubit control.

4.5. OPTIMAL SENSITIVITY FOR SENSING A SINGLE NUCLEAR SPIN

To highlight the practical significance of the presented insights, we demonstrate how to optimise the DDRF sequence for sensing a single, weakly coupled nuclear spin (with hyperfine coupling Δ). For example, this nuclear spin could be a single proton or ^{13}C spin, potentially outside of the host crystal[32]. The goal is to minimise the (single-spin) sensitivity, defined as[33](Appendix B.4):

$$\nu_{\mathrm{min}} = \frac{2\pi e^{\chi(N,t)}}{\tilde{\Omega}_{\mathrm{max}}(\Delta, N, t)\sqrt{t}}\,, \tag{4.8}$$

where $\chi(N,t)$ is the sensor decoherence function (here taken from the experimental observations of Ref.[15]), $\tilde{\Omega}_{\mathrm{max}}$ is the maximum attainable effective Rabi frequency (given Δ and N), and $t = 2N\tau$ is the single-experiment sensing time[33]. For simplicity, we assume unity readout contrast and zero sensor overhead (Appendix B.4).

The expression for ν_{min} in Eq. 4.8 conveys the minimum number of nuclear spins required that together yield a detectable signal in 1 s of integration time. Evidently, to achieve single-spin sensitivity ($\nu_{\mathrm{min}} < 1$), the *effective* Rabi frequency $\tilde{\Omega}$, which sets the effective coupling to the signal, should be as large as possible, while retaining sufficient electron coherence ($e^{-\chi(N,t)}$). The choice of N presents us with an inherent trade-off between these two factors. Generally, larger N (shorter τ-values) increase the electron coherence, but decrease $\tilde{\Omega}_{\mathrm{max}}$ (see Sec. 4.4). However, optimising over the large parameter space is challenging.

We first reduce the parameter space size by calculating the RF detuning that maximises $\tilde{\Omega}$. For $\Delta \gtrsim 2\pi/\tau$, the RF driving when the electron in in the $|0\rangle$ state can be neglected

and the optimal effective Rabi frequency is always attained when driving on resonance ($\Delta_1 = 0$). However, when $\Delta \lesssim 2\pi/\tau$, significant enhancement is possible by detuning the RF frequency. We find that the optimum setting for Δ_1 is (approximately) given by (Appendix B.5):

$$\Delta_1 = \begin{cases} -\frac{w_s}{\tau} + \Delta/2, & \text{if } \tau \lesssim 2\pi/|\Delta|. \\ 0, & \text{otherwise.} \end{cases} \tag{4.9}$$

where $w_s \approx 2.082$ is the first root of the second derivative of the sinc function. Conceptually, this condition is satisfied when the detuning is such that the gradient of the RF pulse envelope is maximal in between the ω_0 and ω_1 transitions (Fig. 4.4a). While for $\Delta_1 = 0$, $\tilde{\Omega} \propto (\Delta\tau)^2$, using the optimum Δ_1 changes the scaling to $\tilde{\Omega} \propto \Delta\tau$ (Fig. 4.4b). We verify that Eq. 4.9 maximises Eq. 4.5 in the small Δ regime (Appendix B.5).

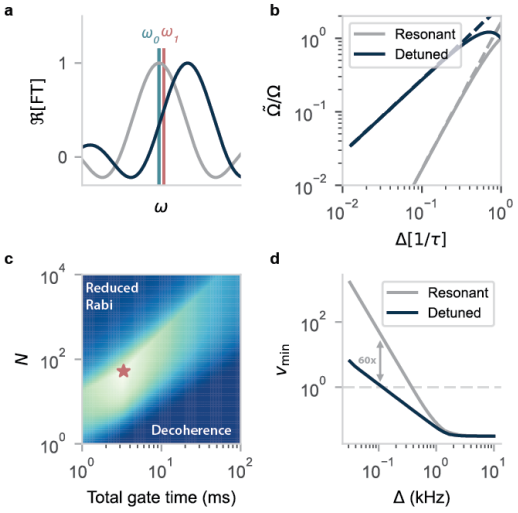

Figure 4.4: **Optimised detuned sensing. a)** Schematic illustrating maximum DDRF contrast if the ω_0 and ω_1 transitions are on the slope of the RF pulse envelope. **b)** Numerical calculation of the Rabi frequency suppression as a function of $\Delta\tau$ for $\Delta < \tau$. When driving on resonance, $\tilde{\Omega} \propto (\Delta\tau)^2$, however by using the optimal detuning (Eq. 4.9) $\tilde{\Omega} \propto \Delta\tau$ (scaling indicated by dashed lines). The effective Rabi frequency can thus be much improved when purposefully driving off-resonance. **c)** Inverse sensitivity (ν_{min}^{-1}), varying the number of pulses N and total sequence time t. Short inter-pulse spacing τ (corresponding to short t and high N) leads to the driving of both transitions, while long τ (i.e. using low N) leads to electron decoherence. The red star denotes the optimal parameters. **d)** Detuned sensing achieves orders of magnitude higher sensitivity, still allowing for single-spin sensitivity (grey dotted line) for small Δ.

Next, we evaluate the optimal RF amplitude. For the situation of a very weakly coupled spin, the reduced Rabi frequency can be partially compensated for by increasing the physical RF amplitude Ω. However, simply setting the RF amplitude to the inverse of $\tilde{\Omega}/\Omega$ leads to unrealistically high values when $\tau \ll 2\pi/\Delta$. Moreover, our model of the effective Rabi frequency strictly only holds for $\Omega\tau \ll 1$. Therefore, in the current analysis, we set an upper bound for the RF amplitude: $\Omega < 1/(2\tau)$. Additionally, we limit the maximum value to

$\Omega < 10\,\text{kHz}$, as higher Rabi frequencies are typically challenging to reach without specialised RF transmitters, especially at cryogenic temperatures[34,35].

Then, to find the optimal sensing parameters, we evaluate (the inverse of) Eq. 4.8, sweeping the number of pulses N and total sequence time $t = 2N\tau$, while continuously updating the RF detuning and RF amplitude to maximise $\tilde{\Omega}$ (Fig. 4.4c and Appendix B.6). As expected, there exists an optimal regime that balances the expected reduction in Rabi frequency and electron decoherence (bright sliver in Fig. 4.4c). We compare the sensitivity of the (conventional) resonant gate with the detuned protocol by extracting the optimal value for various Δ (Fig. 4.4d) and find that the latter outperforms the former for small Δ. A divergence between the two can be observed at $\Delta/(2\pi) \sim 1/T_2 \approx 1$ kHz, with the detuned protocol still achieving single-spin sensitivity at a mere 115 Hz hyperfine coupling, a performance enhancement by a factor 60. Conversely, a statistically polarised ensemble of 100 ^{13}C spins would be detectable from a distance of ~ 26 nm, compared to ~ 6 nm for the resonant protocol (assuming the spin coherence of Ref. [15] continues to hold).

4

4.6. QUANTUM GATE SELECTIVITY

Finally, we consider the use of the DDRF gate sequence for qubit control[9,14,21]. The challenge is to realise a high-fidelity (two-qubit) gate on a selected nuclear spin, while avoiding crosstalk to other spins. First, we consider the selectivity of the gates starting from the above results (Eqs. 1-5). In the next section, we simulate a realistic spin register and identify the parameter regime(s) in which high fidelity gates are possible.

We identify two selectivity mechanisms for the DDRF gate: selective driving due to the limited bandwidth of a single RF pulse (Fig. 4.5a), and the constructive build-up of small rotations due to the phase-increment condition being met for a specific nuclear spin (Fig. 4.5b). Selective control can be achieved through either mechanism, or through a combination thereof (see e.g. Fig. 4.5c and d). To quantitatively study these mechanisms, we consider a target nuclear spin qubit t, and a second, bystander, nuclear spin b for which crosstalk is to be avoided.

For the selectivity stemming from the individual RF pulses, Eq. 4.5 can directly be used to yield the smallest difference in nuclear-spin transitions for which $\tilde{\Omega}_b = 0$:

$$\left|\Delta^t_{0/1} - \Delta^b_{0/1}\right| \gtrsim \frac{\pi}{\tau}, \tag{4.10}$$

where the superscript t and b are used to denote the target and bystander spins, respectively, and difference between either the Δ_0 or Δ_1 frequency must be large enough. Evidently, the selectivity stemming from the RF pulses is limited by their bandwidth ($\sim 1/\tau$). For the NV electron spin-1 system considered here, the minimum difference between nuclear-spin hyperfine couplings required for achieving selectivity within a single RF pulse is

$$\left|A^t_\parallel - A^b_\parallel\right| \gtrsim \frac{\pi}{\tau}. \tag{4.11}$$

Next, to describe the selectivity due to the phase increments, it is instructive to realise that the phase increments effectively modulate the bare RF frequency (also known as 'phase ramping'[36]), so that we can define a phase-increment frequency:

$$\omega_\phi = \omega_{\text{RF}} + \frac{\delta_\phi}{2\tau}. \tag{4.12}$$

We can then rewrite the phase-increment resonance condition (Eq. 4.3) as:

$$\omega_\phi = \bar{\omega} + \frac{(2k+1)\pi}{2\tau}, \tag{4.13}$$

with $k \in \mathbb{N}$. Here, selectivity arises due to the difference in the mean frequencies $\bar{\omega}$ of the target and bystander spins, which has to be large enough for selective control.

A lower bound on the mean frequency difference can be attained by considering the Fourier-limited frequency resolution of the phase ramp (determined by its length $\sim 1/(2N\tau)$):

$$\left|\left(\bar{\omega}^{\mathrm{t}} \mod \frac{\pi}{\tau}\right) - \left(\bar{\omega}^{\mathrm{b}} \mod \frac{\pi}{\tau}\right)\right| \gtrsim \frac{\pi}{N\tau}, \tag{4.14}$$

where the modulo stems from the π/τ periodicity in Eq. 4.13. Although Eq. 4.14 strictly speaking constitutes an upper bound to the selectivity, it allows for a potential selectivity enhancement by a factor N compared to Eq. 4.10. Whether such an enhancement is possible in practice depends on the the spectrum of $\bar{\omega}$ for the electron-nuclear spin system of interest. For example, for a spin-1/2 defect spin, the left-hand side of Eq. 4.14 vanishes, up to second order corrections due to the perpendicular hyperfine component $A_\perp$ [29–31].

For the spin-1 system considered here, an exact bound for the selectivity can be derived, under the assumption of negligible driving in the electron $|0\rangle$ state (Appendix B.7). In particular, fixing $\Omega N\tau = \pi/2$ to create a fully entangling gate, the condition for a selective gate on the target spin is given by:

$$\left|\left(\frac{A_\parallel^t}{2} \mod \frac{\pi}{\tau}\right) - \left(\frac{A_\parallel^b}{2} \mod \frac{\pi}{\tau}\right)\right| \gtrsim \frac{\sqrt{15}\pi}{4N\tau}. \tag{4.15}$$

To illustrate the selectivity mechanisms, we again perform DDRF spectroscopy (similar to Fig. 4.2a), but instead of δ_ϕ, we now plot the data as a function of $\omega_\phi - \pi/(2\tau)$ (Fig. 4.5c, d). This is a useful quantity as it is independent of the RF frequency, and directly relates to a spin's mean frequency. Spins appear at their $\bar{\omega}$ frequency along the ω_ϕ axis (mod π/τ), with their signal intensity modulated by the effective Rabi frequency (Eq. 4.5), which varies with Δ_0 (x-axis). The signal from the spin bath (slanted band-like features) is pushed away from $\Delta_0 = 0$ due to the form of Eq. 4.5 in the weak-coupling regime (section 4.4).

The widths of the spin response along both axes partly determine if the spin can be selectively controlled or overlaps with other spins (crosstalk), as given in equations 4.11 and 4.15. The $\frac{\pi}{\tau}$ periodicity of ω_ϕ creates opportunities for unexpected crosstalk to occur. For example, both the ω_0 and ω_1 transition of nuclear spin C_1 ($\Delta = -45.9$ kHz, Table B.1), somewhat overlap with sidelobes of the spin bath, limiting the expected gate fidelity of that spin for these gate parameters. In contrast, the transitions of spin C_0 ($\Delta = -30.7$ kHz, Table B.1) is not affected by such crosstalk, due to the particular value of τ used here. Note that for electron spin-1/2 systems, all nuclear spins will appear at approximately $\omega_\phi - \pi/(2\tau) = \omega_{\mathrm{L}}$ (up to second order corrections due to $A_\perp$), so that selective control depends more on whether spins can be resolved along the Δ_0-axis [29].

4.7. A MULTI-QUBIT NUCLEAR-SPIN REGISTER

We apply the insights from the previous section to investigate the boundaries of the gate parameter space that allows for high-fidelity control in a multi-qubit nuclear-spin system.

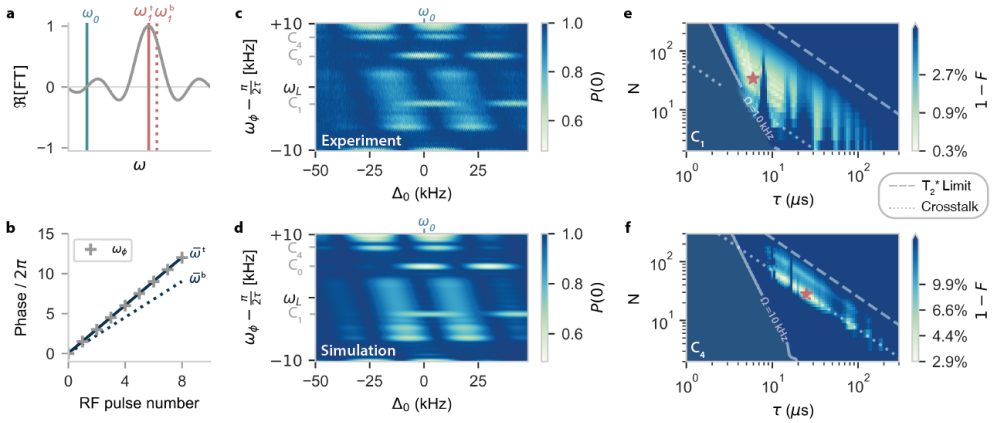

Figure 4.5: **Quantum gate selectivity. a)** Schematic as in Fig. 4.1c. Due to their high bandwidth, single RF pulses may drive transitions of bystander spins (ω_1^b, dotted line), potentially inducing crosstalk (Eq. 4.10). **b)** Schematic showing the phase build-up for the target spin (solid blue line) and the bystander spin (dotted blue line). The target spin can be selectively addressed by implementing the appropriate phase increment (grey crosses, Eq. 4.3, for clarity plotted without the extra π increments). **c)** Experimental spectroscopy data as in Fig. 4.2a, with different $\tau = 24.654\,\mu$s. Plotting the data as a function of the phase-increment frequency ω_ϕ (Eq. 4.12) and Δ_0 highlights the different selectivity mechanisms. Nuclear spins appear at $\omega_\phi - \pi/(2\tau) = \bar{\omega}$ (linewidth $\sim (2N\tau)^{-1}$), modulated along the Δ_0 ($\propto \omega_{\mathrm{RF}}$) axis by their effective Rabi frequency (C_0, C_1 and C_4 resonances annotated).The bandwidth of the y-axis (here ~ 20 kHz) is set by the π/τ periodicity of Δ_ϕ, resulting in aliases that can cause spins to overlap. Jagged artifacts are due to the limited resolution of the data (taken as a function of δ_ϕ). **d)** Simulation of (c) (Appendix B.2). **e)** Numerical simulation of the maximum attainable DDRF gate fidelity for nuclear spin C_1 in a 6-spin register (including C_0, C_1, C_4, C_6, C_8, see Table B.1). The fidelity is calculated for the full 6-qubit unitary (red star denotes optimal parameters). The dotted line indicates $2N\tau = 131\,\mu$s, the minimum gate time that satisfies the selectivity bound (Eq. 4.15). The dashed line indicates $2N\tau = 5$ ms, corresponding to the limit on gate time imposed by nuclear spin T_2^*. The color bar has logarithmic spacing. **f)** Simulation for C_4, a more weakly coupled and spectrally crowded spin, resulting in lower fidelities. Here the dotted line indicates $2N\tau = 1.4$ ms.

Considering the 15 identified spins near this NV center (Table B.1), we select a register of 5 nuclear spins that are most isolated in frequency space (Appendix B.8).

For a register with M nuclear spins, the ideal operation is given by:

$$U_{\mathrm{t}} = \mathrm{CR_x}(\pm\pi/2) \otimes \mathbb{I}^{\otimes(M-1)}, \tag{4.16}$$

where the controlled rotation acts on the electron and target spin subspace.

In addition to the unitary evolution of the 6-qubit register dictated by H_{RF} (Eq. 4.2), we include three additional contributions to the infidelity (Appendix B.8): (i) the electron-spin T_2 dephasing time under dynamical decoupling (phenomenological, taken from Abobeih et al.[15]). (ii) Electron-spin dephasing due to the direct interaction (Eq. 4.2) with the characterised nuclear spins outside the register, and the nuclear spin bath (in a mixed state). (iii) $T_2^\star$ dephasing (≈ 10 ms[14]) of the nuclear spins in the register, simulated as quasi-static magnetic field noise. As is commonly done in experimental settings, we introduce a post-gate echo pulse on the register spins to partially mitigate this dephasing[14,21]. Additionally, we restrict the RF amplitude to a maximum value of $\Omega = 10$ kHz (as in section 4.5).

To identify optimal gate parameters, we vary the interpulse delay τ and the number of

pulses N, while ensuring the RF amplitude Ω is set to create the desired $\pm\pi/2$ rotation (compensating for the reduction in effective Rabi frequency using Eq. 4.5). We set ω_{RF} to the target spin's ω_1 transition and calculate δ_ϕ accordingly (Eq. 4.3), applying a second-order correction due to the AC-Stark shift (Appendix B.3).

We obtain (6-qubit) average gate fidelity maps[37], such as presented in Fig. 4.5e and f, for target nuclear spins C_1 and C_4, respectively (Table B.1). We identify the following bounds on the available parameter space for high-quality gates. First, the maximum gate time is limited by nuclear- and electron-spin decoherence, the latter of which depends on N and τ. A minimum gate time is dictated by the degree of spectral crowding of the target spin, as predicted by Eq. 4.14. Contrary to C_1, C_4 is spectrally close to another spin (C_3, ~ 1.4 kHz), so that high-fidelity gates are only found for larger gate times ($2N\tau \gtrsim 1.4$ ms). In particular, through the definition of the selectivity (Appendix B.7), equalising Eq. 4.15 (dotted line in Fig. 4.5f) ensures zero crosstalk with the nearest bystander spin (C_3).

Furthermore, even though the reduction in effective Rabi frequency $\tilde{\Omega}$ can in principle be fully compensated for, when $\Omega \sim \Delta$, the assumptions underlying Eq. 4.5 break down (Appendix B.10), and our prediction for the optimal gate parameters no longer produces high-fidelity gates (top left corner of Figs. 4.5e and f). For spins with smaller hyperfine couplings (e.g. C_4), this effect is more detrimental to the maximum attainable fidelity. Finally, the remaining parameter space is interspersed with sharp drops in fidelity at τ-values for which crosstalk occurs with other individual spins, or with the nuclear spin bath. The combination of these effects results in maximimum 6-qubit gate fidelities of $F = 99.7\%$ and $F = 97.1\%$ for target spins C_1 and C_4, respectively. See Appendix B.8 for the other register spins, and breakdowns of the different infidelity contributions.

Note that here we did not optimize ω_{RF}, which could further reduce crosstalk and realize improved effective Rabi frequencies (see section 4.5).

4.8. CONCLUSIONS

In conclusion, we presented an improved, and generalised framework for electron-nuclear DDRF gates. Our model reveals that these gates can be deconstructed into two independent components: (1) the driving induced by individual RF pulses (Eq. 4.5) and (2) the RF phase increments that enable constructive rotational build-up throughout the sequence (Eq. 4.3). Considering these components independently allows for increased versatility in gate optimisation for sensing and quantum control (e.g. by detuning the RF frequency), but also reveals inherent limitations in gate speed and selectivity.

A first, general, insight is that the *effective* Rabi frequency for short interpulse delays ($\Delta\tau \lesssim \pi$) can be strongly suppressed for conditional gates and enhanced for unconditional gates. This reveals an inherent trade-off between protecting electron spin coherence by faster decoupling, and retaining nuclear spin selectivity and gate efficiency. This trade-off has important implications for the sensing and control of nuclear spins, including in typical physical systems, such as for an electron spin in a dilute nuclear spin bath[5,7,21,23,30]. The presented detuned sensing scheme partially compensates for this reduction in Rabi frequency, making DDRF a promising alternative to conventional dynamical-decoupling spectroscopy in the context of nano-NMR[12,18,38]. Future work might extend this principle to high-fidelity quantum gates.

A second key insight is that quantum gate selectivity stems both from direct RF driving of the spin transition frequencies, as well as the targeting of the mean spin evolution frequency by the phase increments. Importantly, for systems in which the mean nuclear-spin frequencies are first-order degenerate (e.g. electronic spin-1/2 systems), the RF pulses can provide the main selectivity mechanism, albeit limited by their bandwidth[29]. A possible mitigation strategy is to create intermediate evolution periods with a nuclear-spin frequency that is dependent on the electron-spin state, for example by temporarily swapping the electron-spin state to a memory qubit[29].

These results provide new opportunities for the optimisation of quantum gate fidelities for quantum information and quantum network applications[2,9,21,39,40]. They are applicable to a large variety systems, such as various spin defects in diamond[29,30], silicon[25] and silicon-carbide[23,41], and might also be transferable to other platforms such as quantum dots[42] and rare-earth ions[43].

4.9. METHODS

SAMPLE AND SETUP

All experiments are conducted on a naturally occurring NV center using a custom-built cryogenic confocal microscopy setup (4K, Montana Cryostation). The diamond sample, which has a natural abundance of 1.1% ^{13}C, was homoepitaxially grown via chemical vapor deposition (Element Six) and cleaved along the ⟨111⟩ crystal direction. A solid immersion lens (SIL) is milled around the NV center to improve photon collection efficiency[44].

A gold stripline is deposited near the edge of the SIL for the application of microwave (MW) and radio-frequency (RF) pulses. Typical nuclear Rabi frequencies can reach up to ~ 1.6 kHz, above which sample heating starts to affect the NV readout. MW and RF signals are generated by a ZI HDAWG Arbitrary Waveform Generator, in combination with a MW mixer and separate RF and MW amplifiers. An external magnetic field of $B_z = 189.1$ mT is applied along the NV-symmetry axis, using a permanent neodymium magnet mounted to the back of the cryostat cold finger. An external permanent magnet is used for fine alignment of the magnetic field, the small remaining perpendicular magnetic field components are neglected here.

The NV spin state is initialized via spin-pumping and read out in a single shot through spin-selective resonant excitation, with fidelities $F_0 = 0.930(3)$ ($F_1 = 0.995(1)$) for the $m_s = 0$ ($m_s = -1$) state, respectively, resulting in an average fidelity of $F_{\text{avg}} = 0.963(3)$. Reported data is corrected for these numbers to obtain a best estimate of the electronic spin state. We drive the electronic $m_s = 0 \leftrightarrow m_s = -1$ spin transition at 2.425 GHz with Hermite-shaped pulses.

PULSE SEQUENCES

In this work, XY-8 type sequences are used for dynamical decoupling during the DDRF gate, to minimize the effects of pulse errors[15]. The length of RF pulses in the DDRF sequences in this work are set to an integer number of periods of the RF radiation, to prevent the NV electron spin from picking up extra phase. Each RF pulse has a $\sin^2(t)$ roll-on and roll-off to prevent signal ringing in the RF signal chain, with a roll-duration of two RF periods. Due to this pulse shaping, the two RF pulses of length τ in the DDRF sequence create a smaller combined rotation than the RF pulses of length 2τ. To correct for this, the amplitude of the single-τ pulses is multiplied by the ratio of the integrals of the 2τ pulse and the two single-τ pulses.

DDRF SPECTROSCOPY

DDRF spectroscopy (Figs. 4.2,4.3 and 4.5c) is performed by (i) preparing the electron spin in the $m_s = 0$ state; (ii) applying a $\pi/2$ MW pulse on the electron spin to prepare the $|+\rangle$ state; (iii) Performing the DDRF sequence; (iv) applying a $-\pi/2$ MW pulse (same axis as the initial $-\pi/2$ pulse); (v) reading out the electron spin state. The experiment is repeated to estimate $P(0)$, the probability to find the electron in the $m_s = 0$ state. $P(0)$ corresponds to the remaining electron spin coherence after the DDRF sequence.

REFERENCES

[1] I. Lovchinsky *et al.*, *Nuclear magnetic resonance detection and spectroscopy of single proteins using quantum logic,* Science **351**, 836 (2016).

[2] M. Pompili *et al.*, *Realization of a multinode quantum network of remote solid-state qubits,* Science **372**, 259 (2021).

[3] M. H. Abobeih *et al.*, *Atomic-scale imaging of a 27-nuclear-spin cluster using a quantum sensor,* Nature **576**, 411 (2019).

[4] J. Randall *et al.*, *Many-body–localized discrete time crystal with a programmable spin-based quantum simulator,* Science **374**, 1474 (2021).

[5] K. S. Cujia, K. Herb, J. Zopes, J. M. Abendroth and C. L. Degen, *Parallel detection and spatial mapping of large nuclear spin clusters,* Nat Commun **13**, 1260 (2022).

[6] R. Budakian *et al.*, *Roadmap on nanoscale magnetic resonance imaging,* Nanotechnology **35**, 412001 (2024).

[7] G. L. Van De Stolpe *et al.*, *Mapping a 50-spin-qubit network through correlated sensing,* Nat Commun **15**, 2006 (2024).

[8] T. Xie *et al.*, *99.92%-Fidelity cnot Gates in Solids by Noise Filtering,* Phys. Rev. Lett. **130**, 030601 (2023).

[9] H. P. Bartling *et al.*, *Universal high-fidelity quantum gates for spin-qubits in diamond,* (2024), arXiv:2403.10633 [cond-mat, physics:quant-ph] .

[10] P. C. Humphreys *et al.*, *Deterministic delivery of remote entanglement on a quantum network,* Nature **558**, 268 (2018).

[11] S. L. N. Hermans *et al.*, *Qubit teleportation between non-neighbouring nodes in a quantum network,* Nature **605**, 663 (2022).

[12] T. H. Taminiau *et al.*, *Detection and Control of Individual Nuclear Spins Using a Weakly Coupled Electron Spin,* Phys. Rev. Lett. **109**, 137602 (2012).

[13] T. van der Sar *et al.*, *Decoherence-protected quantum gates for a hybrid solid-state spin register,* Nature **484**, 82 (2012).

[14] C. E. Bradley *et al.*, *A Ten-Qubit Solid-State Spin Register with Quantum Memory up to One Minute,* Phys. Rev. X **9**, 031045 (2019).

[15] M. H. Abobeih *et al.*, *One-second coherence for a single electron spin coupled to a multi-qubit nuclear-spin environment,* Nat Commun **9**, 2552 (2018).

[16] H. P. Bartling *et al.*, *Entanglement of Spin-Pair Qubits with Intrinsic Dephasing Times Exceeding a Minute,* Phys. Rev. X **12**, 011048 (2022).

[17] I. Schwartz *et al.*, *Robust optical polarization of nuclear spin baths using Hamiltonian engineering of nitrogen-vacancy center quantum dynamics,* Sci. Adv. **4**, eaat8978 (2018).

[18] T. Staudacher *et al.*, *Nuclear Magnetic Resonance Spectroscopy on a (5-Nanometer)* ^{3} *Sample Volume,* Science **339**, 561 (2013).

[19] K. S. Cujia, J. M. Boss, K. Herb, J. Zopes and C. L. Degen, *Tracking the precession of single nuclear spins by weak measurements,* Nature **571**, 230 (2019).

[20] T. H. Taminiau, J. Cramer, T. van der Sar, V. V. Dobrovitski and R. Hanson, *Universal control and error correction in multi-qubit spin registers in diamond,* Nat. Nanotechnol. **9**, 171 (2014).

[21] M. H. Abobeih *et al.*, *Fault-tolerant operation of a logical qubit in a diamond quantum processor,* Nature **606**, 884 (2022).

[22] S. K. Parthasarathy *et al.*, *Scalable Quantum Memory Nodes Using Nuclear Spins in Silicon Carbide,* Phys. Rev. Applied **19**, 034026 (2023).

[23] C. Babin *et al.*, *Fabrication and nanophotonic waveguide integration of silicon carbide colour centres with preserved spin-optical coherence,* Nat. Mater. **21**, 67 (2022).

[24] M. T. Uysal *et al.*, *Coherent Control of a Nuclear Spin via Interactions with a Rare-Earth Ion in the Solid State,* PRX Quantum **4**, 010323 (2023).

[25] D. B. Higginbottom *et al.*, *Optical observation of single spins in silicon,* Nature **607**, 266 (2022).

[26] R. Debroux *et al.*, *Quantum Control of the Tin-Vacancy Spin Qubit in Diamond,* Phys. Rev. X **11**, 041041 (2021).

[27] A. Sipahigil *et al.*, *An integrated diamond nanophotonics platform for quantum-optical networks,* Science **358**, 847 (2016).

[28] W.-R. Hannes, R. Finsterhoelzl and G. Burkard, *Fidelity of photon-mediated entanglement between remote nuclear-spin multi-qubit registers,* (2024), arXiv:2401.06705 [cond-mat, physics:quant-ph] .

[29] H. K. C. Beukers *et al.*, *Control of solid-state nuclear spin qubits using an electron spin-1/2,* (2024), arXiv:2409.08977 [quant-ph] .

[30] C. T. Nguyen *et al.*, *Quantum Network Nodes Based on Diamond Qubits with an Efficient Nanophotonic Interface,* Phys. Rev. Lett. **123**, 183602 (2019).

[31] M. Zahedian, V. Vorobyov and J. Wrachtrup, *Blueprint for efficient nuclear spin characterization with color centers,* Phys. Rev. B **109**, 214111 (2024).

[32] I. Schwartz *et al.*, *Blueprint for nanoscale NMR,* Sci Rep **9**, 6938 (2019).

[33] C. L. Degen, F. Reinhard and P. Cappellaro, *Quantum sensing,* Rev. Mod. Phys. **89**, 035002 (2017).

[34] K. Herb, J. Zopes, K. S. Cujia and C. L. Degen, *Broadband radio-frequency transmitter for fast nuclear spin control,* Rev Sci Instrum. **91**, 113106 (2020).

[35] D. Yudilevich *et al.*, *Coherent manipulation of nuclear spins in the strong driving regime,* New J. Phys. **25**, 113042 (2023).

[36] L. M. K. Vandersypen and I. L. Chuang, *NMR techniques for quantum control and computation,* Rev. Mod. Phys. **76**, 1037 (2005).

[37] M. A. Nielsen, *A simple formula for the average gate fidelity of a quantum dynamical operation,* Physics Letters A **303**, 249 (2002).

[38] H. J. Mamin *et al.*, *Nanoscale Nuclear Magnetic Resonance with a Nitrogen-Vacancy Spin Sensor,* Science **339**, 557 (2013).

[39] C. E. Bradley *et al.*, *Robust quantum-network memory based on spin qubits in isotopically engineered diamond,* npj Quantum Inf **8**, 122 (2022).

[40] S. De Bone, P. Möller, C. E. Bradley, T. H. Taminiau and D. Elkouss, *Thresholds for the distributed surface code in the presence of memory decoherence,* AVS Quantum Sci. **6**, 033801 (2024).

[41] A. Bourassa *et al.*, *Entanglement and control of single nuclear spins in isotopically engineered silicon carbide,* Nat. Mater. **19**, 1319 (2020).

[42] B. Hensen *et al.*, *A silicon quantum-dot-coupled nuclear spin qubit,* Nat. Nanotechnol. **15**, 13 (2020).

[43] A. Ruskuc, C.-J. Wu, J. Rochman, J. Choi and A. Faraon, *Nuclear spin-wave quantum register for a solid-state qubit,* Nature **602**, 408 (2022).

[44] L. Robledo *et al.*, *High-fidelity projective read-out of a solid-state spin quantum register,* Nature **477**, 574 (2011).

5

MAPPING A 50-SPIN-QUBIT NETWORK THROUGH CORRELATED SENSING

G.L. van de Stolpe, D. P. Kwiatkowski, C.E. Bradley, J. Randall, M.H. Abobeih, S. A. Breitweiser, L. C. Bassett, M. Markham, D.J. Twitchen,T.H. Taminiau

Spins associated to optically accessible solid-state defects have emerged as a versatile platform for exploring quantum simulation, quantum sensing and quantum communication. Pioneering experiments have shown the sensing, imaging, and control of multiple nuclear spins surrounding a single electron-spin defect. However, the accessible size of these spin networks has been constrained by the spectral resolution of current methods. Here, we map a network of 50 coupled spins through high-resolution correlated sensing schemes, using a single nitrogen-vacancy center in diamond. We develop concatenated double-resonance sequences that identify spin-chains through the network. These chains reveal the characteristic spin frequencies and their interconnections with high spectral resolution, and can be fused together to map out the network. Our results provide new opportunities for quantum simulations by increasing the number of available spin qubits. Additionally, our methods might find applications in nano-scale imaging of complex spin systems external to the host crystal.

The results of this chapter have been published in *Nat Commun* **15**, 2006 (2024)

5.1. INTRODUCTION

Optically interfaced spin qubits associated to defects in solids provide a versatile platform for quantum simulation [1], quantum networks [2,3] and quantum sensing [4–6]. Various systems are being explored [7], including defects in diamond [1–3,8,9], silicon carbide [10,11], silicon [12,13], hexagonal boron nitride (hBN) [14], and rare-earth ions [15]. The defect electron spin provides a qubit with high-fidelity control, optical initialization and readout, and a (long-range) photonic quantum network interface [2,3]. Additionally, the electron spin can be used to sense and control multiple nuclear spins surrounding the defect [15–17]. This additional network of coupled spins provides a qubit register for quantum information processing, as well as a test bed for nanoscale magnetic resonance imaging [18–23]. Examples of emerging applications are quantum simulations of many-body physics [1,24–27], as well as quantum networks [2,3], where the nuclear spins provide qubits for quantum memory [28], entanglement distillation [29], and error correction [30–32].

State-of-the-art experiments have demonstrated the imaging of spin networks containing up to 27 nuclear spins [18,19,33–35]. The ability to map larger spin networks can be a precursor for quantum simulations that are currently intractable, would provide a precise understanding of the noise environment of spin-qubit registers [32,36,37], and might contribute towards efforts to image complex spin systems outside of the host material [20–23,38,39]. A key open challenge for mapping larger networks is spectral crowding, which causes overlapping signals and introduces ambiguity in the assignment of signals to individual spins and the interactions between them.

Here, we develop correlated sensing sequences that measure both the network connectivity as well as the characteristic spin frequencies with high spectral resolution. We apply these sequences to map a 50-nuclear-spin network comprised of 1225 spin-spin interactions in the vicinity of a nitrogen vacancy (NV) center in diamond. The key concept of our method is to concatenate double-resonance sequences to measure chains of coupled spins through the network. The mapping of spin chains removes ambiguity about how the spins are connected and enables the sensing of spins that are farther away from the electron-spin sensor in spectrally crowded regions. These results significantly increase the size and complexity of the accessible spin network. Additionally, our methods are applicable to a wide variety of systems, and might inspire future methods to magnetically image complex samples such as individual molecules or proteins [22,33,39].

5.2. SPIN-NETWORK MAPPING

We consider a network of N coupled nuclear spins in the vicinity of a single electron spin that acts as a quantum sensor [18,19]. The effective dynamics of the nuclear-spin network, with an external magnetic field along the z-axis, are described by the Hamiltonian (see Appendix C.1):

$$\hat{H} = \sum_{i=1}^{N} A_i \hat{I}_z^{(i)} + \sum_{i=1}^{N} \sum_{j=i+1}^{N} C_{ij} \hat{I}_z^{(i)} \hat{I}_z^{(j)}, \tag{5.1}$$

where $\hat{I}_z^{(i)}$ denotes the nuclear Pauli spin-$\frac{1}{2}$ operator for spin i, A_i are the precession frequencies associated with each spin, and C_{ij} denotes the nuclear-nuclear coupling between spin i and j. The frequencies A_i might differ due to differences in species (gyromagnetic

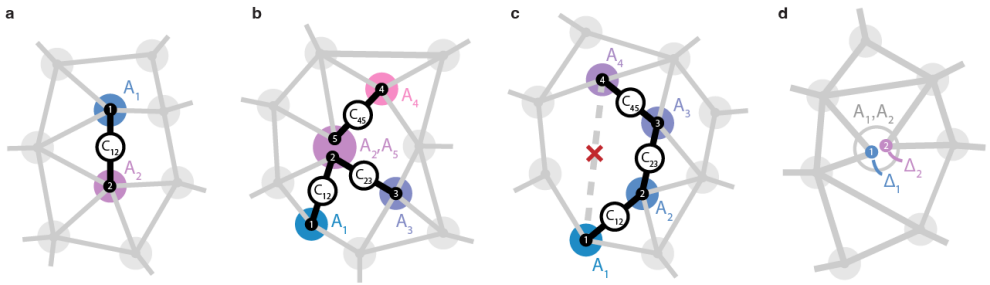

Figure 5.1: **Mapping spin networks.** Graph representing a spin network, where vertices denote spins and edges denote spin-spin interactions (C_{ij}). Spins are distributed among spectral regions (coloured disks) by their precession frequency (A_i). **a)** If all spin frequencies are unique (one spin in each disk), the network can be mapped by measuring only pairwise interactions (C_{12}) between frequencies (A_1, A_2). **b)** If spins spectrally overlap (e.g. spins 2 and 5 with $A_2 \approx A_5$) due to the finite line width set by the dephasing time $T_2^\star$, pairwise measurements alone are ambiguous when assigning interactions to specific spins. By measuring chains (e.g. through A_1, A_2, A_3) we directly retrieve the connectivity of the network. **c)** We also exploit spin chains to measure interactions between spins that are otherwise challenging to access. As an example, couplings belonging to Spin 4 are not directly accessible from the spin at A_1 – due to spectral crowding or negligible couplings – but can be obtained through a chain. **d)** Finally, we complement the spin chains with a correlated double-resonance method that enhances the spectral resolution for the spin-frequency shifts (Δ_i) from $\sim 1/T_2^\star$ to $\sim 1/T_2$, so that spectrally overlapping spins can also be resolved directly. This figure shows a conceptual network with vertices organized in frequency space. In Fig. C.1, we discuss the specific relations between frequency and spatial position for the experimental system considered here: an NV center in diamond and surrounding ^{13}C-spin network, for which increased spectral crowing (panels b-d) naturally occurs for ^{13}C spins that are farther away from the NV center.

ratio), the local magnetic field and spin environment, and due to coupling to the sensor electron spin. Our goal is to extract the characteristic spin frequencies A_i and spin-spin couplings C_{ij} that capture the structure of the network.

Fig. 5.1 shows an example network, with coloured disks denoting frequency regions, and numbered dots inside signifying spins at these frequencies. Although in principle all spins are coupled to all spins, we draw edges only for strong, resolvable, spin-spin couplings, defined by: $C_{ij} \gtrsim 1/T_2$, where T_2 is the nuclear Hahn-echo coherence time ($\sim 0.5\,$s) [16]. The network connectivity constitutes the presence (or absence) of such resolvable couplings. In general, the number of frequency disks is smaller than the number of spins, as multiple spins might occupy the same frequency region (i.e. overlap in frequency).

State-of-the-art spin-network mapping relies on isolating individual nuclear-nuclear interactions through spin-echo double resonance (SEDOR) [18]. Applying simultaneous echo pulses at frequencies A_i and A_j preserves the interaction C_{ij} between spins at A_i and A_j, while decoupling them from (quasi-static) environmental noise and the rest of the network, so that the coupling C_{ij} is encoded in the nuclear-spin polarisation with high spectral resolution (set by the nuclear T_2-time rather than $T_2^\star$-time). The signal is acquired by mapping the resulting nuclear spin polarisation, for example at frequency A_i, on the NV electron spin and reading it out optically [16]. Such a measurement yields a correlated list of three frequencies $\{A_i, C_{ij}, A_j\}$ (Fig. 5.1a). If all spins are spectrally isolated, so that the A_i do not overlap, these pairwise measurements completely characterise the network.

However, due to their finite spectral line widths (set by $1/T_2^\star$), multiple spin frequencies A_i may overlap (indicated by multiple spins occupying a disk). This introduces ambiguity

when assigning measured couplings to specific spins in the network, and causes complex overlapping signals, which are difficult to resolve and interpret [18,19]. Figure 5.1b shows an example where pairwise measurements break down; spins 2 and 5 overlap in frequency ($A_2 \approx A_5$). Applying pairwise SEDOR between frequencies A_1, A_3, A_4 and a frequency that overlaps with A_2 and A_5 returns three independent pairwise correlations: $\{A_1, C_{12}, A_2\}, \{A_3, C_{23}, A_2\}$ and $\{A_4, C_{45}, A_5\}$. Crucially, however, such measurements cannot distinguish this uncoupled 2-spin and 3-spin chain (Fig 1b) from a single 4-spin network (with a single central spin at A_2), nor from a network of 3 uncoupled 2-spin chains (three spectrally overlapping spins). Without introducing additional a-priori knowledge or assumptions about the system, pairwise measurements cannot be assigned to specific spins and are thus insufficient to reconstruct the network [18].

Our approach is to measure connected chains through the network, and combine these with high-resolution spin frequency measurements. First, spin-chain sensing (detailed in Section 5.4) correlates multiple frequencies and spin-spin couplings, directly accessing the underlying network connectivity, and thus reducing ambiguity due to (potential) spectral overlap. Consider the previous example: by probing the correlation between the three frequencies A_1, A_2 and A_3 in a single measurement, we directly reveal that Spin 1 and Spin 3 are connected to the same spin at A_2 (Spin 2). Such a spin-chain measurement yields a correlated list of 5 frequencies: $\{A_1, C_{12}, A_2, C_{23}, A_3\}$, characterising the 3-spin chain. Applying the same method but now with spin 4 ($A_3 \leftarrow A_4$) reveals that it is not connected to Spin 2, but couples to another spin (spin 5) that overlaps in frequency with Spin 2.

Second, spin-chain sensing enables measuring couplings that are otherwise challenging to access, enabling exploration further into the network. Consider the case where starting from some spin (e.g. Spin 1 in Fig. 5.1c) it is challenging to probe a part of the network, either because the couplings to Spin 1 are too weak to be observed or spectral crowding causes signals to overlap. The desired interactions (e.g. those belonging to Spin 4 in Fig. 5.1c) can be reached by constructing a spin chain, in which each link is formed by a strong and resolvable spin-spin interaction. The chain iteratively unlocks new spins that can be used as sensors of their own local spatial environment.

Finally, we combine the spin-chain measurements with a correlated double-echo spectroscopy scheme that increases the resolution with which different A_i are distinguished from $\sim 1/T_2^\star$ to $\sim 1/T_2$ (Fig. 5.1d). This directly reduces spectral overlap of spin frequencies, further removing ambiguity.

In principle, the entire network can be mapped by expanding and looping a single chain. In practice, measuring limited-size chains is sufficient. A N-spin chain measurement yields a correlated list of N spin frequencies A, alongside $N-1$ coupling frequencies C, which quickly becomes uniquely identifiable, even when some spin frequencies in the network are degenerate. This allows for the merging of chains that share a common section to reconstruct the network (Methods).

5.3. EXPERIMENTAL SYSTEM

We demonstrate these methods on a network of 50 ^{13}C spins surrounding a single NV center in diamond at 4 K. The NV electron spin is initialized and measured optically and is used as the sensor spin [18]. We employ dynamical decoupling sequences to sense nuclear

spins at selected frequency bands, using sequences with and without radio-frequency driving (DDRF) of the nuclear spins to ensure sensitivity in all directions from the NV (Methods) [16,18]. The nuclear spins are polarized via the electron spin, using global dynamical-nuclear-polarisation techniques (PulsePol sequence [1,40]), or by selective projective measurements or SWAP gates [16,18].

The ^{13}C nuclear spin frequencies are given by $A_i = \omega_L + m_s\Delta_i$, with ω_L the global Larmor frequency and Δ_i a local shift due to the hyperfine interaction with the NV center (see for example Ref. [41] and Appendix C.1). Here, we neglected corrections due to the anisotropy of the hyperfine interaction, which are treated in Appendix C.4. The experiments are performed with the electronic spin in the $m_s = \pm 1$ states. Because, for the spins considered, Δ_i is typically two to three orders of magnitude larger than the nuclear-nuclear couplings C_{ij}, nuclear-spin flip-flop interactions are largely frozen, and Eq. 5.1 applies (Appendix C.1).

In the NV-nuclear system, spectral crowding forms a natural challenge for determining the spin-network structure. The spin frequencies are broadened by the inhomogeneous linewidth $\sim 1/T_2^\star$, which is mainly set by the coupling to all other nuclear spins. A limited number of nuclear spins close to the NV center are spectrally isolated (defined as: $|A_i - A_j| > 1/T_2^\star \ \forall\ j$), making them directly accessible with electron-nuclear gates [16,18], and making pairwise measurements sufficient to map the interactions. However, the hyperfine interaction, and thus Δ_i, decreases with distance ($\sim r^{-3}$), resulting in an increasing spectral density for lower Δ_i (larger distance). Interestingly, there exists a spectrally crowded region ($|A_i - A_j| < 1/T_2^\star$) for which nuclear spins still do not couple strongly to other spins in the same spectral region ($C_{ij} \lesssim 1/T_2 \ \forall\ j$), for example when they are on opposite sides of the NV center. Contrary to previous work [18], the methods outlined in Section 5.2 allow us to measure interactions between spins in the spectrally crowded region (see Appendix C.2), unlocking a part of the network that was previously not accessible.

5.4. SPIN-CHAIN SENSING

We experimentally demonstrate the correlated sensing of spin chains up to five nuclear spins (Fig. 5.2), by sweeping a multi-dimensional parameter space (set by 5 spin frequencies and 4 spin-spin couplings). We start by polarizing the spin network [1,40] and use the electron spin to sense a nuclear spin (Spin 1) at frequency A_1, which marks the start of the chain.

First, we perform a double-resonance sensing sequence (Fig. 5.2b) consisting of a spin-echo sequence at frequency A_1 and an additional π-pulse at frequency RF_2. The free evolution time t_{12} is set to 50ms, to optimise sensitivity to nuclear-nuclear couplings (typically $\sim$ 10Hz). By sweeping RF_2, strong connections ($C_{1j} \gg 1/T_2$) are revealed through dips in the coherence signal of Spin 1 (Fig. 5.2d, left). We select a connection to a spin at $\mathrm{RF}_2 = A_2$ (Spin 2) and determine (C_{12}) by sweeping t_{12} (Fig. 5.2d, right).

Next, we extend the chain. To map the state of Spin 2 back to the electron sensor through Spin 1, we change the phase of the first $\frac{\pi}{2}$-pulse (labelled 'yx') and set $t_{12} = 1/(2C_{12})$ to maximise signal transfer (see Appendix C.3). We then insert a double-resonance block for frequencies $\mathrm{RF}_2 = A_2$ and RF_3 in front of the sequence (Fig. 5.2c and e,left) to explore the couplings of Spin 2 to the network. This concatenating procedure can be continued to extend the chain, with up to 5 nuclear spins shown in Fig. 5.2. In general, the signal strength decreases with increasing chain length, as it is set by a combination of the degree of polari-

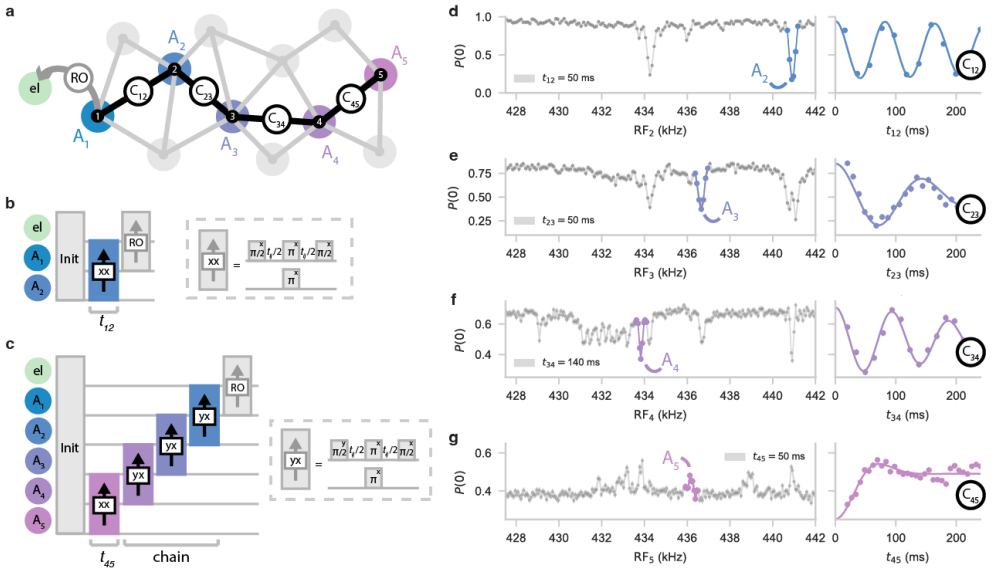

Figure 5.2: **Sensing spin chains. a)** Schematic of a $N = 5$ nuclear-spin chain through different spectral regions $\{A_1, A_2, A_3, A_4, A_5\}$ (coloured disks), starting from the NV electron spin ('el'). Even though there might be multiple spins at each of the nuclear frequencies, only a single one is connected to this chain. **b)** Pulse sequence (Methods) for the prototypical $N = 2$ sequence (SEDOR)[18]. **c)** Pulse sequence for sensing a chain of $N = 5$ nuclear spins, correlating 5 spin frequencies and 4 spin-spin interactions. In this case, the RF frequency (RF_5) and free-evolution time (t_{45}) are varied to probe the connections of the spin at A_4 to other spins. The resulting signal is mapped back via concatenated SEDOR sequences and finally read out ('RO') through the electron spin (Methods). **d-g)** Experimental data, sweeping the frequency RF_N of the recoupling pulse (left) to detect the frequencies of spins coupled to Spin 1, and varying the free evolution time $t_{N-1,N}$ (right) to extract their coupling strengths (for $N = \{2,3,4,5\}$). For the frequency sweeps, evolution times t_{ij} are selected a-priori (annotated). Colored highlights denote the signals due to the spins in the chain and solid lines are fits to the data (see Appendix C.3). The signal in the bottom panel is inverted, due to the coupling C_{34} being negative.

sation and decoherence (T_2 relative to C_{ij}) of all spins in the chain (See Appendix C.3). This limits the chain lengths that can be effectively used.

By mapping back the signal through the spin chain, the five spin frequencies and the 4 coupling frequencies are directly correlated: they are found to originate from the same branch of the network. As spins are now characterized by their connection to the chains, rather than by their individual, generally degenerate, frequencies (Fig. 5.1b), they can be uniquely identified. Additionally, the chains enable measuring individual spin-spin couplings in spectrally crowded regions (Fig. 5.1c). As an example, the expected density of spins at frequency A_4 is around 30 spins per kHz (Fig. C.3), making Spin 4 challenging to access directly from the electron spin. However, because Spin 3 probes only a small part of space, Spin 4 can be accessed through the chain, as demonstrated by the single-frequency oscillation in Fig. 5.2f. Another advantage over previous methods[18] is that our sequences are sensitive to both the magnitude and the sign of the couplings, at the cost of requiring observable polarisation of the spins in the chain. The sign of the couplings provides additional information for reconstructing the network (Fig. 5.2g).

5.5. HIGH-RESOLUTION MEASUREMENT OF SPIN FREQUENCIES

While the sensing of spin chains unlocks new parts of the network and reduces ambiguity by directly mapping the network connections, the spectral resolution for the spin frequencies (A_i) remains limited by the nuclear inhomogeneous dephasing time $T_2^\star \sim 5\,\text{ms}$ [16]. Next, we demonstrate high-resolution (T_2-limited) measurements of the characteristic spin frequency shifts Δ_i. These frequencies provide a way to label spins, and thus further reduce ambiguity regarding which spins participate in the measured chains, particularly when a spectral region in the chain contains multiple spins (see Fig. 5.1d).

We isolate the interaction of nuclear spins with the electron spin through an electron-nuclear double-resonance block acting at a selected nuclear-spin frequency region. The key idea is that the frequency shift imprinted by the electron-spin sensor can be recoupled by controlling the electron spin state. We use microwave pulses that transfer the electron population from the $|-1\rangle$ to the $|+1\rangle$ state (Fig. 5.3b, Methods). The nuclear spin is decoupled from quasi-static noise and the rest of the spins, extending its coherence time, while the interaction of interest (Δ_i) is retained.

Figure 5.3 shows an example for a nuclear spin at A_1, for which we measure a hyperfine shift $\Delta_1 = 14549.91(5)$ Hz and a spectral linewidth of 1.8 Hz (Fig. 5.3d and e). Besides a tool to distinguish individual spins in the network with high spectral resolution, this method has the potential for improved characterisation of the hyperfine interaction in electron-nuclear spin systems.

The observed coherence time $T_2 = 0.36(2)$s is slightly shorter than the bare nuclear spin-echo time $T_{2,\text{SE}} = 0.62(5)$ s. This reduction is caused by a perturbitive component of the hyperfine tensor in combination with the finite magnetic field strength (see Appendix C.4). Flipping the electron spin between $m_s = \pm 1$ changes the quantization axes of the nuclear spins, which causes a change of the nuclear-nuclear interactions [18], which is not decoupled by the spin-echo sequence (see Fig. C.1). The effect is strongest for spins near the NV center. For larger fields or for spins with weak hyperfine couplings, we expect that further resolution enhancement is possible by applying multiple refocusing pulses (see Appendix C.4).

Finally, we combine spin-chain sensing and electron-nuclear double resonance to correlate high-resolution spin frequencies (Δ_i) with specific spin-spin couplings (C_{ij}), even when a chain contains multiple spins with overlapping frequencies. We illustrate this scheme on a chain of spins, where two spins (2 and 3) have a similar frequency ($A_2 \approx A_3$) and both couple to A_1 and A_4 (Fig. 5.4a). The goal is to extract Δ_2, Δ_3 and the couplings to Spin 4 (C_{24}, C_{34}). As a reference, standard double-resonance shows a quickly decaying time-domain signal, indicating couplings to multiple spins that are spectrally unresolved (Fig. 5.4b).

Figure 5.4c shows how the electron-nuclear double resonance sequence (mint green) is inserted in the spin-chain sequence to perform high-resolution spectroscopy of the A_2, A_3 frequency region. Sweeping the interaction time t_1 shows multiple frequencies (Fig. 5.4e), hinting at the existence of multiple spins with approximate frequency A_2. The result is consistent with two spins at frequencies $\Delta_2 = 8019.5(2)$ Hz and $\Delta_3 = 7695.2(1)$ Hz, split by an internal coupling of $C_{23} = 7.6(1)$ Hz (Fig. 5.4a and Fig. C.4e,f).

Next, we add a nuclear-nuclear block (pink block in Fig. 5.4d) and sweep both electron-nuclear (t_1) and nuclear-nuclear (t_2) double-resonance times to correlate Δ_2 and Δ_3 with nuclear-nuclear couplings C_{24} and C_{34}. After the t_1 evolution, the hyperfine shifts Δ_i are im-

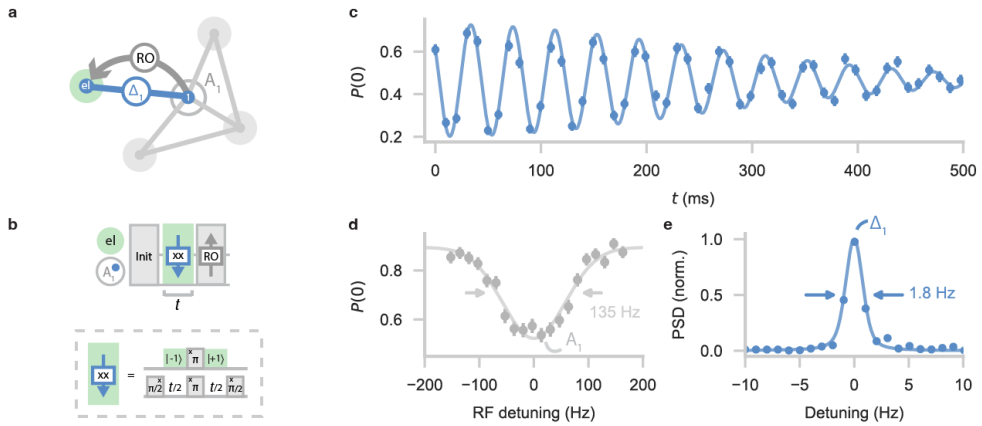

Figure 5.3: **Electron-nuclear double resonance. a)** The nuclear-spin frequencies A_i are shifted by the hyperfine interaction with the electron spin Δ_i (blue dotted line). Performing double resonance between the nuclear spin and the electron spin (mint green) retains this interaction while decoupling from quasi-static noise. **b)** Pulse sequence for measuring Δ_1 for a spin at $\approx A_1$. The nuclear spin undergoes a double resonance sequence, picking up a phase (downward arrow) from the interaction with the electron spin, whose population is synchronously transferred from the $|-1\rangle$ to the $|+1\rangle$ state. Finally, the signal is read out (denoted 'RO') via the electron spin (Methods) **c)** Time domain signal of $\Delta_1 = 14549.91(5)$ Hz (undersampled), with a coherence time of $T_2 = 0.36(2)$ s, fitted by a sinusoid with Gaussian decay. **d)** Zoom-in of spectroscopy data as in Fig. 5.2d, showing a broad resonance (135 Hz FWHM), limited by the nuclear $T_2^\star$-time. **e)** Power spectral density (PSD) of (c), showing a line width that is ~ 75 times improved compared to (c).

printed in the z-expectation value of each spin, effectively modulating the nuclear-nuclear couplings observed in t_2. The 2D power spectral density (PSD) shows signals in two distinct frequency regions along the f_1-axis, corresponding to Δ_2 and Δ_3 (Fig. 5.4f). Analysing the nuclear-nuclear (f_2) signal at these frequencies (Fig. 5.4g), we find $C_{24} = -11.8(2)$ Hz and $C_{34} = -0.2(5)$ Hz. We attribute the splitting to the coupling C_{23} between Spins 2 and 3 (Methods, Fig. C.4g,h). Varying RF_4 enables the measurement of the interactions of spins 2 and 3 to other parts of the network (for example to determine C_{12}, C_{13}). Beyond the examples shown here, the electron-nuclear block can be inserted at specific positions in the spin-chain sequence (Fig. 5.2c) to extract Δ_i of all spins in the chain (Fig. C.8).

5.6. RECONSTRUCTION OF A 50-SPIN NETWORK

Finally, we apply these methods to map a 50-spin network. The problem resembles a graph search (Methods)[42]. By identifying a number of spin chains in the system, and fusing them together based on overlapping sections, we reconstruct the connectivity (Fig. 5.5). Limited sized chains are sufficient because the couplings are highly non-uniform, so that a few overlapping vertices and edges enable fusing chains with high confidence. We use a total of 249 measured interactions through pairwise and chained measurements. Fusing these together provides a hypothesis for the network connectivity (Fig. 5.5b).

To validate our solution for the network we use the additional information that the

nuclear-nuclear couplings can be modeled as dipolar and attempt to reconstruct the spatial distribution of the spins. Compared to work based on pairwise measurements[18], our spin-chain measurements provide additional information on the connectivity and coupling signs, reducing the complexity of the numerical reconstruction. Additionally, we constrain the position using the measured hyperfine shift Δ_i (Methods). Because the problem is highly overdetermined[18], the fact that a spatial solution is found that closely matches the measured frequencies and assignments validates the obtained network connectivity. Additionally, the reconstruction yields a spatial image of the spin network and predicts the remaining unmeasured 976 spin-spin interactions, most of which are weak (< 1Hz). An overview of the complete 50 spin cluster, characterized by 50 spin frequencies and 1225 spin-spin couplings can be found in Table C.1 and in Fig. 5.5b.

5.7. DISCUSSION

In conclusion, we developed correlated double-resonance sensing that can map the structure of large networks of coupled spins, with high spectral resolution. We applied these methods to reconstruct a 50-spin network in the vicinity of an NV center in diamond. The methods can be applied to a variety of systems in different platforms, including electron-electron spin networks[7–15,43]. Mapping larger spin systems might be in reach using machine-learning-enhanced protocols and sparse or adaptive sampling techniques, which can further reduce acquisition times[44,45]. Combined with control fields[1,16,32], the methods developed here provide a basis for universal quantum control and readout of the network, which has applications in quantum simulations of many-body physics[1]. Furthermore, the precise characterisation of a 50-spin network provides new opportunities for optimizing quantum control gates in spin qubit registers[16,32,36], for testing theoretical predictions for defect spin systems[46], and for studying coherence of solid-state spins on the microscopic level, including quantitative tests of open quantum systems and approximation of the central spin model[47]. Finally, these results might inspire high-resolution nano-MRI of quantum materials and biologically relevant samples outside the host crystal.

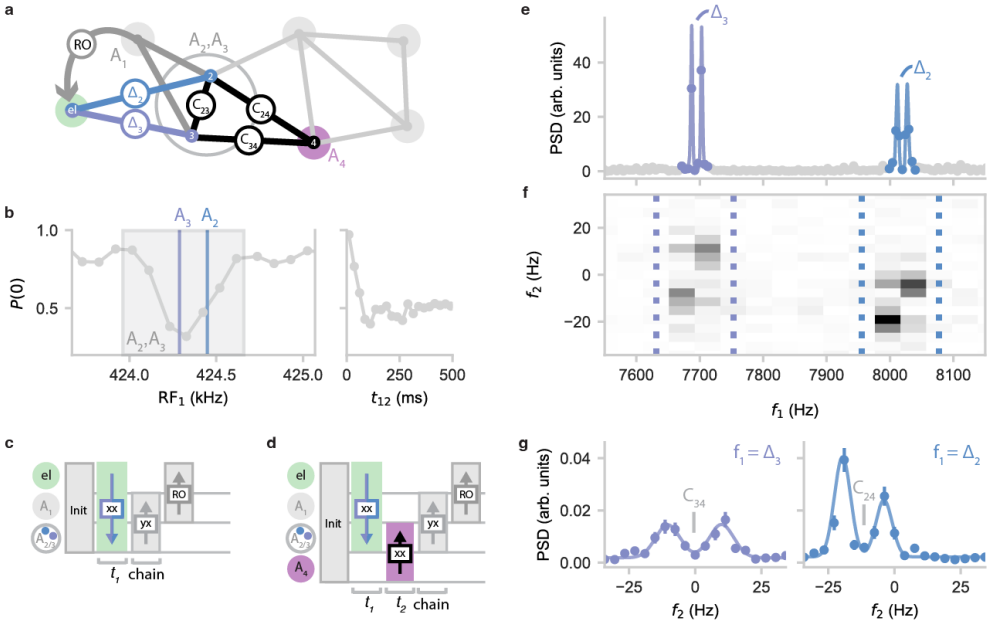

Figure 5.4: **Two-dimensional spectroscopy of spectrally crowded spins. a)** Schematic of the studied system, which contains two spins with overlapping frequencies $A_2 \approx A_3$ (grey circle), with slightly different hyperfine shifts (Δ_2, Δ_3). Both are coupled to the spin at A_1, which is used for to transfer the signal to the electron spin for readout ('RO'). **b)** SEDOR spectroscopy (as in Fig. 5.2d) of the frequency region A_2, A_3, with the estimated spin frequencies indicated. Sweeping the t_{12} evolution time results in a quick decay. **c)** Pulse sequence for the electron-nuclear double resonance sequence used in (e), where the Δ_i are extracted by sweeping t_1. **d)** Pulse sequence combining electron-nuclear and nuclear-nuclear double resonance, used in (f). Adding a nuclear-nuclear block (pink) and sweeping both t_1 and t_2 reveals the correlation between Δ_i and spin-spin couplings. **e)** Sweeping t_1 yields a high-resolution PSD of the A_2, A_3 frequency region, showing two (split) frequencies Δ_2 and Δ_3. The solid curve is a four-frequency fit to the data. **f)** Signal (PSD) for the two-dimensional sequence, revealing two distinct regions along the f_1-axis at Δ_2 and Δ_3. **g)** Binned line cut of (f) along the f_2-axis at frequencies Δ_2, Δ_3 (region indicated by dotted lines). The positions of the (split) peaks indicate the coupling to the spin at A_4 ($C_{24} = -11.8(2)$ Hz, $C_{34} = -0.2(5)$ Hz). The solid line is a fit of two Gaussians to extract the couplings.

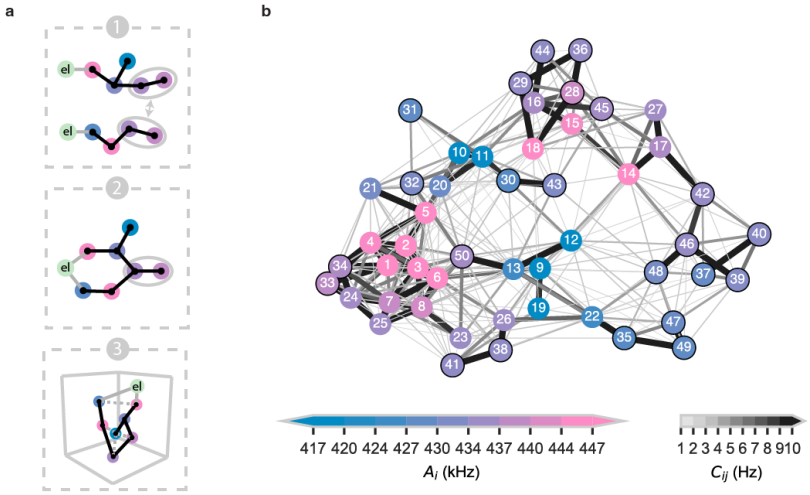

Figure 5.5: **Mapping a 50-spin network. a)** Schematic illustrating the procedure for mapping large networks. 1: Separate high-resolution chains through the network are measured (two example chains shown here). 2: We merge chains that share a common section of the network. 3: Optionally, an algorithm adapted from [18] estimates the most likely spin positions (Methods), which predicts all unmeasured nuclear-nuclear couplings (dotted lines) and provides a validation for the assignment and merging of step 2. **b)** Graph of the 50-spin network mapped in this work, with edges indicating spin-spin interactions above 2 Hz and vertex colors denoting spin frequencies A_i. The spins are labelled according to Table C.1. Black circles indicate the 23 newly mapped spins compared to previous work [18]. A 3D spatial image of the network is presented in Fig. C.9.

5.8. METHODS

SAMPLE AND SETUP

All experiments are performed on a naturally occurring NV center at a temperature of 3.7K (Montana S50 Cryostation), using a home-built confocal microscopy setup. The diamond sample was homoepitaxially grown using chemical vapor deposition and cleaved along the ⟨111⟩ crystal direction (Element Six). The sample has a natural abundance of ^{13}C (1.1 %). The NV center has been selected on the absence of couplings to ^{13}C stronger than ≈ 500 kHz. No selection was made on other properties of the ^{13}C nuclei distribution. A solid immersion lens (SIL) that enhances photon collection efficiency is fabricated around the NV center. A gold stripline is deposited close to the edge of the SIL for applying microwave (MW) and radio-frequency (RF) pulses. An external magnetic field of $B_z = 403.553$ G is applied along the symmetry axis of the NV center, using a (temperature-stabilized) permanent neodymium magnet mounted on a piezo stage outside the cryostat[16]. The field is aligned to within 0.1 degrees using a thermal echo sequence[18].

5

ELECTRON AND NUCLEAR SPINS

The sample was previously characterized in Abobeih et al.[18] and the 27 nuclear spins imaged in that work are a subset of the 50 nuclear-spin network presented here. The NV electron spin has a dephasing time of $T_2^\star = 4.9(2)\,\mu$s, a Hahn spin echo time of $T_2 = 1.182(5)$ ms, and a relaxation time of $T_1 > 1$ hr[18]. The spin state is initialized via spin-pumping and read out in a single shot through spin-selective resonant excitation, with fidelities $F_0 = 89.3(2)$ ($F_1 = 98.2(1)$) for the the $m_s = 0$ ($m_s = -1$) state, resulting in an average fidelity of $F_{\text{avg}} = 0.938(2)$. The readout is corrected for these numbers to obtain a best estimate of the electronic spin state. The nuclear spins have typical dephasing times of $T_2 = 5 - 10$ ms and Hahn echo $T_{2,n}$ up to 0.77(4) s[16]. T_2-times for spins with frequencies closer to the nuclear Larmor frequency ($\Delta_i \lesssim 5$ kHz) typically decrease to below 100 ms (see e.g. Fig. 5.2g, right panel), as the spin echo simultaneously drives other nuclear spins at these frequencies which are re-coupled to the target (instantaneous diffusion).

PULSE SEQUENCES

We drive the electronic $m_s = 0 \leftrightarrow m_s = -1$ ($m_s = 0 \leftrightarrow m_s = +1$) spin transitions at 1.746666 (4.008650) GHz with Hermite-shaped pulses. For transferring the electron population from the $m_s = -1$ to the $m_s = +1$ state (Fig. 5.3 and 5.4), we apply two consecutive π-pulses at the two MW transitions, spaced by a waiting time of 3 μs. For all experiments, we apply RF pulses with an error-function envelope in the frequency range $400 - 500$ kHz. Details on the electronics to generate these pulses can be found in Ref. [1].

For most experiments described in this work, the measurable signal is dependent on the degree of nuclear spin polarisation. We use a dynamical nuclear polarisation sequence, PulsePol,to transfer polarisation from the electron spin to the nuclear spin bath[1,40]. The number of repetitions of the sequence is dependent on the specific polarisation dynamics of the spins being used in the given experiment, but ranges from 500-10000. The PulsePol sequence is indicated by the 'Init' block in the sequence schematics. All double resonance sequences follow the convention illustrated in the dotted boxes in Fig. 5.2b,c and Fig. 5.3b,

where the horizontal grey lines denote different RF frequencies and the top line the electronic MW frequency. The two letters in the double resonance blocks ('xx' or 'yx') denote the rotation axes of the first and final $\pi/2$-pulses. The π-pulses (along the x-axis) are applied sequentially (following Ref. [18]). The lengths of all RF pulses are taken into account for calculating the total evolution time. Nuclear spins are read out via the electron by phase-sensitive ('yx') dynamical decoupling; DD or DDRF sequences [16], indicated by the 'RO'-marked block in the sequence schematics. Typically, the spin that is read out with the electron is reinitialised via a SWAP gate before the final SEDOR block in order to maximise its polarisation. However, all experiments presented here can be performed by using just the DNP initialisation, albeit with a slightly lower signal to noise ratio.

2D SPECTROSCOPY EXPERIMENTS

For the 2D measurement we concatenate an electron-nuclear double resonance with a nuclear-nuclear SEDOR. For every t_1-point, we acquire 20 t_2 points, ranging from 10 to 260 ms. The final $\pi/2$-pulse of the electron double resonance and the first of the SEDOR are not executed, as they can be compiled away. To correct for any slow magnetic field drifts that lead to miscalibration of the two-qubit gate used for read-out, causing a small offset in the measured signal, we set our signal baseline to the mean of the final five points ($\approx 200-260$ ms), where we expect the signal to be mostly decayed. Note that these field drifts do not affect any of the double resonance blocks in which the quantities to be measured are encoded (due to the spin-echo).

Both the 1D (Fig. 5.4d) and 2D (Fig. 5.4e) signals are undersampled to reduce the required bandwidth. To extract $\Delta A_2, \Delta A_3$, we fit a sum of cosines to the time domain signal of Fig. 5.4d. To extract the frequencies along the f_2-axis, which encode the nuclear-nuclear couplings (C_{24}, C_{34}), we take an (extended) line-cut at $f_1 = \Delta A_2$ and $f_1 = \Delta A_3$. To increase the signal, we sum over the four bins indicated by the dotted lines. We fit two independent Gaussians to the f_2-data to extract C_{24} and C_{34}. We find splittings of 7.8(2) Hz and 10.2(5) Hz, respectively, whose deviation with respect to measurements in Fig. 5.4d is unexplained. The skewed configuration of the two peaks (lower left, upper right) is a result of the correlation of the neighbouring spin state between the t_1 and t_2 evolution times. The different ratio of signal amplitudes belonging to Spin 2 and Spin 3, between the 1D and 2D electron-nuclear measurements are due to using different settings for the chained readout (evolution time, RF power). As we are only interested in extracting frequencies, we can tolerate such deviations.

Figure C.4 shows numerical simulations of the experiments presented in Fig. 5.4. These are generated by evaluating the Hamiltonian in Eq. C.3, taking into account the two spins at A_2, A_3, the spin at A_1 and the electron spin.

NETWORK RECONSTRUCTION

Here, we outline a general procedure for mapping the network by performing specific spin-chain and high-resolution Δ_i measurements. The mapping-problem resembles a graph search, with the NV electron spin used as root [42]. We base the protocol on a breadth-first like search, which yields a spanning tree as output, completely characterising the network. The following pseudocode describes the protocol:

```
Input : physical spin network, initial vertex el
Output : breadth-first tree T from root el
V_0 = {el}                                   ▷ Make el the root of T, V_i denotes the set of vertices at distance i
i = 0
while V_i ≠ ∅ do                             ▷ Continue until network is exhausted
    for each vertex v ∈ V_i do
        for each frequency f do
            C, singlecoupling = MeasureCoupling(v, f)   ▷ Returns C between vertex v and frequency f
            if singlecoupling then          ▷ Checks if MeasureCoupling returned a single, resolvable coupling
                create vertex w
                A_w = f
                C_vw = C
                unique, duplicate = CheckVertex(w, T)   ▷ Checks if w was already mapped in T
                if unique then                          ▷ w was not yet mapped
                    add w to V_{i+1} in T               ▷ w is added to T as a new vertex
                end if
                if not unique and duplicate == k then   ▷ w is the same vertex as k in T
                    add C_vk = C_vw in T                ▷ The measured coupling is assigned to k
                    delete w
                end if
                if not unique and duplicate == None then   ▷ Undecided if spin was mapped
                    delete w                               ▷ w is not added to T
                end if
            end if
        end for
    end for
    i = i + 1
end while
```

New vertices that are detected by chained measurements are iteratively added, once we verify that a vertex was not characterised before (i.e. has a duplicate in the spanning tree T). The function MeasureCoupling(v, f) performs a spin-echo double resonance sequence between vertex v and a frequency f, (a spin chain of length $i-1$ is used to access v) and checks whether a single, resolvable coupling is present (stored in the boolean variable 'singlecoupling'). In the case that v is the electron spin (el) an electron-nuclear DD(RF) sequence is performed [16,41]. The function CheckVertex(w, T) instructs the experimenter to perform a number of spin-chain and electron-nuclear double resonance measurements, comparing the vertex w and its position in the network with that of the (possibly duplicate) vertex k (see Appendix C.5). If one of these measurements is not consistent with our knowledge of k, we conclude w is a unique vertex and add it to T. If all measurements coincide with our knowledge of k, we conclude it is the same vertex and merge w and k. If the CheckVertex(w, T) is inconclusive (e.g. due to limited measurement resolution), we do not add w to T. Note that the measurement resolution, determined by the nuclear T_2-time, is expected to decrease for spins further away from the NV center (See Appendix C.2). This eventually limits the number of unique spins that can be identified and added to the network map.

The platform-independent procedure outlined above can be complemented by logic based on the 3D spatial structure of the system [18]. For example, when the CheckVertex(w, T) function is inconclusive, one can sometimes still conclude that w must be unique (or vice versa equal to k), based on the restricted number of possible physical positions of these two spins in 3D space [18]. In practice, we alternate the graph search procedure with calls to a positioning algorithm [18], which continuously checks whether the spanning tree T is physical

and aides in the identification of possible duplicates.

3D SPATIAL IMAGE

For the 3D reconstruction of the network, we use the positioning algorithm developed in Ref.[18]. To limit the experimental time we re-use the data of Ref.[18] and add the new measurements to it in an iterative way. We set the tolerance for the difference between measured and calculated couplings to 1 Hz. Although we only measure the new spin-spin couplings and chains when the electron is in the $m_s = -1$ state, we can assume this is within tolerance to the average value of the coupling if the perpendicular hyperfine component is small (< 10kHz)[18]. The spin positions are restricted by the diamond lattice. Spins that belong to the same chain are always added in the same iteration and up to 10000 possible configurations are kept. Chains starting from different parts of the known cluster can be positioned in a parallel fashion if they share no spins, reducing computational time. For spins that are relatively far away from the NV, we also make use of the interaction with the electron spin, approximating the hyperfine shift Δ_i to be of dipolar form within a tolerance of 1 kHz (neglecting the Fermi contact term[46]). For those cases, we model the electron spin as a point dipole with origin at the center of mass, as computed by density functional theory[46]. If multiple solutions are found, we report the standard deviation of the possible solutions as a measure of the spatial uncertainty (see Table C.1).

ERROR MODEL AND FITTING

Confidence intervals assume the measurement of the electron state is limited by photon shot-noise. The shot-noise-limited model is propagated in an absolute sense, meaning the uncertainty on fit parameters is not rescaled to match the sample variance of the residuals after the fit. For all quoted numbers, the number between brackets indicates one standard deviation or error indicated by the fitting procedure. We calculate the error on the PSD according to Ref.[48], assuming normally distributed errors.

REFERENCES

[1] J. Randall *et al.*, *Many-body–localized discrete time crystal with a programmable spin-based quantum simulator,* Science **374**, 1474 (2021).

[2] M. Pompili *et al.*, *Realization of a multinode quantum network of remote solid-state qubits,* Science **372**, 259 (2021).

[3] S. L. N. Hermans *et al.*, *Qubit teleportation between non-neighbouring nodes in a quantum network,* Nature **605**, 663 (2022).

[4] C. L. Degen, F. Reinhard and P. Cappellaro, *Quantum sensing,* Rev. Mod. Phys. **89**, 035002 (2017).

[5] F. Casola, T. van der Sar and A. Yacoby, *Probing condensed matter physics with magnetometry based on nitrogen-vacancy centres in diamond,* Nat Rev Mater **3**, 17088 (2018).

[6] E. Janitz *et al.*, *Diamond surface engineering for molecular sensing with nitrogen—vacancy centers,* J. Mater. Chem. C **10**, 13533 (2022).

[7] D. D. Awschalom, R. Hanson, J. Wrachtrup and B. B. Zhou, *Quantum technologies with optically interfaced solid-state spins,* Nat. Photon. **12**, 516 (2018).

[8] R. Debroux *et al.*, *Quantum Control of the Tin-Vacancy Spin Qubit in Diamond,* Phys. Rev. X **11**, 041041 (2021).

[9] A. Sipahigil *et al.*, *An integrated diamond nanophotonics platform for quantum-optical networks,* Science **358**, 847 (2016).

[10] A. Bourassa *et al.*, *Entanglement and control of single nuclear spins in isotopically engineered silicon carbide,* Nat. Mater. **19**, 1319 (2020).

[11] D. M. Lukin, M. A. Guidry and J. Vučković, *Integrated Quantum Photonics with Silicon Carbide: Challenges and Prospects,* PRX Quantum **1**, 020102 (2020).

[12] A. Durand *et al.*, *Broad Diversity of Near-Infrared Single-Photon Emitters in Silicon,* Phys. Rev. Lett. **126**, 083602 (2021).

[13] D. B. Higginbottom *et al.*, *Optical observation of single spins in silicon,* Nature **607**, 266 (2022).

[14] X. Gao *et al.*, *Nuclear spin polarization and control in hexagonal boron nitride,* Nat. Mater. **21**, 1024 (2022).

[15] A. Ruskuc, C.-J. Wu, J. Rochman, J. Choi and A. Faraon, *Nuclear spin-wave quantum register for a solid-state qubit,* Nature **602**, 408 (2022).

[16] C. E. Bradley *et al.*, *A Ten-Qubit Solid-State Spin Register with Quantum Memory up to One Minute,* Phys. Rev. X **9**, 031045 (2019).

[17] C. Babin *et al.*, *Fabrication and nanophotonic waveguide integration of silicon carbide colour centres with preserved spin-optical coherence,* Nat. Mater. **21**, 67 (2022).

[18] M. H. Abobeih *et al.*, *Atomic-scale imaging of a 27-nuclear-spin cluster using a quantum sensor,* Nature **576**, 411 (2019).

[19] K. S. Cujia, K. Herb, J. Zopes, J. M. Abendroth and C. L. Degen, *Parallel detection and spatial mapping of large nuclear spin clusters,* Nat Commun **13**, 1260 (2022).

[20] N. Zhao, J.-L. Hu, S.-W. Ho, J. T. K. Wan and R. B. Liu, *Atomic-scale magnetometry of distant nuclear spin clusters via nitrogen-vacancy spin in diamond,* Nat. Nanotechnol. **6**, 242 (2011).

[21] I. Schwartz *et al.*, *Blueprint for nanoscale NMR,* Sci Rep **9**, 6938 (2019).

[22] V. S. Perunicic, C. D. Hill, L. T. Hall and L. Hollenberg, *A quantum spin-probe molecular microscope,* Nat Commun **7**, 12667 (2016).

[23] Z.-Y. Wang, J. F. Haase, J. Casanova and M. B. Plenio, *Positioning nuclear spins in interacting clusters for quantum technologies and bioimaging,* Phys. Rev. B **93**, 174104 (2016).

[24] T. Unden *et al.*, *Coherent control of solid state nuclear spin nano-ensembles,* npj Quantum Inf **4**, 39 (2018).

[25] J. Cai, A. Retzker, F. Jelezko and M. B. Plenio, *A large-scale quantum simulator on a diamond surface at room temperature,* Nat. Phys. **9**, 168 (2013).

[26] J. Geng, V. Vorobyov, D. Dasari and J. Wrachtrup, *Ancilla assisted Discrete Time Crystals in Non-interacting Spin Systems,* arXiv:2107.11748 [cond-mat, physics:quant-ph] (2021), arXiv:2107.11748 [cond-mat, physics:quant-ph] .

[27] E. J. Davis *et al.*, *Probing many-body dynamics in a two-dimensional dipolar spin ensemble,* Nat. Phys. **19**, 836 (2023).

[28] H. P. Bartling *et al.*, *Entanglement of Spin-Pair Qubits with Intrinsic Dephasing Times Exceeding a Minute,* Phys. Rev. X **12**, 011048 (2022).

[29] N. Kalb *et al.*, *Entanglement distillation between solid-state quantum network nodes,* Science **356**, 928 (2017).

[30] G. Waldherr *et al.*, *Quantum error correction in a solid-state hybrid spin register,* Nature **506**, 204 (2014).

[31] T. H. Taminiau, J. Cramer, T. van der Sar, V. V. Dobrovitski and R. Hanson, *Universal control and error correction in multi-qubit spin registers in diamond,* Nat. Nanotechnol. **9**, 171 (2014).

[32] M. H. Abobeih *et al.*, *Fault-tolerant operation of a logical qubit in a diamond quantum processor,* Nature **606**, 884 (2022).

[33] F. Shi *et al.*, *Single-protein spin resonance spectroscopy under ambient conditions,* Science **347**, 1135 (2015).

[34] J. Zopes and C. Degen, *Reconstruction-Free Quantum Sensing of Arbitrary Waveforms,* Phys. Rev. Applied **12**, 054028 (2019).

[35] J. Zopes *et al.*, *Three-dimensional localization spectroscopy of individual nuclear spins with sub-Angstrom resolution,* Nat Commun **9**, 4678 (2018).

[36] T. Xie *et al.*, *99.92%-Fidelity cnot Gates in Solids by Noise Filtering,* Phys. Rev. Lett. **130**, 030601 (2023).

[37] D. F. Wise, J. J. Morton and S. Dhomkar, *Using Deep Learning to Understand and Mitigate the Qubit Noise Environment,* PRX Quantum **2**, 010316 (2021).

[38] I. Lovchinsky *et al.*, *Nuclear magnetic resonance detection and spectroscopy of single proteins using quantum logic,* Science **351**, 836 (2016).

[39] A. Ajoy, U. Bissbort, M. D. Lukin, R. L. Walsworth and P. Cappellaro, *Atomic-Scale Nuclear Spin Imaging Using Quantum-Assisted Sensors in Diamond,* Phys. Rev. X **5**, 011001 (2015).

[40] I. Schwartz *et al.*, *Robust optical polarization of nuclear spin baths using Hamiltonian engineering of nitrogen-vacancy center quantum dynamics,* Sci. Adv. **4**, eaat8978 (2018).

[41] T. H. Taminiau *et al.*, *Detection and Control of Individual Nuclear Spins Using a Weakly Coupled Electron Spin,* Phys. Rev. Lett. **109**, 137602 (2012).

[42] J. L. Gross and J. Yellen, eds., *Handbook of Graph Theory*, Discrete Mathematics and Its Applications (CRC Press, Boca Raton, 2004).

[43] A. Ungar, P. Cappellaro, A. Cooper and W. K. C. Sun, *Control of an Environmental Spin Defect beyond the Coherence Limit of a Central Spin,* PRX Quantum **5**, 010321 (2024).

[44] S. Martina, S. Hernández-Gómez, S. Gherardini, F. Caruso and N. Fabbri, *Deep learning enhanced noise spectroscopy of a spin qubit environment,* Mach. Learn.: Sci. Technol. **4**, 02LT01 (2023).

[45] K. Jung *et al.*, *Deep learning enhanced individual nuclear-spin detection,* npj Quantum Inf **7**, 41 (2021).

[46] A. P. Nizovtsev *et al.*, *Non-flipping ^{13} C spins near an NV center in diamond: Hyperfine and spatial characteristics by density functional theory simulation of the C_{510} [NV]H_{252} cluster,* New J. Phys. **20**, 023022 (2018).

[47] W. Yang, W.-L. Ma and R.-B. Liu, *Quantum many-body theory for electron spin decoherence in nanoscale nuclear spin baths,* Rep. Prog. Phys. **80**, 016001 (2017).

[48] P. Hoyng, *An error analysis of power spectra,* Astron. & AstroPhys. **47**, 449 (1976).

6

CONCLUSIONS AND OUTLOOK

In this chapter, I summarise the key results of this thesis and evaluate them according to the feedback loop framework introduced in chapter 1. What tools did we develop? How do they increase our knowledge of the system? And how do they contribute to the moonshot goals?

6.1. SUMMARY

In this thesis, we characterised, and developed partial control over, the charge- and spin environment of solid-state defects in diamond and silicon carbide. First, I summarise the findings per chapter and how they impact the research field in the near-term. Then, I explain how they contribute to the three moonshot goals and provide an outlook for achieving these. Table 6.1 summarises the main results in the framework of the *feedback loop* introduced in chapter 1.

In **chapter 3**, we studied the spectral diffusion dynamics of V2 centers in commercially available bulk-grown silicon carbide. We developed a charge-resonance check that enables the initialisation of the charge environment, which we use to track the charge dynamics. Then, we investigated the optical coherence of these centers at sub-millisecond timescales (by introducing a fast optical spectroscopy method) and found that they display near-lifetime-limited optical coherence even when they are confined to nanopillars. Additionally, we showed that the large inhomogeneous broadening of these single centers can be used as an asset, allowing for the probabilistic tuning of the emission frequency of over a gigahertz. Finally, the methods developed in this work may be used to study charge dynamics in silicon carbide and other semiconductors [1,2].

In **chapter 4**, we proposed, and studied, a more general class of the DDRF gates introduced by Bradley [3]. By incorporating the effects of detuned driving of the applied RF fields, we found that nuclear spins can actually be driven coherently over a broad RF frequency range, allowing for an increased flexibility (and fidelity) of applied quantum gates. From a quantum sensing perspective, we found that the sensitivity for detecting weakly coupled nuclear spins can also be enhanced by driving far-detuned from the nuclear transition frequency, which might have direct implications for studying the magnetic environment of defect centers [4,5].

In **chapter 5**, we mapped a network consisting of 50 nuclear spins surrounding a single NV center. We developed sensing sequences that directly access the connectivity of the network and measured the nuclear spin frequencies with high spectral resolution. These sequences can alternatively be used to read out nuclear spins participating in quantum simulations (see Fig. 6.1), for observing polarisation dynamics [6–8], or for conducting test of the central spin model [9]. Furthermore, characterising the nuclear spin environment to such detail, has allowed for the validation, and fine-tuning, of models calculating hyperfine [10,11] or nuclear-nuclear interactions [10] in the solid state.

Table 6.1: Summary of the main results in this thesis in the context of the *feedback loop* introduced in chapter 1 (Fig. 1.1). Here, I state the developed technology, the accompanying potential for scientific discovery and its contribution to the moonshot goals.

Technology	Science	Contribution to moonshot goal
Spectral diffusion modelling, charge-environment control, and fast optical spectroscopy (**Ch. 3**)	Charge dynamics in semiconductors [1,2], optical characteristics and charge stability of solid-state defects [12,13]	Frequency-tunable, optically-coherent emitters in nanostructures (in commercially available SiC) for quantum networks (**DQC**)
Generalised DDRF quantum gates (**Ch. 4**)	Understanding the limits of quantum control sequences	High-fidelity quantum control inside a quantum network node [14] (**DQC**)
High-sensitivity DDRF spectroscopy (**Ch. 4**)	Understanding of the magnetic noise environment [4]	Improved sensitivity for sensing samples outside the host crystal (**nano-NMR**)
Spin-network mapping and high-resolution hyperfine spectroscopy (**Ch. 5**)	Density-functional theory of the NV center [10,11], modelling nuclear-nuclear interactions in the solid-state [15]	Structural analysis of (single) molecules outside the host crystal (**nano-NMR**)
Readout of a coupled nuclear-spin network (**Ch. 5 & 6**)	Tests of the central spin model [9], studying hyperpolarisation dynamics [7,8]	Intermediate-scale quantum simulations, when combined with initialisation [16] and RF control fields [6] (**QS**)

6.2. OUTLOOK

We now return to the three moonshot goals introduced in chapter 1 and describe how the results in this thesis contribute to those, as well as touching upon the challenges that lay ahead.

1. **Distributed quantum computation (DQC)**. This thesis contributes to this goal in two ways. First, to move past proof-of-principle demonstrations of quantum networks [17,18], increasing the rates (and fidelity) of entanglement generation between nodes is of key importance [19,20]. For solid-state defects, optical cavities are likely needed to improve the spin-photon interface [21]. The optical coherence demonstrated for V2 centers in nanostructures in chapter 3 (even in the relatively impure HPSI material [2]) holds promise for integrating these centers in nano-scale photonic crystal cavities without degrading their optical performance [22,23]. Second, high-fidelity control of additional (nuclear-spin) qubits is central to (fault-tolerant) DQC schemes [19,20,24]. The fundamental insights on, and proposed generalisation of, the DDRF gates in chapter 4 allow for the systematic improvement of electron-nuclear gate fidelities [14]. Furthermore, the detailed characterisation of the spin environment presented in chapter 5 might aid noise-mitigation efforts for quantum control in these systems [4].

   Looking ahead, major challenges remain. Practical quantum advantage will likely require a sub-µs clock cycle [25], meaning that both internal (i.e. electron-nuclear)

gate speeds as well as external entanglement-generation rates need to be at least in the megahertz regime. Currently, the preparation rate of (low-fidelity) entangled states across the network remains in the hertz regime[17,18,26], while typical electron-nuclear gate speeds are in the (tens of) kilohertz[3,14]. A particular challenge is that fast electron-nuclear gates require strongly coupled nuclei, which are naturally more prone to decoherence during the slow remote-entanglement generation in currently used schemes[27,28].

However, if high clock speeds can be attained in a modular, network architecture, scaling up is presumably more straightforward than for monolithic designs, as there would be far fewer restrictions on the physical lay-out of the qubits[20]. For example, multiple chips could be positioned freely (e.g. 'stacked' vertically or distributed among cryostats) in order to save precious cryostat space or to limit crosstalk between qubits. Additionally, more efficient, low-overhead quantum error-correction codes might be attainable in an non-local coupling architecture, reducing the required number of physical qubits[20,29].

2. **Quantum simulation of many-body physics (QS).** The coupled nuclear-spin network mapped in chapter 5 can act as a test bed for intermediate-scale quantum simulations. If all 50 spins are used, computing the full density-matrix evolution may be intractable using classical computers[30,31]. In practice however, approximation methods such as cluster-correlation expansion techniques, would probably be sufficient to calculate the evolution at short timescales[32]. Nevertheless, this system might shed light on interesting open questions, such as the existence of many-body localisation in three-dimensional systems[33]. For this, our spin network is a natural candidate due to its three-dimensional structure and inherent disorder in couplings and precession frequencies[6]. Next to that, the ability to create specific initial states and readout the spins individually (see Fig. 6.1) would mitigate challenges associated with the use of global observables[34,35] and gives insight in the diverse, microscopic system dynamics[4–6]. Our first efforts towards reading out the 50-spin network is shown in Fig. 6.1.

   The most pressing challenge for this system in the near-term is again the effective clock speed of the simulator. Spreading of entanglement between nearest-neighbours in the network typically takes hundreds of milliseconds[6] (due to the tens of hertz nuclear-nuclear couplings[36]), and initialisation- and readout times are of the same order of magnitude, resulting in a $\sim$ hertz clock cycle. This severely limits the length and complexity of experiments that can be performed and will continue to be a bottleneck for systems scaled beyond the 50 spins demonstrated in this thesis. In the long run, more strongly interacting spin networks, such as those consisting of electronic spins (for example P1 centers[37]), could improve the clock speed by orders of magnitude[38–40]. An exciting thought is that the insights gained in chapter 5 will largely also hold true for the mapping of such electronic-spin networks[41].

3. **Nano-scale nuclear magnetic resonance (nano-NMR).** The NMR-sensing methods developed in chapter 5 might contribute to structure determination of single molecules outside the host crystal, although higher nuclear-nuclear coupling strength would be required to compensate for reduced nuclear-spin coherence times outside the diamond[42,43]. Furthermore, the predicted increase in DDRF sensitivity outlined

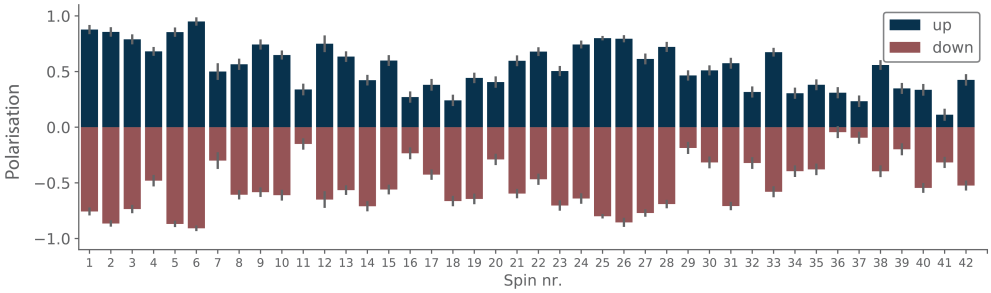

Figure 6.1: **Individual readout of the spin network**. Measured polarisation ($p \in [-1, 1]$) on the defect electron spin when reading out the nuclear spins in the network. The network is first polarised globally using the PulsePol sequence, after which a selective nuclear π-pulse is either applied (red), or not applied (blue). To read out the spin state of a specific nuclear spin, we project it onto the electron-spin via a series of nuclear-nuclear and electron-nuclear gates (as detailed in Fig. 5.2), after which we optically read out the electron spin (see also Randall [6]). The data are only corrected for the NV single-shot readout, not for the fidelity of the nuclear-nuclear and electron-nuclear gates [6]. Note that the nuclear-spin labels used here are different from those used in chapter 5.

in chapter 4 would allow for nuclear-spin detection with higher signal-to-noise ratios. This is especially exciting for sensors with a magnetic dipole aligned perpendicular to the sample surface [44], for which conventional dynamical decoupling spectroscopy is challenging. Further research is needed to establish how the sensitivity of the DDRF sequence, and that of alternative sequence designs relate [45,46]. In general, more research is needed to determine the optimal sensing protocols for structure determination outside the host crystal.

Besides that, further challenges remain on the path towards single-molecule NMR spectroscopy. Creating near-surface (< 10 nm) defects with suitable spin and charge characteristics is a field of research on its own [47–52]. Additionally, the preparation of single molecules close to the surface, keeping them stable for a sufficient amount of time without changing their structural characteristics, is a formidable task [47,53,54]. However, if these obstacles can be overcome, single-molecule NMR could give insight in the folding of specific proteins which are hard to access with current experimental techniques, and difficult to predict using machine learning methods [55,56].

In conclusion, this thesis presents a number of advances (column 1 of Table 6.1) that allow for a more accurate, or more complete, characterisation of the spin and charge environment of solid-state defects. Hopefully, in the near-term, these technologies lead to a better understanding of the research field spanning solid-state physics, condensed matter physics and atomic, molecular and optical physics (column 2 of Table 6.1). This in turn might aid further development of quantum technologies, with the ultimate goal of scaling these beyond the realms of academia for achieving the moonshot goals (column 3 of Table 6.1). I hope that this work contributes to those goals, bringing the charm, weirdness and beauty of quantum mechanics closer to the real world.

REFERENCES

[1] D. R. Candido and M. E. Flatté, *Suppression of the Optical Linewidth and Spin Decoherence of a Quantum Spin Center in a p - n Diode,* PRX Quantum **2**, 040310 (2021).

[2] N. T. Son and I. G. Ivanov, *Charge state control of the silicon vacancy and divacancy in silicon carbide,* J. Appl. Phys. **129**, 215702 (2021).

[3] C. E. Bradley *et al.*, *A Ten-Qubit Solid-State Spin Register with Quantum Memory up to One Minute,* Phys. Rev. X **9**, 031045 (2019).

[4] M. H. Abobeih *et al.*, *One-second coherence for a single electron spin coupled to a multi-qubit nuclear-spin environment,* Nat Commun **9**, 2552 (2018).

[5] H. P. Bartling *et al.*, *Entanglement of Spin-Pair Qubits with Intrinsic Dephasing Times Exceeding a Minute,* Phys. Rev. X **12**, 011048 (2022).

[6] J. Randall *et al.*, *Many-body–localized discrete time crystal with a programmable spin-based quantum simulator,* Science **374**, 1474 (2021).

[7] O. T. Whaites and T. S. Monteiro, *Hyperpolarisation Dynamics: Asymptotic Polarisation,* (2024), arXiv:2404.07578 [physics, physics:quant-ph] .

[8] O. T. Whaites *et al.*, *Hyperpolarization of nuclear spins: Polarization blockade,* Phys. Rev. Research **5**, 043291 (2023).

[9] W. Yang, W.-L. Ma and R.-B. Liu, *Quantum many-body theory for electron spin decoherence in nanoscale nuclear spin baths,* Rep. Prog. Phys. **80**, 016001 (2017).

[10] A. P. Nizovtsev *et al.*, *Non-flipping ^{13} C spins near an NV center in diamond: Hyperfine and spatial characteristics by density functional theory simulation of the C_{510} [NV]H_{252} cluster,* New J. Phys. **20**, 023022 (2018).

[11] I. Takács and V. Ivády, *Accurate hyperfine tensors for solid state quantum applications: Case of the NV center in diamond,* Commun Phys **7**, 178 (2024).

[12] L. Orphal-Kobin *et al.*, *Optically Coherent Nitrogen-Vacancy Defect Centers in Diamond Nanostructures,* Phys. Rev. X **13**, 011042 (2023).

[13] J. Heiler *et al.*, *Spectral stability of V2 centres in sub-micron 4H-SiC membranes,* npj Quantum Mater. **9**, 34 (2024).

[14] H. P. Bartling *et al.*, *Universal high-fidelity quantum gates for spin-qubits in diamond,* (2024), arXiv:2403.10633 [cond-mat, physics:quant-ph] .

[15] A. Nizovtsev *et al.*, *Indirect interaction of 13C nuclear spins in diamond with NV centers: Simulation of the full J-coupling tensors,* Front. Quantum Sci. Technol. **3**, 1332264 (2024).

[16] I. Schwartz *et al.*, *Robust optical polarization of nuclear spin baths using Hamiltonian engineering of nitrogen-vacancy center quantum dynamics,* Sci. Adv. **4**, eaat8978 (2018).

[17] M. Pompili *et al.*, *Realization of a multinode quantum network of remote solid-state qubits,* Science **372**, 259 (2021).

[18] S. L. N. Hermans *et al.*, *Qubit teleportation between non-neighbouring nodes in a quantum network,* Nature **605**, 663 (2022).

[19] N. H. Nickerson, J. F. Fitzsimons and S. C. Benjamin, *Freely Scalable Quantum Technologies Using Cells of 5-to-50 Qubits with Very Lossy and Noisy Photonic Links,* Phys. Rev. X **4**, 041041 (2014).

[20] S. Simmons, *Scalable Fault-Tolerant Quantum Technologies with Silicon Color Centers,* PRX Quantum **5**, 010102 (2024).

[21] M. Ruf, N. H. Wan, H. Choi, D. Englund and R. Hanson, *Quantum networks based on color centers in diamond,* J. Appl. Phys. **130**, 070901 (2021).

[22] D. M. Lukin *et al.*, *4H-silicon-carbide-on-insulator for integrated quantum and nonlinear photonics,* Nat. Photon. **14**, 330 (2020).

[23] C. Babin *et al.*, *Fabrication and nanophotonic waveguide integration of silicon carbide colour centres with preserved spin-optical coherence,* Nat. Mater. **21**, 67 (2022).

[24] S. De Bone, P. Möller, C. E. Bradley, T. H. Taminiau and D. Elkouss, *Thresholds for the distributed surface code in the presence of memory decoherence,* AVS Quantum Sci. **6**, 033801 (2024).

[25] M. E. Beverland *et al.*, *Assessing requirements to scale to practical quantum advantage,* (2022), arXiv:2211.07629 [quant-ph] .

[26] P. C. Humphreys *et al.*, *Deterministic delivery of remote entanglement on a quantum network,* Nature **558**, 268 (2018).

[27] C. E. Bradley *et al.*, *Robust quantum-network memory based on spin qubits in isotopically engineered diamond,* npj Quantum Inf **8**, 122 (2022).

[28] C. Bradley, *Order from Disorder: Control of Multi-Qubit Spin Registers in Diamond*, Ph.D. thesis, [object Object] (2021).

[29] L. Z. Cohen, I. H. Kim, S. D. Bartlett and B. J. Brown, *Low-overhead fault-tolerant quantum computing using long-range connectivity,* Sci. Adv. **8**, eabn1717 (2022).

[30] F. Arute *et al.*, *Quantum supremacy using a programmable superconducting processor,* Nature **574**, 505 (2019).

[31] H.-S. Zhong *et al.*, *Quantum computational advantage using photons,* Science **370**, 1460 (2020).

[32] T. Maier, M. Jarrell, T. Pruschke and M. H. Hettler, *Quantum cluster theories,* Rev. Mod. Phys. **77**, 1027 (2005).

[33] F. Alet and N. Laflorencie, *Many-body localization: An introduction and selected topics,* Comptes Rendus. Physique **19**, 498 (2018).

[34] E. J. Davis *et al.*, *Probing many-body dynamics in a two-dimensional dipolar spin ensemble,* Nat. Phys. **19**, 836 (2023).

[35] S. Choi *et al.*, *Observation of discrete time-crystalline order in a disordered dipolar many-body system,* Nature **543**, 221 (2017).

[36] M. H. Abobeih *et al.*, *Atomic-scale imaging of a 27-nuclear-spin cluster using a quantum sensor,* Nature **576**, 411 (2019).

[37] M. J. Degen *et al.*, *Entanglement of dark electron-nuclear spin defects in diamond,* Nat Commun **12**, 3470 (2021).

[38] S. J. H. Loenen, *Spins in Diamond and Silicon Carbide for Quantum Networks*, Ph.D. thesis, TU Delft (2024).

[39] F. Dolde *et al.*, *Room-temperature entanglement between single defect spins in diamond,* Nat. Phys. **9**, 139 (2013).

[40] W. Ji *et al.*, *Correlated sensing with a solid-state quantum multisensor system for atomic-scale structural analysis,* Nat. Photon. (2024), 10.1038/s41566-023-01352-4.

[41] A. Ungar, P. Cappellaro, A. Cooper and W. K. C. Sun, *Control of an Environmental Spin Defect beyond the Coherence Limit of a Central Spin,* PRX Quantum **5**, 010321 (2024).

[42] T. Staudacher *et al.*, *Nuclear Magnetic Resonance Spectroscopy on a (5-Nanometer)* ^{3} *Sample Volume,* Science **339**, 561 (2013).

[43] N. Aslam *et al.*, *Nanoscale nuclear magnetic resonance with chemical resolution,* Science **357**, 67 (2017).

[44] R. Nagy *et al.*, *Quantum Properties of Dichroic Silicon Vacancies in Silicon Carbide,* Phys. Rev. Applied **9**, 034022 (2018).

[45] C. Munuera-Javaloy, A. Tobalina and J. Casanova, *High-Resolution NMR Spectroscopy at Large Fields with Nitrogen Vacancy Centers,* Phys. Rev. Lett. **130**, 133603 (2023).

[46] M. J. Biercuk, A. C. Doherty and H. Uys, *Dynamical decoupling sequence construction as a filter-design problem,* J. Phys. B: At. Mol. Opt. Phys. **44**, 154002 (2011).

[47] E. Janitz *et al.*, *Diamond surface engineering for molecular sensing with nitrogen—vacancy centers,* J. Mater. Chem. C **10**, 13533 (2022).

[48] I. Schwartz *et al.*, *Blueprint for nanoscale NMR,* Sci Rep **9**, 6938 (2019).

[49] B. A. Myers, A. Ariyaratne and A. C. B. Jayich, *Double-Quantum Spin-Relaxation Limits to Coherence of Near-Surface Nitrogen-Vacancy Centers,* Phys. Rev. Lett. **118**, 197201 (2017).

[50] D. Bluvstein, Z. Zhang, C. A. McLellan, N. R. Williams and A. C. B. Jayich, *Extending the Quantum Coherence of a Near-Surface Qubit by Coherently Driving the Paramagnetic Surface Environment,* Phys. Rev. Lett. **123**, 146804 (2019).

[51] M. Kim *et al.*, *Decoherence of Near-Surface Nitrogen-Vacancy Centers Due to Electric Field Noise,* Phys. Rev. Lett. **115**, 087602 (2015).

[52] V. Petráková *et al.*, *Luminescence properties of engineered nitrogen vacancy centers in a close surface proximity,* physica status solidi (a) **208**, 2051 (2011).

[53] J. M. Abendroth *et al.*, *Single-Nitrogen–Vacancy NMR of Amine-Functionalized Diamond Surfaces,* Nano Lett. **22**, 7294 (2022).

[54] M. Xie *et al.*, *Biocompatible surface functionalization architecture for a diamond quantum sensor,* Proc. Natl. Acad. Sci. U.S.A. **119**, e2114186119 (2022).

[55] R. Evans *et al.*, *Protein complex prediction with AlphaFold-Multimer,* (2021).

[56] A. David, S. Islam, E. Tankhilevich and M. J. Sternberg, *The AlphaFold Database of Protein Structures: A Biologist's Guide,* Journal of Molecular Biology **434**, 167336 (2022).

ACKNOWLEDGEMENTS

I've had a lot of fun with the science, but the great atmosphere at QuTech (and beyond) is what made my PhD such an enjoyable experience. I realise I am quite fortunate in this regard, as this is generally not a given when pursuing a PhD. Therefore, I would like to take this opportunity to thank those that made this journey so great.

Tim, first, let me thank you for believing in me when I applied. Looking back, I realise I was rather unqualified for the position: there were some serious gaps in my knowledge and understanding of (quantum) physics and I'm not sure if I would have hired myself. After many hour-long one-on-one sessions, you finally got me up to speed. I don't think that there are many supervisors who would go through such trouble for a student and I respect that a lot. During my time, you have taught me about all aspects that constitute a good researcher. Although writing papers has been painful for me (especially when precise statements are required), I now believe that this is the area I experienced most growth, mainly thanks to your critical attitude. I think our shared enthousiasm for physics, and intellectual pursuit in general, is what made us a great match. Discussing with you is an exciting experience, and I hope that we will keep that going in the future.

Ronald, thank you for being my promotor, and **Toeno**, **Florian**, **Florian**, **Sander** and **Simon** for being on my committee. **Toeno** in particular, as you also played a pivotal role in the process of finding my project.

Sjoerd, it was great having you as my partner in crime throughout my time here. Already from the start we really hit it off, even during the tricky COVID times, during which we were not allowed to go to university. We had some great laughs about practically anything happening at the TU and beyond; nothing beats you complaining about university bureaucracy! Let's play some more tennis soon, so I can beat you again!

Laurens, when you first joined the SiC project, we had to get accustomed to our different working styles. You are very precise and diligent, while I spend most of my time in the lab making a mess or breaking things (like piezo controllers). I think we really figured out how to work together in the end, demonstrated by the beautiful results in chapter 3. Also, I think your social attitude is vital to the success and great atmosphere of the SiC project!

Damian, we spent quite some time on M1 together having basically no clue what we were doing. You're a warm, sensitive character with a healthy dose of self-mockery, which I really admire. I know that things were tough for you at some point and I should have been more aware of that!

Gerben, it was great supervising you and **Tijmen** on the SiC project. It's amazing to see how quickly you have developed the cleanroom capabilities in our group. I think we'll be in a healthy competition in the coming years when I'm at Stanford. Looking forward to coming conferences where we can drink tequila together. **Tijmen**, sorry for taking you with me on the Titanic...

Anta, you really boosted the atmosphere in the SiC team with your humour and social mindset, making fun of **Sjoerd** (always booked for social events), **Laurens** (spy), **Gerben**

(party animal), **Dani** ("is Taminiau coming?"), and me (always running). **Dani**, I think you did a great job at our lab, and was sad to see you switch to the *dark side* (we did try our best to keep you around)!

Ben, we used to say that if anyone wants to discuss DDRF, they are "stepping into our arena". However, when discussing with you, it definitely feels more like your arena than mine. This has always been fun and educational for me, thank you for that. You are also very adept at commenting on some of the crazy things going on at the TU, much appreciated!

Nicolas, **Kian** and **Sjoerd**, it's been a pleasure sharing our office, even though we rarely witness a *full house*... **Kian**, the engineering feat that you and **Arian** pulled off is commendable, and it has been a joy listening to your guys' unsalted opinions. **Nicolas**, we really connected when I joined the band (as well as with **Christopher**!) and during our road trip in Minnesota. I will never forget the creepy cabin in the woods that we shared with **Hans** and **Matteo** (legend has it the chair is still rocking). Getting cooking lessons from **Matteo** and chatting about QMI with **Hans** (for multiple hours) was a distraction from the bloodthirsty murderers that were likely circling the house. **Hans** in particular, your unmatched persistence in arguments, and (secret) appreciation of dissenting opinions, has been a joy to experience.

Christina, **Kai** and **Benjamin**, it's been real good to see how the quantum simulation project has taken flight. Starting from onerous beginnings, I recently noticed that my contribution was becoming dispensable, which is great! The vibe at M1 is always cheerful, even when qt-lab is having its way again. Remember: *when the going gets tough, the tough get going!*

Jiwon, together with **Hans** and **Margriet**, you were a great team on M2. Your enthusiasm and seemingly unlimited positivity is definitely contagious and your impersonations of typical academics are world-class. **Hans**, you really know how to immerse yourself and soak up new experiences, which was evident on our trips to Barcelona (Sagrada familia) and the U.S. (the real American road trip). **Margriet**, your sense of humour and infectious laugh make you a pleasure to be around.

Julia, **Nina**, **Alejandro** and **Yanik**, our road trip to the American canyons was amazing. **Julia**, it has always been very easy talking to you, starting from the Bad Honnef conference, where I drove you back in my car which by then I had only crashed once (or twice). You are definitely a core member of Team Diamond, keep doing what you do! During the road trip we also covered a bunch of intimate, non-work-related topics (especially **Alejandro** was adept at initiating these with **Nina**). However, I'm afraid that Sjoerd and I were fooling you when we outed his lucrative side business! **Yanik**, your quirky humour and kindness are a great combo, and I loved the introduction to German efficiency when organising the Diamond cup together with **Julius**.

Mohamed, **Conor**, **Joe** and **Maarten**, I consider you the original crew, who have helped me on my way. **Conor** and **Joe**, you showed me the ropes on M1, and **Mohamed**, you are a kind and wise person, supporting me during our summer school in Corsica, when I had a difficult time.

I want to thank all current and previous members of Team Diamond, and Qutech in general (shout-out to the band!). The social fabric that comes with pursuing a PhD at QuTech is truly unique, and we should not take this for granted. In particular I want to extend my gratitude to the technicians and support staff (**Sara**, **Marja**, **Esther**), not in the least for co-

organising the incredible social events at QuTech.

To **JC Hefboom** and **de Drukkerij**, thank you for being a great group of friends, who made the past four years such an adventure also outside work.

Mama and **Papa**, thank you for all the encouragement and praise that you often give me, already starting from a young age. This is the reason I dare to dream big. Of course I shouldn't forget **Marnix** and **Laurine** for making my childhood so much fun (rollerblading and making movies).

Then finally, **Alex**, you were made to listen to all my stories about quantum mechanics, about spectral diffusion, about DDRF. Sadly, I've not lived up to your initial expectation of teleporting live spiders, but luckily I have managed to at least find some of them in the 'lettuce'. You've always been extremely supportive of me, even though I can be quite absent when immersed in my measurements. Thank you that I can be so truly myself around you and for making my life so adventurous. I hope you also got something out of it: a beautiful wedding day and many adventures awaiting in sunny California!

List of Publications

1. *Check-probe spectroscopy of lifetime-limited emitters in bulk-grown silicon carbide*
G. L. van de Stolpe*, L.J. Feije*, S.J.H. Loenen*, A. Das, G.M. Timmer, T.W. de Jong and T. H. Taminiau.
arXiv 2409.13018 (2024)

2. *Improved electron-nuclear quantum gates for spin sensing and control*
H. B. van Ommen*, **G.L. van de Stolpe***, N. Demetriou, H.K.C. Beukers, J. Yun, T. Fortuin, M. Iuliano, A. R.-P. Montblanch, R. Hanson and T. H. Taminiau.
arXiv 2409.13610 (2024)

3. *Mapping a 50-spin-qubit network through correlated sensing*
G. L. van de Stolpe, D. P. Kwiatkowski, C. E. Bradley, J. Randall, S. A. Breitweiser, L. C. Bassett, M. Markham, D. J. Twitchen, and T. H. Taminiau.
Nature Communications **15**, 2006 (2024)

4. *Hyperpolarization of nuclear spins: Polarization blockade*
O. T. Whaites, C. I. Ioannou, B. J. Pingault, **G.L. van de Stolpe**, T.H. Taminiau, and T.S. Monteiro.
Physical Review Research, **5**(4), 043291 (2023)

5. *Micrometer-sized TPM emulsion droplets with surface-mobile binding groups*
C. Van der Wel, **G.L. van de Stolpe**, R.W. Verweij, and D.J. Kraft.
Journal of Physics: Condensed Matter **30**(9), 094005 (2018)

*Equally contributing authors

CURRICULUM VITÆ

Guido Luuk VAN DE STOLPE

06/12/1994	**Born in 's-Hertogenbosch, The Netherlands**
2007–2013	**Secondary School**
	Gymnasium Beekvliet
2013–2017	**BSc in Physics**
	Leiden University
2017	Research Student, Kraft group, Leiden University
2017–2020	**MSc in Physics** (cum laude)
	Leiden University
	Thesis: *"Global warming through wavefunction collapse"*
	Supervisor: Prof. T.H. Oosterkamp
2020	Research Student, van der Sar group, Delft University of Technology
2020–2024	**PhD in Physics**
	Delft University of Technology
	Thesis: *"Quantum sensing in diamond and silicon carbide: mapping spins and taming charges"*
	Group: Taminiau Lab, QuTech and Kavli Institute of Nanoscience
	Promotor: Prof. dr. ir. Ronald Hanson
	Co-promotor: Dr. ir. Tim H. Taminiau

A

APPENDIX FOR CHAPTER 3

A

A.1. SPECTRAL DYNAMICS MODEL DERIVATION

The Lorentzian spectral propagator is given by[1]:

$$P_f(t) = \pi^{-1} \frac{\frac{1}{2}\gamma(t)}{f^2 + \left(\frac{1}{2}\gamma(t)\right)^2}, \tag{A.1}$$

where f is the detuning from resonance. The FWMH $\gamma(t)$ is linear in time[1]:

$$\gamma(t) = \gamma_\mathrm{d}\, t. \tag{A.2}$$

The mean detected counts a function of detuning f between the laser and the emitter's resonance frequency is given by a Lorentzian:

$$\lambda_\mathrm{L}(f) = C_0 \frac{\left(\frac{\Gamma}{2}\right)^2}{f^2 + \left(\frac{\Gamma}{2}\right)^2}, \tag{A.3}$$

with C_0 the observed counts on resonance and Γ the emitters homogeneous line width (FWHM). This Lorentzian is normalised such that $\lambda(0) = C_0$. We can add the effect of ionisation by describing the ionisation probability as:

$$P_\mathrm{i}(t) = 1 - e^{-\gamma_\mathrm{i} t}, \tag{A.4}$$

Here, γ_i is assumed to be independent of emitter detuning. However, if ionisation is caused by a two-photon process, we would expect the ionisation rate to scale with the square of the excitation rate:

$$\gamma_\mathrm{i}(f) = \gamma_\mathrm{i}^0 \left(\frac{(\frac{1}{2}\Gamma)^2}{f^2 + (\frac{1}{2}\Gamma)^2} \right)^2, \tag{A.5}$$

where γ_i^0 is the ionisation rate on resonance. Then,

$$\gamma_\mathrm{i} = \int_{-\infty}^{\infty} P_f\, \gamma_\mathrm{i}(f) df = \frac{\gamma_i^0}{2} \frac{\Gamma\gamma(t) + 2\Gamma^2}{(\gamma(t) + \Gamma)^2} \tag{A.6}$$

The mean counts can then be calculated as:

$$\lambda(f,t) = (1 - P_\mathrm{i}(t))\ \lambda_\mathrm{L}(f), \tag{A.7}$$

Next, we integrate over the spectral density:

$$C(t) = \int_{-\infty}^{\infty} P_f(t)\, \lambda(f,t)\, df, \tag{A.8}$$

which can be solved to yield:

$$C(t) = C_0 \frac{1}{1 + \gamma_\mathrm{d}\, t/\Gamma} e^{-\gamma_\mathrm{i} t}. \tag{A.9}$$

where we can either decide to model γ_i as a constant, or by equation (A.6). Additionally, if we neglect the recapture or de-ionisation rate, then for values of $t < 0$, effectively $\gamma_i = 0$.

A.2. MODEL PERFORMANCE AND DEPENDENCE ON SET COUNTS THRESHOLD

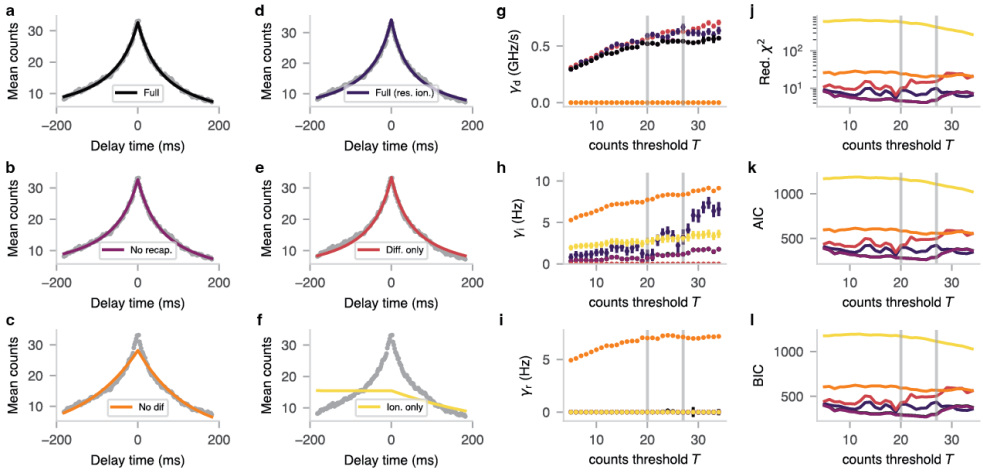

Figure A.1: **Comparison of models for perturbation by the NIR lasers. a-f)** Data from Fig. 3.3d, overlayed with the various models, which are described in Table A.1. **g-i)** Estimated rates $\gamma_d, \gamma_i^0, \gamma_r$ as a function of counts threshold T for the different models. We observe a saturating behaviour for high T, as the defect is initialised in a more specific frequency range. For very high treshold values, the lack of data creates large fluctuations in the obtained rates. To determine the rate values in Table A.1, we take an average over the values indicated by the grey solid lines and take the standard deviation as uncertainty. **j-l)** Various goodness of fit models (reduced χ-squared, AIC, BIC) indicate that the model presented in the main text (Std.) captures the data best. Here, we also observe a saturation behaviour, where the sudden drop for very high T is attributed to overfitting due to lack of data. Colors in (g-l) match the models described in (a-f). The 'Full' data overlaps with the 'Full (res.ion.)' curve. Errorbars are based on photon shot noise (grey data), or represent fit uncertainties (panels g-i).

The model presented in the main text describes spectral diffusion caused by a macroscopic bath of fluctuating dipoles (described by the spectral propagator in Eq. A.1). We can compare the performance of this model compared to other versions of the model, which restric certain parameters, for example one that assumes that no spectral diffusion (or ionisation) occurs. Table A.1 presents the description of the models we fitted to the data.

Sweeping the counts threshold value T, we observe that all models saturate to a range of values for higher T, consistent with the intuition that stringent thresholds initialise the emitter more precisely on resonance with the lasers. At very high tresholds ($T \gtrapprox 35$), only very little data is available, and rates obtained with all models start to fluctuate heavily (due to the noisy data). Hence, we emperically determine a convergence region: $20 \leq T \leq 27$ (grey solid lines in Fig. A.1 and $12 \leq T \leq 21$ in Fig. A.2), over which we average to obtain the rates presented in the main text.

Comparing various goodness of fit metrics (reduced χ-squared, AIC, BIC), we learn that the 'No recap' model describes the data best (Fig. A.1j-l), indicating that recapture is virtually not present under NIR-laser illumination.

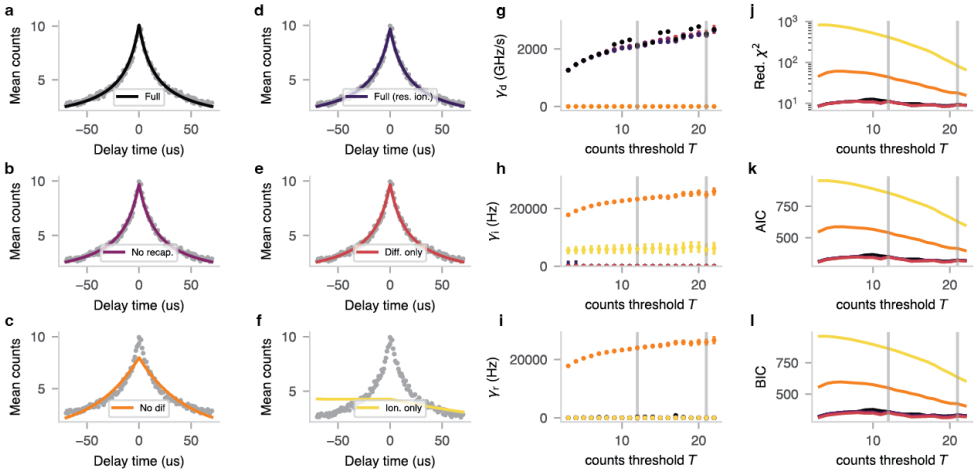

Figure A.2: **Comparison of models for perturbation by the repump laser. a-i)** Same as Fig.A.1, but for the data presented in Fig. 3.3e.

Table A.1: Models used for fitting in Figs. A.1 and A.2

Model name	Description
Full	$C(t)/C_0 = \begin{cases} (1+\gamma_d\, t/\Gamma)^{-1}\, e^{-\gamma_i t}, & \text{if } t>0. \\ (1-\gamma_d\, t/\Gamma)^{-1}\, e^{\gamma_r t}, & \text{otherwise.} \end{cases}$
Full (res. ion.)	$C(t)/C_0 = \begin{cases} (1+\gamma_d\, t/\Gamma)^{-1}\, e^{-\frac{\gamma_i^0}{2}\frac{\Gamma\gamma(t)+2\Gamma^2}{(\gamma(t)+\Gamma)^2}t}, & \text{if } t>0. \\ (1-\gamma_d\, t/\Gamma)^{-1}\, e^{\gamma_r t}, & \text{otherwise.} \end{cases}$
No recap.	$C(t)/C_0 = \begin{cases} (1+\gamma_d\, t/\Gamma)^{-1}\, e^{-\gamma_i t}, & \text{if } t>0. \\ (1-\gamma_d\, t/\Gamma)^{-1}, & \text{otherwise.} \end{cases}$
Diff. only	$C(t)/C_0 = \begin{cases} (1+\gamma_d\, t/\Gamma)^{-1}, & \text{if } t>0. \\ (1-\gamma_d\, t/\Gamma)^{-1}, & \text{otherwise.} \end{cases}$
No diff.	$C(t)/C_0 = \begin{cases} e^{-\gamma_i t}, & \text{if } t>0. \\ e^{\gamma_r t}, & \text{otherwise.} \end{cases}$
Ion. only	$C(t)/C_0 = \begin{cases} e^{-\gamma_i t}, & \text{if } t>0. \\ 1, & \text{otherwise.} \end{cases}$

A.3. DIFFUSION POWER DEPENDENCE

Here we plot the diffusion rates extracted by the method in figure 3.3 for different resonant and NIR laser powers. The data in figure 3.3 was averaged over the powers corresponding to the last two data points in figure A.3a and b for the repump and NIR laser respectively.

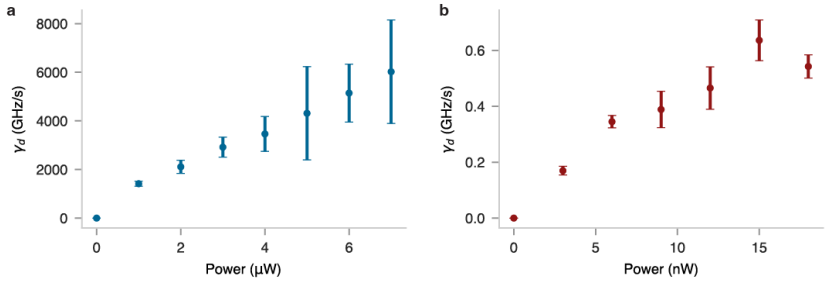

Figure A.3: **Diffusion rates as function of laser power. a)** Diffusion rate γ_d as a function of applied repump laser power (785 nm, as in Fig. 3.3c). Data from 8-10 μW are omitted as the CR-check was not passed, due to drifting of the objective (leading to a diminished collection efficiency). **b)** Diffusion rate γ_d as a function of applied resonant laser power (916 nm, single laser). Data points for both panels are an average over fits with thresholds $T = \{10, 14, 18\}$, and error bars denote the standard deviation of the extracted rates. Laser powers are measured at the entrance of the objective. The rates presented in Fig. 3.3d are an average of the two final (saturation) data points for both panels (with their standard deviation as error bar).

In another sample (same wafer and fabrication method, but with an irradiation dose of $2 \times 10^{12}\,\mathrm{cm}^{-2}$), we investigated a V2 center with significantly lower (saturation) spectral diffusion rates under NIR laser illumination (~ 6 times smaller compared to the emitter from the main text, see Fig. A.3). The extracted diffusion and ionisation rates for different NIR laser powers can be found in A.4b-d. We observe a saturation-type behaviour for spectral diffusion (up to 70 nW) and an (approximately quadratic) increase in (on-resonance) ionisation rate for higher powers.

A

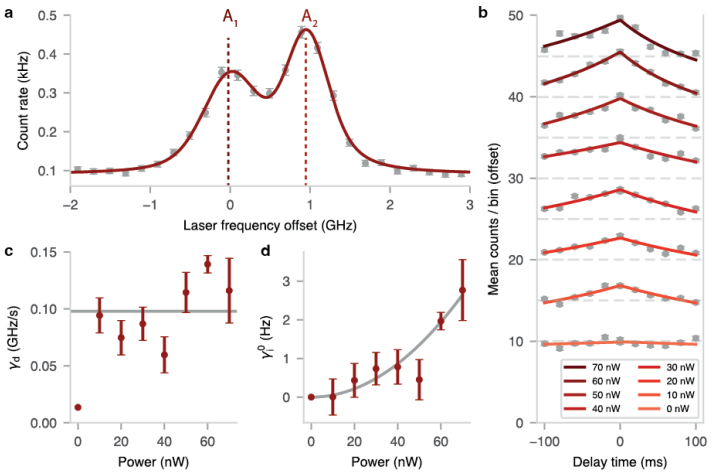

Figure A.4: **Diffusion rates of a** V2 **center in a different nanopillar a)** Diffusion-averaged PLE of the V2 center in a different nanopillar (in a different sample) compared to Fig. 3.1f, yielding FWHMs of ~ 802 MHz and ~ 680 MHz for the A_1 and A_2 transitions, respectively. **b)** Diffusion check-probe spectroscopy as in Fig. 3.3d in the main text, for different NIR-laser powers (916 nm). We explicitly set $\gamma_\Gamma = 0$ (as suggested by Fig. A.1) to ensure convergence of the fit. The grey dotted lines indicate the threshold $T = 10$ used for the 'probe' block. Data are offset by 3 for visual clarity. **c)** Diffusion rates extracted from (b). with a mean diffusion rate of 0.098 GHz/s **d)** (On resonance) ionisation rates extracted from (b). Solid grey line is a guide to the eye: $y = Ax^2$, with $A = 5.4 \times 10^{-4}$ HznW^{-2} and x the NIR laser power.

A.4. BAYESIAN ANALYSIS OF THE CHECK-PROBE SPECTROSCOPY SIGNAL

The spectrum obtained from the *check-probe* spectroscopy measurements in Figs. 3.4 and 3.5 contains residual inhomogeneous broadening, due to non-perfect initialisation on-resonance with the f_1 laser frequency during the 'check' block. To account for such residual broadening, we need to considere the spectral probability density of the emitter immediately after the 'check' block, given that the minimum counts threshold T was passed. Evidently, such a spectral probability density will strongly depend on T, with higher threshold values resulting in sharper distributions around f_1. To quantify this intuition, we apply Bayes' theorem to compute the spectral probability density after detecting $m \geq T$ photons:

$$P(f \,|\, m \geq T) = \frac{P(m \geq T \,|\, f)\, P(f)}{P(m)} = \frac{1}{N_T} P(m \geq T \,|\, f)\,, \tag{A.10}$$

with f the emitter frequency and N_T some (numerically determined) normalisation constant. In the second step, we have assumed minimal knowledge on the spectral distribution before the 'check' block, by taking the (improper) prior $P(f)$ to be (locally) flat. This assumption is justified if the diffusion-averaged inhomogeneous linewidth (Fig. 3.1f) is much larger than the homogenous linewidth (Fig. 3.4b). Otherwise, a different prior function may be used (e.g. the Gaussian used for fitting the data in Fig. 3.1f).

Assuming Poissonian photon statistics, Eq. A.10 can be solved to yield:

$$P(f \,|\, m \geq T) = \frac{1}{N_T} \sum_{T}^{\infty} \frac{\lambda(f-f_1)^m\, e^{-\lambda(f-f_1)}}{m!} = \frac{1}{N_T} \left(1 - \Gamma_{\mathrm{i}}\left[T, \lambda(f-f_1)\right]\right), \tag{A.11}$$

with $\lambda(f)$ the expected mean number of counts during a single 'check' block when the emitter is at frequency f and the laser at frequency f_1, and $\Gamma_{\mathrm{i}}[a,z] = \frac{1}{\Gamma_{\mathrm{c}}[a]} \int_z^\infty t^{a-1} e^{-t}\, dt$, the incomplete Gamma function, with $\Gamma_{\mathrm{c}}[a]$ the Euler Gamma function.

Here, $\lambda(f)$ encodes (our model of) the 'pure' spectral response of the emitter, independent of residual inhomogeneous broadening, and solely governed by the underlying physical parameters whose value we aim to extract. For a simple Lorentzian lineshape, $\lambda(f)$ is given by:

$$\lambda_{\mathrm{L}}(f) = C_0 \frac{\left(\frac{\Gamma}{2}\right)^2}{f^2 + \left(\frac{\Gamma}{2}\right)^2} \tag{A.12}$$

with Γ the homogeneous linewidth (FWHM) and C_0 the mean number of detected counts on resonance. Conversely, the Landau-Zener-Stückelberg spectrum can be described by (see also Eq. 3.6):

$$\lambda_{\mathrm{LZS}}(f) = C_0 \sum_k \frac{\Omega_k^2}{\frac{1}{T_1 T_2} + \frac{T_2}{T_1}\left(k\omega - f\right)^2 + \Omega_k^2}\,, \tag{A.13}$$

The spectral probability densities can then be computed by inserting λ_{L} or λ_{LZS} into Eq. A.11, the results of which are shown in Fig. A.5a and e, respectively.

Finally, to obtain an expression for the spectroscopy signal (i.e. the mean number of detected photons C during the probe block), we take the convolution of the spectral probability density (i.e. the residual inhomogeneous broadening) and the pure spectral response

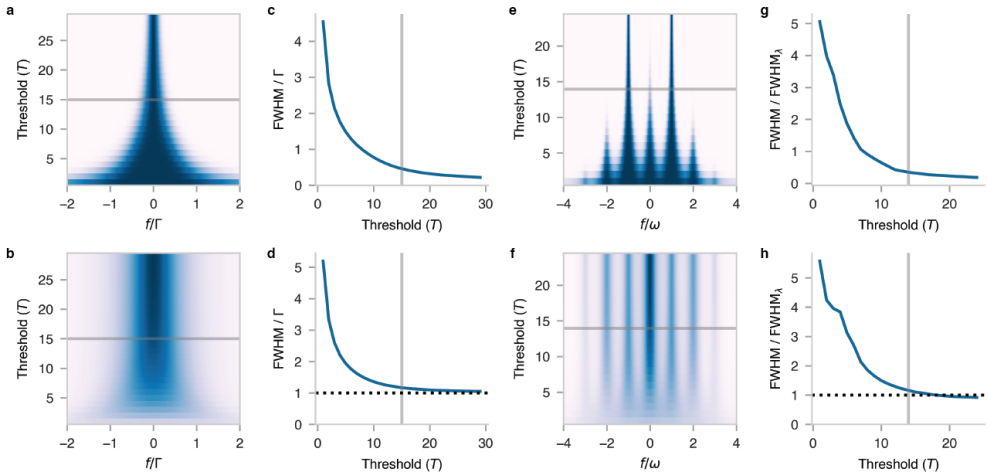

Figure A.5: **Bayesian spectrum analysis. a)** Spectral probability density $P(f \mid m \geq T)$ as a function of threshold for $\lambda(f) = \lambda_{\mathrm{L}}(f)$ (Lorentzian, Eq. A.12). Probabilities at each threshold value are normalised to their maximum value for visual clarity. Solid grey line denotes the maximum of $\lambda(f)$ for all panels. **b)** Check-probe spectroscopy signal, obtained by evaluating Eq. A.14 for the spectral density calculated in (a). **c)** Full width at half maximum (FWHM) of the spectral density in (a). In the high-threshold regime ($T \gg \max\left[\lambda(f)\right]$, the linewidth becomes negligible compared to the linewidth of $\lambda(f)$ itself. **d)** Linewidth of the spectroscopy signal, which converges to that of the pure spectral response $\lambda(f)$ for high thresholds (black dotted line). **e)** Same as in (a), but for $\lambda(f) = \lambda_{\mathrm{LZS}}(f)$, which has two global maxima (Eq. A.13). LZS parameters are chosen to be equal to those extracted from the 6.5 V measurement in the main text (see Fig. 3.5 and Fig. A.6). **f)** Same as in (b), but for the spectral density calculated in (e). **g)** FWHM of (e), computed by integrating the frequency ranges for which $P(f \mid m \geq T) > \frac{1}{2}\max\left[P(f \mid m \geq T)\right]$ (and normalised to the range for which: $\lambda_{\mathrm{LZS}}(f) > \frac{1}{2}\max\left[\lambda_{\mathrm{LZS}}(f)\right]$). **h)** Same as in (d), but for the signal shown in (f). Note that for the LZS spectrum, which contains multiple global maxima, the FWHM does not neccesarily converge to the FWHM of $\lambda(f)$.

$\lambda(f)$ (assuming equal duration of the 'check' and 'probe' blocks):

$$C(f) = P(f \mid m \geq T) * \lambda(f), \tag{A.14}$$

Importantly, both terms in the convolution involve $\lambda(f)$ (through Eq. A.11), and the first is strongly dependent on the chosen threshold value (see Fig. A.5a and e), allowing for the extraction of the pure spectral response by sweeping T (in post-processing). Moreover, as expected, the degree of residual inhomogeneous broadening diminishes for higher threshold values (see Fig. A.5c and d).

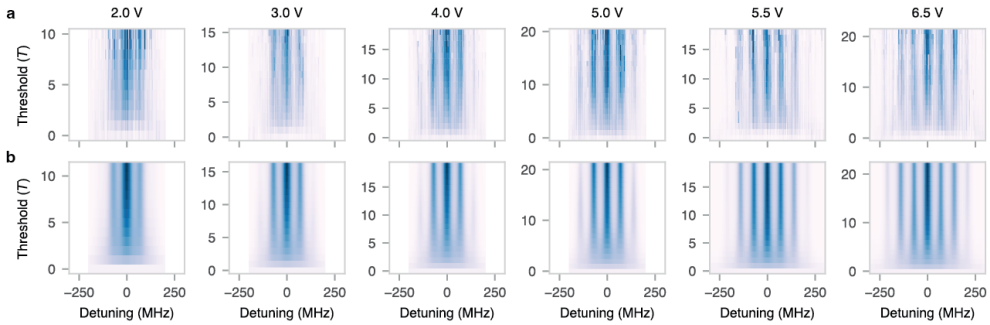

Figure A.6: **Bayesian analysis of the LZS interference signal. a)** Experimental data underlying the extracted parameters presented in Fig. 3.5i and j (applied voltage annotated), as a function of the two-laser detuning ($f_2 - f_1$) and the set threshold T. **b)** Fit of the data in (a) to Eq. A.14, using only three free fit parameters: A, Ω and T_2, together with a general scaling and offset. The fixed fit parameters ω and T_1 are set to 70 MHz and 7 ns, respectively. The dependence on T is fixed by the model (Eq. A.11).

A

A.5. MEAN LINEWIDTH APPROXIMATION

As noted in the main text, for the check-probe spectroscopy experiments that are executed with the MW mixing instead of the two NIR lasers, there is an approximately equal chance of initialising the system on the A_1 transition, or the A_2 transition. Hence, we expect the observed spectrum to be a (weigthed) average of both spectra, weighted by the respective initialisation probabilities. Assuming near-equal brightness of the transitions[2], we approximate this weighting to be roughly 50/50.

To compare the measured linewidth (after accounting for residual inhomogeneous broadening, see A.4), with the expected lifetime limit, we approximate the weigthed mean of the two Lorentzian transitions, to be a Lorentzian with linewidth given by the weighted mean of the respective linewidths:

$$\Gamma = p\Gamma_{\mathrm{A}_1} + (1-p)\Gamma_{\mathrm{A}_2} \tag{A.15}$$

with p the probability of initialising on the A_1 transition, and $\Gamma_{\mathrm{A}_1} \approx 26\,\mathrm{MHz}$ and $\Gamma_{\mathrm{A}_2} \approx 14\,\mathrm{MHz}$ the linewidths (FWHM) of the A_1 and A_2 transitions, respectively[2]. For these values, Eq. A.15 approximates the true linewidth with deviation less than 5% (Fig. A.7b).

A more rigorous treatment for estimating the individual A_1 and A_2 linewidths consists of explicitly specifying both transitions (separated by $\Delta \approx 1\,\mathrm{GHz}$) with their respective amplitudes and lifetimes in the spectral response function $\lambda(f)$ (instead of using Eqs. 3.4 and 3.6). A more straightforward solution is to use an additional third laser (not available in this work) to perform the 'check' block as is done in Fig. 3.3a, which leaves no ambiguity for the initialisation configuration. Both the A_1 or A_2 transitions can then be measured individually by using a single NIR laser (together with the MW radiation) to probe around the two laser frequencies used in the 'check' block.

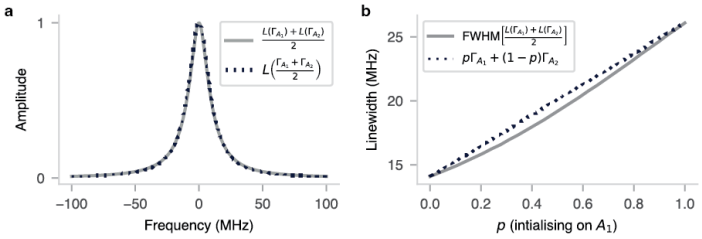

Figure A.7: **Mean linewidth approximation. a)** Comparison between the equal mean of two Lorentzians with FWHM $\Gamma_{\mathrm{A}_1} = 26\,\mathrm{MHz}$ and $\Gamma_{\mathrm{A}_2} = 14\,\mathrm{MHz}$ (grey line) and a single Lorentzian function with a FWHM of $\Gamma = \frac{\Gamma_{\mathrm{A}_1}+\Gamma_{\mathrm{A}_2}}{2} = 20\,\mathrm{MHz}$ (blue dotted line), showing qualitative agreement (< 1% amplitude deviation). Legend: $L(\Gamma)$ denotes the Lorentzian distribution with FWHM Γ. **b)** Numerically determined linewidth (FWHM) of the weighted mean (with weights p and $1-p$) of two Lorentzians with FWHM Γ_{A_1} and Γ_{A_2} as in (a) (grey line). The blue dotted approximates the actual linewidth by a (linear) weighted mean (Eq. A.15), showing deviations of less than 5%.

A.6. SPECTRAL DIFFUSION DYNAMICS DURING 'SCANNING' PLE

Complementary to the measurements in Fig. 3.4, we perform repetitive PLE linescans of a V2 center (as in Refs.[3–7], among others). This is a different V2 center than the one studied in the main text, in particular, it resides in a different sample diced from the same wafer, but electron-irradiated at a slight lower dose of $2 \times 10^{12}\,\mathrm{cm}^{-2}$. For fair comparison, we include the diffusion-averaged PLE measurement, and the NIR-lasers diffusion measurement (see Fig. 3.1f and as in Fig. 3.3d of main text) in Fig. A.8. These measurements indicate large diffusion-averaged linewidth and a high spectral diffusion rate (8(2) GHz/s). As noted in earlier work[3,6,7], summing individual scans may result in underestimation of the homogeneous linewidth due to limited photon statistics[6], or to overestimation of the linewidth if the emitter frequency changes during, and in between, repetitions. From the spectral diffusion measurements we can roughly distill the diffusion timescale to be $\sim 10\,\mathrm{ms}$. Since a single PLE linescan cannot be performed (with our current hardware) faster than the diffusion timescale, we limit the time during which the NIR laser is on. We scan the frequency by ramping an external voltage to the cavity of the laser (1.4 V). Each PLE scan takes 500 ms, where each voltage step (19 mV) the NIR-laser is turned on for 1 ms with 10 nW of power, resulting in a total NIR-laser time of 71 ms during a single repetition.

A

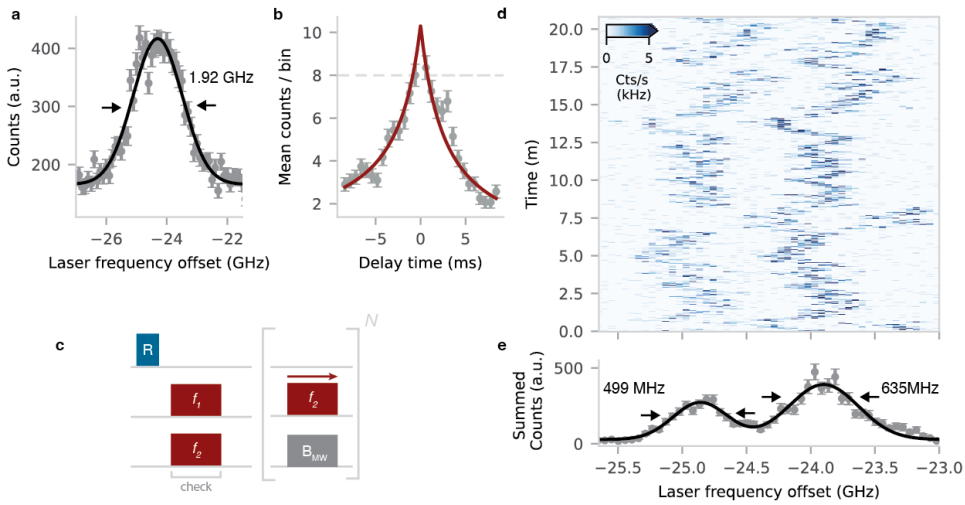

Figure A.8: **Spectral diffusion during repetitive NIR-laser PLE scans. a)** Diffusion-averaged broadening of the defect in a different nanopillar (in a different sample) compared to the main text with ~ 1.92 GHz FWHM. **b)** Spectral diffusion measurement and fit under 10 nW of NIR laser excitation (916 nm) (same measurement as Fig. 3.3). **c)** Experimental sequence used for the repetitive-scanning experiment. A 'check' block is executed until the collected counts exceed a set threshold (here T = 30). Subsequently, the f_2 laser is scanned by ramping an external voltage to the cavity of the laser (1.4 V), while applying microwave resonant with the ground-state spin transition (6 V, different wire-sample distance compared to main text) with $N = 500$ scans. Each scan takes 500 ms, where each voltage step (19 mV) the resonant laser is turned on for 1 ms with 10 nW of power, resulting in a total resonant laser time of 71 ms during a single repetition. Before and after the voltage scan, the laser frequency is measured (1 s) and a linear extrapolation between the start end and frequency is created to convert the applied voltage to an applied laser frequency. **d)** 500 PLE scans of the same defect as in b). Each repetition, the laser is scanned over ~ 3 GHz). **e)** Summed counts of all the repetitions, indicating the A1 and A2 transition at −24.86 GHz and −23.90 GHz respectively, with FWHMs of 499(14) MHz, and 635(11) MHz, respectively (Gaussian fit). The laser frequency is offset to 327.112 THz.

A.7. CONFOCAL MICROSCOPY SETUP

In Fig. A.9 the schematics of the optical setup is shown, which is divided into two parts, in-fiber (left) and free-space (right). The electronics are not depicted in the figure.
In Fiber: Two NIR lasers (916 nm, Toptica DL Pro and the Spectra-Physics Velocity TLB-6718-P, are frequency-locked to a wavemeter (HF-Angstrom WS/U-10U), using a 99:1 beamsplitter. Their optical power is modulated by acousto-optic-modulators (AOM, G&H SF05958). The power of the 785 nm repump laser (Cobolt 06-MLD785) is directly controlled via analog modulation. A wavelength division multiplexer (WDM, OZ Optics) combines the 785 nm repump and 916 nm NIR laser light, after which the light is coupled out to free space using a zoom fiber collimator (Thorlabs, ZC618APC).
Free Space: The collimated beam passes through a variable neutral density filter (ND, Thorlabs NDC-50C-4-B), after which a shortpass filter (Semrock, FF01-945/SP-25) is used to remove any residual noise from the NIR lasers. A $\frac{\lambda}{2} - \frac{\lambda}{4}$ waveplate combination allows for polarisation control. The excitation path and detection path are separated with a broadband 90:10 beamsplitter (Thorlabs, BS041).

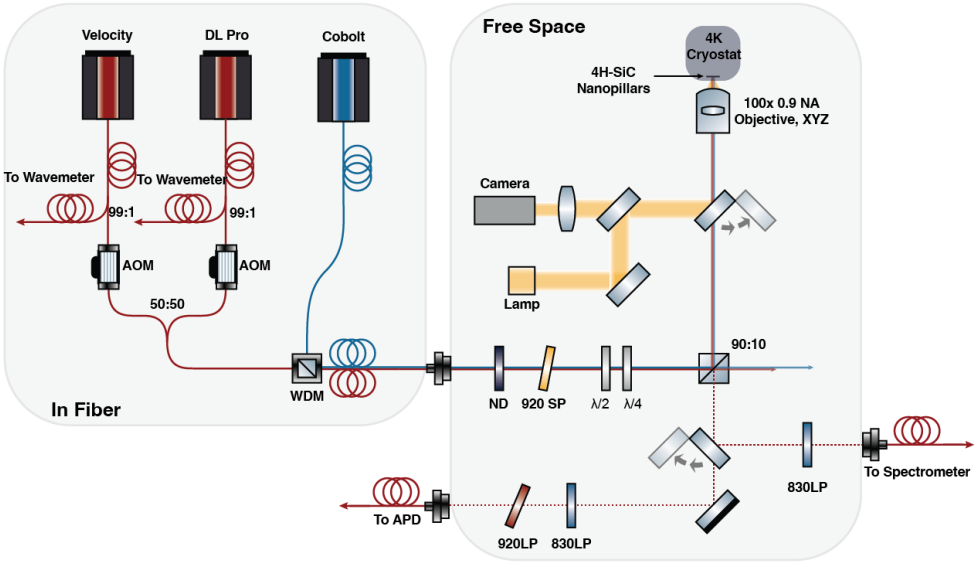

Figure A.9: **Optical setup.** Description of elements is given in the text.

A flip mirror and 50:50 pellicle beamsplitter (Thorlabs, BP150) enable imaging of the sample with a visible LED (MCWHL6-C2) and a CCD-camera (ClearView Imaging, BFS-U3-16S2M-CS). A 0.9 NA microscope objective (Olympus, MPLFLN 100x) is used to focus excitation light onto the nanopillars, and to collect fluorescence. The objective is kept at room temperature and under vacuum, and can be moved using a configuration of 3 piezo-electric stages (PI Q545.140). The sample is cooled down to 4 K in a cryostat (Montana Instruments S100), while a heat shield kept at 30 K limits thermal radiation from the objective.

Collected fluorescence passes through a 90:10 beamsplitter, after which it can be routed either to a spectrometer (Princeton Instruments IsoPlane 81), filtered with an 830 nm long-pass filter (Semrock, BLP01-830R-25), or to an avalanche photon detector (APD, Laser components, COUNT-50N) with an expected detection efficiency of 35% at 920 nm and 18% at 1000 nm. Next to a 830 nm long pass filter, an additional long-pass filter (Semrock, FF01-937/LP-25), placed at an angle, is used to filter out reflected light originating from the NIR lasers (916 nm).

Electronics Microwave pulses are generated with an arbitrary waveform generator (Zurich Instruments, HDAWG8), and subsequently amplified (Mini-circuits LZY-22+). A bondwire is spanned across the sample to deliver the MW radiation close to the sample surface ($\sim 50\,\mu$m). The coarse time scheduling (1 µs resolution) of the experiments is managed by a microcontroller (ADwin Pro II).

A.8. LITERATURE REVIEW ON SILICON CARBIDE QUANTUM EMITTER LINEWIDTHS

In this section we provide an overview of the work done using silicon vacancies and divacancies in silicon carbide in the context of optical coherence. In table A.2, we report on multiple parameters that can impact the optical coherence. These parameters include the defect generation method, the annealing strategy, the measured optical absorption linewidth, material parameters of the layer that contains the investigated defect, and the use of a potential nanostructure for efficient light extraction.

Work	Defect	Defect generation	Annealing	PLE linewidth	Sample parameters in the defect layer	Nanostructure
Banks 2019 [8]	V2	e: 1e12 cm^{-2}, 2 MeV	-	~65 MHz	18µm n-doped epi layer. [N]=~3e14 cm^{-3}	-
Nagy 2019 [9]	V1	e: 1e12 cm^{-2}, 2 MeV	30 m, 600°C	~60 MHz	110µm [^{28}Si]>99.85%, [^{13}C]>99.98% epi layer. [N] = ~3.5e13 cm^{-3}	SIL
Udvarhelyi 2020 [10]	V1 & V2	e: 1e13 cm^{-2}, 2 MeV	30 m, 600°C	~100 MHz	110µm [^{28}Si]>99.85%, [^{13}C]>99.98% epi layer. [N]=~3.5e13 cm^{-3}	SIL
Nagy 2021 [11]	V2	e: 1e13 cm^{-2}, 2 MeV	-	~300 MHz*	[N]=~5e13 cm^{-3}	-
Babin 2022 [4]	V2	He^{+}: 1e11 cm^{-2}, 6 keV	30 m, 600°C	~25-40 MHz	110µm [^{28}Si]>99.85%, [^{13}C]>99.98% epi layer. [N]=~4e13 cm^{-3}	-
Babin 2022 [4]	V2	e: 5e11 cm^{-2}, 2 MeV	30 m, 600°C	Best: ~30 MHz	28µm [^{28}Si]>99.85%, [^{13}C]>99.98% epi layer. [N]=~3e15 cm^{-3}	Triangular waveguides
Lukin 2020 [12]	V2	e: 1e13 cm^{-2}, 2 MeV	30 m, 300°C	~100 MHz	100µm ^{28}Si^{13}C epi layer.	-
Lukin 2020 [12]	V2	e: 5e12 cm^{-2}, 23 MeV	30 m, 300°C	~100 MHz	100µm ^{28}Si^{13}C epi layer.	-
Lukin 2023 [13]	V2	e: 1e13 cm^{-2}, 2 MeV	2 h, 550°C†	~40 MHz	20µm n-doped epi layer. [N]=~2e13 cm^{-3}	Disk resonator
Fang 2023 [14]	V1	e: 2.3e12 cm^{-2}, 10 MeV	30 m, 500°C	~60 MHz	80µm epi layer. [N]=~2e13 cm^{-3}	SIL
Christle 2017 [15]	VV	e: 5e12 cm^{-2}, 2.5 MeV	30 m, 750°C	~2 GHz	730µm sublimation epitaxially grown 3C-SiC layer. [N]~5e15 cm^{-3}	-
Christle 2017 [15]	VV	e: 5e12 cm^{-2}, 2 MeV	30 m, 745°C	~100 MHz	120µm 4H-SiC epi layer. [N]<5e13 cm^{-3}	-
Miao 2019 [16]	VV	e: 3e12 cm^{-2}, 2 MeV	30 m, 850°C	~21 MHz	20µm i-type epi layer. [N]<1e15 cm^{-3}	-
Anderson 2019 [5]	VV	-	-	~31 MHz	-	-
Crook 2020 [17]	VV	e: 1e16 cm^{-2}, 2 MeV	30 m, 850°C	~4 GHz	n-p-n-i-n epi layers. ([N_n]=1e18, [Al_p]=1e18, [N_i]<1e15) cm^{-3}	Photonic crystal cavity
Anderson 2022 [18]	VV	e: 1e13 cm^{-2}, 2 MeV	810°C	<0.5 GHz	90µm [^{28}Si]>99.85%, [^{13}C]>99.98% epi layer. [N]=~6e13 cm^{-3}	No nanostructure

Table A.2: Sample parameters on literature publications that demonstrated PLE measurements with silicon vacancy (V1, V2) defects and divacancy (VV) defects in silicon carbide. A dash (-) indicates the information is not specified in the respective publication. *: Increased linewidth attributed to global sample properties, such as an increased Fermi level due to the elevated [N], rather than defect density. †: Annealing tailored to HSQ bonding for sample preparation.

REFERENCES

[1] G. Zumofen and J. Klafter, *Spectral random walk of a single molecule,* Chemical Physics Letters **219**, 303 (1994).

[2] D. Liu *et al.*, *The silicon vacancy centers in SiC: Determination of intrinsic spin dynamics for integrated quantum photonics,* npj Quantum Inf **10**, 72 (2024).

[3] J. Heiler *et al.*, *Spectral stability of V2 centres in sub-micron 4H-SiC membranes,* npj Quantum Mater. **9**, 34 (2024).

[4] C. Babin *et al.*, *Fabrication and nanophotonic waveguide integration of silicon carbide colour centres with preserved spin-optical coherence,* Nat. Mater. **21**, 67 (2022).

[5] C. P. Anderson *et al.*, *Electrical and optical control of single spins integrated in scalable semiconductor devices,* Science **366**, 1225 (2019).

[6] L. Orphal-Kobin *et al.*, *Optically Coherent Nitrogen-Vacancy Defect Centers in Diamond Nanostructures,* Phys. Rev. X **13**, 011042 (2023).

[7] M. K. Koch, V. Bharadwaj and A. Kubanek, *Limits for coherent optical control of quantum emitters in layered materials,* (2023), arXiv:2312.11090 [quant-ph] .

[8] H. B. Banks *et al.*, *Resonant Optical Spin Initialization and Readout of Single Silicon Vacancies in 4H-SiC,* Phys. Rev. Appl. **11**, 024013 (2019).

[9] R. Nagy *et al.*, *High-fidelity spin and optical control of single silicon-vacancy centres in silicon carbide,* Nat Commun **10**, 1954 (2019).

[10] P. Udvarhelyi *et al.*, *Vibronic States and Their Effect on the Temperature and Strain Dependence of Silicon-Vacancy Qubits in 4H-SiC,* Phys. Rev. Appl. **13**, 054017 (2020).

[11] R. Nagy *et al.*, *Narrow inhomogeneous distribution of spin-active emitters in silicon carbide,* Appl. Phys. Lett. **118**, 144003 (2021).

[12] D. M. Lukin *et al.*, *Spectrally reconfigurable quantum emitters enabled by optimized fast modulation,* npj Quantum Inf **6**, 1 (2020).

[13] D. M. Lukin *et al.*, *Two-Emitter Multimode Cavity Quantum Electrodynamics in Thin-Film Silicon Carbide Photonics,* Phys. Rev. X **13**, 011005 (2023).

[14] R.-Z. Fang *et al.*, *Experimental Generation of Spin-Photon Entanglement in Silicon Carbide,* Phys. Rev. Lett. **132**, 160801 (2024).

[15] D. J. Christle *et al.*, *Isolated Spin Qubits in SiC with a High-Fidelity Infrared Spin-to-Photon Interface,* Phys. Rev. X **7**, 021046 (2017).

[16] K. C. Miao *et al.*, *Electrically driven optical interferometry with spins in silicon carbide,* Sci. Adv. **5**, eaay0527 (2019).

[17] A. L. Crook *et al.*, *Purcell Enhancement of a Single Silicon Carbide Color Center with Coherent Spin Control,* Nano Lett. **20**, 3427 (2020).

[18] C. P. Anderson *et al.*, *Five-second coherence of a single spin with single-shot readout in silicon carbide,* Sci. Adv. **8**, eabm5912 (2022).

B

APPENDIX FOR CHAPTER 4

B

B.1. NV HAMILTONIAN

The NV center is described by a spin-1 electron coupled to a spin-1 nitrogen spin, with additional couplings to spin-1/2 ^{13}C spins. This work is limited to the $m_s = 0, -1$ subspace of the electron spin. The interaction with the spin-1 nitrogen spin is neglected, as it is initialized in the $m_N = 0$ state and the decoupling sequences effectively cancel the interaction between electron and nitrogen spin. Considering one ^{13}C spin, the Hamiltonian of the system is, in the interaction picture and after the rotating-wave and secular approximation, given by:

$$H = \omega_0 I_z + A_\parallel S_z I_z + A_\perp S_z I_x + 2\Omega \cos\big(\omega_{\mathrm{RF}} t + \phi\big) I_x, \tag{B.1}$$

where $A_\parallel = A_{zz}$ and $A_\perp = \sqrt{A_{zx}^2 + A_{zy}^2}$ are the parallel and perpendicular components of the NV-nuclear hyperfine tensor, S_z, I_z and I_x are the electron and nuclear (pseudo) spin-1/2 operators, Ω is the physical RF amplitude, ω_{RF} is the RF frequency, and ϕ is some phase offset of the RF field. Note that, in general, the axis of $A_\perp$ and the axis along which the RF-radiation is applied are not the same. In the present work, for simplicity, the effect of $A_\perp$ is neglected[1], further motivated by the high magnetic field (189.1 mT) at which experiments were performed. At such high fields, the tilt of the nuclear quantisation axis is small ($< 1°$ for $A_\perp \sim 30$ kHz). We do take into account the changed nuclear precession frequency due to $A_\perp$, given by: $\omega_1 = \sqrt{A_\perp^2 + (\omega_0 - A_\parallel)^2}$. In the rotating frame at the RF frequency (and again making the rotating wave approximation) Eq. B.1 simplifies to:

$$H_{\mathrm{RF}} = |0\rangle\langle 0| \otimes \Delta_0 I_z + |1\rangle\langle 1| \otimes \Delta_1 I_z + \hat{\mathbb{1}} \otimes \Omega(\cos\phi I_x + \sin\phi I_y), \tag{B.2}$$

B.2. SIMULATION OF DDRF SPECTROSCOPY

Spectroscopy experiments (Figs. 4.2b, 4.5d) have been simulated assuming the presence of 15 individual nuclear spins (Table B.1) and a bath of weakly coupled spins.

For an individual nuclear spin c, the unitary operation U of an $N = 2$ DDRF unit-cell was calculated starting from H_{RF} (Eq. 4.2). For starting electron state $|0\rangle$ ($|1\rangle$), the rotation axis $\hat{\mathbf{n}}_{0,c}$ ($\hat{\mathbf{n}}_{1,c}$) and angle $\theta_{0,c} (= \theta_{1,c})$ of the nuclear spin rotation was determined. If the electron spin starts in the $|x\rangle$ state, the $\langle\sigma_x\rangle_c$ expectation value after a DDRF gate with N pulses is given by[2]

$$\langle\sigma_x\rangle_c = 1 - (1 - \hat{\mathbf{n}}_{0,c} \cdot \hat{\mathbf{n}}_{1,c}) \sin^2 \frac{N\theta_c}{2}. \tag{B.3}$$

The total signal from the individual spins is given by the product of the expectation values:

$$\langle\sigma_x\rangle = \prod_c \langle\sigma_x\rangle_c \tag{B.4}$$

For the nuclear spin bath, a mean density of parallel hyperfine shifts Δ is used[3]

$$\rho(\Delta) = \frac{\pi^2 \alpha \rho_{^{13}\mathrm{C}}}{\Delta^2}, \tag{B.5}$$

where $\alpha = \hbar\mu_0\gamma_e\gamma_c/4\pi$, and $\rho_{^{13}\mathrm{C}} = n_{13}\rho_C = 1.950\mathrm{nm}^{-3}$ is the density of ^{13}C in natural abundance diamond, where n_{13} is the relative abundance of ^{13}C atoms in the environment (1.109%), and ρ_C is the density of C atoms in diamond.

Instead of calculating the bath signal for a random sample of individual spins[4], we calculate the signal for a sufficient number of bins (300 in this work) of Δ of width $d\Delta$. The expected number of spins in such a bin is given by $\rho(\Delta)d\Delta$. The spectroscopy signals for each bin $\langle\sigma_x(\Delta)\rangle$ are calculated with Eq. B.3 and combined to yield the total signal of the spin bath:

$$\langle\sigma_x\rangle_{\mathrm{bath}} = \prod_{\Delta=-\Delta_{\mathrm{lim}}}^{\Delta_{\mathrm{lim}}} \langle\sigma_x(\Delta)\rangle^{\rho(\Delta)d\Delta} \tag{B.6}$$

where Δ_{lim} defines the maximum coupling strength of spins that are still considered part of the spin bath, in this work $\Delta_{\mathrm{lim}} = 2\pi \times 6$ kHz. Note that this approach breaks down when the signal due to a single spin with Δ becomes large. The total signal is given by the product of the signals of individual spins and the spin bath.

Index	Δ (Hz)	Index	Δ (Hz)	Index	Δ (Hz)
C_0^*	-30693	C_5	-12570	C_{10}	-9500
C_1^*	-45870	C_6^*	15744	C_{11}	-9000
C_2	20000	C_7	-10020	C_{12}	-13060
C_3	19900	C_8^*	-11160	C_{13}	-6193
C_4^*	18500	C_9	-7660	C_{14}	-7200

Table B.1: Characterised nuclear spin hyperfine shifts. Spins marked with * form the register considered in Section 4.6.

The Rabi frequency Ω was determined from the waveform amplitude of the RF pulses and an experimentally determined conversion factor from waveform amplitude to Ω. The pulse length τ_{rf} is adjusted by half the length of the pulse roll-on time (Appendix 4.9) to approximately account for the smaller effective pulse amplitude, and the dead-time around the MW pulses is subtracted. The RF Hamiltonian is applied for a duration of τ_{rf}, and during the dead-time we set $\Omega = 0$. The simulation could be made more accurate by considering a time-dependent Ω, matching the pulse shape, at the cost of computation time.

From the spectroscopy signal, we qualitatively identify 15 individual nuclear spins that can be distinguished from the spin bath (listed in Table B.1).

B.3. THEORETICAL FIDELITY OF DETUNED GATES

We present a closer study of the theoretically achievable fidelity of DDRF gates on a single nuclear spin, neglecting $A_\perp$. We consider the spin and gate parameters from Fig. 4.2c: $\Delta = -30.7$kHz, $\tau = 24.654$us, $\Omega = 313$Hz. We numerically calculate the DDRF gate unitary U using H_{RF} (Eq. 4.2) and compare it to the ideal unitary

$$U_{\text{ideal}} = |0\rangle\langle 0| \otimes R_x(\pi/2) + |1\rangle\langle 1| \otimes R_x(-\pi/2)\,. \tag{B.7}$$

To compare U and U_{ideal}, we decompose U into its rotation angle θ, and rotation axes $\hat{\mathbf{n}}_0$ and $\hat{\mathbf{n}}_1$, for each starting electron spin state (See more detail in Section B.9). We then calculate

$$U' = |0\rangle\langle 0| \otimes e^{-i\frac{\pi}{2}\hat{\mathbf{n}}_0\cdot\vec{\sigma}} + |1\rangle\langle 1| \otimes e^{-i\frac{\pi}{2}\hat{\mathbf{n}}_1\cdot\vec{\sigma}}\,, \tag{B.8}$$

and compare that to U_{ideal} (Fig. B.1). This assumes that the rotation angle of the gate can be tuned to be $\pi/2$, which could experimentally be achieved with a calibration sequence. Tuning the rotation angle with N has no effect on $\hat{\mathbf{n}}_{0,1}$, and fine tuning with Ω would only slightly affect $\hat{\mathbf{n}}_{0,1}$.

First we consider resonant and off-resonant DDRF gates (Fig. B.1,a). We find that high gate fidelities ($F > 0.999$) are achievable for a wide range of detunings. To maximise gate fidelity, it is necessary to adjust the single-pulse phase increment δ_ϕ slightly from the previously derived resonance condition (Eq. 4.3).

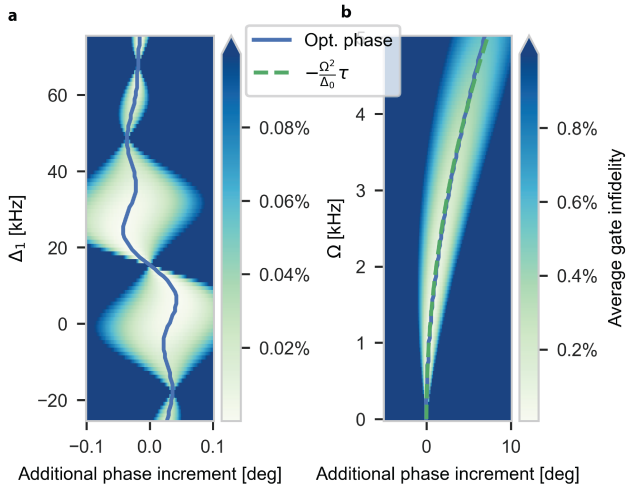

Figure B.1: **Optimal single-pulse phase increment**. **a)** Average gate infidelity of a DDRF gate, over a range of RF detunings Δ_1 and phase increments δ_ϕ. The phase increment on the x-axis is added to the resonant δ_ϕ as derived in Eq. 4.3. The optimal phase increment (that yielding the highest fidelity) varies with the applied RF frequency. **b)** As a function of Rabi frequency Ω, the optimal phase increment for a gate on-resonance with one of the nuclear spin frequencies (here $\Delta_1 = 0$) can be predicted using the AC-Stark shift.

Increasing the Rabi frequency reveals why the optimal δ_ϕ changes (Fig. B.1b). When

driving on resonance ($\Delta_1 = 0$), the optimal phase increment is shifted by

$$\delta_{\mathrm{AC}} = -\frac{\Omega^2}{\Delta_0}\tau\,. \tag{B.9}$$

We attribute this effect to the AC-Stark shift[5]. The presence of RF radiation at the ω_1 frequency causes the ω_0 frequency of the nuclear spin to shift, resulting in a different amount of phase being picked up by the spin while the electron is in the $|0\rangle$ state. For other RF frequencies a combined effect of shifting both nuclear spin resonance frequencies occurs.

B.4. EXPRESSION FOR THE SENSITIVITY

We define the single spin sensitivity according to Ref. [6]:

$$\nu_{\min} = \frac{e^{\chi(t)}\sqrt{t+t_m}}{\gamma C(t_m)\, t}, \tag{B.10}$$

where t is the single experiment sensing time, t_m is the readout time, C is a readout efficiency parameter, γ is the signal transduction parameter and $\chi(t)$ is the coherence function of the sensor spin. For simplicity, We assume an ideal, instantaneous readout ($C = 1$, $t_m = 0$). For the system under study here, this assumption is reasonable as the (single-shot) readout fidelity is $\gtrapprox 90\%$ and the readout time ($t_m < 50$ µs) is significantly shorter than the typical sensing time ($t \sim 1$ ms) [1]. In our case, γ is equal to the (effective) Rabi frequency $\tilde{\Omega}/(2\pi)$ and has units Hz/spin, as a single nuclear spin induces phase on the sensor at this rate. Eq. B.10 then reduces to:

$$\nu_{\min} = \frac{2\pi e^{\chi(N,t)}}{\tilde{\Omega}_{\max}(\Delta, N)\sqrt{t}}, \tag{B.11}$$

which is equal to Eq. 4.8 in the main text.

Note that the electron coherence function $\chi(N,t)$ during the DDRF sequence is dependent on the number of applied decoupling pulses N [4]:

$$\chi(N,t) = \left(\frac{t}{T(N)}\right)^n, \tag{B.12}$$

with $n = 2$, and the coherence time $T(N)$ given by:

$$T(N) = T_{N=4}\left(\frac{N}{4}\right)^{\eta}, \tag{B.13}$$

with $T_{N=4} = 2.99$ ms and $\eta = 0.799$ [4].

B.5. OPTIMAL RF DETUNING

The optimal RF detuning condition for a specific Δ and τ, is found by choosing Δ_1 (and corresponding $\Delta_0 = \Delta_1 - \Delta$) so that Eq. 4.5 is maximised. As Eq. 4.5 and its derivatives are transcendental, it is not trivial to find these maxima. Therefore, we look for an approximate solution, by considering the function's behaviour in the limit of long and short τ.

In the limit of long τ (defined as $\tau \gg 2\pi/|\Delta|$), the optimal detuning is (trivially) $\Delta_1 = 0$. In this limit, the two sinc functions in Eq. 4.5 are completely separated and the global maximum is simply the maximum of the sinc function centered around ω_1 (Fig. B.2a).

However, for short τ, the spectral width of the sinc functions increases, so that they interfere destructively, which pushes the optimal detuning condition outwards (Fig. B.2a). In the short τ limit ($\tau \ll 2\pi/|\Delta|$), we can conceptually see that maximum $\tilde{\Omega}$ will be attained when the difference in driving between the ω_0 and ω_1 transitions is largest, as this maximises the conditional character of the gate. For the square RF pulses considered in this work, this condition is satisfied when the sinc pulse envelope has maximum gradient at $\bar{\omega} = (\omega_1 + \omega_0)/2$ (schematically illustrated in Fig 4.4a). By evaluating the second derivative of the sinc function, we find that the (maximum gradient) inflexion point is located at a distance w_s away from the peak center, with $w_s \approx 2.082$ the first root of the second derivative of the sinc function. Requiring this point to be positioned precisely in between the two transitions (i.e. $\Delta/2$ away from ω_1), we arrive at the condition:

$$\Delta_1 = -\frac{w_s}{\tau} + \Delta/2\,. \tag{B.14}$$

It is not a priori obvious that these two limiting cases perform well in describing the optimal condition in the intermediate regime ($\tau \sim 2\pi/|\Delta|$). To evaluate the validity of the limiting cases, and to investigate their performance in the intermediate regime, we compute Eq. 4.5 for a range of τ-values (Fig. B.2a) and extract numerically its maximum value (Fig. B.2b, solid blue line). We compare this numerical value to a composite function, generated by joining the limiting descriptions at condition $\tau = 2\pi/|\Delta|$:

$$\Delta_1 = \begin{cases} -\frac{w_s}{\tau} + \Delta/2, & \text{if } \tau \lesssim 2\pi/|\Delta|. \\ 0, & \text{otherwise} \end{cases} \tag{B.15}$$

which is equal to Eq. 4.9 in the main text. We find good agreement between the numerical maximum, and the effective Rabi frequency obtained by inserting Eq. B.15 in Eq. 4.5, which yields:

$$\tilde{\Omega}/\Omega = \begin{cases} \mathrm{sinc}\left(w_s - \frac{\Delta\tau}{2}\right) - \mathrm{sinc}\left(w_s + \frac{\Delta\tau}{2}\right), & \text{if } \tau \lesssim 2\pi/|\Delta| \\ 1 - \mathrm{sinc}(\Delta\tau)\,, & \text{otherwise} \end{cases} \tag{B.16}$$

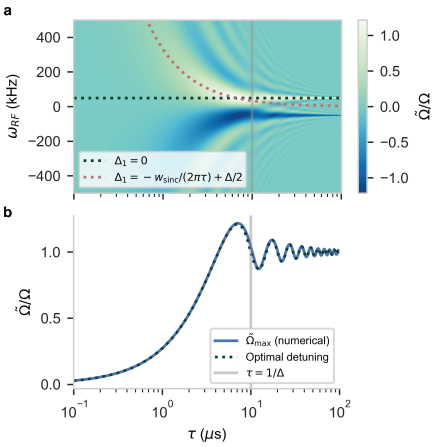

Figure B.2: **Optimal RF detuning a)** Evaluation of Eq. 4.5 for a range of interpulse spacings τ, sweeping the RF detuning (by varying ω_{RF}). The simulated nuclear spin has a hyperfine coupling $\Delta = 50\,\mathrm{kHz}$. The darkgreen dotted line indicates resonant driving, while the red dotted line indicates the (optimal) RF detuning in the regime $\tau < 1/\Delta$ (grey solid line). **b)** Maximum (relative) effective Rabi frequency as a function of τ, computed by taking the maximum value in (a) (blue solid line). We find good agreement with the analytical (maximum) expression, obtained by evaluating Eq. 4.5 with RF detuning described by Eq. 4.9 (blue dotted line).

We observe only a $< 5\%$ deviation between Eq. B.16 and the maximum of Eq. 4.5 across the full range (Fig. B.2b, blue dotted line). Thus, we conclude that Eq. B.15 is suitable for finding the optimal RF detuning in a sensing setting.

B.6. SENSING OPTIMISATION PROCEDURE

To find optimal sensing parameters we follow the steps described in Fig. B.2 and in the main text. First, we compute the effective Rabi frequency for a range of realistic N and τ values[4]. Then, we compute the optimal physical RF amplitude Ω. Ideally, this power is increased to exactly counter the reduction in Rabi frequency. However, this requires setting the Rabi amplitude to very large values for small τ. As Eq. 4.5 is only valid in the regime $\Omega\tau \ll 1$, we limit the amplitude to: $\Omega = \min[1/(2\tau), 10\,\text{kHz}]$. Figure B.3b shows the set RF amplitude under this limitation. In the bottom-right region of the graph, the modification of the Rabi frequency is small (see Fig. B.3a), and therefore Ω is not increased significantly. In the top-left corner however, the desired RF amplitude exceeds our set limits, and its values is capped at 10 kHz. Note that the optimal sensing parameters depend on the precise choice of the limits. Therefore, it will be important to re-evaluate these in practice, depending on the specific limitations of the experimental setup (e.g. RF delivery efficiency or cryogenics).

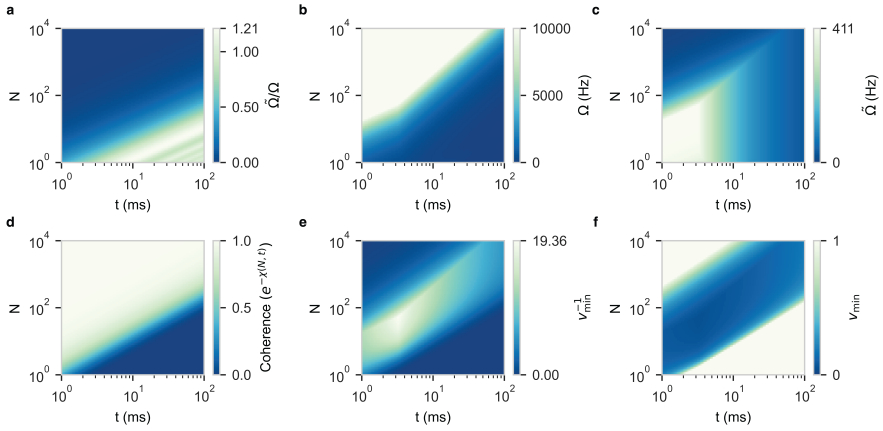

Figure B.3: **Optimal parameters for sensing. a)** Relative effective Rabi frequency as a function of the total DDRF sequence length (t) and number of applied electron pulses (N), obtained by evaluating Eq. B.16. **b)** Physical RF amplitude Ω, which is set to counter the suppression of the Rabi frequency visible in (a). **c)** The effective Rabi frequency, calculated by taking the product of (a) and (b). **d)** The electron coherence function, taken from Ref.[4]. Adding more pulses (shortening the interpulse spacing τ) leads to increased electron coherence at constant gate time t. **e)** The inverse of the sensitivity, defined in Eq. 4.8 in the main text, calculated by multiplying (c) and (d). **f)** The sensitivity function, showing a significant region where single-spin selectivity ($\nu_{\text{min}} < 1$) is attainable. To generate the data in Fig. 4.4d, we generate this plot for a range of Δ values and numerically pick the minimum value.

Next, the effective Rabi frequency is computed by multiplying the values obtained in Fig. B.3a and b. Then, we compute the expected electron coherence for all values of N and τ, based on the decoherence function from Ref.[4]. We compute the sensitivity according to Eq. 4.8 and plot its value, and its inverse, in Fig B.3f and e, respectively. A sensitivity below one (blue region in Fig. B.3f) means the sequence is sensitive to a single nuclear spin.

Finally, we generate these plots for a number of coupling strengths Δ, ranging from 30 Hz to 10 kHz, and numerically select the maximum value for the sensitivity. Then, we repeat the

process without allowing for detuned driving, which results in significantly lower sensitivity. The results are shown in Fig. 4.4 in the main text.

B.7. BOUND FOR GATE SELECTIVITY

We present a brief mathematical justification for the DDRF gate selectivity that accumulates over the duration of the gate (4.14). If we assume negligible driving of the nuclear spin when the electron is in the $|0\rangle$ state (i.e. assuming $\Delta_0\tau \gg \pi$, which also implies $\Delta_0 \gg \Omega$, given that $\Omega\tau \ll 1$), the dynamics can be approximated by the Hamiltonian:

$$H_{\mathrm{RF},|1\rangle} = |0\rangle\langle 0| \otimes \Delta_0 I_z + |1\rangle\langle 1| \otimes (\Delta_1 I_z + \Omega(\cos\phi I_x + \sin\phi I_y)). \tag{B.17}$$

A compact expression for the electron spin's spectroscopy response $\langle S_x\rangle$ can be found when the phase increment $\delta_\phi = -\Delta_0\tau + \pi$ (Section B.9):

$$\langle S_x\rangle = \frac{1}{2}\left(1 - \frac{2}{1+\Delta_1^2/\Omega^2}\sin^2\left(\frac{N\tau}{2}\sqrt{\Omega^2+\Delta_1^2}\right)\right). \tag{B.18}$$

Note that this δ_ϕ is the optimal phase increment when $\Delta_1 = 0$ (Eq. 4.3). For $\Delta_1 \neq 0$, and for $|0\rangle$ being the electron $m_s = 0$ state (giving all spins the same Δ_0), the above equation predicts the electron spin's response to a bystander spin, which diminishes due to the mismatch between δ_ϕ and the bystander spin's actual evolution. The minimum detuning Δ_1 between the bystander spin and the target spin which causes no crosstalk is given by the first zero of the electron spin's response. Considering the case of an entangling gate between the electron and target spin ($\Omega N\tau = \pi/2$), there is no crosstalk if

$$\Delta_1 = \frac{\sqrt{15}\pi}{2N\tau}. \tag{B.19}$$

Translating this to a difference in mean frequency results in

$$\frac{\Delta_0^t + \Delta_1^t}{2} - \frac{\Delta_0^b + \Delta_1^b}{2} = \bar{\omega}^{\mathrm{t}} - \bar{\omega}^{\mathrm{b}} = \frac{\sqrt{15}\pi}{4N\tau}. \tag{B.20}$$

Furthermore, the selectivity can be argued from the lorentzian factor $\frac{2}{1+\Delta_1/\Omega^2}$ in Eq. B.18. Under the entangling gate condition $\Omega = \frac{\pi}{2N\tau}$, this lorentzian has a full-width at half-maximum of $\frac{\pi}{N\tau}$.

B.8. MULTI-QUBIT REGISTER OPTIMISATION

In this section we provide more details on the spin register simulations (Fig. 4.5). The M two-qubit DDRF unitaries between the electron spin and each nuclear spin in the register are calculated using Eqs. B.40 and B.41. The unitaries are corrected for deterministic phase offsets on the idling qubits, which could be taken into account experimentally at no fidelity cost by calibrating virtual-Z gates. The total $(M+1)$-qubit unitary U_c is subsequently constructed from these two-qubit unitaries, by extending them to the $M+1$ qubit register space and concatenating them, which assumes that they commute. The resulting unitary is an approximation that neglects nuclear-nuclear interactions, as well as electron-nuclear interactions with spins outside the register. Below we will introduce the effects of such interactions in a phenomenological way. We also assume idealised (i.e. instantaneous) electron spin pulses that neglect the effect of the electron-nuclear coupling during the pulse.

The $M+1$-qubit gate fidelity is calculated according to:

$$F(U_t, U_c) = \frac{\sum_j \mathrm{Tr}\left(U_t U_j^\dagger U_t^\dagger U_c U_j U_c^\dagger\right) + d^2}{d^2(d+1)}, \tag{B.21}$$

where the summation j is over the Pauli matrices and d is the dimension of the Hilbert space[7].

To incorporate electron-spin dephasing, which commutes with the unitary U_c, a dephasing error channel is applied after U_c. The single-qubit error channel on the electron spin is given by the transformation:

$$\epsilon(\rho) = \sum_i \hat{K}_i \rho \hat{K}_i^\dagger, \tag{B.22}$$

with Kraus operators:

$$\hat{K}_0 = \sqrt{\frac{(1+\lambda)}{2}}\hat{\mathbb{I}}, \qquad \hat{K}_1 = \sqrt{\frac{(1-\lambda)}{2}}\hat{Z}, \tag{B.23}$$

Leading to an error channel for the $M+1$-qubit unitary:

$$\epsilon_{M+1}(\rho) = \frac{(1+\lambda)}{2}\hat{\mathbb{I}}^{\otimes(M+1)}\rho\hat{\mathbb{I}}^{\otimes(M+1)} + \frac{(1-\lambda)}{2}(Z\otimes\hat{\mathbb{I}}^{\otimes M})\rho(Z\otimes\hat{\mathbb{I}}^{\otimes M}). \tag{B.24}$$

The average gate fidelity of the operator U_c, followed by the dephasing channel ϵ_{M+1}, is then given by:

$$F(U_t, U_c, \lambda) = \frac{(1+\lambda)}{2}F(U_t, U_c) + \frac{(1-\lambda)}{2}F(U_t, Z' U_c), \tag{B.25}$$

where $Z' = Z\otimes\hat{\mathbb{I}}^{\otimes M}$.

The parameter λ quantifies the dephasing of the electron spin, which may have one or more independent origins. Considering the dephasing due to the T_2 of the electron spin (λ_{T_2}, due to the nuclear spin bath dynamics) and the direct DDRF-gate-mediated interaction with (mixed) bath spins (λ_{bath}), the total dephasing is given by $\lambda = \lambda_{\mathrm{bath}}\lambda_{T_2}$, with

$$\lambda_{\mathrm{bath}} = \langle\sigma_x\rangle_{\mathrm{bath}}, \qquad \lambda_{T_2(N,t)} = e^{-(\frac{t}{T(N)})^n}, \tag{B.26}$$

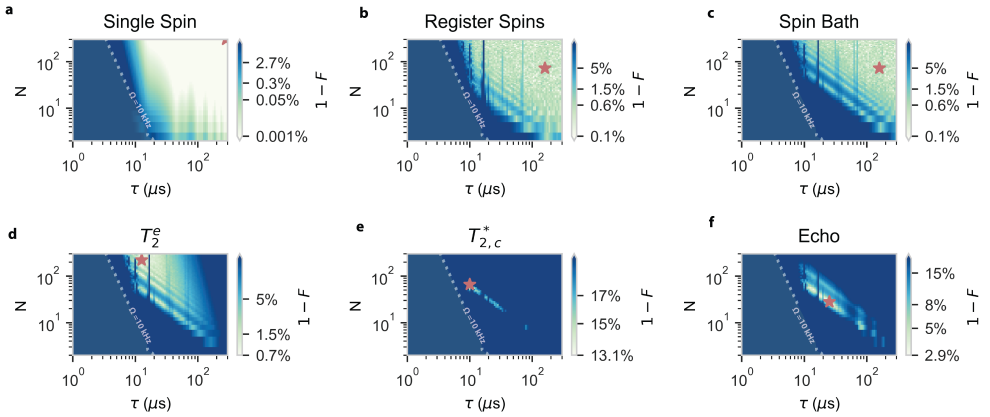

Figure B.4: **Infidelity contributions in a 6-qubit register.** F is the 6-qubit gate fidelity. Panel (a-e) show the different contributions in infidelity with C_4 as target qubit. **a)** Considering only the target, for which high-fidelity gates exist across the parameter space. The RF amplitude is limited to $\Omega < 10\,\text{kHz}$ (dotted line) resulting in a sharp fidelity drop-off. At larger N, the approximation used for obtaining Eq. 4.5 loses validity. **b)** Considering unitary evolution of all 6 spins in the register (from U_c). **c)** Also including the signal of a sampled spin bath, using Eq. B.6 for λ_{bath} (Eq. B.26) and the remaining identified individual bystander spins (Table B.1) **d)** Also including the electron-spin T_2 dephasing under dynamical decoupling (Eq. B.26), which limits both τ and gate times. **e)** Also including the $T_2^\star$ dephasing of the nuclear-spin register qubits by averaging over a distribution of magnetic fields δ_B. This hinders the performance, both by stochastic detuning of the target qubit operation, and by direct dephasing of the register. **f)** Also including a correction on the phase of all register qubits (Eq. B.27), akin to performing a spin-echo operation on all register qubits, meant to decouple the qubits from quasi-static noise [1,8].

where $\langle\sigma_x\rangle_{\text{bath}}$ quantifies the RF-mediated electron dephasing due to the nuclear spin bath (Appendix B.2) and $T_2(N,t)$ is the dephasing time of the electron spin during a dynamical decoupling sequence of N pulses and duration t (Appendix B.4).

We implement $T_2^\star$ nuclear-spin dephasing, which does not commute with the unitary evolution during the DDRF gate, by sampling static magnetic fields offsets δ_B from a Gaussian distribution with standard deviation $\sigma_B = 1/\left(\sqrt{2}\pi\gamma_c T_2^\star\right)$, where γ_c is the ^{13}C gyromagnetic ratio and $T_2^\star$ the decoherence time for ^{13}C nuclear spins (≈ 10 ms). We calculate average gate fidelities (Eq. B.25) for 10 magnetic fields uniformly sampled within 2 σ_B. To calculate the final fidelity, we compute an average weighted by the magnetic field probability distribution.

In typical experimental settings [1,8], RF spin-echo pulses are performed after the gate to counter nuclear-spin dephasing. We simulate this by explicitly correcting for additional phases acquired by the spins in the register due to the sampled magnetic field offsets. We update the calculated unitary according to:

$$U_c' = R_z(-2N\tau\gamma_c\delta_B)U_c \tag{B.27}$$

To give further insight into the effect of each source of infidelity, we investigate their cumulative effects on the infidelity for C_4 (Fig. B.4). We also present the gate fidelity maps for all 5 electron-controlled gates in the 6-qubit register (Fig. B.5).

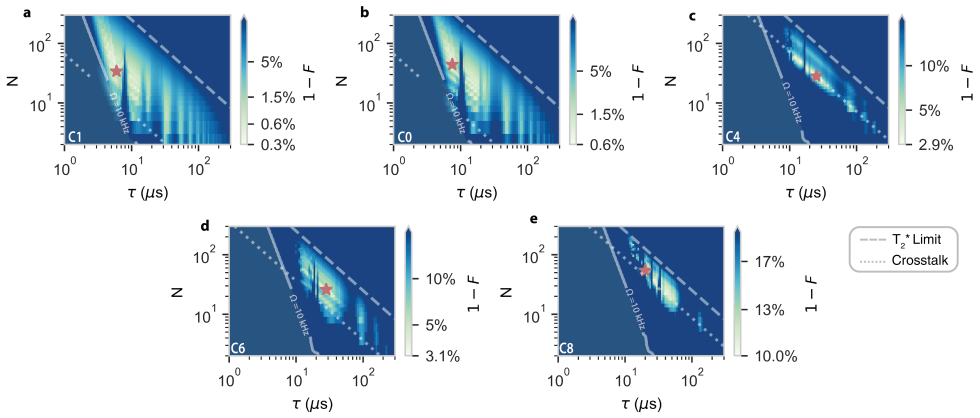

Figure B.5: **Characterisation for all 5 electron-nuclear spin controlled gates in the 6-qubit register. a-e)** For each nuclear spin participating in the register we calculate the 6-qubit average gate fidelity for the U_t gate, given by Eq. B.25. The τ for which crosstalk occurs with other nuclear spins is different for each target spin. The spectral isolation of a spin sets a minimum gate length (dotted lines, Eq. 4.11), and the nuclear spin T_2^* a maximum gate length (dashed lines indicate $2N\tau$ = 5,ms). For C_8 the many spins in close spectral proximity result in a lower attainable gate fidelity.

B.9. ANALYTIC DESCRIPTION OF DDRF GATES

In this section, we present an exact analytical solution to the evolution during a DDRF gate, when RF driving is neglected when the electron is in $|0\rangle$. Although this approximation is only valid in the regime where $\Delta > 1/\tau$, it provides much insight in the spin dynamics for the general $\Delta < 1/\tau$ case.

The electron-nuclear Hamiltonian, only considering driving the electron $|1\rangle$ state, in the rotating frame of the RF radiation, is given by:

$$H_{\mathrm{RF},|1\rangle} = |0\rangle\langle 0| \otimes \Delta_0 I_z + |1\rangle\langle 1| \otimes (\Delta_1 I_z + \Omega(\cos\phi I_x + \sin\phi I_y)), \tag{B.28}$$

The following derivation shows similarities to the derivation used to analyse resonant DD control of nuclear spins[2]. In this approximation of driving during only one electron state, there are two differences between DD and DDRF: the Rabi frequency Ω takes the role of $A_\perp$ in resonant DD, and the phase of the RF driving can be changed between pulses, while for DD $A_\perp$ always acts along the same axis in the lab frame.

The unitary operator $U_{\mathrm{N=2}}$ that describes the action of a single (N=2) DDRF block is given by

$$U_{\mathrm{DDRF,N=2}} = e^{-iH_{\mathrm{RF}}\tau}(R_x(\pi)\otimes R_z(\delta_\phi))e^{-2iH_{\mathrm{RF}}\tau}(R_x(\pi)\otimes R_z(\delta_\phi))e^{-iH_{\mathrm{RF}}\tau}, \tag{B.29}$$

where $R_z(\delta_\phi) = e^{-i\delta_\phi\sigma_z/2}$ are the phase jumps of the RF radiation in between pulses, represented as z-rotations of the nuclear-spin qubit's rotating frame, and $R_x(\pi)$ are rotations of angle π around the x-axis of the electron spin, representing the decoupling pulses.

Due to the block-diagonal nature of the driving Hamiltonian we can define $e^{-iH_{\mathrm{RF}}\tau} = |0\rangle\langle 0| \otimes T_0 + |1\rangle\langle 1| \otimes T_1$, with the unitary operators T_i describing the nuclear spin evolution if the electron spin is in state $|i\rangle$. A DDRF gate with 2 decoupling pulses can then be written as:

$$\begin{aligned} U_{\mathrm{DDRF,N=2}} &= -|0\rangle\langle 0| \otimes T_0 R_z(\delta_\phi) T_1^2 R_z(\delta_\phi) T_0 - |1\rangle\langle 1| \otimes T_1 R_z(\delta_\phi) T_0^2 R_z(\delta_\phi) T_1 && \text{(B.30)}\\ &= -|0\rangle\langle 0| \otimes V_0 - |1\rangle\langle 1| \otimes V_1, && \text{(B.31)} \end{aligned}$$

which is a similar form as obtained for DD in ref.[2]. Any DDRF gate with more pulses can be found from $(U_{\mathrm{DDRF,N=2}})^{N/2}$. The operator V_0 (V_1) is the unitary evolution of the nuclear spin during one DDRF gate $N = 2$ unit cell with the electron spin initially in $|0\rangle$ ($|1\rangle$).

Again analogous to Ref.[2], V_0 and V_1 can be interpreted as rotations of the nuclear spin under an angle $\theta_0 = \theta_1 = \theta$, and around axes $\hat{\mathbf{n}}_0$ and $\hat{\mathbf{n}}_1$: $V_i = e^{-i\theta/2\hat{\mathbf{n}}_i\cdot\vec{\sigma}}$, with $\vec{\sigma} = \{\sigma_x, \sigma_y, \sigma_z\}$. The rotation angle and the inner product of the rotation axes are given by

$$\cos\theta = \cos(\Omega_{\mathrm{rot}}\tau)\cos\big(\Delta_0\tau + \delta_\phi\big) - \frac{\Delta_1}{\Omega_{\mathrm{rot}}}\sin(\Omega_{\mathrm{rot}}\tau)\sin\big(\Delta_0\tau + \delta_\phi\big) \tag{B.32}$$

$$1 - \hat{\mathbf{n}}_0\cdot\hat{\mathbf{n}}_1 = \frac{\Omega^2}{\Omega_{\mathrm{rot}}^2}\frac{(1-\cos(\Omega_{\mathrm{rot}}\tau))(1-\cos\big(\Delta_0\tau+\delta_\phi\big))}{1+\cos\theta}, \tag{B.33}$$

where $\Omega_{\mathrm{rot}} = \sqrt{\Omega^2 + \Delta_1^2}$. For larger N, the solution is given by the same rotation axes, but by a rotation angle $\Theta = N\theta/2$.

The key difference with the analytical result for DD gates is that the resonance condition for an entangling gate can be fulfilled by setting δ_ϕ appropriately, whereas for DD only the decoupling time τ is used. Tracking the nuclear spin evolution by setting $\delta_\phi = -\Delta_0\tau + \pi$, we find:

$$\cos\theta = -\cos\Omega_{\text{rot}}\tau \tag{B.34}$$

$$1 - \hat{\mathbf{n}}_0 \cdot \hat{\mathbf{n}}_1 = \frac{2}{1 + \Delta_1^2/\Omega^2}. \tag{B.35}$$

A fully entangling gate (e.g. $\hat{\mathbf{n}}_0 \cdot \hat{\mathbf{n}}_1 = -1, N\theta/2 = \pi/2$) can be performed when $\Delta_1 = 0, \Omega = \frac{\pi}{2N\tau}$.

Due to the $(S_z I_x)$ nature of the interaction, it is useful to consider an experiment where the electron is prepared in $|x\rangle = \frac{1}{\sqrt{2}}(|0\rangle + |1\rangle)$ and a DDRF sequence is applied. With the nuclear spin in a mixed state, the probability for the electron spin to remain in the $|x\rangle$ state is given by $P_x = \langle S_x\rangle + \frac{1}{2}$, with[2]:

$$\langle S_x\rangle = \frac{1}{2}\left(1 - (1 - \hat{\mathbf{n}}_0 \cdot \hat{\mathbf{n}}_1)\sin^2\frac{N\theta}{2}\right) \tag{B.36}$$

which, under the resonance condition $\delta_\phi = -\Delta_0\tau + \pi$, is equal to:

$$\langle S_x\rangle = \frac{1}{2}\left(1 - \frac{2}{1 + \Delta_1^2/\Omega^2}\sin^2\left(\frac{N\tau}{2}\sqrt{\Omega^2 + \Delta_1^2}\right)\right). \tag{B.37}$$

Alternatively, δ_ϕ can be set to optimally drive a target spin for $\Delta_1 \neq 0$, tracking its phase evolution during the gate. The solution is $\delta_\phi \approx -\Delta_1\tau - \Delta_0\tau + \pi$ (same as Eq. 4.3, see B.10 for a derivation). In this case, Eq. B.32 can be approximated in the limit of small rotations per RF pulse ($\Omega\tau \ll 1$) to yield:

$$\cos\theta = -\left(1 - \frac{1}{2}\left(\Omega\tau\,\text{sinc}(\Delta_1\tau)\right)^2\right) + O\left(\Omega^4\tau^4\right), \tag{B.38}$$

so that each $N = 2$ DDRF block induces a rotation of the nuclear spin by:

$$\theta \approx \Omega\tau\,\text{sinc}(\Delta_1\tau) + \pi, \tag{B.39}$$

This matches the effective Rabi frequency in the main text(Eq. 4.5), in the limit considered here where the driving in the $|0\rangle$ state is neglected ($\Delta_0\tau \ll 1$) and demonstrates the RF pulse bandwidth due to τ. The more general case is derived in the next section (B.10).

B.10. EFFECTIVE RABI FREQUENCY DERIVATION

As additional justification to the equation for $\tilde{\Omega}$ (Eq. 4.5), next to the experimental data in the main text, we present a derivation that shows that the DDRF gate can be approximated by a rotation with a reduced Rabi frequency.

The matrix exponentials T_0 and T_1, as defined in section B.9, can be explicitly calculated:

$$T_0 = \cos\left(\tau\sqrt{\Delta_0^2+\Omega^2}/2\right)\hat{\mathbb{I}} - i\Omega\tau/2\ \mathrm{sinc}(\tau\sqrt{\Delta_0^2+\Omega^2}/2)\sigma_x - i\Delta_0\tau/2\ \mathrm{sinc}(\tau\sqrt{\Delta_0^2+\Omega^2}/2)\sigma_z, \tag{B.40}$$

$$T_1 = \cos\left(\tau\sqrt{\Delta_1^2+\Omega^2}/2\right)\hat{\mathbb{I}} - i\Omega\tau/2\ \mathrm{sinc}(\tau\sqrt{\Delta_1^2+\Omega^2}/2)\sigma_x - i\Delta_1\tau/2\ \mathrm{sinc}(\tau\sqrt{\Delta_1^2+\Omega^2}/2)\sigma_z, \tag{B.41}$$

where σ_x and σ_z are the Pauli spin matrices. This form allows an efficient and accurate numerical calculation of the unitary operator of the DDRF gate (as only multiplication of 2×2 matrices is required), which was used to calculate the individual spin signals in Fig. 4.2b, Fig 4.5d (Appendix B.2).

Directly calculating V_0 or V_1 results in an analytically complex expression that is not easily simplified. Progress can be made by considering the limit $\Omega\tau \ll 1$. This is justified as DDRF is designed to target weakly-coupled nuclear spins ($\Delta < 1/T^*_{2,e}$) for which decoupling of the electron spin is needed, breaking up the rotation of the nuclear spin into small amounts.

To first order in $\Omega\tau$, $U_{\mathrm{DDRF,N=2}}$ (Eq. B.30) can be approximated by

$$\begin{aligned}
V_0 = {} & \hat{\mathbb{I}}\left[\cos\left(\tau(\Delta_0+\Delta_1)+\delta_\phi\right)+O\left(\Omega^2\tau^2\right)\right] \\
& -\sigma_x\left[\frac{i\Omega\tau(\Delta_1(\sin\left(\tau(\Delta_0+\Delta_1)+\delta_\phi\right)-\sin\left(\Delta_1\tau+\delta_\phi\right))+\Delta_0\sin(\Delta_1\tau))}{\Delta_0\Delta_1\tau}+O\left(\Omega^3\tau^3\right)\right] \\
& -\sigma_z\left[i\sin\left(\tau(\Delta_0+\Delta_1)+\delta_\phi\right)+O\left(\Omega^2\tau^2\right)\right] \\
V_1 = {} & \hat{\mathbb{I}}\left[\cos\left(\tau(\Delta_0+\Delta_1)+\delta_\phi\right)+O\left(\Omega^2\tau^2\right)\right] \\
& -\sigma_x\left[\frac{i\Omega\tau(\Delta_0(\sin\left(\tau(\Delta_0+\Delta_1)+\delta_\phi\right)-\sin\left(\Delta_0\tau+\delta_\phi\right))+\Delta_1\sin(\Delta_0\tau))}{\Delta_0\Delta_1\tau}+O\left(\Omega^3\tau^3\right)\right] \\
& -\sigma_z\left[i\sin\left(\tau(\Delta_0+\Delta_1)+\delta_\phi\right)+O\left(\Omega^2\tau^2\right)\right]
\end{aligned}$$

Thus the action of the DDRF gate on the nuclear spin can be approximated by a z-rotation, and an x-rotation by an angle that scales linearly with Ω, as would be expected. The derivation also shows the δ_ϕ resonance conditions. Setting $\delta_\phi = -\Delta_0\tau - \Delta_1\tau + \pi$ results in:

$$V_{0,\mathrm{con}} = \hat{\mathbb{I}} - \sigma_x i\Omega\tau(\mathrm{sinc}(\Delta_1\tau) - \mathrm{sinc}(\Delta_0\tau)) + O\left(\Omega^2\tau^2\right) \tag{B.42}$$

$$V_{1,\mathrm{con}} = \hat{\mathbb{I}} + \sigma_x i\Omega\tau(\mathrm{sinc}(\Delta_1\tau) - \mathrm{sinc}(\Delta_0\tau)) + O\left(\Omega^2\tau^2\right), \tag{B.43}$$

which describes (to first order) an x-rotation conditional on the electron state, with a modified Rabi frequency $\tilde{\Omega}$ described by equation 4.5.

Setting $\delta_\phi = -\Delta_0\tau - \Delta_1\tau$ results in the operators

$$V_{0,\text{uncon}} = V_{1,\text{uncon}} = \hat{\mathbb{I}} - \sigma_x i\Omega\tau(\text{sinc}(\Delta_0\tau) + \text{sinc}(\Delta_1\tau)) + O\left(\Omega^2\tau^2\right), \tag{B.44}$$

which describe an unconditional x-rotation.

One higher order effect neglected in this analysis is the AC-Stark shift[5], quadratic in Ω^2, which can shift the resonant phase increment δ_ϕ (see also Appendix B.3). Furthermore, in the regime where $\Omega \gg \Delta$, the nuclear spin is driven by the RF field regardless of the electron spin state and the conditionality of the interaction is no longer dependent on the set phase increment (Eq. 4.3). Instead, the nuclear eigenstates become dressed along the x-axis and decoupling the electron results in a perturbation along the z-axis (whose magnitude scales with $A_\parallel$). This regime can also be used for spin-selective sensing and control, and forms the basis for the recently developed AERIS protocol[9]

REFERENCES

[1] C. E. Bradley *et al., A Ten-Qubit Solid-State Spin Register with Quantum Memory up to One Minute,* Phys. Rev. X **9**, 031045 (2019).

[2] T. H. Taminiau *et al., Detection and Control of Individual Nuclear Spins Using a Weakly Coupled Electron Spin,* Phys. Rev. Lett. **109**, 137602 (2012).

[3] G. L. Van De Stolpe *et al., Mapping a 50-spin-qubit network through correlated sensing,* Nat Commun **15**, 2006 (2024).

[4] M. H. Abobeih *et al., One-second coherence for a single electron spin coupled to a multi-qubit nuclear-spin environment,* Nat Commun **9**, 2552 (2018).

[5] L. M. K. Vandersypen and I. L. Chuang, *NMR techniques for quantum control and computation,* Rev. Mod. Phys. **76**, 1037 (2005).

[6] C. L. Degen, F. Reinhard and P. Cappellaro, *Quantum sensing,* Rev. Mod. Phys. **89**, 035002 (2017).

[7] M. A. Nielsen, *A simple formula for the average gate fidelity of a quantum dynamical operation,* Physics Letters A **303**, 249 (2002).

[8] M. H. Abobeih *et al., Fault-tolerant operation of a logical qubit in a diamond quantum processor,* Nature **606**, 884 (2022).

[9] C. Munuera-Javaloy, A. Tobalina and J. Casanova, *High-Resolution NMR Spectroscopy at Large Fields with Nitrogen Vacancy Centers,* Phys. Rev. Lett. **130**, 133603 (2023).

C

APPENDIX FOR CHAPTER 5

C.1. NV SYSTEM

HAMILTONIAN

We consider the Hamiltonian of the ground-state NV electron spin, surrounded by N ^{13}C nuclei[1]:

$$\hat{H} = \Delta_{\mathrm{ZFS}}\hat{S_z}^2 + \gamma_e B_z \hat{S_z} + \sum_{i=1}^{N} \gamma_c B_z \hat{I}_z^{(i)} + \sum_{i=1}^{N} \hat{\vec{S}} \cdot \boldsymbol{A}^{(i)} \cdot \hat{\vec{I}}^{(i)} + \sum_{i=1}^{N}\sum_{j=i+1}^{N} \hat{\vec{I}}^{(i)} \cdot \boldsymbol{C}^{(ij)} \cdot \hat{\vec{I}}^{(j)}, \tag{C.1}$$

with Δ_{ZFS} the zero-field splitting, γ_e and γ_c the electron and ^{13}C nuclear gyromagnetic ratio and B_z an external magnetic field applied along the NV-symmetry axis (z-axis). Here, $\hat{\vec{S}} = (\hat{S_x}, \hat{S_y}, \hat{S_z})$ and $\hat{\vec{I}}^{(i)} = (\hat{I}_x^{(i)}, \hat{I}_y^{(i)}, \hat{I}_z^{(i)})$ are the electronic and nuclear spin vectors, respectively, consisting of spin-1 matrices $\hat{S_\alpha}$ and spin-$\frac{1}{2}$ matrices $\hat{I}_\alpha^{(i)} = \hat{\sigma}_\alpha^{(i)}/2$ (with $\hat{\sigma}_\alpha^{(i)}$ the Pauli spin matrices). Furthermore, $\boldsymbol{A}^{(i)}$ is the electron-nuclear hyperfine tensor and $\boldsymbol{C}^{(ij)}$ is the nuclear-nuclear dipole-dipole coupling.

For the sensing schemes presented in this work, the NV-electron spin is either in the $m_s = +1$ or $m_s = -1$ eigenstate during evolution of the nuclear spins, except for sub-μs timescales between electron pulses. As a result of the disorder induced by the hyperfine interaction $|{A_{zz}}^{(i)} - {A_{zz}}^{(j)}| \gg {C_{zz}}^{(ij)}$, nuclear flip-flops are suppressed (frozen core). Note that this condition breaks down in general when there is a high degree of spectral crowding in the system. However, in this work, we focus on spectral regions where ${C_{zz}}^{(ij)}$ (denoted as C_{ij} in the main text and from here on) is generally small if $|{A_{zz}}^{(i)} - {A_{zz}}^{(j)}|$ is small, so that the condition still holds. Furthermore, based on the large zero-field splitting Δ_{ZFS} we apply the secular approximation, so that the hyperfine tensor simplifies to just the parallel ($A_\parallel = A_{zz}$) and perpendicular($A_\perp = \sqrt{A_{zx}^2 + A_{zy}^2}$) components. Considering only the nuclear Hamiltonian while the electron is in the ±1 eigenstate:

$$\hat{H}_{\pm1} = \sum_{i=1}^{N} \left[(\gamma_c B_z \pm A_\parallel^{(i)}) \hat{I}_z^{(i)} + A_\perp^{(i)} (\cos\phi_\perp^{(i)} \hat{I}_x^{(i)} + \sin\phi_\perp^{(i)} \hat{I}_y^{(i)}) \right] + \sum_{i=1}^{N}\sum_{j=i+1}^{N} \hat{\vec{I}}^{(i)} \cdot \boldsymbol{C}^{(ij)} \cdot \hat{\vec{I}}^{(j)}, \tag{C.2}$$

where $\phi_\perp^{(i)}$is the perpendicular hyperfine azimuthal angle. Here, we neglect the small correction on C_{ij} due to the electron spin state ($C_{ij}^+ = C_{ij}^-$)[2]. Appendix C.4 discusses the non-neglible effect of this correction observed in the specific experiments.

Under the application of a strong magnetic field ($\gamma_c B_z \pm A_\parallel \gg A_\perp$), we can further simplify the Hamiltonian, with the purpose of generalizing the effective dynamics of our system. To this end, we include the perpendicular hyperfine component ($A_\perp$) as a correction to the $\hat{I}_z^{(i)}$ terms, describing the increased nuclear precession frequency[3]. This results in Eq. 5.1 in the main text:

$$\hat{H}_{\pm1} \approx \sum_{i=1}^{N} A_i^\pm \hat{I}_z^{(i)} + \sum_{i=1}^{N}\sum_{j=i+1}^{N} C_{ij} \hat{I}_z^{(i)} \hat{I}_z^{(j)}, \tag{C.3}$$

with $A_i^\pm = \sqrt{(\gamma_c B_z \pm A_\parallel^{(i)})^2 + (A_\perp^{(i)})^2}$ the effective nuclear spin frequencies. In the main text, A_i describes the spin frequencies when the electron is in the $m_s = -1$ state ($\pm$-sign is omitted for simplicity).

INITIALISATION

For the experiments in the main text, the nuclear spins are polarised via two techniques. We employ a combination of dynamical nuclear polarisation (PulsePol, [4]) and SWAP sequences with the electron spin [5]. The latter method typically yields a higher degree of polarisation [5], but is restricted to a limited number of spectrally isolated nuclear spins (see Table C.1). If any of these SWAP-initialised spins participate in a sensing chain, we re-initialise them right before the final SEDOR-yx sequence to maximize the signal. All other spins are polarised via the PulsePol sequence, which is known to produce varying degrees of polarisation [1,6,7]. Following the definitions given in the supplement of Ref. [1], we set $\tau = 0.434\,\mu s$, resonant with the nuclear Larmor frequency, $N = 4$ and choose R in the range $500 - 10000$, dependent on the rate of polarisation of the spins in the chain. For resonant reset of the electron state after each PulsePol step, the repump laser power was set to 1000 nW, with a repump time of 5 µs. For some experiments (in particular the 2D spectroscopy) the laser power was reduced to 333 nW (and the repump time increased to 10 µs), to limit electron ionisation for $R > 5000$.

For the analytical expressions derived in the supplement, we capture the varying degree of polarisation of N nuclear spins by a partially mixed system initial state:

$$\hat{\rho_0} = \hat{\rho}_{e,0} \bigotimes_{i=1}^{N} \frac{1}{2} \left(\hat{\mathbb{I}} + p_i \hat{I}_z^{(i)} \right), \tag{C.4}$$

with $\hat{\mathbb{I}}$ the (two-dimensional) identity matrix, the polarisation degree $p_i \in [-1, 1]$ for spin i and $\hat{\rho}_{e,0}$ the initial state of the NV electron spin. The p_i can be obtained by independent state preparation and measurement characterisations [1].

READOUT

For all experiments presented in this work, the signal is read out via dynamical-decoupling sensing sequences (DD or DDRF [3,5]) with the electron spin. Only a limited number of spins can be read out selectively (see Table C.1), due to spectral overlap between nuclear spins. Hence, we choose the first spin in all sensing chains to be one that is directly accessible to the electron spin. Combined initialisation and readout fidelity varies between spins (0.44(2) – 0.95(2), corrected for electron readout fidelity).

Table C.1: Information on the nuclear spins mapped in this work. A dash denotes that no Δ_i signal could be obtained due to low polarisation, coherence, or readout contrast. Value in parentheses denotes standard deviation on the last digit. Spins C1-C27 were previously characterised in Ref. [2] and the used labels are consistent with their work. These data are also available online at: *https://doi.org/10.4121/aba1cc84-0aea-4cdc-93ca-68b0db38bd81.v1*

Label	Initialisation	Readout	A_i (kHz)	Δ_i (Hz)	x (Å)	y (Å)	z (Å)
C1	PulsePol	Chain-1	452.83(2)	-20840.2(6)	0.0	0.0	0.0
C2	PulsePol	Chain-1	455.37(2)	-22939.6(1)	2.52	2.91	-0.51
C3	PulsePol	Chain-1	463.27(2)	-31257.8(1)	3.78	0.73	-0.51
C4	PulsePol	Chain-1	446.23(4)	-14056.7(2)	-1.26	2.18	0.0
C5	SWAP	Direct	447.234(1)	-11291(3)	0.0	4.37	-6.18
C6	SWAP	Direct	480.625(1)	-48488.0(8)	5.04	-1.46	-2.06
C7	PulsePol	Chain-1	440.288(6)	-8332.8(1)	5.04	-1.46	5.66
C8	PulsePol	Chain-1	441.77(1)	-9803.6(8)	7.57	1.46	3.6
C9	SWAP	Direct	218.828(1)	213147.2(2)	7.57	-4.37	-10.81
C10	SWAP	Direct	414.407(1)	17643.3(4)	0.0	8.74	-12.36
C11	SWAP	Direct	417.523(4)	14549.91(4)	6.31	9.46	-12.87
C12	SWAP	Direct	413.477(1)	20546.7(3)	11.35	0.73	-14.42
C13	PulsePol	Chain-1	424.449(1)	8017.1(2)	12.61	2.91	-6.69
C14	SWAP	Direct	451.802(1)	-19760.5(3)	5.04	-2.91	-22.65
C15	PulsePol	Chain-1	446.01(5)	-13958.0(3)	1.26	3.64	-22.65
C16	PulsePol	Chain-1	436.67(5)	-4647.8(1)	2.52	8.74	-23.17
C17	PulsePol	Chain-1	437.61(1)	-5682.1(1)	6.31	-2.18	-29.34
C18	SWAP	Direct	469.02(1)	-36184.3(2)	0.0	-1.46	-19.05
C19	SWAP	Direct	408.317(1)	24219.15(8)	3.78	-9.46	-8.75
C20	PulsePol	Chain-1	429.403(4)	2692.5(5)	3.78	10.92	-4.63
C21	PulsePol	Chain-1	430.937(3)	1214.8(4)	-5.04	5.82	-4.12
C22	PulsePol	Chain-1	424.289(3)	7696.07(9)	16.39	-3.64	-8.24
C23	PulsePol	Chain-1	435.143(7)	-3195.6(1)	13.88	0.73	5.66
C24	PulsePol	Chain-2	436.183(3)	-	1.26	-0.73	9.78
C25	PulsePol	Chain-2	435.829(5)	-	7.57	1.46	9.78
C26	PulsePol	Chain-1	435.547(2)	-	12.61	-5.82	-0.51
C27	PulsePol	Chain-1	435.99(3)	-3935.9(2)	1.26	-3.64	-31.4
C28	PulsePol	Chain-1	440.9(1)	-8915.47(3)	-1.26	2.18	-24.71
C29	PulsePol	Chain-1	434.3(1)	-2185.7(1)	-6.31	0.72	-19.05
C30	PulsePol	Chain-1	427.1(1)	4871.11(4)	12.62	10.19	-14.93
C31	PulsePol	Chain-1	428.3(1)	-	11(4)	15(4)	-11(4)
C32	PulsePol	Chain-1	431.6(1)	-	6(3)	12(2)	-3(9)
C33	PulsePol	Chain-1	439.0(1)	-	-2.52	-1.46	4.12

Continued on next page

Table C.1: Information on the nuclear spins mapped in this work. A dash denotes that no Δ_i signal could be obtained due to low polarisation, coherence, or readout contrast. Value in parentheses denotes standard deviation on the last digit. Spins C1-C27 were previously characterised in Ref.[2] and the used labels are consistent with their work. These data are also available online at: *https://doi.org/10.4121/aba1cc84-0aea-4cdc-93ca-68b0db38bd81.v1*

Paper label	Initialisation	Readout	A_i (kHz)	Δ_i (Hz)	x (Å)	y (Å)	z (Å)
C34	PulsePol	Chain-1	437.3(1)	-	-2.52	-0.0	6.18
C35	PulsePol	Chain-1	427.4(1)	4591.33(4)	20(3)	-1(7)	-8(1)
C36	PulsePol	Chain-1	434.4(1)	-2214.2(8)	-8(7)	-0(7)	-23(9)
C37	PulsePol	Chain-1	429.1(1)	2899.5(2)	13(2)	-12(1)	-18(1)
C38	PulsePol	Chain-1	434.0(1)	-	12.61	-8.73	0.0
C39	PulsePol	Chain-2	432.5(1)	-450(5)	16(5)	-8(5)	-24(4)
C40	PulsePol	Chain-2	433.3(1)	-1173(5)	11(3)	-14(3)	-26(4)
C41	PulsePol	Chain-2	434.1(1)	-2189.3(6)	8(4)	-12(4)	2(6)
C42	PulsePol	Chain-2	434.8(1)	-	10.09	-7.28	-28.83
C43	PulsePol	Chain-2	432.2(1)	-270.1(6)	11(3)	7(3)	-19(3)
C44	PulsePol	Chain-2	433.9(1)	-1882.8(6)	-0.0	11.65	-26.77
C45	PulsePol	Chain-3	436.2(1)	-4174(1)	6.3	6.56	-29.35
C46	PulsePol	Chain-3	434.8(1)	-	14(4)	-5(4)	-24(5)
C47	PulsePol	Chain-2	429.4(1)	2587.8(3)	21(4)	-7(7)	-14(7)
C48	PulsePol	Chain-2	431.0(1)	-	16(4)	-4(4)	-21(9)
C49	PulsePol	Chain-2	428.3(1)	3744.4(2)	23(4)	-4(8)	-12(3)
C50	PulsePol	Chain-2	436.2(1)	-4227.0(4)	11(7)	5(7)	-2(9)

Table C.2: Spin labels of spins featuring in the experiments in the main text.

Figure	Spin number	Spin label
Fig. 5.2	Spin 1	C18
	Spin 2	C28
	Spin 3	C16
	Spin 4	C44
	Spin 5	C45
Fig. 5.3	Spin 1	C11
Fig. 5.4	Spin 1	C12
	Spin 2	C13
	Spin 3	C22

C.2. SPECTRAL CROWDING IN THE NV-NUCLEAR SYSTEM

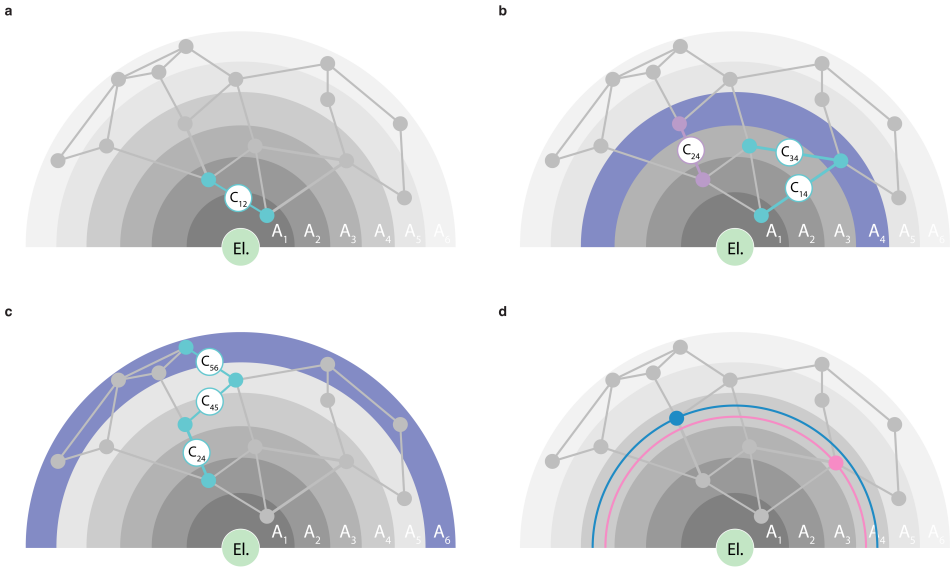

Figure C.1: **Mapping complex spin networks. a)** Spatial representation of Fig. 5.1, specific to the electron-nuclear system. Nuclear spins (dots) are connected by lines denoting observable couplings ($C_{ij} > 1/T_2$). The bands indicate spin frequencies A_i, shifted by the hyperfine interaction Δ_i with the electron spin (mint green). This interaction diminishes with distance from the NV center, leading to spectral crowding (multiple spins per band). For simplicity we do not visualize the angular dependence of the hyperfine interaction. Frequencies A_1, A_2 and A_3 contain only a single spin, allowing for a direct readout with the electron spin. Additionally, the measured couplings between these frequencies (e.g. C_{12}) can be assigned unambiguously from pairwise measurements (see Fig. 5.1a). **b)** When multiple spins occupy the same frequency band (e.g. at A_4), spin-chain measurements resolve ambiguity by retrieving the connectivity of the network (see also Fig. 5.1b). **c)** Spins in spectrally crowded areas (e.g. at A_6, see also Fig. C.1), can still be accessed via a spin-chain, starting from a directly accessible spin (e.g. at A_2) (see Fig. 5.1c). **d)** High-resolution measurements of Δ_i (indicated by narrow pink and blue bands) allow for directly distinguishing multiple spins in a single frequency band (e.g. at A_4) (see Fig. 5.1d). Note that we use different frequency labels compared to Fig. 5.1.

The schematic in the main text (Fig. 5.1), describes the challenge of mapping a spectrally crowded spin network in a general sense, for an abstract spin network described by frequencies A_i, C_{ij} (Eq. 5.1). In the system studied here, all nuclear spins are ^{13}C spins and the nuclear spin frequencies A_i are set by the coupling to the NV electron spin. Therefore, there is a specific relationship between the nuclear-spin frequencies and their 3D position with respect to the electron spin (see also Fig. C.1). In this section we discuss how different spectral regions can be defined, and which regions can and cannot be accessed with different methods.

To understand which parts of the network can be mapped with the new methods, and where different methods break down, we define three spectral regions: *isolated, spectrally*

crowded and *spatially crowded*. The *isolated* region is the set of spins i, for which:

$$|A_i - A_j| > 1/T_2^\star \ \forall \ j\,, \tag{C.5}$$

which states that the frequency of spin i is unique. Here, we define this condition as being satisfied if there are at least 4 spectral widths (s.d.) between the resonances of two spins. In a natural abundance (1.1%) sample, we calculate that 20(3) spins typically satisfy this condition, and only about 8(3) are isolated by more than 2 kHz from any other spin (assuming $T_2^\star \sim 5$ ms and a purely dipolar hyperfine interaction). In the NV-nuclear system, only this set of spins can be read out selectively with the electron spin[2,3,5] (ignoring notable exceptions in the form of strongly-coupled spin-pairs[8,9]), even though the electron spin typically couples to the majority of nearby nuclear spins ($\Delta_i > 1/T_{2,e}$).

Next, we define the *spectrally crowded* region as the set of spins i for which:

$$|A_i - A_j| < 1/T_2^\star \implies C_{ij} \lesssim 1/T_2 \ \forall \ j\,, \tag{C.6}$$

meaning that spins may overlap spectrally, but if they do, they are typically not coupled strongly together. In the NV-nuclear system, this region includes nuclear spins which have similar hyperfine interaction with the electron, but are *spatially* separated, for example when they are on opposite sides of the NV center in the x, y-plane.

Finally, the *spatially crowded* region includes all other spins, which may be overlapping spectrally as well as coupling strongly together.

We schematically draw the three spectral regions in Fig. C.2, with the bottom color bar denoting the three spectral regions (green = *isolated*, orange = *spectrally crowded* and red = *spatially crowded*). The blue through violet bands indicate spin frequencies A_i (analogous to the colored circles in the main text), shifted by the hyperfine interaction to the electron spin. In the schematic, we simplify the more complex dipolar isoplane shape[10] and consider only the radial dependence ($A_i \propto r_i^{-3}$). A particular nuclear-spin-network configuration is drawn as an example.

Only limited information can be attained from the network using pairwise SEDOR sequences[2]. If we allow no assumptions on the underlying coupling structure, pairwise measurements can only unambiguously assign couplings to the spins in the isolated region (coloured white). Using SEDOR, it is possible to measure couplings between one spin in the *isolated* region and one in the *spectrally crowded* region. However, those couplings cannot be assigned to a spin in the latter region without resorting to a detailed microscopic model[2]. As an example, using SEDOR, we find that the frequencies A_1, A_2 and A_3 all exhibit coupling to some spin at A_4 (coloured grey), but the couplings could belong to either of the spins at A_4. Also, couplings for which both spins lie in the *spectrally crowded* region (coloured black) cannot be accessed, as the spin-selective readout with the electron spin breaks down in this region.

SPECTRAL REGIONS

The spin-chain sensing (Fig. 5.2) unlocks new parts of the crowded region that can be mapped (Fig. C.2c). Consider the previously discussed couplings between A_1, A_2, A_3 and A_4. If we measure a chain connecting A_1, A_4 and A_2, we conclude that A_1 and A_2 couple to the same spin at A_4. Measuring a chain between A_1, A_4 and A_2 does not result in an

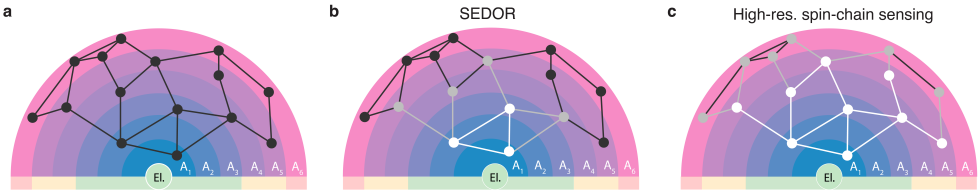

C

Figure C.2: **Unlocking spectral regions.** **a** Alternative representation of Fig. 5.1, specific to the electron-nuclear system. Nuclear spins are drawn as black dots, connected by lines denoting observable couplings ($C_{ij} > 1/T_2$). The colored bands indicate spin frequencies A_i, shifted by the hyperfine interaction (Δ_i) with the NV electron spin (mint green). The green, orange and red color scales at the bottom denote three spectral regions: *isolated*, *spectrally crowded* and *spatially crowded*, respectively. In the *isolated* region, spin frequencies are well-separated in frequency, (single spin per band) and can be read out directly with the electron[5]. In the *spectrally crowded* region (orange), multiple spins may occupy a single frequency band, but do not couple among each other. In the *spatially crowded* region (red), spins may also couple to spins within their frequency band, resulting in a decreased spin-echo coherence. **b)** Spins that can be mapped using standard pairwise SEDOR[2]. The color of the coupling line indicates whether it can be measured and conclusively assigned (white), measured but not assigned (grey), or not measured at all (black). **c)** Spin-chain sensing increases the number of couplings that can be measured and assigned (e.g. when *both* spins are in the *spectrally crowded* region) and unlocks spins in the *spatially crowded* region. Additionally, the high-resolution measurements of Δ_i allow for assigning otherwise ambiguous couplings in the *spectrally crowded* region.

observable coupling, so we conclude that A_2 is coupled to another spin at A_4. Note that this reasoning relies on the fact that it is possible to assert that A_1, A_2 and A_3 couple only to a *single* spin at A_4. Experimentally, this can be verified by observing a single dominant oscillation in the signal (instead of beatings or decay).

Besides assigning measured couplings to spins, spin-chain sensing allows for access to an extended number of couplings, particularly in the *spectrally crowded* and *spatially crowded* regions (Fig. C.2c). For example, by measuring a looped spin chain through frequencies $A_1, A_2, A_4, A_5, A_3, A_1$, we access the coupling between two spins in the spectrally crowded region (at A_4 and A_5) and directly map the connectivity of the 5 spins in the loop. In addition, we can use the newly unlocked spins (at A_4 and A_5) to probe couplings to the *spatially crowded* region (grey spins at A_6). Finally, by increasing the spectral resolution (Figs. 3 and 4), we resolve remaining ambiguity in the *spectrally crowded* region.

Even though the high-resolution spin-chain sensing fully unlocks the *spectrally crowded* region and allows us to probe the *spatially crowded* region, the latter also imposes a limit on the applicability of the method. In particular, the spin-chain sensing relies on an extended nuclear spin-echo coherence time (ideally from $T_2^\star$ to T_2). However, in this region, a decoupling pulse inadvertently also acts on other nuclei, so that their spin-spin couplings are retained. This results in the re-emergence of quasi-static ($T_2^\star$-like) noise also known as instantaneous diffusion[11], limiting the spin-echo coherence time $T_{2,\mathrm{SE}}$ to:

$$T_2^\star \leq T_{2,\mathrm{SE}} \leq T_2\,. \tag{C.7}$$

In the case when many strongly coupled spins reside in the same frequency band (see Eq. C.6), we expect the coherence to be effectively reduced to $T_2^\star$, rendering the effect of the

double resonance sequence useless. Hence, utilizing spins inside the *spatially crowded* region as probes of their environment is infeasible (except for strongly interacting spins, if $C_{ij} > 1/T_2^\star$), which sets the limit of the functional range of spin-chain sensing.

NUMERICAL SIMULATIONS

To quantitatively investigate the regions visualised in Fig. C.2, we perform Monte Carlo simulations of randomly generated NV-nuclear systems. First, we compute the spectral spin density (i.e. number of spins within a frequency bin) as a function of the hyperfine shift Δ (Fig. C.3a). We find that the mean spin density is well described by (dotted line):

$$\bar{\rho}(\Delta) = \frac{\pi^2 \alpha \rho_0}{\Delta^2}, \tag{C.8}$$

with $\bar{\rho}$ the mean spin density in frequency space (Hz^{-1}), $\rho_0 = 1.950\,\mathrm{nm}^{-3}$ the spatial ^{13}C density and $\alpha = \mu_0 \gamma_e \gamma_c \hbar / 4\pi$, with μ_0 the Bohr magneton, $\hbar$ the reduced Planck constant and γ_e and γ_c the electron and carbon nuclear gyromagnetic ratios, respectively. Figure C.3a shows the expected number of ^{13}C spins within a frequency bin of 100 Hz $\sim 1/(2\,T_2^\star)$, which gives a measure for the probability to find spectrally overlapping spins. As described above, here we choose to define the start of the *spectrally crowded* region at the condition:

$$\bar{\rho} \approx T_2^\star, \tag{C.9}$$

yielding $|\Delta| \approx 3.5$ kHz. For larger $|\Delta|$, we expect on average less than one spin per $T_2^\star$-limited frequency bin (*isolated region*, see green region in Fig. C.3a).

To quantify the transition between the *spectrally crowded* and *spatially crowded* regions, we compute the expected drop in spin-echo coherence, taking into account instantaneous diffusion [11] (Fig. C.3b). Assuming linear addition of the dephasing rates [12]:

$$1/T_{2,\mathrm{SE}} = 1/T_2 + 1/T_{2,\mathrm{ID}}, \tag{C.10}$$

with $1/T_{2,\mathrm{ID}}$ the instantaneous diffusion dephasing rate and $T_2 \approx 500$ ms the isolated spin-echo coherence time [5]. We compute $T_{2,\mathrm{ID}}$ by examining the mean $T_2^\star$ of the subsystem of spins that occupy a frequency bin of size 100 Hz for all Δ. We mark the start of the *spatially crowded* region at the point $T_{2,\mathrm{SE}} \approx 0.5\,T_2$, which implies $|\Delta| \lesssim 1$ kHz (Fig. C.3b). For the 23 newly characterised spins in this work, most belong to the *spectrally crowded* or *spatially crowded* regions (8 satisfy $3.5 < |\Delta_i| < 7.5$ kHz, 10 satisfy $1 < |\Delta_i| < 3.5$ kHz, and 4 satisfy $|\Delta_i| < 1$ kHz, see Table C.1).

The discussion so far has focused on the degree of spectral crowding using the numerical values for a natural abundance sample (1.1% ^{13}C). We now examine how these relations depend on the isotope concentration. In the basic picture of a point-dipole electron spin, surrounded by a bath of nuclear spins with spatial density ρ_0, the system exhibits a form of scale invariance. That is, we can define the (dimensionless) spectral density:

$$\frac{\bar{\rho}(\Delta)}{T_2^\star} = \frac{\pi^2 \alpha \rho_0}{T_2^\star \Delta^2}, \tag{C.11}$$

describing the number of spins per line width. For dipolar interactions, both the electron-nuclear hyperfine shift Δ as well as the nuclear line width ($\sim 1/T_2^\star$) scale linearly with the

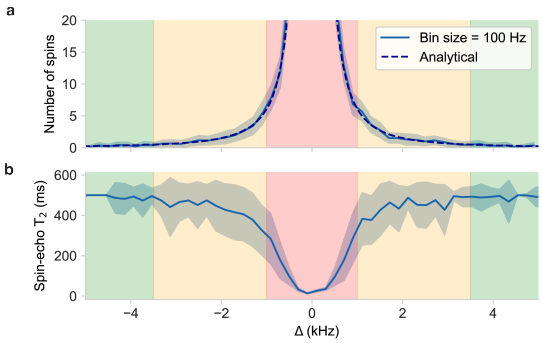

Figure C.3: **Spectral spin-density and spin-echo coherence reduction. a)** Expected spectral density (number of spins per 100 Hz) as a function of the hyperfine shift Δ, assuming dipolar electron-nuclear coupling. The blue solid line denotes the mean of 100 randomly generated systems (containing > 15000 spins). The analytical expression in Eq. C.8 (dashed line) describes the simulated distribution well. **b)** Expected spin echo coherence time (Eff. T_2) as a function of the hyperfine shift Δ (considering systems of > 1000 spins), taking into account only quasi-static effects and limiting the maximal coherence to $T_2 = 500$ ms. Coherence is reduced as the pulses in the spin-echo are resonant with multiple spins (see (a)), resulting in a recoupling of nearby spins. Here, the Rabi frequency is set to $f_{\text{Rabi}} \approx 1/2T_2^\star$. Broader pulses (higher f_{Rabi}) increase the number of recoupled spins, further reducing the nuclear coherence. Shaded areas denote the spread (one s.d.) between simulated systems .

density, so that the dimensionless spectral density (Eq. C.11) is independent of ρ_0. Intuitively, this can by understood as both the nuclear-spin line widths and the spacing between nuclear-spin frequencies scaling with ρ_0, keeping their ratio (i.e. the degree of spectral crowding) constant. In principle, in this elementary system, the physics and quantities like the number of spins that can be mapped are independent of concentration, with only absolute time and distances being rescaled.

In practice, however, this scale invariance breaks down for both for low and high isotope concentrations. At low isotope concentrations, other noise sources will start to limit both the nuclear line widths (via reduced $T_2^\star$), as well as the spin-echo coherence times (via reduced T_2). At high concentrations — including around the natural 1.1% abundance — the discreteness of the lattice and the contact hyperfine interaction due to the finite NV electron wave function need to be taken into account. Predictions for the optimal concentration for a given goal, such as controlling the largest network, likely need detailed numerical simulations taking these details into account, which we do not pursue here.

C.3. SPIN-CHAIN SENSING

SIGNAL ANALYSIS

Here, we analyse the system evolution under the spin-chain sensing sequences developed in this work, and give analytic expressions for the expected resulting signals. Given the initial state in Eq. C.4, we calculate the z-expectation value of the first nuclear spin (1) in the chain, for a chain of length N after applying the concatenated SEDOR sequence (Fig. 5.2c). We analyse the evolution of the system by dividing it up into separate blocks, set by the subsequent SEDOR sequences. As the nuclear spins are initialized along the z-axis (have no off-diagonal component, see Eq. C.4), the spins in the chain do not evolve, except for those participating in a SEDOR block. Therefore, we can restrict our analysis to the subspace spanned by the spins in each block.

We find a recursive expression for the evolution of two subsequent spins ($j+1$ and j) under a SEDOR block (for both 'xx' and 'yx' type sequences). To this end, we trace out the $j+1$-subspace, as only the density matrix of spin j is needed to calculate the subsequent SEDOR evolution between spin j and $j-1$. This allows us to find two recursive formulas involving only the diagonal elements of each spin density matrix. By applying these expressions $N-1$ times, we retrieve the z-expectation value of spin 1, which is a function of all nuclear-nuclear couplings in the chain.

Evolution during a single SEDOR-xx or SEDOR-yx block for two subsequent spins in the chain can be described by the unitary:

$$U_{\mathrm{kx}}^{(j+1\to j)} = R_{\mathrm{x}}(\tfrac{\pi}{2})^{(j)}\, U_{-}\, R_{\mathrm{x}}(\pi)^{(j+1)}\, R_{\mathrm{x}}(\pi)^{(j)}\, U_{-}\, R_{\mathrm{k}}(\tfrac{\pi}{2})^{(j)}, \tag{C.12}$$

with $R_{\mathrm{k}}(\theta)^{(j)}$ a rotation of spin j by an angle θ around axis $k \in \{x, y\}$ and U_{-} the free evolution under the Hamiltonian $\hat{H}_{-1}$ in Eq. C.3, considering only spin $j+1$ and j[1]. Without loss of generality, we can write the initial state of any two subsequent spins as:

$$\rho_{j+1,j}(0) = \frac{1}{4}\begin{pmatrix} 1+\alpha_{j+1} & \beta_{j+1} \\ \beta_{j+1}^{*} & 1-\alpha_{j+1} \end{pmatrix} \otimes \begin{pmatrix} 1+p_j & 0 \\ 0 & 1-p_j \end{pmatrix}, \tag{C.13}$$

where the first density matrix denotes the subspace of spin $j+1$, which can be in any arbitrary quantum state and the second density matrix describes the subspace of spin j, initialised according to Eq. C.4. We let the system evolve for time t under $U_{\mathrm{kx}}^{(j+1\to j)}$, after which we trace out the $j+1$ subspace, resulting in the density matrix for spin j:

$$\begin{aligned} \rho_j(t) &= \mathrm{Tr}_{j+1}\left(U_{\mathrm{kx}}^{(j+1\to j)}\, \rho_{j+1,j}(0)\, U_{\mathrm{kx}}^{(j+1\to j)\dagger} \right) \\ &= \frac{1}{2}\begin{pmatrix} 1+\alpha_j^k & \beta_j^k \\ \beta_j^{k\,*} & 1-\alpha_j^k \end{pmatrix}, \end{aligned}$$

leading to the following update rule for the diagonal density matrix elements of spin j under

SEDOR-xx and SEDOR-yx:

$$\alpha_j^x = p_j \cos\frac{2\pi C t}{2}, \tag{C.14}$$

$$\alpha_j^y = p_j \sin\frac{2\pi C t}{2}\,\alpha_{j+1}, \tag{C.15}$$

with $C = C_{j,j+1}$ the coupling between the spins in Hz. Note that the off-diagonal terms β_{j+1} drop out when we only consider the diagonal elements of spin j. To calculate the z-expectation value of the first spin in the chain after a SEDOR-xx block and $N-2$ concatenated SEDOR-yx blocks according to Fig. 5.2c, we iteratively apply Eqs. C.14 and C.15 to find:

$$\langle \hat{I}_z^{(1)} \rangle = \frac{1}{2}\alpha_1 = \frac{1}{2} p_{N-1} \cos\left(\pi C_{N-1,N} t_{N-1,N}\right) \prod_{j=1}^{N-2} p_j \sin\left(\pi C_{j,j+1} t_{j,j+1}\right), \tag{C.16}$$

DECOHERENCE OF THE CHAIN

Eq. C.16 does not take into account any imperfections due to decoherence or pulse errors. In the following, we model the effect of decoherence, which is the main factor limiting the signal. Here, we do not take into account the effect of pulse errors, but this can be implemented analogous to Ref. [1].

We model decoherence by multiplying the signal of each SEDOR block by an exponential decay function, parameterised by a characteristic spin-echo decay time τ_j. In the case that the spin-echo in the SEDOR is perfectly effective, meaning that spin j is fully decoupled from all other nuclei, the decay is governed by dynamic noise sources ($\tau_j \sim 250-800$ ms) [5]. However, for a spin at a spectrally crowded frequency, the decoupling pulse inadvertently also acts on other nuclei, so that their coupling to spin j is retained. This results in the re-emergence of quasi-static noise (instantaneous diffusion) discussed in Appendix C.2, which we model by adding a Gaussian decay to Eq. C.16:

$$\langle \hat{I}_z^{(1)} \rangle = \frac{1}{2} p_{N-1} \cos\left(\pi C_{N-1,N} t_{N-1,N}\right) e^{-\left(\frac{t_{N-1,N}}{\tau_{N-1}}\right)^2} \prod_{j=1}^{N-2} p_j \sin\left(\pi C_{j,j+1} t_{j,j+1}\right) e^{-\left(\frac{t_{j+1,j}}{\tau_j}\right)^2}, \tag{C.17}$$

Even though the recoupled spins are partially polarised, we expect them to impart only a decay and no frequency shift on the signal, as they will also undergo the $\frac{\pi}{2}$-pulse, negating any z-axis polarisation. For the experiments in Fig. 5.2d-f, we set $t_{i,i+1} = \frac{1}{2}C_{i,i+1}^{-1}$ for all SEDOR-yx blocks, which reduces Eq. C.17 to:

$$\langle \hat{I}_z^{(1)} \rangle = A_{N-1} \cos\left(\pi C_{N-1,N} t_{N-1,N}\right) e^{-\left(\frac{t_{N-1,N}}{\tau_{N-1}}\right)^2}, \tag{C.18}$$

with $A_{N-1} = \frac{1}{2} p_{N-1} \prod_{j=1}^{N-2} p_j e^{-\left(\frac{C_{j+1,j}}{2\tau_j}\right)^2}$ the signal amplitude. We use Eq. C.18 to fit the data in Fig. 5.2d-f with free parameters $A_{N-1}, C_{N-1,N}, \tau_{N-1}$ and an arbitrary offset. Note that even though the signal amplitude A_{N-1} is affected by the coherence and polarisation of all spins in the chain, the spectral resolution with which $C_{N-1,N}$ can be determined is only limited by

the coherence of spin $N-1$ (i.e. τ_{N-1}). The decay of the signal A_{N-1} with increasing number of spins due to the imperfect polarisation ($p_j < 1$) and finite coherence times τ_j limits how long a chain can be practically formed. Note that for spins further from the NV τ_j tends to decrease due to imperfect decoupling (instantaneous diffusion in the spatially crowded region, see Appendix C.2), ultimately limiting the range for high-resolution sensing.

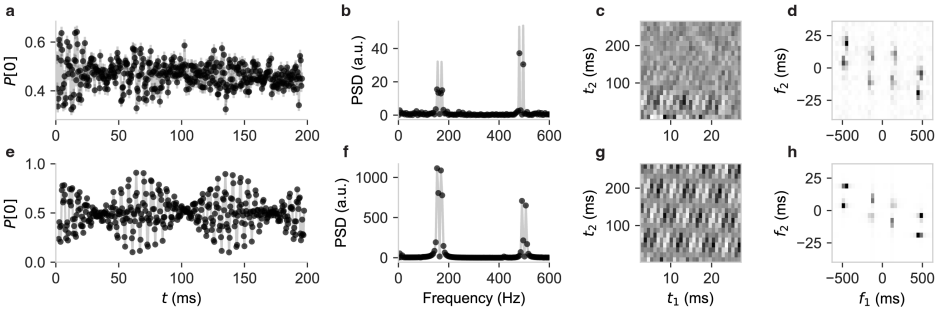

Figure C.4: **Comparison to numerical simulations**. **a)** Time domain data of the experiment in Fig. 5.4d and corresponding PSD **(b)**. **c)** Time domain data of the experiment in Fig. 5.4e and corresponding 2D PSD **(d)**, showing both the positive and negative f_1-axis. **e-h)** Numerical simulations of the experimental data in (a-d). Spin parameters are based on the spin positions. The simulations show good agreement with experiment (up to nuclear decoherence effects), reconfirming the characterisation of the system and the interpretation of the spectroscopy data.

C.4. ELECTRON-NUCLEAR DOUBLE RESONANCE SEQUENCE

SIGNAL ANALYSIS

Next, we analyse the system evolution under the electron-nuclear double resonance sequence (see Fig. 5.3). To this end, we consider the interaction between the electron ('el') and nuclear spin j (Fig. 5.3) by considering the following unitary:

$$U_{\mathrm{xx}}^{(\mathrm{el}\rightarrow j)} = R_{\mathrm{x}}(\tfrac{\pi}{2})^{(j)}\, U_{+}\, R_{\mathrm{x}}(\pi)^{(j)}\, U_{-}\, R_{\mathrm{x}}(\tfrac{\pi}{2})^{(j)}\,, \tag{C.19}$$

with $U_{\pm}$ the unitary evolution under Hamiltonian $\hat{H}_{\pm 1}$ (Eq. C.3). We compute the z-expectation value of nuclear spin j after applying $U_{\mathrm{xx}}^{(\mathrm{el}\rightarrow j)}$ (starting in initial state given by Eq. C.4):

$$\left\langle \hat{I}_{\mathrm{z}}^{(j)} \right\rangle = \frac{1}{2} p_j \cos\left(2\pi\Delta_j\, t\right). \tag{C.20}$$

Note that for some experiments in this work, the final $\pi/2$-rotation was performed along the $-x$-axis instead of the x-axis, which leads to a minus sign on the signal, but has no impact on the frequency or amplitude. The frequency (in Hz) is defined as the hyperfine shift referred to in the main text:

$$\Delta_j = \frac{1}{2}(A_j^{-} - A_j^{+})\,, \tag{C.21}$$

Δ_j provides a high-resolution measurement of the frequency shift due to the electron-nuclear hyperfine interaction. In this work, the function of this measurement is to distinguish different spins with similar precession frequencies. That is, Δ_j provides a high-resolution label for the spins.

An additional application is to perform precise spectroscopy of the system to determine the hyperfine interaction, for example for comparison to density functional theory calculations[13] or to determine the Hamiltonian parameters for developing precise quantum control. Next, we analyze the relation of Δ_j to the hyperfine parameters.

We use the spin frequencies $A_j^{\pm}$ introduced in Eq. C.3, but now allow for a slight misalignment of the external magnetic field away from the NV-axis (z-axis):

$$\begin{aligned}\Delta = &\frac{1}{2}\sqrt{(\gamma_{\mathrm{c}}B_{\mathrm{z}} - A_{\mathrm{zz}})^2 + (\gamma_{\mathrm{c}}B_x - A_{\mathrm{zx}})^2 + (\gamma_{\mathrm{c}}B_y - A_{zy})^2} \\ &- \frac{1}{2}\sqrt{(\gamma_{\mathrm{c}}B_{\mathrm{z}} + A_{\mathrm{zz}})^2 + (\gamma_{\mathrm{c}}B_x + A_{\mathrm{zx}})^2 + (\gamma_{\mathrm{c}}B_y + A_{zy})^2}\,,\end{aligned} \tag{C.22}$$

where we omit the spin-subscript j for readability. Here, B_x and B_y are the perpendicular field components. Note that for simplicity we use a purely geometric argument and do not take into account spin mixing for the eigenstates (i.e. the eigenstates are set as the electron and nuclear spin states), which would introduce additional (small) frequency shifts. Equation C.22 shows that measuring Δ for different magnetic field vectors makes it possible to determine the hyperfine parameters, given that the field components are known. As the magnetic field components generally are not exactly known, we now analyze various situations and approximations.

For a strong field aligned along the z-axis, the perpendicular hyperfine components are a small perturbation:

$$\Delta = \frac{1}{2}\left(\sqrt{(\gamma_c B_z - A_{zz})^2 + {A_\perp}^2} - \sqrt{(\gamma_c B_z + A_{zz})^2 + {A_\perp}^2}\right) \tag{C.23}$$

$$\approx -A_{zz}\left(1 - \frac{{A_\perp}^2}{2(\gamma_c B_z - A_{zz})(\gamma_c B_z + A_{zz})}\right). \tag{C.24}$$

Equation C.23 shows that the measurement predominantly probes the hyperfine component parallel to the magnetic field. For the magnetic field used in this work ($B_z \sim 403$ G) and typical hyperfine values ($A_{zz} \sim A_\perp \sim 10$ kHz), the typical deviation from A_{zz}, due to $A_\perp$, is smaller than 0.03 % (less than 3 Hz). Note that the effect of a finite $A_\perp$ is suppressed because both terms in the top line of Eq. C.23 tend to shift in the same manner.

A misaligned field, with non-zero B_x and B_y components, in combination with a non-zero $A_\perp$, causes an additional frequency shift of Δ. Due to the sign difference in the first and second terms in Eq. C.22, the effect is relatively large and a perpendicular field of ~ 0.5 G causes a frequency shifts of a few Hz.

These results show that additional measurements and/or analysis are required to fully exploit the high-spectral-resolution measurements presented here for precision spectroscopy of the Hamiltonian parameters. However, this does not affect the capability used in this work to resolve different spins with high spectral resolution.

PULSE ERRORS

To investigate how pulse errors affect the measured frequency Δ, we model the first $\pi/2$-pulse and the spin-echo π-pulse on nuclear spin j as imperfect X-rotations with excitation probability f^2:

$$R_x(f)^{(j)} = \sqrt{1-f^2}\,\hat{\mathbb{1}} - i f \hat{I}_x^{(j)}, \tag{C.25}$$

leading to the adapted unitary (Eq. C.19):

$$U_{xx}^{(\mathrm{el}\to j)} = R_x(\tfrac{\pi}{2})^{(j)}\, U_+\, R_x(f_2)^{(j)}\, U_-\, R_x(f_1)^{(j)}. \tag{C.26}$$

We find the signal contains three frequency components:

$$\left\langle \hat{I}_z^{(j)} \right\rangle = \kappa_1 \cos(\Delta_j\, t) + \kappa_2 \cos(\omega_L\, t) + \kappa_3 \cos\left(\frac{1}{2} A_j^+\, t\right), \tag{C.27}$$

with $\kappa_1, \kappa_2, \kappa_3$ some real constants, determined by the pulse excitation probabilities f_1^2 and f_2^2. For perfect $\pi/2$-pulse and π-pulse, only the first term remains, corresponding to the hyperfine shift that we aim to measure. The second term arises from the spin-echo π-pulse not being effective, so that the hyperfine interaction with the electron spin cancels. The third term arises from the $\pi/2$-pulse not exciting the nuclear spin and the π-pulse creating some coherence, analogous to performing a Ramsey during the second half of the sequence (when the electron is in the $m_s = +1$ state). These spurious frequencies are easily identifiable in the signal, as ω_L and A_j^+ are typically > 100 kHz, while Δ_j ($\sim 1-50$ kHz) is tightly bound by the bandwidth of the RF pulses (~ 1 kHz). Furthermore, the second and third terms decay quickly ($T_2^\star$-limited), as the spin-echo is not effective. Hence, any signal remaining after ~ 10 ms contains only the Δ_j term of interest.

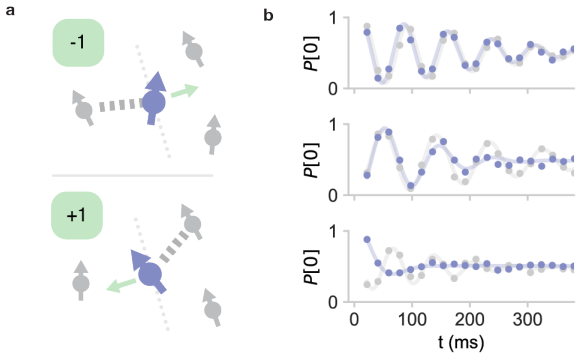

Figure C.5: **Electron-state-dependent dephasing a)** Schematic of the dephasing effect for a target nuclear spin (purple), coupled to a local spin bath (grey) under the electron-nuclear double resonance sequence (see Fig. 5.3). Due to the perpendicular hyperfine component (mint-green arrow), the nuclear quantisation axes change when the electron changes spin state (from $|-1\rangle$ to $|+1\rangle$). As a result, the nuclear spin couples differently to its environment in the first and second half of the spin-echo, limiting the effectiveness of the echo if the environment is in an unpolarised state. **b)** Experimental data of the electron-nuclear double resonance experiment (as in Fig. 5.3) for three different nuclear spins (C19, C18 and C5). The surrounding spin-bath is either initialised in a mixed state (purple) or polarised 'up' (grey). Solid lines are fits to the data (as in Fig. 5.3). For some spins (most notably C5), the described dephasing effect leads to a quick drop in coherence, which can be partially regained by polarising the bath. This effect can be accurately modelled based on the extracted spin positions (see Fig. C.6). The data is corrected for the difference in global and selective polarisation direction.

ELECTRON-STATE-DEPENDENT DEPHASING

At finite B_z field, a particular dephasing mechanism that we denote electron-state-dependent dephasing (ESD), prevents nuclear spins from attaining the full T_2 coherence time. The magnitude of this effect is highly spin-dependent and can be accurately modelled using the nuclear-spin interactions obtained here. As detailed in Ref.[2], the spin-spin couplings ($C_{ij} \neq C_{ij}^{+} \neq C_{ij}^{-}$), weakly depend on the electron spin state, resulting in an effective frequency shift of all spin-spin couplings during the electron-nuclear double resonance sequence (Eq. C.19):

$$\Delta C_{ij} = \frac{1}{2}\left(C_{ij}^{+} - C_{ij}^{-}\right). \tag{C.28}$$

The dominant contribution is due to a change in the nuclear quantisation axes[2]:

$$\Delta C_{ij} \approx \frac{(A_{zx}^{(i)} + A_{zx}^{(j)})C_{zx}^{(ij)} + (A_{zy}^{(i)} + A_{zy}^{(j)})C_{zy}^{(ij)}}{\gamma_c B_z}, \tag{C.29}$$

with $A_{z\alpha}^{(i)}$ and $C_{z\alpha}^{(ij)}$ the perpendicular components of the hyperfine and nuclear-nuclear dipole tensor, respectively. The key insight is that the couplings of spin j to the network change between the first and second half of the spin-echo sequence. With the surrounding spin bath in a mostly mixed state (Eq. C.4), the quasi-static noise is not completely eliminated by the spin echo, as the ΔC_{ij}-terms do not cancel. Typically these terms do not exceed ~ 2 Hz (see also Ref.[2]), but for some spins with strong couplings to the electron spin

($A_\perp \gg 10$ kHz), the effect leads to a loss of coherence comparable to $T_2^\star$ decay (see Fig. C.6, C5 and C6).

To model the effect on the measured signal, we consider two limiting cases: one where the surrounding spin bath is in a completely polarised state (denoted by 'up' or 'down' in Fig. C.6) and one in which it is in a mixed state. Considering the effect of N nuclear spins on a target nuclear spin j, we find that the signal frequency gets shifted when the bath is polarised ($p_i = \pm 1 \,\forall\, i$ in Eq. C.4).

$$\left\langle \hat{I}_z^{(j)} \right\rangle = \frac{1}{2} p_j \cos\left[2\pi(\Delta_j \pm \phi_j)\, t\right], \quad \phi_j = \sum_i^N \frac{\Delta C_{ij}}{2}, \tag{C.30}$$

where the $\pm$-sign is given by the direction of the bath polarisation ('up' or 'down').

Next, assuming a mixed state for the bath spins ($p_i = 0 \,\forall\, i$ in Eq. C.4), we find:

$$\left\langle \hat{I}_z^{(j)} \right\rangle = \frac{1}{2} p_j \cos\left(2\pi\Delta_j\, t\right) \prod_{i=1}^{N} \cos\left(2\pi \frac{\Delta C_{ij}}{2}\, t\right) \tag{C.31}$$

In this case, the coupled spins will cause frequency beatings on the signal, leading to a decay:

$$\left\langle \hat{I}_z^{(j)} \right\rangle \approx \frac{1}{2} p_j \cos\left(2\pi\Delta_j\, t\right) e^{-\left(t/T_{2,\mathrm{ESD}}\right)^2} \tag{C.32}$$

with characteristic decay time:

$$T_{2,\mathrm{ESD}} = \sqrt{\frac{2}{\sum_{i=1}^{N}\left(2\pi \frac{\Delta C_{ij}}{2}\right)^2}} \tag{C.33}$$

Figure C.6b-e shows the experimental observation of the ESD effect for seven selected spins in both polarised and mixed spin bath conditions. These conditions are achieved by using either the global PulsePol sequence or a selective SWAP initialisation of the target nuclear spin (Methods). The obtained signals display significant coherence and frequency variation between spins and depend strongly on the state of the bath.

To model this behaviour, we first extract the frequency, amplitude, phase and coherence time of the 'up' data. Next, we calculate how the signal should change for different bath states due to the ESD effect, using Eqs. C.31 and C.30 to generate a spin-specific model. To this end, the ΔC_{ij} for each of the spins are calculated according to Eq. C.29, based solely on the known spin positions (assuming dipolar hyperfine coupling). Figure C.6f-i shows the modelled signal, for which we observe good qualitative agreement for each of the spins. The difference in initial phase between 'up' and 'mixed' data for some spins (Fig. C.6b,e) is due to a difference in polarisation direction between the selective and global initialisation sequences. Furthermore, using experimentally determined values of ${\Delta C_{ij}}^2$ (since we know Eq.C.29 to be approximate), further diminishes the discrepancy between model and data.

Typically, spins that are more strongly coupled to the electron spin (e.g. panel b) show a quick decoherence behaviour for unpolarized environments(see Eq. C.29). For more weakly coupled spins, the decoherence becomes determined by the basic T_2-echo time. For such more weakly coupled spins as well for highly polarised baths, we expect multiple refocussing pulses can further enhance coherence and therefore the resolution of the sequence.

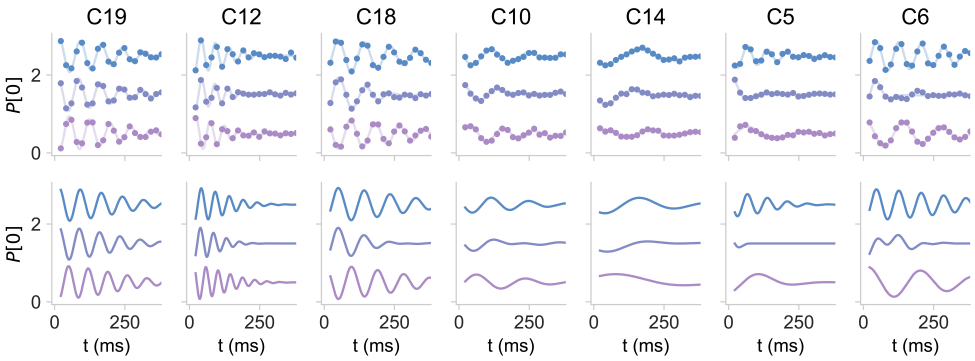

Figure C.6: **Simulating electron-state-dependent dephasing for various nuclear spins.** Top: Experimental data (as in Fig. C.5) for seven different nuclear spins after initialising the spin bath 'up' (blue), 'down' (pink) or in a 'mixed' (purple) state (offset for clarity). The 'mixed' signals exhibit a highly spin-dependent coherence decay, while polarising the bath leads to increased coherence and a shift in the frequency. The experimental data are corrected for difference in polarisation direction for selective and global initialisation (which leads to a minus sign). Bottom: Analytical model for the signal of the spins, obtained by evaluating Eqs. C.31 and C.30, reproducing both the observed coherence decay and frequency shifts qualitatively, taking into account the couplings to all other 49 spins. The amplitude, phase, frequency and (limiting) T_2-decay of the base signal are extracted from a fit to the 'up' data.

ELECTRON-NUCLEAR DOUBLE RESONANCE SPECTROSCOPY

Next, we discuss how to use the electron-nuclear double resonance sequence to perform *direct* high-resolution spectroscopy of nuclear spins. Since the sequence only enhances coherence for spins resonant with the RF-pulses, we take multiple data sets at varying RF frequencies and stitch them together to create a larger scan. To this end, we implement the sequence sketched in Fig. C.7a. For the spectroscopy data in Fig. C.7b, we sweep frequency $\mathrm{RF}_1 \approx \omega_\mathrm{L} - \Delta$ from $\sim 434 - 436$ kHz (RF_1 in the 'xx'-block), keeping the pulse Rabi frequency at 0.38 kHz and updating the DD readout parameters as ('RO'-block in Fig. C.7):

$$\tau_\mathrm{DD} = \frac{k}{4\,(\omega_\mathrm{L} - \Delta/2)}, \tag{C.34}$$

with $k = 41$ the DD resonance order and keeping the number of pulses fixed to $N = 208$. The update rule ensures that the readout remains resonant with the frequency of interest (A_1)[3,14]. For each frequency, we sweep the double resonance evolution time t (Fig. C.7a) up to 200 ms (bandwidth of 200 Hz) and compute the PSD, which we stitch together to create the large bandwidth, high resolution spectroscopy data (Fig. C.7b).

The spectral region interrogated in Fig. C.7b is known to contain four nuclear spins (dotted lines), three of them being visible in the signal with almost transform-limited linewidth ($\sim$ 10 Hz). The amplitude of the signal is determined by a combination of polarisation efficiency (see Eq. C.20) and readout fidelity[3,8]. The colored arrow denotes suspected aliasing, which can be easily mitigated by increasing the sampling bandwidth.

The double resonance spectroscopy presented here can be readily implemented for

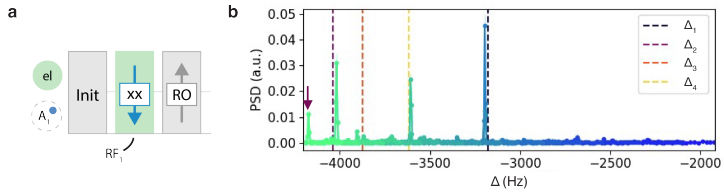

Figure C.7: **Direct nuclear spectroscopy. a)** Experimental sequence for performing double resonance spectroscopy directly with the electronic quantum sensor (as in Fig. 5.3). The pulses and readout can be tuned so that only signal from spins in a frequency region of interest (A) is picked up. This region of interest is then swept over a larger region to create a stitched spectrum. **b)** Stitched spectrum (color shading shows individual datasets) as a function of hyperfine shift Δ, demonstrating transform-limited spectral resolution (~ 10 Hz). Dashed lines denote the estimated Δ_i of four previously characterized spins in the frequency region. The purple arrow denotes a spurious alias, corresponding to Δ_1. The error is smaller than the data points (calculated according to Ref. [15]).

other color center platforms [16–19] to interrogate the nuclear spin environment with high spectral resolution. By using DDrf readout sequences, the protocol is further simplified and can be used for nuclear spins with small perpendicular hyperfine coupling [5].

ELECTRON-NUCLEAR DOUBLE RESONANCE OF THE 50-SPIN-NETWORK

We perform the electron-nuclear double resonance sequence on all known spins in the network. As we can only access a number of spins directly, we implement the electron-nuclear double resonance block with a spin chain of varying length (See Fig. C.8). The used sequence for each spins can be found in Table C.1.

To retrieve the absolute signal frequency from undersampled data, we take at least two data sets with different bandwidths and sampling rates [20]. Next, we correct for aliasing by minimizing the mean squared error between the multiple measurements, and selecting the most likely alias. We use prior knowledge of the $m_s = -1$ frequency of the spin to limit this analysis to a frequency range of 400 Hz around the expected resonance.

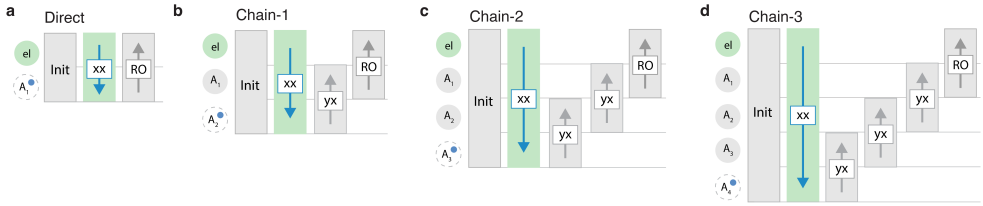

Figure C.8: **Electron-nuclear double resonance of the spin-network. a-d)** Pulse sequences used in this work to extract Δ_i for all spins in Table C.1. We try to use chains of minimum length to limit experimental time and complexity. The exact sequence that was used is denoted in the 'Readout' column in Table C.1.

The values obtained for Δ_i are shown in Table C.1, where the error denotes the weighted error on the mean of multiple measurements (whose error is determined from an exponentially decaying fit). For many of the previously characterised spins [2], we find good agreement

with Ramsey measurements. However, for some spins (most notably C19), we find a deviation that cannot be explained by off-axis fields or a correction due to the (reported) Fermi contact term [13]. Further research is needed to identify the discrepancy between the Ramsey method used in Ref. [2] and values reported in this work.

C.5. NETWORK RECONSTRUCTION ALGORITHM

The network mapping procedure outlined in the Methods section relies on the (pseudo) function CheckVertex(w, T). Here, we present pseudo-code for the procedure of checking whether vertex w has already been mapped in T.

```
function CHECKVERTEX(w, T)                ▷ Checks if w was already characterised and returns the duplicate vertex

    unique = True                          ▷ Boolean, keeps track whether vertex w is unique
    duplicate = None                       ▷ Specifies duplicate vertex if applicable, otherwise None

    for k in T do
        if |A_w − A_k| < σ_A then          ▷ Compare frequency of w to mapped vertices, σ_A denotes uncertainty
            unique = False                 ▷ w and k might be duplicates

            V_0^w = {w}                    ▷ Create a spanning tree T_w with root w
            i = 0                          ▷ Keeps track of depth of search
            j = 0                          ▷ Keeps track of number of equivalent edges
            while not unique and duplicate == None and i < maxdepth do
                for each vertex v^w ∈ V_i^w and v^k ∈ V_i^k do   ▷ Find equivalent vertex in tree T_k with root k
                    Δ = MeasureDelta(v^w)  ▷ Electron-nuclear double resonance measurement
                    if |Δ − Δ_k| > σ_Δ then   ▷ σ_Δ denotes uncertainty
                        unique = True      ▷ w is unique, different Δ
                    end if
                    if |Δ − Δ_k| < σ_Δ and σ_Δ < threshold then
                        unique = False     ▷ w is equal to k, similar Δ unlikely
                        duplicate = k
                    end if
                    for each vertex r^k ∈ V_{i+1}^k do   ▷ Get known neighbours of k from T_k
                        C = MeasureCoupling(v^w, A_r^k)   ▷ Between vertex v^w in T_w and r^k's frequency in T_k
                        if |C − C_vr^k| > σ_C then   ▷ Compare to edge in T_k
                            unique = True  ▷ w is unique, different spanning tree
                        end if
                        if |C − C_vr^k| < σ_C and σ_C < threshold then   ▷ Measurement has reasonable uncertainty
                            j = j + 1      ▷ Another edge of the spanning tree coincides
                            create r^w in T_w   ▷ Expand T_w
                            A_r^w = A_r^k
                            C_vr^w = C
                            add r^w to V_{i+1}^w in T_w
                        end if
                    end for
                end for
                i = i + 1
            end while
            if j > equaledges then
                unique = False
                duplicate = k              ▷ w and k are the same vertex, similar spanning tree unlikely
            end if
        end if
    end for

    return unique, duplicate
end function
```

The function starts by comparing the ($T_2^\star$-limited) frequency A_w of vertex w to the fre-

quencies of all mapped vertices in T. If the frequencies coincide within the measurement uncertainty ($\sigma_A \sim 100$ Hz) for a vertex k, we initiate a procedure to check whether w is that vertex. We do this by comparing information we have on vertex k and its surroundings to specific measurements taken from w. In particular, we measure the spanning tree T_w with root w, and compare it to the spanning tree T_k with root k (for some maximum depth). If all couplings (C_{ij}, up to some threshold 'equaledges') and hyperfine frequency shifts (Δ_i) of the two spanning trees are the same, we conclude w and k are the same vertex. If we measure a single deviation, we conclude w must be unique. If the procedure is inconclusive, for example because the uncertainty of all measurements is large, 'duplicate' remains `None`.

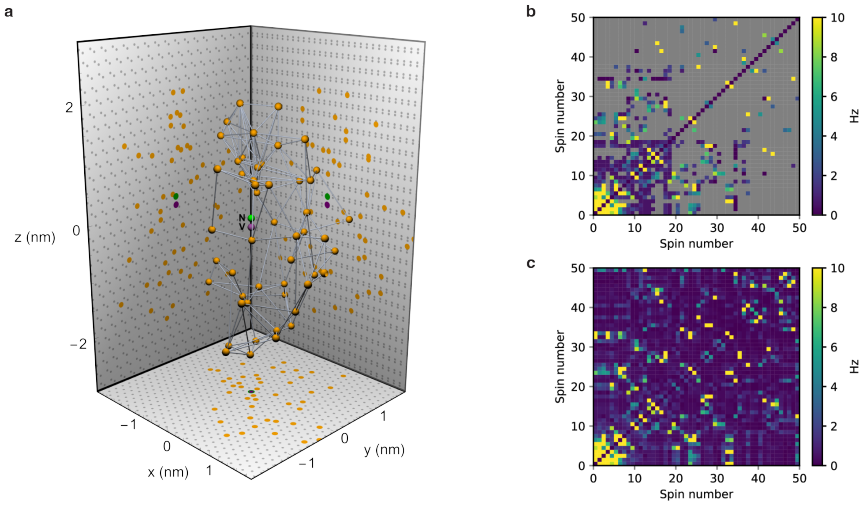

Figure C.9: **Spatial structure of the 50-spin network. a)** Most likely positions for the 50 ^{13}C nuclear spins mapped in this work. Couplings larger than 3 Hz are visualised by the grey connections. The NV vacancy site is placed at the origin. **b)** Measured coupling matrix. Elements that were not measured, or did not return a clear signal (due to spectral crowding) are colored grey. **c)** Predicted coupling matrix, based on the most likely spin positions (Methods).

REFERENCES

[1] J. Randall *et al.*, *Many-body–localized discrete time crystal with a programmable spin-based quantum simulator,* Science **374**, 1474 (2021).

[2] M. H. Abobeih *et al.*, *Atomic-scale imaging of a 27-nuclear-spin cluster using a quantum sensor,* Nature **576**, 411 (2019).

[3] T. H. Taminiau *et al.*, *Detection and Control of Individual Nuclear Spins Using a Weakly Coupled Electron Spin,* Phys. Rev. Lett. **109**, 137602 (2012).

[4] I. Schwartz *et al.*, *Robust optical polarization of nuclear spin baths using Hamiltonian engineering of nitrogen-vacancy center quantum dynamics,* Sci. Adv. **4**, eaat8978 (2018).

[5] C. E. Bradley *et al.*, *A Ten-Qubit Solid-State Spin Register with Quantum Memory up to One Minute,* Phys. Rev. X **9**, 031045 (2019).

[6] D. D. B. Rao, A. Ghosh, D. Gelbwaser-Klimovsky, N. Bar-Gill and G. Kurizki, *Spin-bath polarization via disentanglement,* New J. Phys. **22**, 083035 (2020).

[7] T. Villazon, A. Chandran and P. W. Claeys, *Integrability and dark states in an anisotropic central spin model,* Phys. Rev. Research **2**, 032052 (2020).

[8] M. H. Abobeih *et al.*, *One-second coherence for a single electron spin coupled to a multi-qubit nuclear-spin environment,* Nat Commun **9**, 2552 (2018).

[9] H. P. Bartling *et al.*, *Entanglement of Spin-Pair Qubits with Intrinsic Dephasing Times Exceeding a Minute,* Phys. Rev. X **12**, 011048 (2022).

[10] V. S. Perunicic, C. D. Hill, L. T. Hall and L. Hollenberg, *A quantum spin-probe molecular microscope,* Nat Commun **7**, 12667 (2016).

[11] A. M. Tyryshkin *et al.*, *Electron spin coherence exceeding seconds in high-purity silicon,* Nat. Mater. **11**, 143 (2012).

[12] E. Bauch *et al.*, *Ultralong Dephasing Times in Solid-State Spin Ensembles via Quantum Control,* Phys. Rev. X **8**, 031025 (2018).

[13] A. P. Nizovtsev *et al.*, *Non-flipping ^{13} C spins near an NV center in diamond: Hyperfine and spatial characteristics by density functional theory simulation of the C_{510} [NV]H_{252} cluster,* New J. Phys. **20**, 023022 (2018).

[14] C. L. Degen, F. Reinhard and P. Cappellaro, *Quantum sensing,* Rev. Mod. Phys. **89**, 035002 (2017).

[15] P. Hoyng, *An error analysis of power spectra,* Astron. & AstroPhys. **47**, 449 (1976).

[16] R. Debroux *et al.*, *Quantum Control of the Tin-Vacancy Spin Qubit in Diamond,* Phys. Rev. X **11**, 041041 (2021).

[17] A. Sipahigil *et al.*, *An integrated diamond nanophotonics platform for quantum-optical networks,* Science **358**, 847 (2016).

[18] A. Bourassa *et al.*, *Entanglement and control of single nuclear spins in isotopically engineered silicon carbide,* Nat. Mater. **19**, 1319 (2020).

[19] A. Durand *et al.*, *Broad Diversity of Near-Infrared Single-Photon Emitters in Silicon,* Phys. Rev. Lett. **126**, 083602 (2021).

[20] J. M. Boss, K. S. Cujia, J. Zopes and C. L. Degen, *Quantum sensing with arbitrary frequency resolution,* Science **356**, 837 (2017).